University of Calgary

PRISM Repository **https://prism.ucalgary.ca**

The Vault Open Theses and Dissertations

2016

Excited-State Studies with the Constricted Variational Density Functional Theory (CV-DF) Method

Seidu, Issaka

Seidu, I. (2016). Excited-State Studies with the Constricted Variational Density Functional Theory (CV-DF) Method (Doctoral thesis, University of Calgary, Calgary, Canada). Retrieved from https://prism.ucalgary.ca. doi:10.11575/PRISM/26035

http://hdl.handle.net/11023/2882

Downloaded from PRISM Repository, University of Calgary

UNIVERSITY OF CALGARY

Excited-State Studies with the Constricted Variational Density Functional Theory (CV-DFT) Method

by

Issaka Seidu

A THESIS

SUBMITTED TO THE FACULTY OF GRADUATE STUDIES

IN PARTIAL FULFILLMENT OF THE REQUIREMENTS FOR THE

DEGREE OF DOCTOR OF PHILOSOPHY

GRADUATE PROGRAM IN CHEMISTRY

CALGARY, ALBERTA

APRIL, 2016

© Issaka Seidu 2016

Abstract

Theoretical calculations have played a vital role in understanding electronic properties of chemically and electronically relevant systems. Some of the roles played by theoretical approaches include the assignment and interpretation of spectra of chemical species such as the transition metal (TM) complexes. However, before these theoretical methods can be used as predictive tools in the chemical analysis of compounds for which experimental results are unavailable, the performance and scope of applicability of these methods must be well understood and improvements made wherever necessary.

In this work, the Constricted Variational Density Functional Theory (CV-DFT) method is used in detailed analyses of excited-state properties of TM and other chemical species. Studies are carried out with the CV-DFT method in areas where the adiabatic Time-Dependent Density Functional Theory (ATD-DFT) method have been found insufficient, such as charge transfer (CT) and Rydberg excitations, as well as areas where ATD-DFT performed well. This was done to ensure that, the CV-DFT method not only show good performance for excitations poorly described by ATD-DFT but those that are sufficiently described as well. For a better understanding of the strengths and weaknesses of the CV-DFT methods, our calculated results are compared to experimental and/or high level $ab\ initio$ results whenever available.

Finally, an extension is made to CV-DFT for double excitation. These double excitations are known to be important for excited-state studies in conjugated systems such as the polyenes. Future work will be carried to examine the performance of this method.

We find, in general, that CV-DFT shows accurate performance for excitations that are poorly described by the ATD-DFT method, and comparable performance for excitations in which ATD-DFT performs adequately.

Preface

Five of the six result chapters (Chapters 3–6 and 8) included in this thesis are published and listed as follows;

Chapter 3: Seidu, I.; Zhekova, H. R.; Seth, M.; Ziegler, T. "Calculation of Exchange Coupling Constants in Triply-Bridged Dinuclear Cu(II) Compounds Based on Spin-Flip Constricted Variational Density Functional Theory", The Journal of Physical Chemistry A (2012), *116*, 2268–2277.

Chapter 4: Seidu, I.; Seth, M.; Ziegler, T. "Role Played by Isopropyl Substituents in Stabilizing the Putative Triple Bond in Ar′EEAr′ [E = Si, Ge, Sn; Ar′ = C_6H_3-2,6-(C_6H_3-2,6-Pr^i_2)$_2$] and Ar*PbPbAr* [Ar* = C_6H_3-2,6-(C_6H_2-2,4,6-Pr^i_3)$_2$]", Inorganic Chemistry (2013), *52*, 8378–8388.

Chapter 5: Seidu, I.; Krykunov, M.; Ziegler, T. "Applications of Time-Dependent and Time-Independent Density Functional Theory to Rydberg Transitions", The Journal of Physical Chemistry A (2015), *119*, 5107–5116.

Chapter 6: Seidu, I.; Krykunov, M.; Ziegler, T. "Applications of Time-Dependent and Time-Independent Density Functional Theory to Electronic Transitions in Tetrahedral d^0 Metal Oxides", The Journal of Chemical Theory and Computation (2015), *11*, 4041–4053.

Chapter 8: Seidu, I.; Krykunov, M.; Ziegler, T. "The formulation of a constricted variational density functional theory for double excitations", Molecular Physics (2014), *112*, 661–668.

Chapter 7 is in the preparation stage. When completed, it would be submitted to a journal to be considered for publication.

The work presented in this thesis had contributions from Dr. Tom Ziegler, Dr. Mykhaylo Krykunov, Dr. Michael Seth, and Issaka Seidu. Their individual contributions are as follows;

Tom Ziegler: Development of CV-DFT theory, design and supervision of the research work presented in chapters 3, 4, 5, 6, and 8.

Michael Seth: Development of Spin-flip codes used in chapters 3 and 4.

Mykhaylo Krykunov: Development of CV-DFT codes used in chapters 6 and 7.

Issaka Seidu: Design of the projects, application of the quantum chemical codes, analyses of results, derivation of formulas within CV-DFT and preparation of manuscripts for publication.

Mykhaylo Krykunov and Michael Seth were not directly involved in any of work presented in this thesis. Tom Ziegler was more involved in the analyses of the results presented in chapter 6. He was also more involved in the preparation of the manuscript as understanding the electronic structure of the tetraoxo transition metal complexes was his life-long passion.

Acknowledgements

I would like to express my gratitude first and foremost to my supervisor, the late Dr. Tom Ziegler, for giving me the opportunity to come work with him, and for his guidance, encouragement and friendship. For that I am forever grateful. I would like to thank my current supervisor Dr. Arvi Rauk for taking up the responsibility at the very end and for his valuable advice and support. I am grateful for the valuable input of my supervisory committee, Dr. Dennis Salahub who has so far played the role of a co-supervisor and Dr. Justin MacCallum for accepting to serve as a member of my supervisory committee without any hesitations. Also, I would like to thank the members of my qualifying and thesis examination committee, Dr. Simon Trudel, Dr. David Cramb, Dr. Barry Sanders and Dr. Marcel Nooijen.

I am grateful for the friendship of the past and present members of Ziegler Research group: Young Choon, Florian, Mykhaylo, Hristina, Michael, Luke, Sylvester, Linta, Maxim, Tebike, Elizabeth, as well as members of the Rauk Research group: Stanley, Anahit, Banafsheh and Zohreh. Thank you all for all the great moments. I am especially grateful to Dr. Michael Seth and Dr. Mykhaylo Krykunov, for their collaborations on the work presented in this thesis.

I would like to acknowledge the financial support of NSERC and the Chemistry Department at the University of Calgary. The computational resources used in this work was provided by WESTGRID through Compute Canada. I am grateful for the help of the administrative staff: Bonnie King, Janice Crawford, Stephanie Olsen, Bethany Lane, Sarah Boschman as well as all members of the Chemistry Department.

Lastly, I would like to thank my family especially my parents, as well as all my friends in Ghana and Calgary for their support and love. A special thanks to the Aboagye family especially Irene. Thanks for your love and support.

Dedication

To My Parents

Table of Contents

Abstract . . . i
Preface . . . ii
. . . iii
Acknowledgements . . . iv
Dedication . . . v
Table of Contents . . . vi
List of Tables . . . ix
List of Figures . . . xii
List of Symbols . . . xv
1 Introduction . . . 1
1.1 General Introduction to Excited States and Excited-State Studies within Density Functional Theory . . . 1
1.2 Types of Excitations . . . 3
1.3 Thesis Objectives . . . 7
2 Theoretical Background . . . 9
2.1 Introduction . . . 9
2.2 Density Functional Theory (DFT) method: Kohn-Sham equations . . . 10
2.3 Time-Dependent DFT (TD-DFT) method . . . 12
2.4 ΔSCF-DFT method . . . 15
2.5 Constricted Variational DFT (CV-DFT) method . . . 16
3 Calculation of Exchange Coupling Constants in Triply-Bridged Binuclear Cu(II) Compounds Based on Spin-Flip Constricted Variational Density Functional Theory . . . 23
3.1 Introduction . . . 23
3.2 Theoretical Details . . . 25
3.2.1 Computational Method . . . 25
3.2.2 Computational Details . . . 27
3.2.3 Molecular Models . . . 27
3.3 Results and Discussion . . . 30
3.3.1 Calculated J values based on SF-CV(2)-DFT . . . 37
3.4 Concluding Remarks . . . 39
4 Role Played by Isopropyl Substituents in Stabilizing the Putative Triple Bond in Ar′EEAr′ [E = Si, Ge, Sn; Ar′ = C_6H_3-2,6-(C_6H_3-2,4-Pr^i_2)$_2$] and Ar*PbPbAr* [Ar* = C_6H_3-2,6-(C_6H_2-2,4,6-Pr^i_3)$_2$] . . . 41
4.1 Introduction . . . 41
4.2 Theoretical Details . . . 43
4.2.1 Computational Method . . . 43
4.2.2 Computational Details . . . 45
4.2.3 Molecular models . . . 46
4.3 Results and Discussion . . . 46
4.3.1 Fragment Orbitals . . . 46
4.3.2 Molecular Orbitals . . . 49
4.3.3 NOCV-ETS analysis of trans-bent compounds based on ArE fragments with a doublet state . . . 51

4.3.4 Singlet-triplet Gap . . . 62
4.3.5 Diradical character . . . 63
4.4 Concluding Remarks . . . 65
5 Application of Time-Dependent and Time-Independent Density Functional Theory to Rydberg Transitions . . . 67
5.1 Introduction . . . 67
5.2 Theoretical Details . . . 69
5.2.1 Computational Methods . . . 69
5.2.2 Computational Details . . . 69
5.2.3 Molecular Models . . . 71
5.3 Results and Discussion . . . 71
5.3.1 TD-DFT Calculations on Rydberg Excitations . . . 71
5.3.2 ΔSCF Calculations on Rydberg Excitations . . . 74
5.4 Concluding Remarks . . . 84
6 Application of Time-Dependent and Time-Independent Density Functional Theory to Electronic Transitions in Tetrahedral d^0 Metal Oxides . . . 86
6.1 Introduction . . . 86
6.2 Theoretical Details . . . 88
6.2.1 Computational Method . . . 88
6.2.2 Computational Details . . . 89
6.2.3 Molecular Models . . . 90
6.3 Results and Discussion . . . 90
6.4 Concluding Remarks . . . 104
7 Assessing the CV-DFT Method for Octahedral Transition Metal Complexes . . . 106
7.1 Introduction . . . 106
7.2 Theoretical Details . . . 107
7.2.1 Computational Details . . . 107
7.2.2 Molecular Models . . . 108
7.3 Results and Discussion . . . 109
7.4 Concluding Remarks . . . 122
8 The formulation of a constricted variational density functional theory for double excitations . . . 124
8.1 Introduction . . . 124
8.2 The constricted variational density functional theory applied to a single transition . . . 125
8.2.1 Generation of excited-state orbitals for a single electron transition 125
8.2.2 Expressing excited-state densities for single electron excitation . 128
8.2.3 Evaluating excitation energies for single electron transitions . . 129
8.3 Double Excitations . . . 130
8.3.1 Generating excited-state orbitals for a double electron transition 130
8.3.2 Expressing excited-state densities for double excitations . . . 131
8.3.3 Evaluating excitation energies for double electron transitions . . 132
8.3.4 Optimization of $R^{I,J}$ and $\tilde{U}^J$ . . . 133
8.3.5 Simplified second-order theory for double excitations . . . 134
8.4 Concluding remarks . . . 136
9 Summary and Outlook . . . 137
A First Appendix . . . 141

B Second Appendix 142
C Third Appendix 143
D Fourth Appendix 144
E Fifth Appendix 147
F Sixth Appendix 148
Bibliography 149
Copyright Permissions 192

List of Tables

3.1 Singlet and Triplet Microstates for Binuclear Triply-Bridged Cupper(II) Compounds in the C_s Symmetry 34
3.2 Singlet and Triplet Microstates for Binuclear Triply-Bridged Cupper(II) Compounds without Symmetry 35
3.3 Lower Excited States for Complex 1 Based on SF-CV(2)-DFT Calculations Using LDA-VWN Functional 35
3.4 Lower Excited States for Complex 2 Based on SF-CV(2)-DFT Calculations Using LDA-VWN Functional 35
3.5 Lower Excited States for Complex 3 Based on SF-CV(2)-DFT Calculations Using LDA-VWN Functional 36
3.6 Lower Excited States for Complex 4 Based on SF-CV(2)-DFT Calculations Using LDA-VWN Functional 36
3.7 Lower Excited States for Complex 5 Based on SF-CV(2)-DFT Calculations Using LDA-VWN Functional 36
3.8 List of the binuclear triply-bridged Cu(II) compounds, the calculated ΔE_{ST} values (SF-CV(2)-DFT), the values obtained from the BS-DFT approach and the experimental values in cm^{-1}. 38

4.1 ETS[a] Analysis for Trans-bent Ar′SiSiAr′ Carried Out with Different Functionals (Energies in kcal/mol) 52
4.2 ETS[a] Analysis for Trans-bent Compounds Carried Out with the BP86 Functional for the Real Systems (Energies in kcal/mol) 53
4.3 ETS[a] Analysis for Trans-bent ArEEAr Model Systems Carried Out with the BP86 Functional (Energies in kcal/mol) 54
4.4 NOCV[a] Contributions[b] to ΔE_{orb} [c] for the Trans-bent Compounds Carried Out with the BP86 Functional for the Real Systems (Energies in kcal/mol) 55
4.5 NOCV[a] Contributions to ΔE_{orb} [b] for the Trans-bent ArEEAr[c] Model Compounds Carried Out with the BP86 Functional (Energies in kcal/mol) 59
4.6 NOCV[a] Contributions[b] to ΔE_{orb} [c] for the Trans-bent Ar′SiSiAr′ [c] Carried Out with different Functionals (Energies in kcal/mol) 60
4.7 ETS[a] Analysis for Ar′SiSiAr′, where the angle (θ) Ar′–Si–Si is varied (Energies in kcal/mol) 61
4.8 ETS[a] Analysis for Ar*PbPbAr*, where the angle (θ) Ar′–Pb–Pb is varied (Energies in kcal/mol) 61
4.9 Singlet–Triplet Energy Gap (ΔE_{ST}) for the four ArEEAr (E = Si, Ge, Sn, Pb) Compounds in their Ground-State Trans-Bent Geometry (Energies in eV) 62

5.1 Rydberg Singlet Excitation Energies[a] for N_2 Calculated with ATD-DFT/TDA Using an extended basis set[b] and five different functionals. . 72
5.2 IP[a] of N_2 and EA[a,b] of N_2^+ Calculated for ATD-DFT/TDA Using an extended basis set[c] and five different functionals. 73

5.3 Rydberg Singlet Excitation Energies[a] for N_2 Calculated with ΔSCF Using an extended basis set[b] and five different functionals. 78
5.4 IP[a] of N_2 and EA[a] of N_2^+ Calculated with ΔSCF Using an extended basis set[b] and five different functionals. 79
5.5 Rydberg Excitation Energies[a] for CO Calculated with ΔSCF Using an extended basis set[b] and five different functionals. 80
5.6 Rydberg Excitation Energies[a] for CH_2O Calculated with ΔSCF Using an extended basis set[b] and five different functionals. 80
5.7 Rydberg Excitation Energies[a] for C_2H_2 Calculated with ΔSCF Using an extended basis set[b] and five different functionals. 81
5.8 Rydberg Excitation Energies[a] for H_2O Calculated with ΔSCF Using an extended basis set[b] and five different functionals. 81
5.9 Rydberg Excitation Energies[a] for C_2H_4 Calculated with ΔSCF Using an extended basis set[b] and five different functionals. 82
5.10 Rydberg Excitation Energies[a] for Be Calculated with ΔSCF Using an extended basis set[b] and five different functionals. 83
5.11 Summary of RMSDs of Rydberg Excitation Energies[a] Calculated with ΔSCF Using an extended basis set[b] and five different functionals. . . . 84

6.1 Calculated Excitation Energies[a,b] for MnO_4^- Based on *ab initio* Wave Function Methods. 92
6.2 Calculated Excitation Energies[a,b] for MnO_4^- Based on DFT Methods. . 94
6.3 RMSDs for Tetraoxo Excitation Energies based on ATD-DFT and a TZ2P basis set.[a,b,c,d,e] 97
6.4 RMSDs for Tetraoxo Excitation Energies based on RSCF-CV(∞)-DFT and a TZ2P basis set.[a,b,c,d,e] 98
6.5 Calculated Excitation Energies based on RSCF-CV(∞)-DFT and ATD-DFT, for MnO_4^- and TcO_4^-.[a,b] 100
6.6 Comparisons between Multiplet Splittings Calculated by Different Methods for MnO_4^- and TcO_4^-.[a,b] 101
6.7 Calculated Triplet-Singlet Energies for the first three T_2 states in MnO_4^- and TcO_4^- based on RSCF-CV(∞)-DFT and ATD-DFT.[a,b] 103

7.1 Calculated Excitation Energies[a] for $Cr(CO)_6$ based on the RSCF-CV(∞)-DFT method. 111
7.2 Calculated IP and EA[a] for the two MLCT excitations in $Cr(CO)_6$ based on the RSCF-CV(∞)-DFT method. 113
7.3 Calculated Excitation Energies[a] for $[Fe(CN)_6]^{4-}$ based on the RSCF-CV(∞)-DFT method. 115
7.4 Calculated Excitation Energies[a] for $[Fe(CN)_5(py)]^{3-}$ based on the RSCF-CV(∞)-DFT method. 119

A.1 Lower Excited States for Complex 6 Based on SF-CV(2)-DFT Calculations Using LDA-VWN Functional 141
A.2 Lower Excited States for Complex 7 Based on SF-CV(2)-DFT Calculations Using LDA-VWN Functional 141
A.3 Lower Excited States for Complex 8 Based on SF-CV(2)-DFT Calculations Using LDA-VWN Functional 141

B.1 Lower Excited States for Complex 9 Based on SF-CV(2)-DFT Calculations Using LDA-VWN Functional 142
B.2 Lower Excited States for Complex 10 Based on SF-CV(2)-DFT Calculations Using LDA-VWN Functional 142
B.3 Lower Excited States for Complex 11 Based on SF-CV(2)-DFT Calculations Using LDA-VWN Functional 142

C.1 Rydberg Excitation Energies[a] for Mg Calculated with ΔSCF Using an extended basis set[b] and five different functionals. 143
C.2 Rydberg Excitation Energies[a] for Zn Calculated with ΔSCF Using an extended basis set[b] and five different functionals. 143

E.1 Calculated Excitation Energies[a] for $Cr(CO)_6$ based on the TD-DFT and DFT/MRI methods. 147
E.2 Calculated Excitation Energies[a] for $[Fe(CN)_5(py)]^{3-}$ based on the DFT/MRI and TD-DFT methods. 147

F.1 Conversion from Atomic unit to SI unit. 148

List of Figures and Illustrations

1.1 Excitation energy for $i \rightarrow a$ transition calculated as ΔE = IP(Neutral system) + EA(Positively charged system). 4

3.1 Structures of the 11 complexes studied, numbered in increasing order of experimental J values 28
3.2 Frontier SUMO orbitals $\bar{a}'$, $\bar{a}''$ with C_s symmetry and $1\bar{a}$, $2\bar{a}$ without symmetry for first 4 complexes with corresponding orbital energies. The SOMO orbitals a', a'' and $1a$, $2a$ are not shown because of they have a similar spatial distribution to their SUMO counterparts. 30
3.3 Frontier SUMO orbitals $\bar{a}'$, $\bar{a}''$ with C_s symmetry and $1\bar{a}$, $2\bar{a}$ without symmetry for complexes 5-8, with corresponding orbital energies. The SOMO orbitals a', a'' and $1a$, $2a$ are not shown because of they have a similar spatial distribution to their SUMO counterparts. 31
3.4 Frontier SUMO orbitals $\bar{a}'$, $\bar{a}''$ with C_s symmetry and $1\bar{a}$, $2\bar{a}$ without symmetry for complexes 9-11, with corresponding orbital energies. The SOMO orbitals a', a'' and $1a$, $2a$ are not shown because of they have a similar spatial distribution to their SUMO counterparts. 32
3.5 Frontier SUMO orbitals $\bar{a}'$, $\bar{a}''$ with C_s symmetry and $1\bar{a}$, $2\bar{a}$ without symmetry for complexes 1-4 using the BHLYP functional, with corresponding orbital energies. The SOMO orbitals a', a'' and $1a$, $2a$ are not shown because of they have a similar spatial distribution to their SUMO counterparts. 33

4.1 Orbital description as a function of the ∠R-E-E angle. 43
4.2 Structures of the four studied compounds from Si to Pb. Also given in each case is the ∠C–E–E, θ. 46
4.3 Fragment orbitals of ArE for E = Si and Pb with corresponding energy levels or E = Si, Ge, Sn, and Pb. 47
4.4 Combinations of σ and π fragment orbitals as a function of the trans-bending angle θ. 48
4.5 Molecular Orbitals of trans-bent ArEEAr for E = Si and Pb as well as the corresponding orbital energies for E = Si, Ge, Sn, and Pb. 50
4.6 Molecular Orbitals of linear ArEEAr for E = Si and Pb and the corresponding orbital energies for E = Si, ge, Sn, and Pb. 51

4.7 NOCV deformation densities for the trans-bent Si compounds based on doublet fragments. The NOCV deformation densities on the left are the individual α contributions and those on right are the sum of α and β contributions. The individual β contributions are omitted. (a) and (b) Contours of the π^y–NOCV deformation density with the corresponding energy contributions. The contour values are 0.003 au. (c) and (d) Contours of the σ^*/π–NOCV deformation density with the corresponding energy contributions. The contour values are 0.003 au. (e) and (f) Contours of the σ/π^*–NOCV deformation density with the corresponding energy contributions. The contour values are 0.003 au. Green represents positive contours and orange negative contours. 56
4.8 NOCVs for the three major contributions to $\Delta\rho_{\text{orb}}$ for trans-bent ArSiSiAr based on doublet fragments. 57
4.9 NOCV deformation densities for the trans-bent Pb compound based on doublet fragments. Contours of the σ–NOCV deformation density with the corresponding energy contributions. The NOCV deformation density, $\Delta\rho^{\sigma,\alpha}_{\text{orb}}$, is the α contribution and $\Delta\rho^{\sigma}_{\text{orb}}$ is the sum of α and β contributions. The β contribution, $\Delta\rho^{\sigma,\beta}_{\text{orb}}$, is omitted. The contour values are 0.002 au. Green represents positive contours and orange negative contours. 59

5.1 Energy terms contributing to the unrelaxed singlet excitation energy $\Delta\tilde{E}_{\text{S}}$ for the Rydberg transition $\psi_v \rightarrow \psi_r$, see eq (5.12), for 5 different functional and the TZ2P basis set. $\tilde{\text{IP}}(\text{N}_2, \psi_v)$ is the unrelaxed ionization potential, eq (5.8). $\tilde{\text{EA}}(\text{N}_2, \psi_r)$ is the unrelaxed electron affinity of N_2 with-respect-to electron capture by the Rydberg orbital ψ_r, eq (5.11). $\tilde{\text{EA}}(\text{N}_2^+, \psi_v, \psi_r, \text{S})$ is the unrelaxed electron affinity with-respect-to electron capture by the Rydberg orbital ψ_r of N_2^+ with a single electron in ψ_v when the product is a singlet, eq (5.9). (Throughout, $\psi_v = \sigma_g$ and $\psi_r = 3s\sigma_g$) 75
5.2 Energy terms contributing to the unrelaxed singlet excitation energy $\Delta\tilde{E}_{\text{S}}$ for the Rydberg transition $\psi_v \rightarrow \psi_r$, see eq (5.12), for 5 different functional and the extended basis set [1]. $\tilde{\text{IP}}(\text{N}_2, \psi_v)$ is the unrelaxed ionization potential, eq (5.8). $\tilde{\text{EA}}(\text{N}_2, \psi_r)$ is the unrelaxed electron affinity of N_2 with-respect-to electron capture by the Rydberg orbital ψ_r, eq (5.11). $\tilde{\text{EA}}(\text{N}_2^+, \psi_v, \psi_r, \text{S})$ is the unrelaxed electron affinity with-respect-to electron capture by the Rydberg orbital ψ_r of N_2^+ with a single electron in ψ_v when the product is a singlet, eq (5.9). (Throughout, $\psi_v = \sigma_g$ and $\psi_r = 3s\sigma_g$) 76

6.1 Orbital level diagram for d^0 tetraoxo complexes. 90
6.2 Frontier molecular orbitals of d^0 tetraoxo complexes. 91

7.1 Structures of the complexes studied. 108

7.2 $\Delta\rho$ associated with the $CrCO_6$, red signifies depletion and green shows accumulation of density. (a) The density change associated with the 1^1T_{1u} state. (b) exemplify the density redistribution associated with the 2^1T_{1u} state. (c) Densities accompanying the calculated 1^1T_{1g} state. (a) and (b) are MLCT-type transitions and (c) is an example of MC-type transition. 112
7.3 $\Delta\rho$ associated with the $Fe(CN)_6^{4-}$. (a) The density change associated with the 1^1T_{1g} state. (b) exemplify the density redistribution associated with the 3^1T_{1u} state. (c) Densities accompanying the calculated 3^1T_{1u} state. (a) is an example of MC-type transition, (b) and (c) are MLCT-type transitions. Red signifies loss and green shows gain in density. . . . 116
7.4 $\Delta\rho$ associated with the $[Fe(CN)_5(py)]^{3-}$. (a), (b), (c) and (d) represent the 1^1A_1, 1^1A_2, 1^1B_1 and 1^1B_2 states, respectively. All plotted density shown here depict MLCT-type transitions. Red signifies depletion and green shows accumulation of density. 120
7.5 $\Delta\rho$ associated with the $[Fe(CN)_5(py)]^{3-}$. (a) The density change associated with the 2^1B_2 state. (b) exemplify the density redistribution associated with the 3^1B_1 state. All densities depict MC-type transitions. Red signifies loss and green shows gain in density. 121

List of Symbols, Abbreviations and Nomenclature

ADF	Amsterdam Density Functional Program Package
ALDA	Adiabatic Local Density Approximation
Ar	Aryl ligand
ATD-DFT	Adiabatic TD-DFT
B3LYP	Becke/3 parameters/Lee-Yang-Parr with 20 % HF exchange
BHLYP	Hybrid form of BLYP with 50 % HF exchange
BLYP	Becke/Lee-Yang-Parr functional
BP86	Becke/Perdew 86 functional
BS-DFT	Broken Symmetry DFT
CAS	Complete Active Space
CC	Coupled Cluster
CCDC	Cambridge Crystallographic Data Centre
COSMO	Conductor-like Continuum Solvent model
CR	Completely Renormalized
CT	Charge Transfer
CV(2)-DFT	Second order CV-DFT
CV-DFT	Constricted Variational Density Functional Theory
DFT	Density Functional Theory
EA	Electron Affinity
EOM	Equation-of-Motion
ET-QZ3P	Even Tempered Quadruple-ζ basis/3 Polarization func.
ETS	Extended Transition State method
GGA	Generalized Gradient Approximation
GUI	Graphic User Interface
HF	Hartree-Fock

HK	Hohenberg-Kohn
HOMO	Highest Occupied Molecular Orbital
IP	Ionization Potential
KS	Kohn-Sham
LC	Length-Corrected
LCBP86	Length-Corrected BP86
LDA	Local Density Approximation
LUMO	Lowest Unoccupied Molecular Orbital
MAE	Mean Average Error
Me	Methyl
MC	Metal Centre
MC	Multi-Configurational
MLCT	Metal to Ligand CT
MO	Molecular Orbital
MRCI	Multi-Reference Configuration Interaction
NEVPT	n-Equation Valence-state Perturbation Theory
NOCV	Natural Orbitals for Chemical Valence method
PBE0	Hybrid form of PBE with 25 % HF exchange
PBE	Perdew-Burke-Ernzerhof functional
PES	Potential Energy Surface
Pr^i	Isopropyl
PT2	Second order Perturbation Theory
R	Alkyl ligand
RAS	Restricted Active Space
R-CV(4)-DFT	orbital Relaxed Fourth order CV-DFT
RMSD	Root Mean Squared Deviation
RSCF-CV(∞)-DFT	orbital Relaxed Self-Consistent Field all order CV-DFT
SAC	Symmetry Adapted Cluster

SCF	Self-Consistent Field
SCF-CV(∞)-DFT	Self-Consistent Field all order CV-DFT
SF	Spin-Flip
SOMO	Singly Occupied Molecular Orbital
SORCI	Spectroscopically Oriented Configuration Interaction
STEOM	Similarity Transformed EOM
STO	Slater-Type Orbital
SUMO	Singly Unoccupied Molecular Orbital
TDA	Tamm-Dancoff Approximation
TD-DFT	Time-Dependent DFT
TM	Transition Metals
TZ2P	Triple-ζ basis set/2 Polarization functions
TZP	Triple-ζ basis set/1 Polarization function
VWN	Vosko-Wilk-Nusair
XC	Exchange-Correlation
ZORA	Zero-Order Regular Approximation

Chapter 1

Introduction

1.1 General Introduction to Excited States and Excited-State Studies within Density Functional Theory

Excited-state properties and behaviour of atoms and molecules are of profound importance in the physical and applied sciences. The quantum mechanical treatment of excited states began shortly after the introduction of quantum mechanics [2, 3, 2, 4, 5, 6, 7, 8, 9, 10, 11, 12, 13, 14]. Calculated excited-state properties of some chemical species such as permanganate for the first time aided in the assignment of experimental spectra [2, 4, 6, 11, 12, 15, 16, 17, 18]. As a result, theoretical calculations became a valuable part of excited-state studies. It became apparent, subsequently, that for a thorough understanding of compounds such as the transition metal (TM) complexes, it is necessary to include some excited states (higher energy configurations) to the lowest possible energy level (ground-state) treatment. Experimental excited-state studies in a wide variety of molecular systems can be used as test sets to determine the accuracy of theoretical excited-state methods. Conversely, theory can be used to make predictions about excited-state properties before experimentation.

The time-dependent Schrödinger equation affords the time-dependent wave function, which contains all the information about the electronic structure and excited-state properties. The drawback here, however, is that solving the time-dependent many-body Schrödinger equation exactly for any system other than hydrogen and related species has so far proved impossible. Consequently, approximate methods have been proposed and developed over the years with new methods still under development.

Some examples which form part of the $ab\ initio$ wave function family of methods

are complete active space self-consistent field (CASSCF) [19], complete active space second-order perturbation theory (CASPT2) [20], multi-configurational self-consistent field (MCSCF) [21, 22], restricted active space self-consistent field (RASSCF) [23], RASPT2 [24], coupled cluster (CC) theory [25, 26], equation-of-motion coupled cluster (EOMCC) [27], *n*-electron valence state perturbation theory (NEVPT) [28], multi-reference configuration interaction (MRCI) [29], spectroscopically oriented configuration interaction (SORCI) [30], and time-dependent Hartree-Fock (TD-HF) [31, 32, 33, 34].

The focus here is on density functional theory (DFT) based methods. Specifically, Kohn-Sham [35] (KS) DFT. The ground-state energy in DFT is written in terms of the ground-state density instead of the ground-state wave function. In the KS-DFT formalism, use is made of a set of fictitious non-interacting electrons that have the same density as the interacting system. The KS-DFT energy expression contains the exchange-correlation (XC) energy term that is a functional of the density. Although the exact relation is not known. Several approximations are made to the XC energy term (in the form of XC functionals) leading to the many different flavours of DFT such as LDA[36], BP86[37, 38], B3LYP[39] etc. (details are shown in Chapter 2). Thus, the XC functional is a defining feature of DFT.

Electronic excitation studies within DFT gained a lot of attention with the increasing success of DFT in ground-state studies. Several excited-state methods have been developed and some are still underway in the DFT formalism. These include ensemble DFT [40, 41, 42], ΔSCF-DFT [13, 15, 14, 43, 44, 45, 46], constricted variational DFT (CV-DFT) [47, 48, 49, 50, 51] and time-dependent DFT (TD-DFT) [52, 53, 54, 55, 56]. TD-DFT has seen a lot of success. As a result, it is a widely used method by both theoreticians and experimentalists alike.

1.2 Types of Excitations

There are different types of excitations depending on where in the lowest occupied orbitals the electron is coming from (core or valence region), where the electron is going (lowest or higher lying virtual orbitals), how long the electron stays in the virtual orbital, and finally the number of electrons that move from the occupied orbitals into the virtual orbitals. Rydberg excitations involves the transfer of an electron from compact occupied to a diffuse virtual orbital; this is observed in compounds such as N_2, CO and C_2H_4. With valence excitations, an electron transfer is between a compact occupied orbital and a compact virtual orbital (these are the "regular" electronic excitations). Charge transfer excitations are similar to valence excitation, the difference is that the occupied and virtual orbital are spatially separated or are even situated on two different molecules. Examples are seen in the transition metal complexes. In double electron transitions, two electrons are removed from the occupied orbitals and placed into the virtual orbitals. Isolated double electron excitations are not usually as interesting as valence excitations with significant double electron excitation character; examples of such excitations are found in conjugated π–systems such as the polyenes.

Vertical excitations are primarily short-lived excitations, i.e. the electrons stay in the higher energy level for a time too short for significant nuclear motions. This is the opposite of what is observed in adiabatic excitation, where the electrons stay in the excited-state for a comparably longer time, enough time for a system to undergo geometric changes. The accurate description of this excitation require excited-state geometry optimisation. Finally, when an adiabatic excitation is corrected for zero point energy, it results in 0–0 excitation. All excitations studied in this work are examples of vertical excitations. As such, no excited state geometry optimisations were carried out.

Figure 1.1 shows the simplest case $i \rightarrow a$; a single orbital replacement where "i" represents a high-lying occupied orbital where the electron is taken from and "a" represents a low-lying virtual orbital into which the electron is placed. This kind of electronic excitation is accurately described by both ΔSCF-DFT [14, 15, 18] and adiabatic TD-

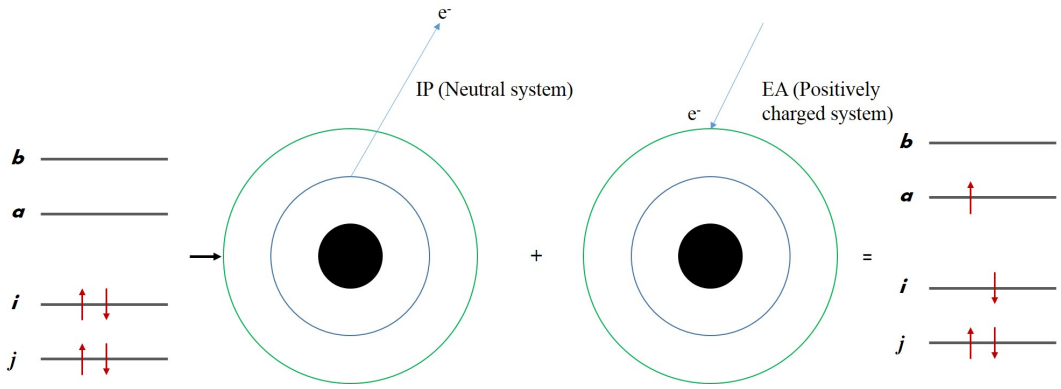

Figure 1.1: Excitation energy for $i \rightarrow a$ transition calculated as ΔE = IP(Neutral system) + EA(Positively charged system).

DFT (ATD-DFT) [57, 58, 59, 60] methods. ΔSCF-DFT is an energy difference method; the excitation energy is calculated as the energy difference between the ground-state energy and the energy obtained from a calculation carried out with a non-Aufbau occupation (representing the excited-state). In TD-DFT, the excitation energy is obtained as a result of the first-order change in density due to an external perturbation. The exact time/frequency-dependent XC term is not known, the ATD-DFT method is the result when use is made of the ground-state XC functionals (see Chapter 2 for details).

ΔSCF-DFT breaks down when we move to the more general case (valence-type transition) where the electron moves from a linear combination of ground-state occupied orbitals to a linear combination of virtual orbitals. Luckily, ATD-DFT performs well and efficiently for this kind of excitation accounting for one of the reasons for its wide usage.

Extensive benchmarking of TD-DFT revealed its weaknesses. These weakness include its deficiency in describing Rydberg transitions [1, 61, 62, 63], charge transfer (CT) transitions [64, 65, 66, 67, 68, 69, 70, 71, 72, 73] and electronic transition with significant doubles contribution [54, 55, 65, 66, 74, 75, 76]. CT transitions involve the transfer of an electron from one region amongst the occupied orbitals (donor region, D^+) to a separate region in the virtual orbital manifold (acceptor region, A^-) or the transfer of an electron from a donor region to an acceptor region perpendicular to the donor region. Here the overlap ($S_{D^+A^-}$) between the donor and acceptor orbitals is

nearly zero. In Rydberg transition, the small overlap ($S_{D^+A^-} \approx 0$) is due to the fact that the electron is removed from a compact occupied orbital and placed into a diffuse orbital (Rydberg orbital). The correct description of the diffuse orbital is achieved by adding diffuse functions to the normal valence basis sets.

The widely used ATD-DFT method relies on the available ground-state exchange-correlation (XC) functionals; these XC functionals do not have the correct long-range behaviour. They decay more rapidly as the distance from the nucleus increases. This deficiency is what is known as the incorrect $\sim$ –1/r behaviour [62]; more details are given in Chapter 5.

For Rydberg transitions, TD-DFT with the conventional functionals performs poorly. This is due to the inability of these XC functionals to accurately describe the ionization potential (IP) of the neutral atoms or molecules and the electron affinity (EA) of the resulting positively charged atoms or molecule [56, 77, 78]. However, the errors in the excitation energies are lower than the errors in the IP and EA alone [79]. The errors in systems with double excitation character (conjugated π–systems) are due to the absence of higher-order terms in the ATD-DFT formulation (see Chapter 2). Further, the errors in CT transitions are related to the inability of ATD-DFT to accurately describe the part of the energy expression that is involved in the electrostatic interaction between the donor and acceptor parts of the system of interest; this is the term linked to the separation of the donor (D^+) and acceptor (A^-) parts $1/|r_{D^+} - r_{A^-}|$ [64, 80, 81, 82].

Attempts to resolve these deficiencies in TD-DFT fall into two broad categories: (a) working to find the XC functionals that have the correct short and long range behaviour, and are computationally inexpensive, as well as going beyond the commonly used adiabatic formulation; (b) developing alternative DFT based methods with the ability to go beyond the second-order formulation in ATD-DFT. Several ways of going beyond the adiabatic formulation have been proposed and some afford significant improvement over the "regular" ATD-DFT (ATD-DFT with ground-state XC functionals). The difficulty in simply making changes that might afford improvements in one area, such as Rydberg transitions, is that the resulting "improved" TD-DFT method

[1, 61, 62, 63, 64, 71, 72, 83, 84, 80, 85, 86, 87, 88, 89, 90] must perform well for not only the Rydberg transitions but all other transitions accurately described by the "regular" ATD-DFT method.

A commonly used test set for newly developed method is the TM complexes which may have complicated electronic structures and properties. An electronic transition in these complexes might include "regular" valence excitations with some hidden CT or Rydberg excitations or even double excitation character. Additionally, TM complexes have been widely used as test sets because there are a large number of experimental as well as high-level theoretical results available for comparison.

Recent attempts to correct the medium to long range behaviour of the functionals resulted in the inclusion of a fraction of the Hartree-Fock (HF) exchange into the DFT functionals. These are the static hybrid functionals. More recently, the hybrid functionals [1, 61, 62, 63, 64, 71, 72, 83, 84, 80, 85, 86, 87, 88, 89, 91, 92] are constructed to switch between the DFT (short range) and HF (long range); these are the length-corrected (LC) functionals, see Chapter 5. These functionals improve ATD-DFT excitation energies for Rydberg and CT transitions. However, they sometimes lead to increased errors in the transitions which were accurately described by "regular" ATD-DFT calculations.

Our recently developed Constricted Variational DFT (CV-DFT) [47, 48, 49, 50, 51] affords a way of combining the strengths of ΔSCF-DFT and ATD-DFT methods without the use of "tuned" functionals. ΔSCF-DFT and ATD-DFT methods can be seen as special cases in the CV-DFT method; for a single orbital replacement, the CV-DFT method (RSCF-CV(∞)-DFT, Chapters 2 and 5) gives identical excitation energies as ΔSCF-DFT, and the general form of CV-DFT method where the variational mixing is carried out to second-order in the mixing coefficient (CV(2)-DFT) is identical to the ATD-DFT method (details are given in Chapter 2).

However, it can be shown, even within the CV(2)-DFT method that we can straightforwardly include the doubles interactions as higher-order terms in the energy expression. This feature is absent in the ATD-DFT method. In the excitation of an α–electron,

the β–electrons are considered frozen; if we allow them to relax and expand the energy expression to $4th$-order, we obtain the R-CV(4)-DFT method. The higher-order (third- and fourth-order) terms and the relaxation lower the energy. Thus the R-CV(4)-DFT method succeeds for CT transitions but performs poorly for "regular" valence excitation energies [93]. Attempts to resolve this drawback led to the all-order orbital relaxed self-consistent field CV-DFT (RSCF-CV(∞)-DFT) method. The performance of the different versions of the CV-DFT method through its development are analyzed in chapters 3 to 7. Finally an extension to the CV-DFT method for double electron excitations is provided in Chapter 8.

1.3 Thesis Objectives

The main objective of the work presented in this thesis is to assess the performance of the CV-DFT method in the analyses of excited state properties of electronically complex systems. A second objective is to provide explanation for its (good) performance for the various possible excitations within relevant compounds such as the TM complexes. The focus was not only for cases where other methods failed but where they succeeded as well, so that complete improvements in the CV-DFT method can be made. This objective is summarized by a quotation by Richard Feynman;

> The only way to have real success in science. . .is to describe the evidence very carefully without regards to the way you feel it should be. If you have a theory, you must try and explain what's good about it and what's bad about it equally. In science you learn a sort of standard integrity and honesty.

The smaller goals set in order to achieve these objectives are;

1. To analyze the shortcomings of the TD-DFT method and provide in-depth explanation of the source of the errors and

2. To compare CV-DFT results to ΔSCF-DFT and TD-DFT methods, as well as experimental and some high level $ab\ initio$ results whenever available. This is necessary to determine the scope of applicability of the CV-DFT method.

The theoretical background of the methods used, including similarities and differences, are outlined in Chapter 2. In Chapter 3, we analyzed the weak exchange coupling interaction in 11 binuclear Cu(II) systems using the spin-flip CV(2)-DFT (SF-CV(2)-DFT) method. In Chapter 4, we applied the SF-CV(2)-DFT method as well as combined Extended Transition State and Natural Orbital for Chemical Valence (ETS-NOCV) method for determining the nature of the bonding in the heavier acetylene analogues (Group 14). This is followed by the analyses of Rydberg transition of 9 systems in Chapter 5. In Chapter 6, we determined the excitation energies in 9 d^0 tetroxo TM complexes. In Chapter 7, we determined excitation energies for octahedral TM complexes with RSCF-CV(∞)-DFT method.

In Chapter 8, we provide an extension of the CV-DFT method for double electron excitation within the RSCF-CV(∞)-DFT formalism as well as the CV(2)-DFT (or TD-DFT) formalism. Finally in Chapter 9, we provide a summary and an extension of the work.

Chapter 2

Theoretical Background

2.1 Introduction

The procedure for calculating the ground-state properties of a system involves the application of the time-independent Schrödinger equation given as

$$\hat{H}\Psi_i = E_i\Psi_i \tag{2.1}$$

where Ψ_i is the ith eigenstate and the corresponding eigenvalue E_i. The non-relativistic Hamiltonian $\hat{H}$ is given in atomic units by

$$\hat{H} = -\sum_{i}^{N}\frac{\bigtriangledown_i^2}{2} + \sum_{i}^{N}\upsilon(\mathbf{r}_i) + \frac{1}{2}\sum_{\substack{i,j\\ j\neq i}}^{N}\frac{1}{r_{ij}} \tag{2.2}$$

the first term on the right is the kinetic energy term for N electrons followed by the potential energy term and finally the electron-electron repulsion term (Coulomb term). For simplicity and convenience, the expressions are written in atomic units (au). The mass of an electron (m_e), electronic charge (e) and reduced Plank's constant $\left(\hbar = \frac{h}{2\pi}\right)$ are all set to 1. Appendix F shows their numerical values in SI unit. Eq (2.1) is a simplification that excludes the nuclear degrees of freedom, the contribution from the nuclei is fixed and independent of the electronic coordinates, but contributes to $\upsilon(\mathbf{r})$. This approximation is referred to as the clamped nuclei (Born-Oppenheimer) approximation. The antisymmetric wave function in eq (2.1) for N-electron system has $3N$ variables (after integrating out the spins) which makes the exact solution of eq (2.1) impossible for $N > 2$. Several schemes have been proposed to solve eq (2.1) approximately.

One way of solving the equation approximately that avoids dealing directly with the wave function and its associated variable dependence is found in the Density Functional

Theory (DFT) method [94, 35]. It is a formally exact theory; the approximation comes as a result of the use of approximate potentials (see the next section for details). One can in principle determine all the properties of a system of interest without solving eq (2.1) explicitly.

2.2 Density Functional Theory (DFT) method: Kohn-Sham equations

Here we start with a non-interacting system of N-electrons that has the same density as the real system, the Hamiltonian is given by

$$\hat{H}_{\text{non}} = -\sum_{i}^{N} \frac{\nabla_i^2}{2} + \sum_{i}^{N} \upsilon_{\text{n}}(\mathbf{r}_i). \tag{2.3}$$

The non-interacting system is represented by a single Slater determinant

$$\Psi^{\text{n}} = |\phi_1 \phi_2 \phi_3 \dots \phi_i \phi_j \dots \phi_n| \tag{2.4}$$

here, the spin-orbitals ϕ_i are solutions to the equation

$$\Big(-\frac{\nabla_i^2}{2} + \upsilon_{\text{n}}(\mathbf{r}) \Big) \phi_i(\mathbf{r}) = \epsilon_i \phi_i(\mathbf{r}). \tag{2.5}$$

The corresponding ground-state density of the non-interacting system is obtained from the occupied set as

$$\rho^{\text{n}}(\mathbf{r}) = \sum_{i=1}^{occ} |\phi_i^*(\mathbf{r}) \phi_i(\mathbf{r})|. \tag{2.6}$$

The energy expression for an interacting system of electrons obtained from the Hohenberg-Kohn (HK) theorem [94] is given as

$$\begin{aligned} E = &\sum_{i}^{N} \int \Big[-\frac{\nabla_i^2}{2} \rho_1(\mathbf{r}, \mathbf{r}') \Big]_{\mathbf{r}=\mathbf{r}'} d\mathbf{r} + \sum_{i}^{N} \sum_{A}^{M} \int \frac{Z_A}{r_{iA}} \rho_1(\mathbf{r}) d\mathbf{r} \\ &+ \iint \frac{\rho_2(\mathbf{r}, \mathbf{r}')}{|\mathbf{r} - \mathbf{r}'|} d\mathbf{r} d\mathbf{r}' \end{aligned} \tag{2.7}$$

where $\rho(\mathbf{r}, \mathbf{r}')$ is the one-electron density matrix defined as

$$\rho_1(\mathbf{r}, \mathbf{r}') = n \int d\mathbf{r}_2 \dots \int d\mathbf{r}_n \int \Psi^*(\mathbf{r}', \mathbf{r}_2, \dots, \mathbf{r}_n) \Psi(\mathbf{r}, \mathbf{r}_2, \dots, \mathbf{r}_n). \tag{2.8}$$

The diagonal element (electron density) $\rho_1(\mathbf{r})$ is obtained when $\mathbf{r} = \mathbf{r}'$. The two-electron density ($\rho_2(\mathbf{r}, \mathbf{r}')$) is given by

$$\rho_2(\mathbf{r}, \mathbf{r}') = \frac{n(n-1)}{2} \int d\mathbf{r}_3 \ldots \int d\mathbf{r}_n \int \Psi^*(\mathbf{r}, \mathbf{r}', \mathbf{r}_3, \ldots, \mathbf{r}_n) \Psi(\mathbf{r}, \mathbf{r}', \mathbf{r}_3, \ldots, \mathbf{r}_n). \tag{2.9}$$

The variable $\mathbf{r}$ is the spatial component and only variable remaining after the spin component is integrated out. The first term on the right hand side of eq (2.7) is the kinetic energy followed by the nuclear-electron attraction and the last term is the electron-electron repulsion.

The actual DFT expressions implemented in most software packages, the Kohn-Sham (KS) equations [35], are obtained by adding and subtracting the non-interacting kinetic energy and electron-electron repulsion terms in eq (2.7).

$$E = \sum_i^N \int \Big[-\frac{\nabla_i^2}{2} \rho_1^{\mathrm{n}}(\mathbf{r}, \mathbf{r}') \Big]_{\mathbf{r}=\mathbf{r}'} d\mathbf{r} + \sum_i^N \sum_A^M \int \frac{Z_A}{r_{iA}} \rho_1^{\mathrm{n}}(\mathbf{r}) d\mathbf{r} + \frac{1}{2} \iint \frac{\rho_1^{\mathrm{n}}(\mathbf{r}) \rho_1^{\mathrm{n}}(\mathbf{r}')}{|\mathbf{r} - \mathbf{r}'|} d\mathbf{r} d\mathbf{r}' + E_{XC}[\rho] \tag{2.10}$$

where the exchange-correlation energy, E_{XC}, containing the parts of eq (2.10) we do not know exactly is expressed as

$$E_{XC}[\rho] = \sum_i^N \int \Big[-\frac{\nabla_i^2}{2} \rho_1(\mathbf{r}, \mathbf{r}') \Big]_{\mathbf{r}=\mathbf{r}'} d\mathbf{r} - \sum_i^N \int \Big[-\frac{\nabla_i^2}{2} \rho_1^{\mathrm{n}}(\mathbf{r}, \mathbf{r}') \Big]_{\mathbf{r}=\mathbf{r}'} d\mathbf{r} + \frac{1}{2} \iint \frac{\rho_2(\mathbf{r}, \mathbf{r}')}{|\mathbf{r} - \mathbf{r}'|} d\mathbf{r} d\mathbf{r}' - \frac{1}{2} \iint \frac{\rho_1^{\mathrm{n}}(\mathbf{r}) \rho_1^{\mathrm{n}}(\mathbf{r}')}{|\mathbf{r} - \mathbf{r}'|} d\mathbf{r} d\mathbf{r}'. \tag{2.11}$$

The first functional derivative of the eq (2.10) with respective to the ρ for the i'th electron gives

$$F_i^{\mathrm{KS}} = -\frac{\nabla_i^2}{2} + \sum_A^M \frac{Z_A}{r_{iA}} + \int \frac{\rho_1^{\mathrm{n}}(r_j)}{r_{ij}} dr_j + \upsilon_{XC}[\rho] \tag{2.12}$$

here

$$\upsilon_{XC}[\rho] = \frac{\delta E_{XC}[\rho]}{\delta \rho}. \tag{2.13}$$

The spin-orbitals for the interacting system can be obtained by solving the one-particle equation

$$F_i^{\mathrm{KS}}\psi_i(\mathbf{r}) = \epsilon_i\psi_i(\mathbf{r}). \tag{2.14}$$

From this set, we can get our ground-state Slater determinant $\Psi = |\psi_1\psi_2\psi_3\ldots\psi_i\psi_j \ldots\psi_n|$ with the associated ground-state density

$$\rho(\mathbf{r}) = \sum_{i}^{occ} |\psi_i^*(\mathbf{r})\psi_i(\mathbf{r})|. \tag{2.15}$$

The advantage of solving the KS equation instead of solving the Schrödinger equation lies is the substitution of the wave function, Ψ, which depends on $3N$ variable with the ground-state density, ρ, which depends on 3 variables. However, the downside is that the exact form of the XC potential ($\upsilon_{XC}[\rho]$) is not known and as a result finding approximate expressions for it is the subject of ongoing research.

The approximation to DFT comes from the approximations made to the XC potential. The local density approximation (LDA) is the earliest formulation. There have been several different approximations formulated since LDA, the broad categories are the generalized gradient approximations (GGAs), meta GGA, the hybrid functionals and hyper-GGAs, and more recently, the length corrected (LC) functionals.

Next, we turn to excited states in DFT. Use has been made of approaches based on both variational theory (ΔSCF-DFT) and response theory (TD-DFT).

2.3 Time-Dependent DFT (TD-DFT) method

The HK theorem [94] proves a unique one-to-one correspondence between the external potential and the density, forming the basis for DFT. A similar proof for a time-dependent process within DFT was provided by Runge and Gross [53]. The formal justification for expressing the time-dependent density in terms of the non-interacting density as in the case of ground-state DFT was provided by van Leeuwen [95]. We start with a ground-state DFT calculation, i.e. a calculation at $t = 0$ (t_0). This is followed by

a calculation carried out with a time-dependent potential, the time-dependent density is given as

$$\rho(\mathbf{r},\mathrm{t}) = \sum_{i}^{occ} |\phi_i^*(\mathbf{r},\mathrm{t})\phi_i(\mathbf{r},\mathrm{t})|. \tag{2.16}$$

The orbitals $\phi_i(\mathbf{r},\mathrm{t})$ are similar to those of eq (2.5), the difference is that the orbitals are nonlocal with-respect-to time. The orbitals in eq (2.16) are obtained from the time-dependent DFT equation

$$\Big(-\frac{\bigtriangledown_j^2}{2} + \upsilon_s[\rho](\mathbf{r},\mathrm{t})\Big)\phi_j(\mathbf{r},\mathrm{t}) = i\frac{\partial}{\partial t}\phi_j(\mathbf{r},\mathrm{t}) \tag{2.17}$$

where the effective potential, $\upsilon_s[\rho](\mathbf{r},\mathrm{t})$ is defined as

$$\upsilon_s[\rho](\mathbf{r},\mathrm{t}) = \sum_{A}^{M}\frac{Z_A}{r_{iA}} + \int\frac{\rho_1(\mathbf{r},\mathrm{t})}{r_{ij}}dr_j + \upsilon_{XC}[\rho](\mathbf{r},\mathrm{t}). \tag{2.18}$$

The terms in this equation are same as defined for eq (2.12) with an additional dependence on time. This is the formal TD-DFT description of a time-dependent system. However, it is not used in practical applications because the exact nature of $\upsilon_{XC}[\rho](\mathbf{r},\mathrm{t})$ is not known as in the case of ground-state DFT. Here use is made of the ground-state XC potential

$$\upsilon_{XC}[\rho](\mathbf{r},\mathrm{t}) \approx \upsilon_{XC}^{\text{Adia}}[\rho](\mathbf{r},\mathrm{t}) \equiv \upsilon_{XC}^{0}[\rho_0](\mathbf{r}). \tag{2.19}$$

This is the adiabatic formulation of the TD-DFT (ATD-DFT) method. The XC potential is local with respect to time, in addition to the aforementioned approximations made to the ground-state XC potentials themselves.

The first-order change in density as a result of a perturbation is given as

$$\Delta\rho(\mathbf{r},\omega) = \sum_{i,a} P_{ia}\phi_i(\mathbf{r})\phi_a^*(\mathbf{r}). \tag{2.20}$$

Eq (2.20) is expressed in the frequency domain, P_{ia} is density matrix element in the frequency domain.

The excitation energies in TD-DFT are obtained as poles of the polarizability of an atom or molecule. The eigenvalue equation from which the excitation energy is

determined is given as

$$\Omega U_I = \omega_{I0}^2 U_I \tag{2.21}$$

here U_I are the eigenvectors and ω_{I0} are the excitation energy corresponding to U_I. Ω is defined as

$$\Omega = \mathbf{S}^{-1/2}(\mathbf{A}+\mathbf{B})\mathbf{S}^{-1/2} \tag{2.22}$$

here

$$\mathbf{S} = (\mathbf{A}-\mathbf{B})^{-1} \tag{2.23}$$

and the elements of the ground-state Hessian ($\mathbf{A}$ and $\mathbf{B}$) are defined as

$$A_{aibj}^{\text{KS}} = \delta_{ab}\delta_{ij}(\epsilon_a^0 - \epsilon_i^0) + K_{aibj}^{\text{KS}} \tag{2.24}$$

$$B_{aibj}^{\text{KS}} = K_{aijb}^{\text{KS}}. \tag{2.25}$$

The K integral is defined as

$$K_{pqst}^{\text{KS}} = K_{pqst}^{\text{C}} + K_{pqst}^{XC} \tag{2.26}$$

where

$$K_{pqst}^{\text{C}} = \int\int \phi_p(\mathbf{r})\phi_q(\mathbf{r})\frac{1}{r_{12}}\phi_s(\mathbf{r}')\phi_t(\mathbf{r}')d\mathbf{r}d\mathbf{r}' \tag{2.27}$$

$$K_{pqst}^{XC(\text{HF})} = -\int\int \phi_p(\mathbf{r})\phi_s(\mathbf{r})\frac{1}{r_{12}}\phi_q(\mathbf{r}')\phi_t(\mathbf{r}')d\mathbf{r}d\mathbf{r}' \tag{2.28}$$

$$K_{pqst}^{XC(\text{KS})} = \int \phi_p^\mu(\vec{\mathbf{r}})\phi_q^\mu(\vec{\mathbf{r}})f_{XC}^{\mu\nu}(\vec{\mathbf{r}},\omega)\phi_s^\nu(\vec{\mathbf{r}})\phi_t^\nu(\vec{\mathbf{r}})d\vec{\mathbf{r}}. \tag{2.29}$$

Eqs (2.27) and (2.28) are integrated over spin and space, whilst eq (2.29) is over space only. The factor $f_{XC}^{\mu\nu}(\vec{\mathbf{r}},\omega)$ in eq (2.29) represents the energy kernel given by

$$f_{XC}^{\mu\nu}(\mathbf{r},\omega) = \left(\frac{\partial^2 E_{XC}}{\partial\rho^\mu\partial\rho^\nu}\right)_0. \tag{2.30}$$

Eq (2.21) reduces to

$$\mathbf{A}U_I = \omega_{I0}U_I \tag{2.31}$$

after applying the Tamm-Dancoff approximation ($B_{aibj}^{\text{KS}} = 0$).

2.4 ΔSCF-DFT method

This is one of the oldest excited state methods within the DFT framework [13, 14, 43, 96, 97]. The excited state is obtained as energy difference between the ground-state energy and the total energy of a state with occupation corresponding to an excited state. The ground-state determinant given by

$$\Psi = |\psi_1\psi_2\psi_3 \dots \psi_i\psi_j \dots \psi_n| \tag{2.32}$$

from which we calculate the ground-state energy, E_0. We construct the excited state determinant from the ground-state determinant by a single orbital replacement, $i \to a$. The resulting Slater determinant is given by

$$\Psi_{i\to a} = |\psi_1\psi_2\psi_3 \dots \psi_a\psi_j \dots \psi_n| \tag{2.33}$$

with the corresponding energy, $E_{i\to a}$. Finally, the energy of the excited state corresponding to this transition is given, as indicated above as,

$$\Delta E^{\mathrm{M}}_{i\to a} = E_{i\to a} - E_0. \tag{2.34}$$

The triplet excited state energy, $\Delta E^{\mathrm{T}}_{i\to\bar{a}}$, is calculated directly from $\Psi_{i\to\bar{a}} = |\psi_1\ \psi_2\ \psi_3\ \dots\ \psi_a\ \psi_j\ \dots \psi_n|$ obtain from $i \to \bar{a}$ substitution of eq (2.32). Finally, the singlet excited state energy, $\Delta E^{\mathrm{S}}_{i\to a}$, is obtained as,

$$\Delta E^{\mathrm{S}}_{i\to a} = 2\Delta E^{\mathrm{M}}_{i\to a} - \Delta E^{\mathrm{T}}_{i\to\bar{a}} \tag{2.35}$$

where $\Delta E^{\mathrm{M}}_{i\to a}$ is the mixed state energy calculated using eq (2.34) and it is defined as

$$\Delta E^{\mathrm{M}}_{i\to a} = \frac{1}{2}\Delta E^{\mathrm{S}}_{i\to a} + \frac{1}{2}\Delta E^{\mathrm{T}}_{i\to\bar{a}}. \tag{2.36}$$

These are calculated as

$$\Delta E^{\mathrm{M}}_{i\to a} = (\epsilon_a - \epsilon_i) + \frac{1}{2}K_{iiii} + \frac{1}{2}K_{aaaa} - K_{aaii} + \Delta E^{\mathrm{M}}_{\mathrm{Rel}} \tag{2.37}$$

$$\Delta E^{\mathrm{T}}_{i\to\bar{a}} = (\epsilon_a - \epsilon_i) + \frac{1}{2}K_{iiii} + \frac{1}{2}K_{aaaa} - K_{aa\bar{i}\bar{i}} + \Delta E^{\mathrm{T}}_{\mathrm{Rel}} \tag{2.38}$$

$$\Delta E^{\mathrm{S}}_{i\to a} = (\epsilon_a - \epsilon_i) + \frac{1}{2}K_{iiii} + \frac{1}{2}K_{aaaa} - 2K_{aaii} + K_{aa\bar{i}\bar{i}} + \Delta E^{\mathrm{S}}_{\mathrm{Rel}} \tag{2.39}$$

here ΔE_{Rel} is the term that comes from orbital relaxation. When this term is excluded, we end up with ΔDFT. The K integrals are defined in eqs (2.27)–(2.29). The self-interaction terms, K_{iiii} and K_{aaaa} are zero for HF and non-zero for pure DFT functionals.

The singlet and triplet energies calculated with this method gives very good agreement with experimental and some high level $ab\ initio$ results. However, this good performance is limited to excitations that can be represented by a single orbital replacement. Additionally, in the practical application of ΔSCF-DFT, the optimization of the orbitals leads to a variational collapse as orthogonality between the $l'th$ excited and the $(l-1)th$ states is not ensured. This is particularly true for excited states with the same symmetry as the ground-state and ΔSCF-DFT breaks down in systems with no symmetry.

2.5 Constricted Variational DFT (CV-DFT) method

The CV-DFT method within the past years has gone through several developmental stages. The method involves the mixing of portions of virtual (unoccupied) orbitals into the occupied orbitals. This mixing can be done to all orders in the variational mixing coefficient, U. The first version is that one in which the mixing is carried out to second-order in U, CV(2)-DFT, given by

$$\phi_i'(1) = \phi_i(1) + \sum_a^{vir} U_{ai}\phi_a - \frac{1}{2}\sum_a^{vir}\sum_j^{occ} U_{ai}U_{aj}\phi_j(1) + \mathcal{O}^{(3)}[U]. \tag{2.40}$$

This is orthonormal to second-order in U. This generates excited state orbitals $\{\phi_i'$; i = 1,$occ\}$ which can be organized in a new excited state Slater determinant $\Psi' = |\phi_1'\phi_2'\phi_3' \ldots \phi_i'\phi_j' \ldots \phi_n'|$. The corresponding density is given as

$$\begin{aligned}\rho'(1) =& \rho^{(0)}(1) + \sum_i^{occ}\sum_a^{vir} U_{ai}\phi_a(1)\phi_i^*(1) + \sum_i^{occ}\sum_a^{vir} U_{ai}^*\phi_a^*(1)\phi_i(1) \\ &+ \sum_i^{occ}\sum_a^{vir}\sum_b^{vir} U_{ai}^*U_{bi}\phi_a(1)\phi_b^*(1) - \sum_i^{occ}\sum_j^{occ}\sum_a^{vir} U_{ai}U_{aj}^*\phi_i(1)\phi_j^*(1)\end{aligned} \tag{2.41}$$

expressed to second-order in U. The reference ground-state density is $\rho^{(0)}$. The accompanying energy to second-order in U is

$$\begin{aligned} E_{\text{KS}}[\rho'(1,1')] =& E_{\text{KS}}[\rho^{(0)}(1,1')] + \sum_{ai} U_{ai}U^*_{ai}\left(\epsilon^0_a - \epsilon^0_i\right) \\ &+ \sum_{ai}\sum_{bj} U_{ai}U_{bj}K^{\text{KS}}_{ai,bj} + \frac{1}{2}\sum_{ai}\sum_{bj} U_{ai}U_{bj}K^{\text{KS}}_{ai,jb} \\ &+ \frac{1}{2}\sum_{ai}\sum_{bj} U^*_{ai}U^*_{bj}K^{\text{KS}}_{ai,jb} + \mathcal{O}[U^3]. \end{aligned} \tag{2.42}$$

$E_{\text{KS}}[\rho^{(0)}]$ is the energy corresponding to $\rho^{(0)}$. In eq (2.42), "a,b" and "i,j" run over virtual and occupied reference state orbitals, respectively. Eq (2.42) can be rewritten in a more compact form as

$$E_{\text{KS}}[\rho'] = E_{\text{KS}}[\rho^{(0)}] + U^+(A^{\text{KS}} + B^{\text{KS}})U \tag{2.43}$$

$$\Delta E_{\text{KS}}[\Delta\rho'] = E_{\text{KS}}[\rho'] - E_{\text{KS}}[\rho^{(0)}] = U^+(A^{\text{KS}} + B^{\text{KS}})U. \tag{2.44}$$

Assuming that the orbitals and elements U_{ai} are real. The matrix (A^{KS} + B^{KS}) is the electronic ground-state Hessian, where the elements A^{KS}_{aibj} and B^{KS}_{aibj} are defined in eqs (2.24) and (2.25).

Here the running numbers are over the occupied and virtual orbital pairs "ai". To solve eq (2.44), we determine points along $E_{\text{KS}}[\rho']$ such that $\Delta E_{\text{KS}}[\Delta\rho']$ represent electronic transition energy. The optimization of eq (2.44) is carried out with the constraint that the density change, $\Delta\rho'$, corresponds to an electronic transition [47]. This is a necessary condition because a direct optimization will lead to $\Delta E_{\text{KS}}[\Delta\rho']$ = 0, giving back the ground-state energy. The constraint enforced in the optimization of eq (2.44) comes from the last two terms of eq (2.41) which represents removing of an electron from the occupied space and placing it in the virtual space. Integrating over the last two terms of eq (2.41) separately leads to

$$\Delta q_{vir} = -\Delta q_{occ} = \sum_{ai} U_{ai}U^*_{ai} = 1. \tag{2.45}$$

Solving eq (2.43) with the constraint in eq (2.45) leads to the eigenvalue equation

$$(A^{\text{KS}} + B^{\text{KS}})U^{(I)} = \lambda_{(I)}U^{(I)} \tag{2.46}$$

here $U^{(I)}$ is the variational mixing coefficient with elements $\{U^{(I)}; I$=1,$occ \times vir\}$ and $\lambda_{(I)}$ is the associated electronic transition energy. When the Tamm-Dancoff approximation (TDA) is applied eq (2.46) reduces to

$$A^{\mathrm{KS}} U^{(I)} = \lambda_{(I)} U^{(I)}. \tag{2.47}$$

Eqs (2.46) and (2.47) are identical to those obtained in ATD-DFT before and after TDA is applied, respectively.

In the CV-DFT method, we are not limited to the second-order formulation. We can extend the method to include all-order terms in U, by carrying out the mixing to all orders in U. That is, going beyond the second-order mixing shown in eq (2.40). A more general all-order mixing is given as

$$Y \begin{pmatrix} \phi_{occ} \\ \phi_{vir} \end{pmatrix} = e^{U} \begin{pmatrix} \phi_{occ} \\ \phi_{vir} \end{pmatrix} = \left(\sum_{m=0}^{\infty} \frac{(U)^m}{m!} \right) \begin{pmatrix} \phi_{occ} \\ \phi_{vir} \end{pmatrix} = \begin{pmatrix} \phi'_{occ} \\ \phi'_{vir} \end{pmatrix}. \tag{2.48}$$

The concatenated column vectors ϕ_{occ} and ϕ_{vir} in the above expression contains the set of occupied $\{\phi_i; i = 1, occ\}$ and virtual $\{\phi_a; a = 1, vir\}$ reference state orbitals. Here ϕ'_{occ} and ϕ'_{vir} are the resulting concatenated column vectors containing the occupied and virtual orbitals corresponding to an excited state, $\{\phi'_i; i = 1, occ\}$ and $\{\phi'_a; a = 1, vir\}$ respectively. Additionally, the unitary transformation matrix Y is expressed in terms of U as

$$Y = e^{U} = I + U + \frac{U^2}{2} + ... = \sum_{m=0}^{\infty} \frac{U^m}{m!} = \sum_{m=0}^{\infty} \frac{(U^2)^m}{(2m)!} + U \sum_{m=0}^{\infty} \frac{(U^2)^m}{(2m+1)!}. \tag{2.49}$$

The first occupied set of elements (occ) run over occupied ground-state reference orbitals starting with α–spin orbitals, whereas the last virtual set of elements (vir) run over the ground-state reference β–spin orbitals in any row or column of U. Also, $U_{ij} = U_{ab} = 0$, where "i, j" refer to the occupied set $\{\phi_i; i = 1, occ\}$, while "a, b" refer to the unoccupied set $\{\phi_a; a = 1, vir\}$, i.e. the occupied and virtual orbitals are not allowed to mix within themselves. However, the mixing between virtual and occupied ground-state orbitals, U_{ai}, are allowed resulting in the excited state with $U_{ai} = -U_{ia}$. There are $occ \times vir$ independent U_{ai} elements in the entire U matrix, which is organized into the

column vector $\vec{U}$, where the running index is now the number of different occupied and virtual orbital pairs (ai).

The "occupied" excited state orbitals generated from eq (2.48) for a given U is

$$\phi_i' = \sum_p^{occ+vir} Y_{pi}\phi_p = \sum_j^{occ} Y_{ji}\phi_j + \sum_a^{vir} Y_{ai}\phi_a. \tag{2.50}$$

Eq (2.50) is orthonormal to all orders in U. The corresponding expression for eq (2.41) to all orders in U is given as

$$\begin{aligned}\rho'(1) = &\sum_i^{occ}\sum_j^{occ}\sum_k^{occ} Y_{ji}Y_{ki}\phi_j(1)\phi_k^*(1) + \sum_i^{occ}\sum_a^{vir}\sum_b^{vir} Y_{ai}Y_{bi}\phi_a^*(1)\phi_b(1) \\ &+ \sum_i^{occ}\sum_a^{vir}\sum_j^{occ} Y_{ai}Y_{ji}[\phi_a^*(1)\phi_j(1) + \phi_a(1)\phi_j^*(1)].\end{aligned} \tag{2.51}$$

In practical applications, eq (2.51) is not useful as it involves the infinite summation in eq (8.2). A reformulation [48] of the excited state orbital in the all-order method in a compact form involved the use of the corresponding orbital representation [98]. Eq (2.50) in the corresponding orbital representation [98] is given as

$$\phi_i' = \cos[\eta\gamma_i]\phi_i^o + \sin[\eta\gamma_i]\phi_i^v; i = 1, occ \tag{2.52}$$

where

$$V^+UW = 1\gamma \tag{2.53}$$

here γ_i(i = 1,occ) is the eigenvalue of eq (2.53), for every occupied orbital ϕ_i^o, there is a corresponding virtual orbital ϕ_i^v which mixed into it. They are defined in terms of the canonical orbitals as

$$\begin{aligned}\phi_i^o &= \sum_i^{occ} W_{ji}\phi_i; \\ \phi_i^v &= \sum_i^{occ} V_{ai}\phi_a.\end{aligned} \tag{2.54}$$

This simplifies the canonical orbital representation. The density change associated with eq (2.52) is given as

$$\begin{aligned}\Delta\rho^{(\infty)}(1) = &\sum_i^{occ} \sin^2[\eta\gamma_i][\phi_i^v(1)\phi_i^{v*}(1) - \phi_i^o(1)\phi_i^{o*}(1)] \\ &+ \sum_i^{occ} \sin[\eta\gamma_i]\cos[\eta\gamma_i][\phi_i^v(1)\phi_i^{o*}(1) + \phi_i^o(1)\phi_i^{v*}(1)].\end{aligned} \tag{2.55}$$

The excitation energy accompanying this change in density is given as

$$\begin{aligned}\Delta E_{\mathrm{M}}^{(\infty)} =& \sum_{i}^{occ} \sin^2[\eta\gamma_i]\Big(F_{i^v i^v}^{\mathrm{KS}}\big[\rho^{(0)} + \frac{1}{2}\Delta\rho^{(\infty)}\big] - F_{i^o i^o}^{\mathrm{KS}}\big[\rho^{(0)} + \frac{1}{2}\Delta\rho^{(\infty)}\big]\Big) \\ &+ \sum_{i}^{occ} \sin[\eta\gamma_i]\cos[\eta\gamma_i]\Big(F_{i^v i^o}^{\mathrm{KS}}\big[\rho^{(0)} + \frac{1}{2}\Delta\rho^{(\infty)}\big] + F_{i^v i^o}^{\mathrm{KS}}\big[\rho^{(0)} + \frac{1}{2}\Delta\rho^{(\infty)}\big]\Big) \\ &+ \mathcal{O}^{[3]}[\Delta\rho^{(\infty)}]. \end{aligned} \tag{2.56}$$

This formulation is the SCF-CV(∞)-DFT method, where only parts of the density directly linked to the electronic transition is altered. That is, for an $\alpha \rightarrow \alpha$ transition, the β–electrons are left frozen. The relaxation of the β–electrons is included in the orbital relaxed SCF-CV(∞)-DFT method (RSCF-CV(∞)-DFT). Here the unitary transformation of eq (2.48) is carried out amongst relaxed occupied reference state orbitals

$$\psi_i(1) = \phi_i(1) + \sum_{a}^{vir} R_{ai}\phi_a(1) - \frac{1}{2}\sum_{a}^{vir}\sum_{j}^{occ} R_{ai}R_{aj}\phi_k + \mathcal{O}^{(3)}[R] \tag{2.57}$$

and virtual reference state orbitals

$$\psi_a(1) = \phi_a(1) + \sum_{i}^{occ} R_{ai}\phi_i(1) - \frac{1}{2}\sum_{i}^{occ}\sum_{b}^{vir} R_{ai}R_{bi}\phi_b + \mathcal{O}^{(3)}[R]. \tag{2.58}$$

The R matrix relaxes the occupied $\{\phi_i; i = 1, occ\}$ and unoccupied $\{\phi_a; a = 1, vir\}$ canonical reference state orbitals obtained by mixing the ground-state occupied and virtual orbitals. The terms in the orbital relaxation and corresponding relaxation energy are taken up to second-order in R [49, 99], the higher-order terms are almost negligible from experience. The relaxation density is given as

$$\begin{aligned}\Delta\rho_{\mathrm{Rel}}(1) =& \sum_{i}^{occ}\sum_{a}^{vir} R_{ai}\phi_a(1)\phi_i^*(1) + \sum_{i}^{occ}\sum_{a}^{vir} R_{ai}^*\phi_a^*(1)\phi_i(1) \\ &+ \sum_{i}^{occ}\sum_{a}^{vir}\sum_{b}^{vir} R_{ai}^*R_{bi}\phi_a(1)\phi_b^*(1) - \sum_{i}^{occ}\sum_{j}^{occ}\sum_{a}^{vir} R_{ai}R_{aj}^*\phi_i(1)\phi_j^*(1) \end{aligned} \tag{2.59}$$

expressed to second-order in R. The total excitation energy to all orders in U and to second-order in R is expressed as

$$\Delta E'_{\mathrm{M}} = \Delta E'_{\mathrm{M}}(R, U). \tag{2.60}$$

The parts of eq (2.60) that depend on U are the same as eq (2.56). The relaxation energy to second-order in R is given as

$$\begin{aligned}\Delta E^{(2)}_{\text{Rel}}[\rho'(1,1')] = &\sum_{ai} R_{ai}R^*_{ai}\left(\epsilon^0_a - \epsilon^0_i\right) + \sum_{ai}\sum_{bj} R_{ai}R_{bj}K^{\text{KS}}_{ai,bj} \\ &+ \frac{1}{2}\sum_{ai}\sum_{bj} R_{ai}R_{bj}K^{\text{KS}}_{ai,jb} + \frac{1}{2}\sum_{ai}\sum_{bj} R^*_{ai}R^*_{bj}K^{\text{KS}}_{ai,jb} \\ &+ \mathcal{O}[U^3]. \end{aligned} \tag{2.61}$$

The matrices U and R are determined self-consistently under the condition that the excitation represents a transfer of one whole electron from the density space spanned by the un-relaxed occupied reference state orbitals $\{\phi_i; i = 1, occ\}$ to the density space spanned by the un-relaxed virtual reference state orbitals $\{\phi_a; a = 1, vir\}$, eq (2.62)

$$\sum_{i}^{occ} \sin^2[\eta\gamma_i] = 1. \tag{2.62}$$

The expanded form of the total energy expression in terms of relaxed orbitals shown in eq (2.60) is given as

$$\begin{aligned}\Delta E'_{\text{M}}(R,U) = &\sum_{i}^{occ} \sin^2[\eta\gamma_i]\left(F^{\text{KS}}_{i^v i^v}\left[\rho^{(0)} + \frac{1}{2}\Delta\rho^{R,U}\right] - F^{\text{KS}}_{i^o i^o}\left[\rho^{(0)} + \frac{1}{2}\Delta\rho^{R,U}\right]\right) \\ &+ \sum_{i}^{occ} \sin[\eta\gamma_i]\cos[\eta\gamma_i]\left(F^{\text{KS}}_{i^v i^o}\left[\rho^{(0)} + \frac{1}{2}\Delta\rho^{R,U}\right] + F^{\text{KS}}_{i^v i^o}\left[\rho^{(0)} + \frac{1}{2}\Delta\rho^{R,U}\right]\right) \\ &+ \mathcal{O}^{[3]}[\Delta\rho^{R,U}]. \end{aligned} \tag{2.63}$$

A Taylor expansion of eq (2.63) followed by a differentiation with respect to ΔU and ΔR leads to

$$\begin{aligned}\begin{pmatrix} \vec{g}^{U^{\alpha\alpha}}(0) \\ \vec{g}^{R^{\alpha\alpha}}(0) \\ \vec{g}^{R^{\beta\beta}}(0) \end{pmatrix} + &\begin{pmatrix} \mathbf{H}^{U^{\alpha\alpha},U^{\alpha\alpha}}(0) & \mathbf{H}^{U^{\alpha\alpha},R^{\alpha\alpha}}(0) & \mathbf{H}^{U^{\alpha\alpha},R^{\beta\beta}}(0) \\ \mathbf{H}^{R^{\alpha\alpha},U^{\alpha\alpha}}(0) & \mathbf{H}^{R^{\alpha\alpha},R^{\alpha\alpha}}(0) & \mathbf{H}^{R^{\alpha\alpha},R^{\beta\beta}}(0) \\ \mathbf{H}^{R^{\beta\beta},U^{\alpha\alpha}}(0) & \mathbf{H}^{R^{\beta\beta},R^{\alpha\alpha}}(0) & \mathbf{H}^{R^{\beta\beta},R^{\beta\beta}}(0) \end{pmatrix} \\ &\times \begin{pmatrix} \Delta\vec{U}^{\alpha\alpha} \\ \Delta\vec{R}^{\alpha\alpha} \\ \Delta\vec{R}^{\beta\beta} \end{pmatrix} = 0 \end{aligned} \tag{2.64}$$

where $\vec{g}$ is the gradient and $\mathbf{H}$ is the Hessian, and the "(0)" included means that the gradients and the Hessians are calculated at $U^{0,\alpha\alpha}$, $R^{0,\alpha\alpha}$ and $R^{0,\beta\beta}$. U is optimized with the constraint shown in eq (2.62). An additional orthogonality constraint, $Tr(U^{I+}U^{K})$ = 0, for an excited states K = 1,$I-1$ that are below the state I in the optimization of both U and R; this prevents the collapse of I into some lower excited states [49, 51]. It must be noted here that, for a single orbital replacement, the energies obtained after optimizaton of U and R are identical to eqs (2.37), (2.38) and (2.39).

Chapter 3

Calculation of Exchange Coupling Constants in Triply-Bridged Binuclear Cu(II) Compounds Based on Spin-Flip Constricted Variational Density Functional Theory

3.1 Introduction

Binuclear copper complexes have been studied extensively in connection with molecular magnetism [100, 101], high-temperature superconductivity [102] and modeling of metalloenzymes [103, 104, 105, 106, 107, 108]. Depending on the coordination of the copper centres and the identity of the bridging ligands these systems can be either ferromagnetic or anti-ferromagnetic. Magnetism in metal clusters can in general be considered as an interaction of the localized spin angular momentum on different metal centres [100]. The weak interaction between the adjacent spins is conveniently described by a Heisenberg Hamiltonian [109],

$$\hat{H} = -\sum_{i,j} J_{ij} \hat{S}_i \hat{S}_j. \tag{3.1}$$

In eq (3.1), J_{ij} is the exchange coupling constant between two spins $\hat{S}_i$ and $\hat{S}_j$ of adjacent metal centers. In dinuclear copper complexes where each center carries a spin of S_i = 1/2, the exchange coupling constant J_{ij} represents the energy difference between the lowest triplet and singlet states of the dimer [110]:

$$J = E_{\text{singlet}} - E_{\text{triplet}}. \tag{3.2}$$

Thus an anti-ferromagnetic singlet ground state has a negative J value whereas a positive J value indicates a ferromagnetic triplet ground state. The exchange cou-

pling constants can be experimentally determined from magnetic susceptibility measurements or neutron dispersion spectroscopy. Copper dinuclear systems have received considerable experimental and theoretical attention. These complexes contain both doubly or triply bridged copper atoms and cover a large range of positive and negative [111, 112, 113, 114, 115, 116, 117, 118, 119, 120, 120, 121, 122] J values. Their structures are determined from X-ray spectroscopy and the J constants are measured from magnetic susceptibility experiments. There have been a number of attempts based on empirical, magneto-structural and theoretical considerations to rationalize trends in the observed values of these complexes [123, 124, 125, 126, 127, 128, 129, 130, 131, 132, 133, 134, 135, 136, 137, 138].

The broken symmetry approach of Noodleman [139, 140, 141] based on density functional theory (BS-DFT) is currently the most used scheme for the first principle calculation of exchange coupling constants. It has been employed to a variety of di- and poly-nuclear metal complexes with a large variety of approximate functionals [110, 111, 113, 114, 136, 137, 138, 142, 143, 144, 145, 146, 147, 148, 149, 150, 151], including LDA [36], GGA [37, 38, 152], hybrid [39], hybrid meta-GGA [92, 153, 154] and long-range separated [88, 155, 156] functionals. Other DFT based methods employed in magnetic studies are the Restricted Ensemble Kohn Sham (REKS), and Restricted Open Shell Kohn Sham (ROKS) schemes [110, 111, 150, 157, 158, 159, 160]. Use has also been made of high level $ab\ initio$ schemes [114, 133, 135, 136, 143, 149, 150, 161, 162, 163, 164, 165] including multi-reference wave function approaches [166, 167, 168, 169].

We have recently [170] introduced Second Order Spin-Flip Constricted Variational DFT (SF-CV(2)-DFT) [47] as an alternative scheme for the evaluation of exchange coupling constants in polynuclear metal complexes. Our method has so far been tested on two trinuclear copper compounds [170] and a number of binuclear copper complexes with two bridging ligands [171]. Our objective with the current study is to extend the test to a series of dinuclear complexes with three bridging ligands. This series has previously been studied by a number of theoretical methods as discussed in a recent

study [151]. The spin-flip approach was originally introduced by Krylov in $ab\ initio$ wave function theory [172].

3.2 Theoretical Details

3.2.1 Computational Method

For the copper complexes studied here a natural reference would be the ferromagnetic triplet state ${}^3\Psi_1$ with two electrons of the same spin in two different orbitals ϕ_r, ϕ_s which we can write as $1^3\Psi_1 = |\phi_r\phi_s|$. A CV(2)-DFT calculation now affords state functions of the general form

$$\Psi^{(I)} = \sum_{a}^{vir}\sum_{i}^{occ} U_{\bar{a}i}^{(I)}\Psi_{i\to\bar{a}} \tag{3.3}$$

where $\Psi_{i\to\bar{a}}$ is a determinantal wave function constructed from $|\phi_r\phi_s|$ by substituting an occupied reference orbital ϕ_i of α–spin by a virtual reference orbital of β–spin. Some of the states of the form $\Psi^{(I)}$ that can be obtained from eq (3.3) are the anti-ferromagnetic singlet state of lowest energy $1^1\Psi_0$, which will have a leading contribution from $U_{\bar{r}s}|\phi_r\bar{\phi}_r| + U_{\bar{s}r}|\phi_s\bar{\phi}_s|$ as well as the ferromagnetic triplet state $1^3\Psi_0$ with $m_s = 0$ which will have a major contribution from $U_{\bar{s}s}|\phi_r\bar{\phi}_s| + U_{\bar{r}r}|\bar{\phi}_r\phi_s|$. We can subsequently calculate J according to eq (3.2) as

$$J = E(1^1\Phi_0) - E(1^3\Phi_0). \tag{3.4}$$

We could alternatively have determined J from $J = E(1^1\Phi_0) - E(1^3\Phi_1)$. We prefer eq (3.4) as it gives a more balanced description where both states are described on the same footing in the form eq (3.3) according to CV(2)-DFT. This is as opposed to the alternative where $1^3\Phi_1$ is described by a single determinantal function and $1^1\Phi_0$ according to CV(2)-DFT on the form eq (3.3). Such a practice is common in studies based on multi-configuration wave function theory [173].

It should be noted that "a, b" and "i, j" in eqs (2.24) and (2.25) are of different spins as all microstates $\Psi_{i\to\bar{a}}$ are generated by a spin-flip $i \to \bar{a}$, where i is of α–spin and $\bar{a}$

is of β–spin. The formula for $K^{\text{KS}}_{\bar{a}i\bar{b}j}$ required in eq (2.47) were first derived by Wang and Ziegler [47, 52, 53, 170, 171, 172, 173, 174, 175, 176, 177, 178], see also Refs. [179, 180]. We have

$$K^{XC(\text{KS})}_{\bar{a}i\bar{b}j} = \int \bar{\phi}^*_a(r_1)\phi_i(r_1)\bar{\phi}_b(r_1)\phi^*_i(r_1) \times \frac{1}{2}\left[\left(\frac{1}{s^0}\left(\frac{\partial E^{\text{KS}}_{XC}}{\partial \rho_\alpha} - \frac{\partial E^{\text{KS}}_{XC}}{\partial \rho_\beta}\right)\right)_{\rho^0,s^0}\right] dr_1 \tag{3.5}$$

where integration over spin already has taken place so that $\bar{\phi}^*_a(r_1)$, $\bar{\phi}^*_b(r_1)$ represent the spatial part of the two virtual orbitals of β–spin. The evaluation of $K^{XC(\text{KS})}_{\bar{a}i\bar{b}j}$ by numerical integration might lead to numerical instabilities if $s^0(\mathbf{r}) = \rho^\alpha(\mathbf{r}) - \rho^\beta(\mathbf{r}) \approx 0$. We can in that case carry out a Taylor expansion of $\partial E^{\text{KS}}_{XC}/\partial\rho_\alpha$, $\partial E^{\text{KS}}_{XC}/\partial\rho_\beta$ from $\rho = \rho^\alpha + \rho^\beta$ and $s^0 = 0$. Thus

$$\begin{aligned} K^{XC(\text{KS})}_{\bar{a}i\bar{b}j} =& \int \bar{\phi}^*_a(r_1)\phi_i(r_1)\bar{\phi}_b(r_1)\phi^*_i(r_1) \\ & \times \frac{1}{2}\left[\left(\frac{\partial^2 E^{\text{KS}}_{XC}}{\partial \rho^2_\alpha} + \frac{\partial^2 E^{\text{KS}}_{XC}}{\partial \rho^2_\beta} - 2\frac{\partial^2 E^{\text{KS}}_{XC}}{\partial \rho_\alpha \rho_\beta}\right)_{\rho^0,s^0=0}\right] dr_1 \\ =& K^{XC(\text{KS})}_{aibj} - K^{XC(\text{KS})}_{ab\bar{i}\bar{j}} \end{aligned} \tag{3.6}$$

where $K^{XC(\text{KS})}_{aibj}$ and $K^{XC(\text{KS})}_{ab\bar{i}\bar{j}}$ are well defined integrals from regular TD-DFT [53, 52]. The expression in eq (3.6) is correct to $(s^0)^3$ and has no singularities for $s^0 = 0$. It can thus be used for small values of s^0 where eq (3.5) becomes singular. In practice we have found that eq (3.5) can be used for VWN [36]. For functionals based on the generalized gradient approximation (GGA) [37, 38, 152] where we can write the exchange-correlation energy as $E^{\text{GGA}}_{XC} = E^{\text{VWN}}_{XC} + \Delta E^{\text{GGA}}_{XC}$, we calculate the contribution from E^{VWN}_{XC} according to eq (3.5) and the contribution from $\Delta E^{\text{GGA}}_{XC}$ in line with eq (3.6). For the hybrid functionals B3LYP [39] and BHLYP [39] we need in addition to calculate the regular exchange integral $K^{XC(\text{HF})}_{aibj} = -\iint \phi^*_{\bar{a}}(r_1)\phi_{\bar{b}}(r_2)\frac{1}{r_{12}}\phi_{\bar{i}}(r_1)\phi^*_{\bar{j}}(r_2)dr_1dr_2$ already implemented in ADF [181].

3.2.2 Computational Details

All SF-CV(2)-DFT calculations were performed with an all electron TZ2P [181] basis set within the unrestricted Kohn-Sham formalism [174] as implemented in ADF2010 [181]. The used functionals include LDA-VWN [36], BP86 [37, 38], BLYP [37, 152], B3LYP [39] and BHLYP [39].

3.2.3 Molecular Models

The eleven studied dinuclear triply-bridged Cu(II) systems are arranged and displayed according to increasing experimental exchange coupling constants J, see Figure 3.1. The penta-coordinated complexes have the following structural characteristics; Complex 1 with the chemical formula [Cu_2(μ-$O_2CC_2H_5$)(μ-$OCOC_2H_5$)(μ-OH)(dpyam)$_2$](-ClO_4) and a Cambridge Crystallographic Data Centre (CCDC) refcode YAHZEN [122] has no symmetry. Both Cu(II) centres have a square pyramidal coordination geometry. The coppers are bridged by two carboxylato ligands and a hydroxo group. The two oxygen atoms of the carboxylato ligand occupy, respectively, the equatorial position on one centre and the apical position on the other centre. The remaining equatorial sites are taken up by OH and nitrogens on the non-coplanar dpyam bases.

Complex 2 with the chemical formula [Cu_2 (μ-O_2CCH_3)(μ-OH)(μ-OH_2)(bpy)$_2$] (ClO_4)$_2$ and CCDC refcode JEJCIK10 [182] is of C_s symmetry with two Cu(II) centres bridged by carboxylato, hydroxo and water ligands. The bidentate 2,2′-bipyridine(bpy), the water, hydroxo and carboxylato ligands are ordered in a square pyramidal geometry with water at the apical position.

Complex 3 with the chemical formula [Cu_2(μ-O_2CH)(μ-OH)(μ-OMe)(dpyam)$_2$] (ClO_4) and a CCDC refcode EBEFIB [121] is of C_s symmetry. Each Cu(II) centre has a trigonal bipyramidal ligand environment. The carboxylato and the methoxo ligands occupy the equatorial position. The O atom at one of the axial positions belongs to the hydroxo ligand and the N atom at the other axial position belongs to the bidentate 2,2′-bipyridylamine(dpyam) ligand. The position of the H atom of the hydroxo ligand

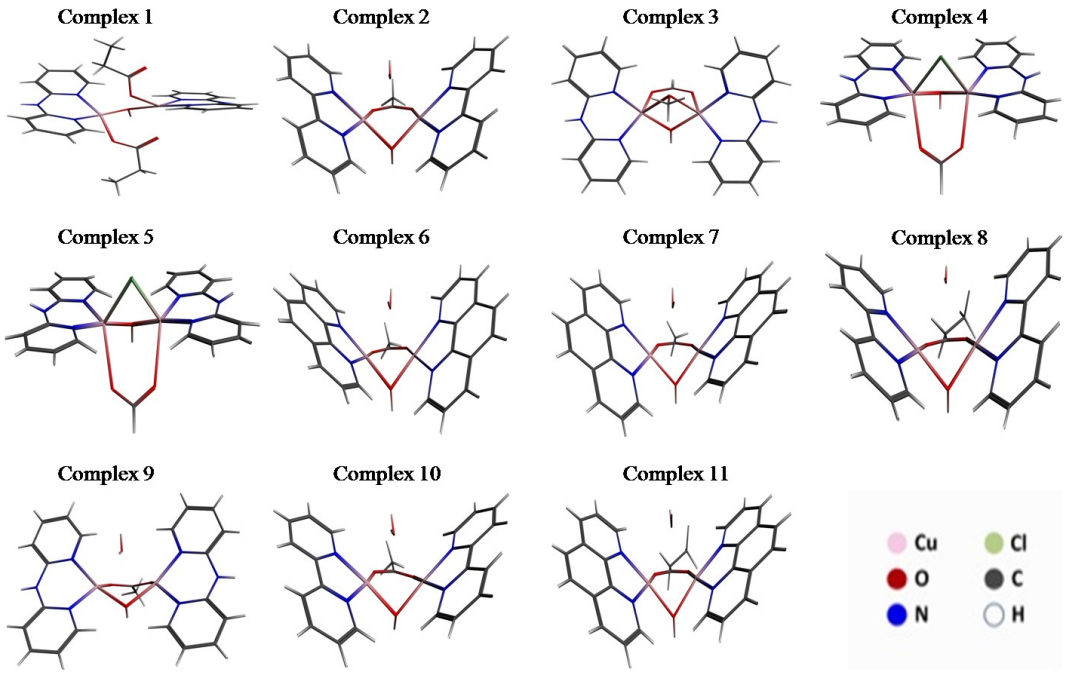

Figure 3.1: Structures of the 11 complexes studied, numbered in increasing order of experimental J values

was adjusted to correspond to the remaining series of complexes, the justification for this is given in reference [151].

Complex 4 with the chemical formula $[Cu_2(\mu\text{-}O_2CH)(\mu\text{-}OH)(\mu\text{-}Cl)(dpyam)_2](ClO_4)$ $0.5H_2O$ and the refcode RUXDIX01 [121] is of C_s symmetry and features non-coplanar bases with a trigonal bipyramidal geometry around each Cu(II) centre. The two Cu(II) centres are bridged by carboxylato, hydroxo and chloro ligands. The O atom on one of the axial positions belongs to the hydroxo ligand and the N atom in the other axial position belongs to the bidentate dpyam ligand.

Complex 5 with the chemical formula $[Cu_2(\mu\text{-}O_2CH)(\mu\text{-}OH)(\mu\text{-}Cl)(dpyam)_2](PF_6)$ and a CCDC refcode YAHYUC [122] is of C_s symmetry and the two Cu(II) centres bridged through the carboxylato, hydroxo and chloro ligands. Each Cu(II) centre has a trigonal bipyramidal geometry. The axial position is occupied by the O atom of the hydroxo ligand and N atom of the bidentate dpyam ligand.

Complex 6 with the chemical formula $[Cu_2(\mu\text{-}O_2CCH_3)(\mu\text{-}OH)(\mu\text{-}OH_2)(phen)_2]$ $(ClO_4)_2$ and a CCDC refcode YEMNIO [120] has the bidentate 1,10-phenanthroline(phen) at each Cu(II) centre. The complex has no symmetry and the two Cu(II) centres are

bridged by the carboxylato, hydroxo and water ligands. Each Cu(II) centre has a square pyramidal coordination. The phen, carboxylato and the hydroxo ligands occupy the basal position with the water at the apical site.

Complex 7 with the chemical formula $[Cu_2(\mu\text{-}O_2CCH_3)(\mu\text{-}OH)(\mu\text{-}OH_2)(phen)_2](BF_4)_2$ and a CCDC refcode CITLOH [119] has no symmetry and has two Cu(II) ions bridged by carboxylato, hydroxo and water ligands. Each Cu(II) ion is five co-ordinated and features a square pyramidal geometry with non-coplanar bases where the bidentate phen, hydroxo and carboxylato ligands at the basal position and the water ligand at the apical position.

Complex 8 with the chemical formula $[Cu_2(\mu\text{-}O_2CCH_2CH_3)(\mu\text{-}OH)(\mu\text{-}OH_2)(bpy)_2](ClO_4)_2$ and a CCDC refcode YEMNEK [120] has no symmetry and two Cu(II) centres bridged by the carboxylato, hydroxo and the water ligands. The complex has non-coplanar bases with a square pyramidal coordination geometry at each Cu(II) centre.

Complex 9 with the chemical formula $[Cu_2(\mu\text{-}O_2CH)(\mu\text{-}OH)(\mu\text{-}OH_2)(dpyam)_2](S_2O_8)$ and a CCDC refcode CITLEX [119] has two dpyam ligands and three bridging groups (hydroxo, carboxylato and water). The complex is of C_s symmetry featuring non-coplanar bases with a square pyramidal coordination geometry around each Cu(II) centre. The dpyam, hydroxo and carboxylato ligands at the basal position and the water at the apical site.

Complex 10 with the chemical formula $[Cu_2(\mu\text{-}O_2CCH_3)(\mu\text{-}OH)(\mu\text{-}OH_2)\ (bpy)_2](NO_3)_2$ and a CCDC refcode CITLIB [119] is of C_s symmetry with a square pyramidal coordination geometry around each Cu(II) centre. The two bidentate bpy bases, a hydroxo group and a carboxylato ligand occupy the basal positions. A water molecule is at the apical site.

Complex 11 with the chemical formula $[Cu_2(\mu\text{-}O_2CCH_2CH_3)(\mu\text{-}OH)(\mu\text{-}OH_2)(phen)_2](NO_3)_2$ and a CCDC refcode YAFZUA01 [119] has two square pyramidal Cu(II) centres bridged by carboxylato, hydroxo and water ligands. No modifications were made to the complexes except that the counter ions were removed and in complex 4, the water of hydration was removed as well. The complexes studied in this work have also

been used in ref. [151].

3.3 Results and Discussion

Electronic Structure of Complexes 1–11. Figures 3.2, 3.3 and 3.4 display the frontier spin orbitals of complexes 1–11 as well as the corresponding orbital energies. The orbitals were obtained from unrestricted Kohn-Sham SCF calculations on the reference triplet state in its optimized geometry using the LDA-VWN functional.

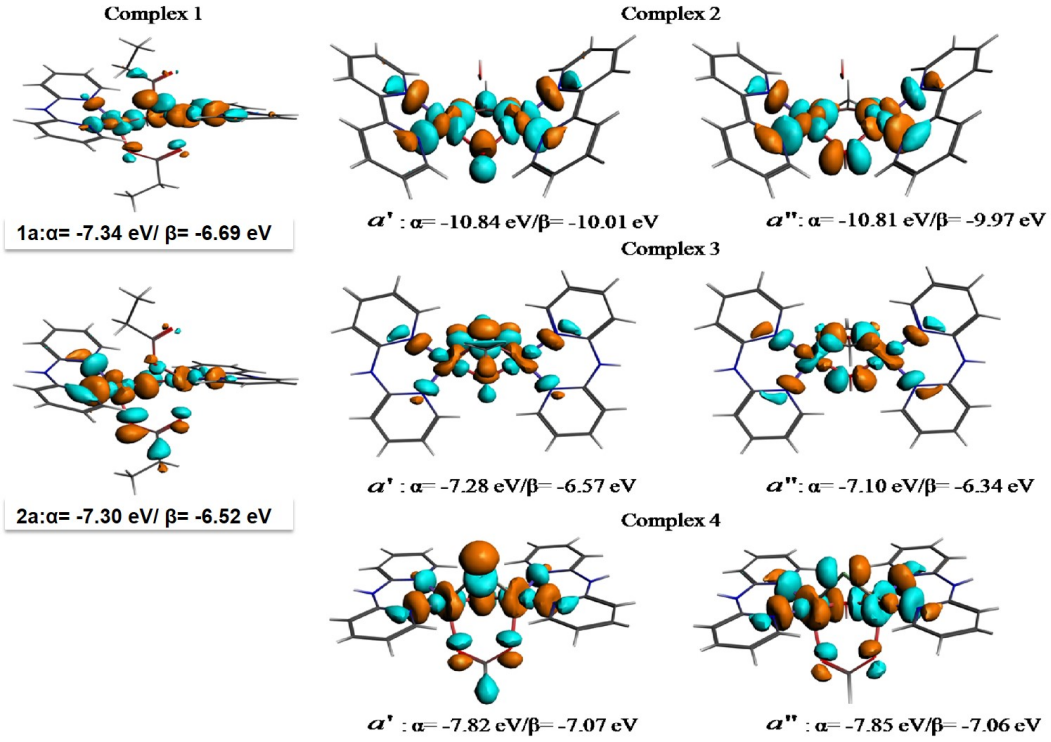

Figure 3.2: Frontier SUMO orbitals $\bar{a}'$, $\bar{a}''$ with C_s symmetry and $1\bar{a}$, $2\bar{a}$ without symmetry for first 4 complexes with corresponding orbital energies. The SOMO orbitals a', a'' and $1a$, $2a$ are not shown because of they have a similar spatial distribution to their SUMO counterparts.

The triplet ground state has 2 unpaired electrons of α–spin in $1a$ and $2a$ or a' and a''. These orbitals are referred to as SOMOs (singly-occupied molecular orbitals) whilst the lowest vacant orbitals of β–spin are referred to as SUMOs (singly-unoccupied molecular orbitals). The SUMOs have almost the same composition as the corresponding SOMOs. However, their energies are higher as the smaller number of β–electrons lead to fewer stabilizing exchange interactions compared to the α–manifold.

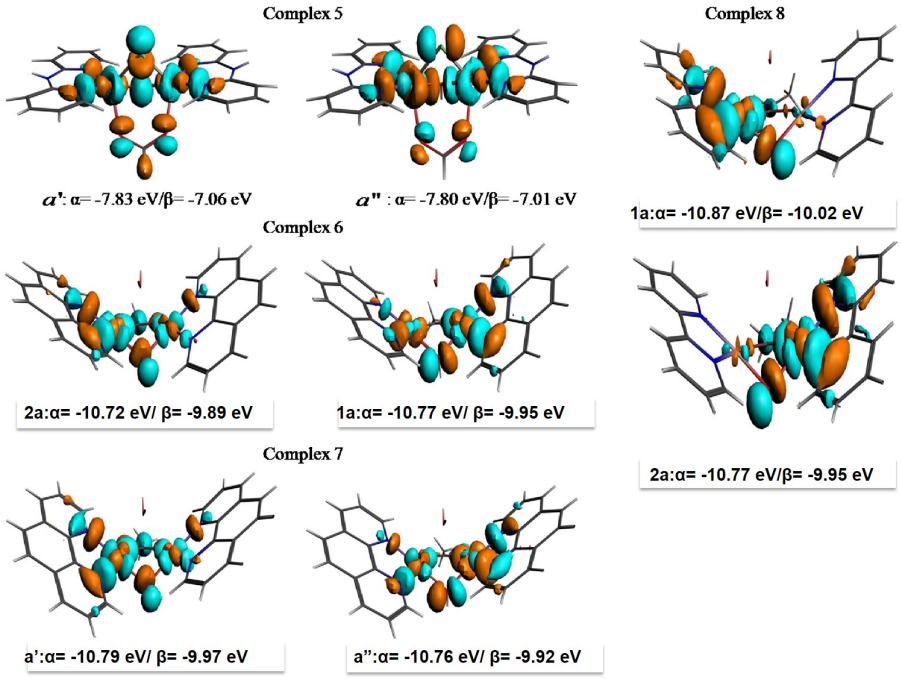

Figure 3.3: Frontier SUMO orbitals $\bar{a}'$, $\bar{a}''$ with C_s symmetry and $1\bar{a}$, $2\bar{a}$ without symmetry for complexes 5-8, with corresponding orbital energies. The SOMO orbitals a', a'' and $1a$, $2a$ are not shown because of they have a similar spatial distribution to their SUMO counterparts.

The two unpaired electrons can be distributed in the four frontier spin-orbitals to give three possible electronic configurations: $(1a\ )^2(2a)^0$, $(1a)^1(2a)^1$ and $(1a)^0(2a)^2$ in the case of no symmetry and $(a')^2(a'')^0$, $(a')^1(a'')^1$ and $(a')^0(a'')^2$ in the case of C_s symmetry. These configurations give rise to microstates of different multiplicity and symmetry.

The construction of the symmetrized microstates was carried out with the clebesch-egordan.exe program [183]. The number of microstates is calculated to be six. Tables 3.1 and 3.2 display all 6 singlet and triplet microstates which can be built with the two unpaired electrons and the four SUMOs and SOMOs of C_s symmetry or no symmetry, respectively.

Tables 3.3 – 3.7 display results from SF-CV(2)-DFT calculations based on the unrestricted LDA KS-DFT geometries of the reference state $a(^3A')_1$ for the C_s symmetry and $a(^3A)_1$ for no symmetry, the remaining are shown in Tables A.1, A.2, A.3, B.1, B.2, and B.3 in Appendices A and B.

The ligands around the Cu(II) ions in the studied complexes 1, 2, 6, 7, 8, 9, 10

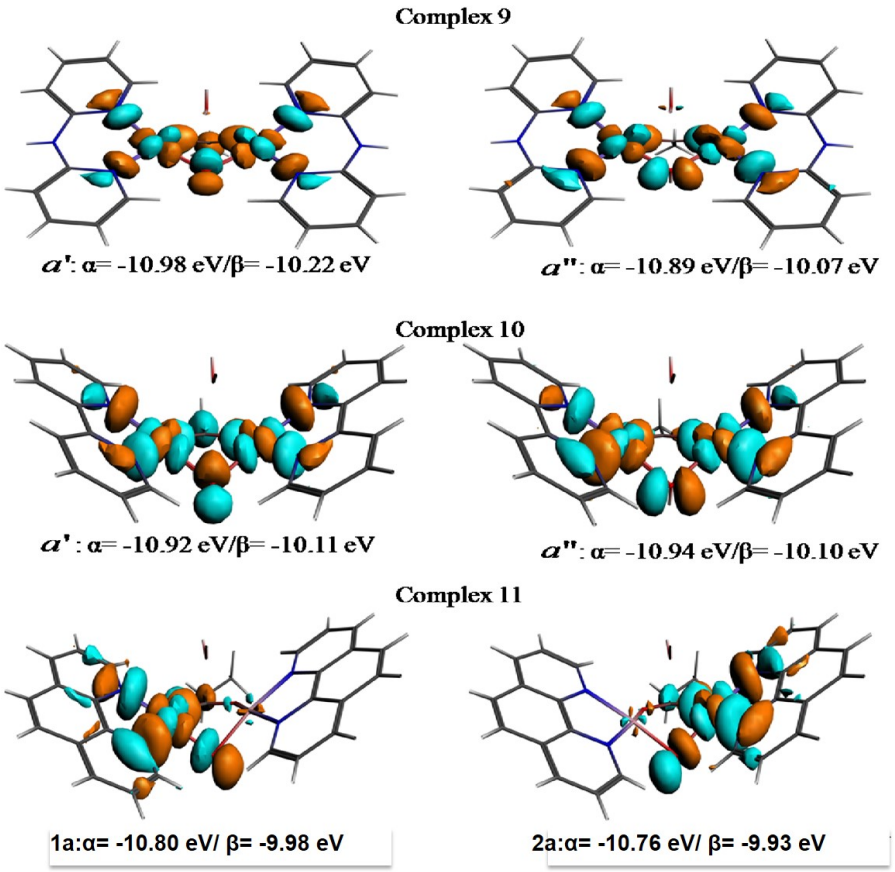

Figure 3.4: Frontier SUMO orbitals $\bar{a}'$, $\bar{a}''$ with C_s symmetry and $1\bar{a}$, $2\bar{a}$ without symmetry for complexes 9-11, with corresponding orbital energies. The SOMO orbitals a', a'' and $1a$, $2a$ are not shown because of they have a similar spatial distribution to their SUMO counterparts.

and 11 adopt a square pyramidal coordination geometry [151] and those around the complexes 3, 4 and 5 adopt a trigonal bipyramidal geometry. The frontier orbital for the complexes that adopt the square pyramidal geometry can be described as an out-of-phase combination of the $d_{x^2-y^2}$–orbitals on the two Cu centres and the ligand p–orbitals at the basal/equatorial sites. Here $d_{x^2-y^2}$ refers to a local coordinate system on each copper site with the z–axis pointing towards the apical ligand. In complexes 1, 2, 6, 7, 9, 10 the two $d_{x^2-y^2}$ orbitals contribute to both SOMOs (and SUMOs) with ++ and +− contributions, respectively. In complexes 8 and 11, the SOMOs (and SUMOs) are symmetry broken with contributing orbitals on either one of the two Cu(II) centres. In complex 1 there is a small anti-bonding contribution from the p–orbital of the apical O atom of the carboxylato ligand on one centre and an additional small anti-bonding contribution from the O atom of the apical monatomic carboxylato ligand.

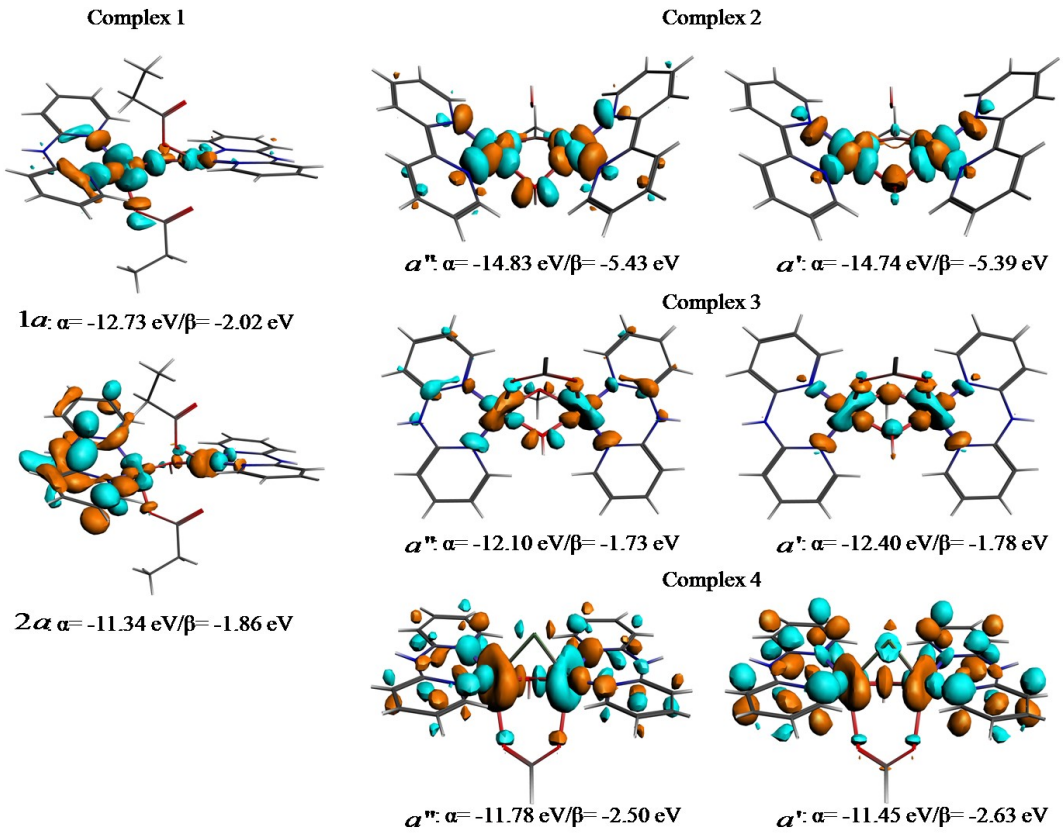

Figure 3.5: Frontier SUMO orbitals $\bar{a}'$, $\bar{a}''$ with C_s symmetry and $1\bar{a}$, $2\bar{a}$ without symmetry for complexes 1-4 using the BHLYP functional, with corresponding orbital energies. The SOMO orbitals a', a'' and $1a$, $2a$ are not shown because of they have a similar spatial distribution to their SUMO counterparts.

For the complexes that adopt a trigonal bipyramidal geometry, the frontier orbitals can be described as an out-of-phase combination of Cu d_{z^2} orbitals and the ligand p–orbitals in the axial position with an anti-bonding contribution from the ligand p–orbitals in the equatorial sites. Here d_{z^2} refers to a local coordinate system centred on each copper with the z–axis pointing towards the axial ligands.

In complexes 2, 3, 4, 5, 9 and 10 the C_s symmetry was imposed and we obtained orbitals of a' and a'' symmetry with a' slightly below a'' in energy. For complexes 1, 6, 7, 8 and 11 where symmetry was not imposed we obtained the orbitals $1a$ and $2a$ with $1a$ of slightly lower energy. We observe for the complexes two structural motifs, in the first (complexes 1, 2 and 6–11), there is a σ–interaction between the Cu d-orbitals and the p-orbital on the hydroxo ligand for a' or $1a$ whereas for a'' or $2a$ there is a π–interaction between the Cu d-orbitals and the p-orbital of the hydroxo ligand. In

Table 3.1: Singlet and Triplet Microstates for Binuclear Triply-Bridged Cupper(II) Compounds in the C_s Symmetry

C_s	M_s	C_s symmetrized microstate functions
		$(a')^2$ configuration[a,b]
$a(^1A')$	0	$\|a'\bar{a}'\|$
		$(a')^1(a'')^1$ configuration
$^1A''$	0	$1/\sqrt{2}\ (\|a'\bar{a}''\| - \|\bar{a}'a''\|)$
$a(^3A'')$	1	$\|a'a''\|$
$b(^3A'')$	0	$1/\sqrt{2}(\|a'\bar{a}''\| + \|\bar{a}'a''\|)$
$c(^3A'')$	-1	$\|\bar{a}'\bar{a}''\|$
		$(a'')^2$ configuration
$b(^1A')$	0	$\|a''\bar{a}''\|$

[a]Electronic configuration. [b] a' and a'' are the frontier orbitals of α–spin, whereas $\bar{a}'$ and $\bar{a}''$are frontier orbitals of β–spin.

the second structural motif (complexes 3–5), there is a σ–interaction between the Cu d–orbitals and the p–orbital on the chloro ligand for a', whereas for a'' there is a π–interaction between the Cu d-orbitals and the p-orbital of the chloro ligand. The spin-states can be expressed as a linear combination of the symmetrized spin-microstates defined by eq (3.3). The lowest singlet for the complexes consists mainly of two single determinantal microstates $|a'\bar{a}'|$ and $|a''\bar{a}''|$ or $|1a1\bar{a}|$ and $|2a2\bar{a}|$ and has the form:

$$1^1\Psi_0 = c_1|a'\bar{a}'| + c_2|a''\bar{a}''|. \tag{3.7}$$

The statistical weights vary from an even contribution to a contribution dominated by one determinantal microstate depending on the energy difference between a' and a'' or $1a$ and $2a$. The difference in energy between a' or $1a$ and a'' or $2a$ is due to the extent of overlap between the Cu d–orbitals and ligand p–orbitals. The σ–interaction that exist in a' or $1a$ is out-of-phase with a smaller overlap whereas the π–interaction in a'' and $2a$ is of relatively larger overlap in absolute terms, as a result we observe that a' and $1a$ are of lower energy than a'' and $2a$. Also, we observe that the complexes with trigonal bipyramidal geometry are of higher energy than those of the square pyramidal geometry as a result of the increase number of out-of-phase interaction between the Cu d–orbitals and the ligand p–orbitals.

Table 3.2: Singlet and Triplet Microstates for Binuclear Triply-Bridged Cupper(II) Compounds without Symmetry

C_1	M_s	C_1 symmetrized microstate functions
		$(1a)^2$ configuration[a,b]
$a(^1A)$	0	$\|1a1\bar{a}\|$
		$(1a)^1(2a)^1$ configuration
$b(^1A)$	0	$1/\sqrt{2}(\|1a2\bar{a}\| - \|1\bar{a}2a\|)$
$a(^3A)$	1	$\|1a2a\|$
$b(^3A)$	0	$1/\sqrt{2}(\|1a2\bar{a}\| + \|1\bar{a}2a\|)$
$c(^3A)$	-1	$\|1\bar{a}2\bar{a}\|$
		$(2a)^2$ configuration
$c(^1A)$	0	$\|2a2\bar{a}\|$

[a]Electronic configuration. [b] $1a$ and $2a$ are the frontier orbitals of α–spin, whereas $1\bar{a}$ and $2\bar{a}$ are frontier orbitals of β–spin.

Table 3.3: Lower Excited States for Complex 1 Based on SF-CV(2)-DFT Calculations Using LDA-VWN Functional

C_1 Symmetry			
State	E, cm^{-1}	Contributing microstates	%
^3A	0	b(^3A)	92
1^1A	144	a(^1A)	44
		c(^1A)	16
2^1A	4454	a(^1A)	45
		c(^1A)	
3^1A	5454	b(^1A)	80

Table 3.4: Lower Excited States for Complex 2 Based on SF-CV(2)-DFT Calculations Using LDA-VWN Functional

C_s Symmetry			
State	E, cm^{-1}	Contributing microstates	%
$^3A''$	0	b($^3A''$)	98
$1^1A'$	287	a($^1A'$)	53
		b($^1A'$)	45
$^1A''$	6183	($^1A''$)	100
$2^1A'$	6593	a($^1A'$)	46
		b($^1A'$)	54

Table 3.5: Lower Excited States for Complex 3 Based on SF-CV(2)-DFT Calculations Using LDA-VWN Functional

C_s Symmetry			
State	E, cm^{-1}	Contributing microstates	%
$^3A''$	0	b($^3A''$)	95
$1^1A'$	358	a($^1A'$)	60
		b($^1A'$)	33
$^1A''$	4993	($^1A''$)	94
$2^1A'$	5760	a($^1A'$)	37
		b($^1A'$)	47

Table 3.6: Lower Excited States for Complex 4 Based on SF-CV(2)-DFT Calculations Using LDA-VWN Functional

C_s Symmetry			
State	E, cm^{-1}	Contributing microstates	%
$^3A''$	0	b($^3A''$)	97
$1^1A'$	407	a($^1A'$)	49
		b($^1A'$)	49
$^1A''$	5492	($^1A''$)	100
$2^1A'$	6066	a($^1A'$)	50
		b($^1A'$)	48

Table 3.7: Lower Excited States for Complex 5 Based on SF-CV(2)-DFT Calculations Using LDA-VWN Functional

C_s Symmetry			
State	E, cm^{-1}	Contributing microstates	%
$^3A''$	0	b($^3A''$)	97
$1^1A'$	332	a($^1A'$)	55
		b($^1A'$)	42
$^1A''$	5644	($^1A''$)	99
$2^1A'$	6153	a($^1A'$)	43
		b($^1A'$)	56

In complexes 2, 4, 5 and 10, where the pair a' and a'' have similar energies, the singlet state is an almost 50–50 % mixture of the two microstates. For complexes 3 and 9 where the orbital energy difference between the two frontier orbital pairs is significant, the singlet state is predominated (60–70 %) by the $|a'\bar{a}'|$ microstate. Complexes 1, 6 and 7 have (30–40 %) contribution from $|1a1\bar{a}|$ and 16–30 % from $|2a2\bar{a}|$. Complexes 8 and 11 of no symmetry consist predominantly ($\sim$100 %) of the open shell singlet composed of $|1a2\bar{a}|$ and $|1\bar{a}2a|$ as ${}^1\Psi_0 = 1/[(2)^{1/2}][|1a2\bar{a}| - |1\bar{a}2a|$. The two orbitals $1a$ and $2a$ are localized on different sites of the complex and ${}^1\Psi_0$ represent a symmetry broken solution. ${}^1\Psi_0$ represents the lowest energy singlet in these complexes. The triplet component $m_s = 0$, which is of lower energy than the singlet is given primarily as

$$ {}^3\Psi_0 = 1/[(2)^{1/2}][|1a2\bar{a}| + |1\bar{a}2a|. \tag{3.8} $$

The complexes, thus exhibit a ferromagnetic behavior due to the triplet ground state just as in the case of all the other systems. Further investigations must be done to explain why we get the symmetry broken solution for complexes 8 and 11 only.

3.3.1 Calculated J values based on SF-CV(2)-DFT

Table 3.8 displays the J values obtained from SF-CV(2)-DFT calculation, the experimentally determined J values and those obtained by employing the Broken Symmetry approach (BS-DFT) [151]. The BS-DFT results were obtained for the hybrid functionals B3LYP and BHLYP. Displayed in Table 3.8 are the J values obtained as the singlet-triplet energy gap (ΔE_{ST}) based on SF-CV(2)-DFT for the LDA-VWN, BP86, BLYP, PBE, B3LYP and BHLYP functionals. We find for the complete series of complexes that the SF-CV(2)-DFT schemes afford positive ΔE_{ST} values for all the functionals. Thus our scheme predicts complexes 1–11 to be ferromagnetic with the triplet (${}^3\Psi_0$) having a lower energy than the singlet (${}^1\Psi_0$), in agreement with experiment. Comparison between the J values obtained from the theoretical methods and the experimental estimates can be made through Table 3.8.

Table 3.8: List of the binuclear triply-bridged Cu(II) compounds, the calculated ΔE_{ST} values (SF-CV(2)-DFT), the values obtained from the BS-DFT approach and the experimental values in cm^{-1}.

	ΔE[a]								
Complexes	LDA[b]	BLYP[b]	BP86[b]	PBE[b]	B3LYP[b]	BHLYP[b]	B3LYP[c]	BHLYP[c]	Expt.
1	143.7	83.0	101.0	98.6	85.1	50.5	99.2	57.6	24.1[d]
2	286.2	208.5	216.2	214.8	150.0	66.9	169.0	83.2	38.6[e]
3	357.7	212.1	242.4	235.8	132.2	50.0	162.6	82.4	62.5[f]
4	407.3	297.3	317.6	307.5	194.2	75.4	185.7	83.6	79.1[f]
5	332.1	227.8	242.6	241.6	163.9	70.0	161.3	78.3	79.7[d]
6	287.8	208.7	217.9	215.8	156.6	68.0	169.7	80.5	120.0[g]
7	283.0	208.1	216.6	214.5	154.8	67.6	166.6	80.4	120.8[h]
8	315.1	230.9	237.8	236.7	162.4	71.8	176.7	87.0	148.9[g]
9	166.1	115.4	129.5	128.2	111.2	40.4	120.9	53.2	
10	303.5	224.5	232.0	230.7	153.2	65.8	166.2	79.6	
11	324.6	239.6	246.0	244.6	166.2	70.7	181.4	85.6	

[a]Note that positive values corresponds to a ferromagnetic ground state. [b] Values obtained from unrestricted SF-CV(2)-DFT. [c]Broken Symmetry values obtained from Ref. [151]. [d]Ref. [122]. [e]Ref. [182]. [f]Ref. [121]. [g]Ref. [120]. [h]Ref. [119].

As observed in previous studies [47, 170] the SF-CV(2)-DFT results demonstrate a strong functional dependence. The LDA and the GGAs strongly overestimate the magnitude of ΔE_{ST} for all complexes. On the other hand, the hybrid functionals B3LYP and BHLYP afford values closer to the experimental estimates.

Where experimental values are available, it can be observed that the BHLYP is in good agreement with experiment for complexes 1–5 and the best agreement with experiment for complexes 6, 7 and 8 is the B3LYP calculation. For complexes 9–11, where the experimental J values are unavailable the calculations with the hybrid functionals compare well with the values obtained for hybrid functionals in the BS-DFT method. The hybrid SF-CV(2)-DFT calculations in general yield results that are comparable to those obtained with the BS-DFT method. We display in Figure 3.5 the SUMOs and SOMOs for complexes 1–4 generated by the BHLYP functional.

A comparison with Figure 3.2 where the same orbitals are displayed based on LDA reveals that the two sets are qualitatively similar. However the contributions from the bridging ligands are reduced for BHLYP compared to LDA. As a result interaction integrals between the two centres are not as large for BHLYP as LDA. Leading to smaller J constants for BHLYP.

3.4 Concluding Remarks

The SF-CV(2)-DFT methodology for the calculation of exchange coupling constants has previously been employed to trinuclear Cu(II) systems [170] and doubly bridged dinuclear Cu(II) complexes [171]. The performance of the same methodology is here tested on a series of dinuclear triply-bridged Cu(II) systems. The comparison of the SF-CV(2)-DFT J values with coupling constants obtained from BS-DFT and experiment demonstrated that the unrestricted SF-CV(2)-DFT scheme in conjunction with hybrid functionals affords values that are comparable to those obtained by the BS-DFT method and experiment. Thus, SF-CV(2)-DFT is a viable alternative to the BS-DFT scheme. The SF-CV(2)-DFT methodology has further the advantage of providing a de-

scription of the different states in terms of a configuration interaction (CI) expansion of microstates. Also it is possible to optimize the geometry of the different spin-states separately [170]. Similar features are not readily available in the BS-DFT scheme.

Chapter 4

Role Played by Isopropyl Substituents in Stabilizing the Putative Triple Bond in Ar′EEAr′ [E = Si, Ge, Sn; Ar′ = C_6H_3-2,6-(C_6H_3-2,4-Pr^i_2)$_2$] and Ar*PbPbAr* [Ar* = C_6H_3-2,6-(C_6H_2-2,4,6-Pr^i_3)$_2$]

4.1 Introduction

Acetylene analogues of heavier group 14 elements, E, (E = Si, Ge, Sn, Pb) have come under scrutiny after the synthesis of the first homonuclear systems with the general formula ArEEAr (Ar = bulky aryl ligands) by Power $et\ al.$ [184, 185, 186, 187, 188, 189]. There have been several theoretical studies [190, 191, 192, 193, 194, 195, 196, 197, 198, 199, 200, 201, 202, 203, 204, 205, 206, 207, 208, 209, 210, 211, 212, 213, 214, 215] on acetylene analogues both before and after the work by Power. Most of these studies have been on model compounds such as E_2H_2 [194, 202] and E_2Me_2 [190, 203, 204, 205, 206]. A remarkable exception is the work by Takagi and Nagase [214] in which calculations on Ar*EEAr* (E = Si, Ge, Sn; Ar* = C_6H_3-2,6-(C_6H_2-2,4,6-Pr^i_3)$_2$) were presented simultaneously with or even prior to the isolation of similar compounds.

The studied E_2H_2 compound revealed that the linear structure is a second-order saddle point and the trans-bent geometry a local minimum or transition state [190] along the potential energy surface (PES) [195, 207, 208, 209]. The global minimum on the PES for E_2H_2 was found to be a structure in which the two E atoms are doubly-bridge by two hydrogens [193, 194, 195, 196, 198, 199, 200, 204, 205, 206, 207, 208, 209]. The synthesis of the first homologous acetylene compound Ar*PbPbAr* [184] was

followed shortly after by the isolation of ArGeGeAr [185, 188, 189] and ArSnSnAr [186, 187, 188, 189, 190]. All three species have a trans-bent structure with ∠E-E-C bond angles of 94.3^o, 125.2^o and 128.7^o for E = Pb, Sn and Ge, respectively. A diaryl ArSiSiAr compound for silicon is yet to be characterized. However, the synthesis of a silicon compound with the composition $(R_2MeSi)SiSi(SiMeR_2)$ [210, 211] where R=Bu^t_3-Si and $(R_2Pr^iSi)SiSi(SiPr^iR_2)28$ with R = $CH(Me_3Si)_2$ has been reported. The silicon compounds have a trans-bent geometry with an electronic structure [210, 211, 212, 213, 214, 215] that is different from the triple-bonded carbon homologues $(R_2MeSi)CC(SiMeR_2)$ with a linear CSiSiC geometry.

It is the primary objective of the present study to assess whether Ar* is able electronically to stabilize the E–E bond either by electron donation from the isopropyl substituents (Pri) on the aryl rings or through dispersive van der Waals attraction between isopropyl groups on aryl rings attached to different E elements. We carried out this assessment by making use of the extended transition state (ETS) energy decomposition scheme [14, 216] and the natural orbitals for chemical valence (NOCV) density decomposition approach [217] as combined recently into the NOCV-ETS [218] scheme with van der Waals dispersion included according to the formulation of Grimme [219]. The pioneering theoretical studies on Ar*EEAr* (E = Si, Ge,S n; Ar* = C_6H_3-2,6-(C_6H_2-2,4,6-Pr^i_3)$_2$) carried out previously [213, 214] by Takagi and Nagase employed a modest basis set. Further, no attempt was made to conduct a bonding analysis and dispersion was neglected. Thus, while the authors could point to the possible steric role played by isopropyl, they were unable to assess in detail its possible electronic influence.

The conventional molecular orbital model used to describe the bonding in the trans-bent REER systems goes back some 25 years to the work by Trinquier and Malrieu [198] as well as Carter and Goddard [199]. It has recently been adopted in a lucid form by Takagi and Nagase [213, 214] for trans-bent systems of interest here. This frontier orbital description will also be the starting point for our description. For the lighter elements with the ∠R-E-E angle less than 180° we have as shown in **1** (Figure 4.1) a single out-of-plane π bond involving $\pi_{r(out)}$ and $\pi_{l(out)}$ as well as two in-plane bonding

σ/π orbitals made up of $\pi_{r(in)}$ and $\pi_{l(in)}$. For the heavier members where the $\angle$R-E-E angle approaches 90° the bonding scheme becomes that described in **2** (Figure 4.1), where the two in-plane $\pi_{r(in)}$ and $\pi_{l(in)}$ orbitals form a single σ–type bond. The relative strengths of the bonding components in **1** and **2** in Figure 4.1 have been the matter of some discussion [190, 191, 193] as has the identity of the element in the series E = Si, Ge, Sn, Pb at which the bonding picture crosses [190, 191, 193] from **1** to **2** (Figure 4.1). We shall for the first time give a quantitative comparison of the three bonding components in **1** (Figure 4.1) for the real system based on energies rather than bond orders or other qualitative measures. The more restricted ETS method has previously been applied to model systems [194]. We shall further give a novel interpretation of the factors that cause the switch from **1** to **2** in Figure 4.1.

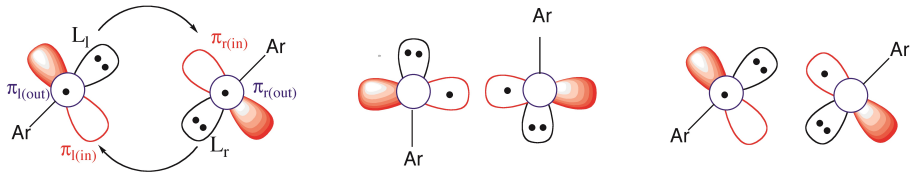

Figure 4.1: Orbital description as a function of the $\angle$R-E-E angle.

A final point is the degree of diradical character present in the bonding of REER. It has been claimed previously based on qualitative considerations [191] that the diradical character could be as high as 30 % for the MeEEMe model systems. Here we shall demonstrate from more quantitative spin-flip calculations on the real systems that the diradical contributions such as **3** in Figure 4.1 at the most amount to 5 %.

4.2 Theoretical Details

4.2.1 Computational Method

In the NOCV-ETS scheme [217, 218] we consider a molecule AB of energy E_{AB} as formed from two fragments A^0 and B^0 with the energies E_A^0 and E_B^0, respectively. The

term ΔE_{AB} representing the formation energy of AB from A^0 and B^0 is defined as:

$$\Delta E_{\mathrm{AB}} = E_{\mathrm{AB}} - E^0_{\mathrm{A}} - E^0_{\mathrm{B}}. \tag{4.1}$$

The formation energy ΔE_{AB} can be decomposed [14, 216] into five chemically meaningful components as:

$$\Delta E_{\mathrm{AB}} = \Delta E_{\mathrm{prep}} + \Delta E_{\mathrm{elstat}} + \Delta E_{\mathrm{Pauli}} + \Delta E_{\mathrm{orb}} + \Delta E_{\mathrm{disp}}. \tag{4.2}$$

The first component, ΔE_{prep}, is often referred to as the preparation or distortion energy. It is the energy required to distort or promote the fragments from their equilibrium geometries to the structure they will assume in the combined molecule. The second term, $\Delta E_{\mathrm{elstat}}$, corresponds to the electrostatic interaction between two distorted fragments as they are combined in the final molecule with the densities kept frozen. It is stabilizing for the neutral fragments studied in this work. The third contribution, $\Delta E_{\mathrm{Pauli}}$, is referred to as the Pauli repulsion term and originates from the destabilizing interaction between the occupied orbitals on the two fragments. The fourth component, ΔE_{orb}, is the orbital interaction energy. It is stabilizing and results from the interaction of occupied and virtual fragment orbitals. We have included the stabilizing van der Waals dispersion interactions between the two fragments A and B. The change in density due to the orbital interactions can be written in terms of the orthogonalized fragment orbitals [217] (λ_μ; μ = 1,M) on A and B as

$$\Delta\rho^{\mathrm{orb}}(r) = \sum_{\mu}^{M}\sum_{\nu}^{M} \Delta P^{\mathrm{orb}}_{\mu\nu}\lambda_\mu\lambda_\nu \tag{4.3}$$

where $\Delta P^{\mathrm{orb}}_{\mu\nu}$ is the deformation density matrix. The orbital interaction energy can further be written as [217]

$$\Delta E_{\mathrm{orb}} = \sum_{\mu}^{M}\sum_{\nu}^{M} \Delta P^{\mathrm{orb}}_{\mu\nu} F^{\mathrm{TS}}_{\mu\nu} = \mathrm{Tr}(\Delta P^{\mathrm{orb}} F^{\mathrm{TS}}). \tag{4.4}$$

Here $F^{\mathrm{TS}}_{\mu\nu}$ is KS-matrix element between two fragment orbitals λ_μ and λ_ν with respect to a Kohn-Sham (KS) operator defined in terms of a density matrix halfway between that of the final molecule and the sum of the distorted fragments [217]. We can

write ΔE_{orb} in a more compact form by first diagonalizing $\Delta P_{\mu\nu}^{\text{orb}}$ according to

$$\Delta P^{\text{orb}} C_i = \nu_i C_i \tag{4.5}$$

where the corresponding eigenvectors called Natural Orbitals for Chemical Valence or NOCVs are given by

$$\psi_j = \sum_k C_{jk} \lambda_k. \tag{4.6}$$

The set of NOCVs [217, 218] can be further divided into corresponding pairs (ψ_{-k}, ψ_k) with eigenvalues of the same magnitude, ν_k, but opposite signs. In the NOCV representation the deformation density takes on the form

$$\Delta\rho^{\text{orb}}(r) = \sum_{k=1}^{M/2} \nu_k \big[-\Psi_{-k}^2(r) + \Psi_k^2(r) \big] = \sum_{k=1}^{M/2} \Delta\rho_k(r) \tag{4.7}$$

whereas ΔE_{orb} now is given as

$$\begin{aligned} \Delta E_{\text{orb}} =& \text{Tr}(\Delta P^{\text{orb}} F^{\text{TS}}) = \text{Tr}(C^{+} \Delta P^{\text{orb}} C C^{+} F^{\text{TS}} C) \\ =& \sum_{k=1}^{M/2} \nu_k [-F_{-k,-k}^{\text{TS}} + F_{k,k}^{\text{TS}}] = \sum_{k=1}^{M/2} \Delta E_k^{\text{orb}} \end{aligned} \tag{4.8}$$

where $F_{-k,-k}^{\text{TS}}$ and $F_{k,k}^{\text{TS}}$ are diagonal KS–matrix elements over ψ_{-k} and ψ_k, respectively. The eq (4.6) and (4.7) relate to each change in density $\Delta\rho_k(r)$ the corresponding energy contribution ΔE_k^{orb}. Further $\Delta\rho_k(r)$ consists of density depletion $-\nu_k \Psi_{-k}^2(r)$ and the corresponding accumulation $\nu_k \Psi_k^2(r)$. In favourable cases [217] different interactions such as σ, π and δ–bonding or σ–donation and π–back-donation can be identified with different k values and thus assessed individually, as we shall see shortly.

4.2.2 Computational Details

All spin-flip calculations were performed with the unrestricted SF-CV(2)-DFT method employing the TZ2P [181] basis set implemented in the ADF [176] program. The functionals used include LDA-VWN [36], BP86 [37, 38] BLYP [37, 152] PBE [220], B3LYP [39] and BHLYP [39]. Relativistic effects were included at the scalar relativistic ZORA [221, 222] level of approximation whereas the dispersion term ΔE_{dis} of eq (4.2) was described by the scheme due to Grimme $et\ al.$ [219].

4.2.3 Molecular models

We studied four of the heavier acetylene congeners of group 14. Crystal structures were available for germanium [185], tin [184] and lead [190]. The silicon compound was optimized at the BP86 level. All the compounds are homonuclear and have a trans-bent geometry with the general formula Ar′EEAr′ (E = Si, Ge, Sn; Ar′ = C_6H_3-2,6-(C_6H_2-2,6-Pr^i_2)$_2$) and Ar*PbPbAr* (Ar* = C_6H_3-2,6-(C_6H_2-2,4,6-Pr^i_3)$_2$). The structures are shown in Figure 4.2.

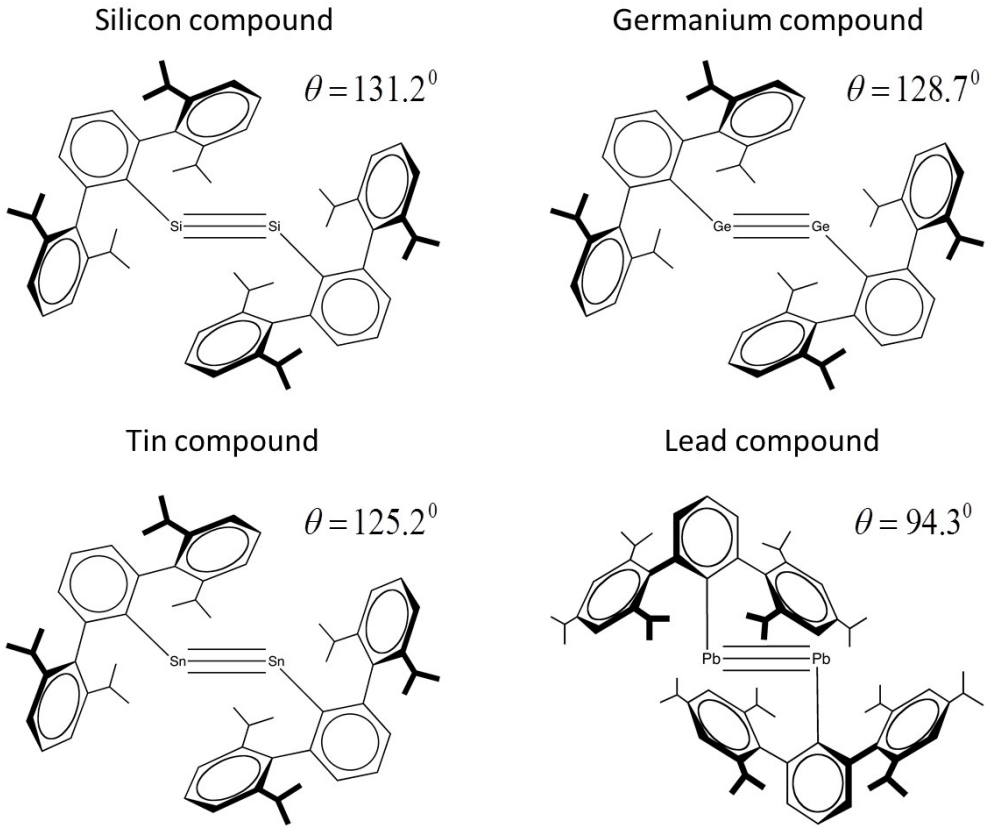

Figure 4.2: Structures of the four studied compounds from Si to Pb. Also given in each case is the ∠C–E–E, θ.

4.3 Results and Discussion

4.3.1 Fragment Orbitals

In the NOCV analysis we consider in line with **1** (Figure 4.1) the compound ArEEAr as formed from two ArE units. Each has two π– and one σ–orbital of importance for the

E–E bond formation, Figure 4.3. The Figure displays the fragment orbitals for Si and Pb with their corresponding energies as well as the levels for Ge and Sn. The fragment orbitals of the Ge and Sn compounds are omitted because they are similar to those of the Si system.

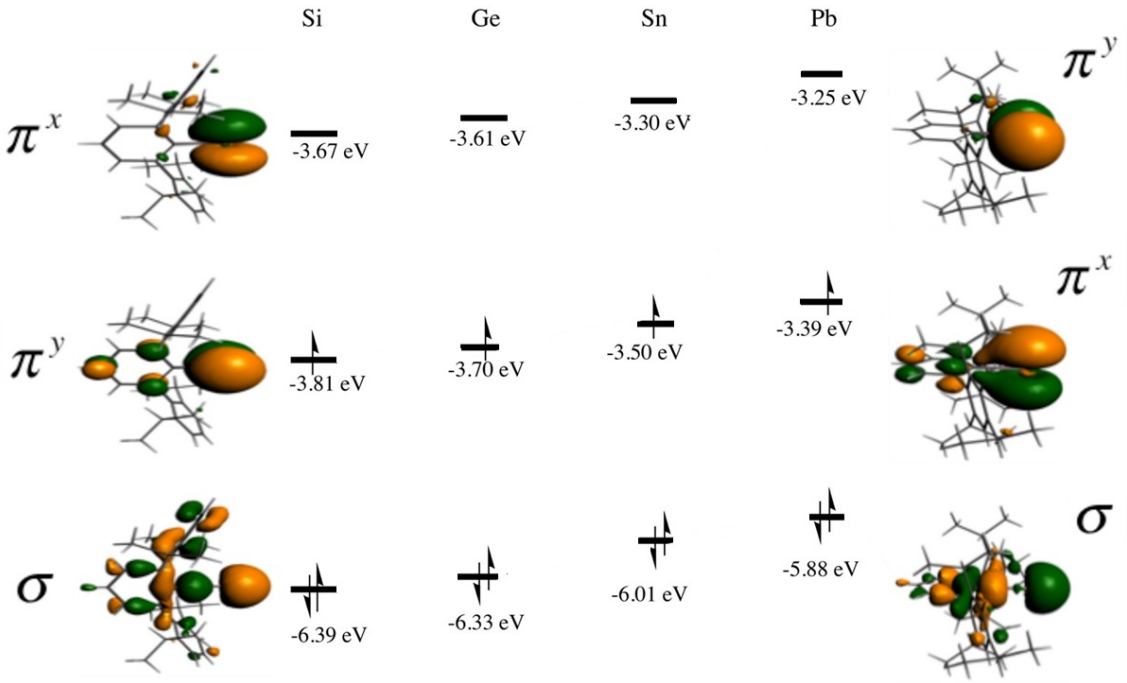

Figure 4.3: Fragment orbitals of ArE for E = Si and Pb with corresponding energy levels or E = Si, Ge, Sn, and Pb.

The π–set on each fragment is not degenerate due to the Ar-ligands. It consists of π^y which is perpendicular to the CEEC plane in the overall ArEEAr molecule and π^x situated in the CEEC plane, Figure 4.3. A study of ArE (E = Si, Ge, Sn and Pb) revealed a doublet ground-state with the valence configuration $(\sigma)^2(\pi^y)^1(\pi^x)^0$ for E = Si, Ge, Sn compared to $(\sigma)^2(\pi^x)^1(\pi^y)^0$ for E = Pb. The doublets with the opposite occupation of the π orbitals were 12.6 kcal/mol (Si), 14.2 kcal/mol (Ge), 20.4 kcal/mol (Sn) and 16.2 kcal/mol (Pb) higher in energy. The different preference for occupation of the π orbitals between E = Si, Ge, Sb on the one hand and E = Pb on the other must reflect that Ar in the case of E = Si, Ge, Sb is C_6H_3-2,6-(C_6H_3-2,6-Pr^i_2)$_2$ compared to C_6H_3-2,6-(C_6H_2-2,4,6-Pr^i_3)$_2$ for E = Pb. However, we have not pursued this question further. The quartet state with the valence configuration $(\sigma)^1(\pi^y)^1(\pi^x)^1$ was found to be 50 kcal/mol to 70 kcal/mol higher in energy than the ground-state doublet depending on E.

For all four elements, the σ–orbital is of lower energy than the two π–components by some 2.5 eV due to a sizable contribution from the ns orbital (n = 3, 6) on E. This is why the σ–level is occupied by two electrons in the fragment ground-state. We shall in the following analyze the bonding in ArEEAr in terms of the two doublet fragments in their electronic ground-state. We illustrate in Figure 4.4, linear combinations of equivalent σ and π^x orbitals on the two fragments as a function of the trans-bent $\angle$C-E-E angle θ. It is important to note that the in-phase π^x–combination $\tilde{\pi}^x$ goes from being π–bonding at 180° to σ–anti-bonding at 90° whereas the out-of-phase π^x–combination $\tilde{\pi}^{x*}$ starts as π–anti-bonding at $\theta = 180^o$ and ends up σ–bonding at 90°.

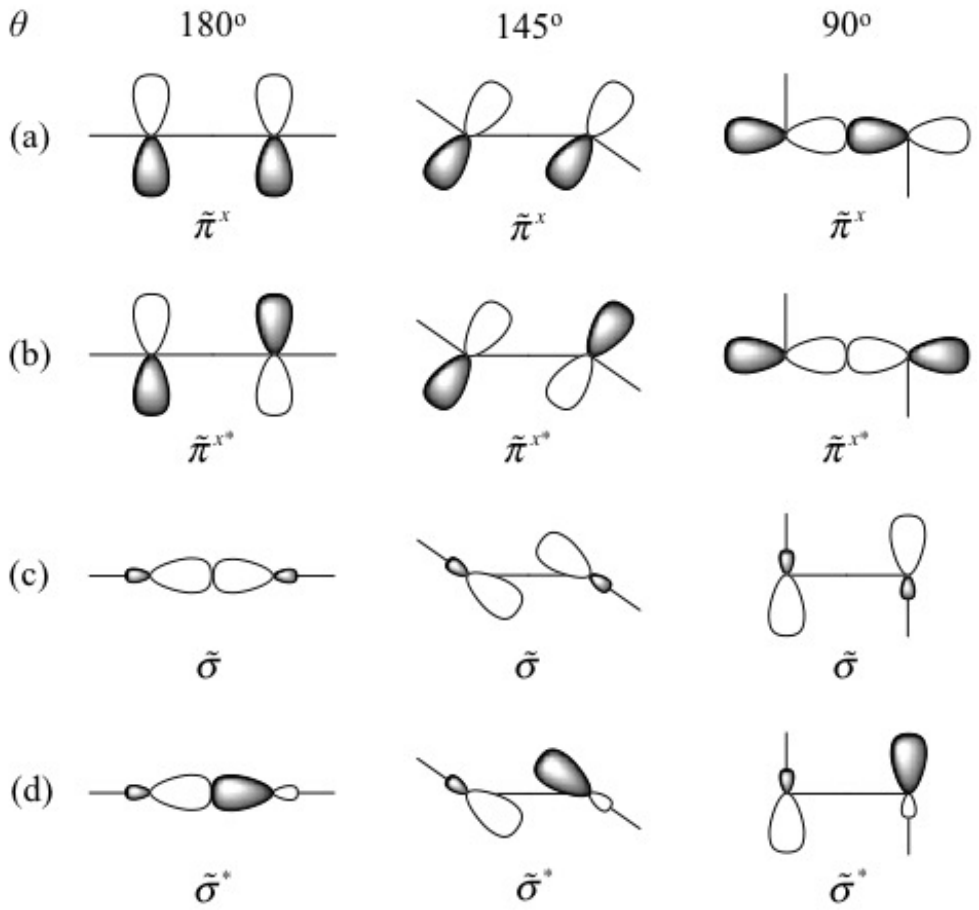

Figure 4.4: Combinations of σ and π fragment orbitals as a function of the trans-bending angle θ.

Around $\theta = 145^o$, $\tilde{\pi}^{x*}$ is already bonding whereas $\tilde{\pi}^x$ is anti-bonding. For the σ–component, the in-phase combination $\tilde{\sigma}$ is σ–bonding at $\theta = 180^o$ and mildly π–anti-bonding at 90° whereas the out-of-phase combination $\tilde{\sigma}^*$ is σ–anti-bonding at $\theta = 180^o$

and mildly π–bonding at 90°. Not shown in Figure 3 are the bonding and anti-bonding combinations $\tilde{\pi}^y$ and $\tilde{\pi}^{y*}$, respectively, of the out-of-plane π^y fragment orbitals. They do not change bonding character with θ.

4.3.2 Molecular Orbitals

The frontier molecular orbitals are shown in Figure 4.5 for the trans-bent Si compound with θ = 131° to the left. The orbital of lowest energy is made up of an in-phase combination of $\tilde{\pi}^{x*}$ and $\tilde{\sigma}$ from Figure 4.4 with a slightly dominant contribution from $\tilde{\sigma}$. It is denoted by σ_{EE} due to its strong σ–bonding character. The second lowest occupied molecular orbital is primarily $\tilde{\sigma}^*$ and labeled σ^*_{EE} although it mostly is π–bonding as discussed above. The occupied orbital of highest energy named π^y_{EE} is a bonding combination of the fragment π^y–orbitals ($\tilde{\pi}^y$) situated perpendicular to the CEEC plane. The unoccupied orbital of lowest energy π^x_{EE} is an out-of-phase combination of $\tilde{\pi}^{x*}$ and $\tilde{\sigma}$ with the largest contribution from $\tilde{\pi}^{x*}$. The occupation and relative energies of the four frontier orbitals for E = Ge, Sn are also shown in Figure 4.5. They differ little from E = Si, thus, their composition is not shown in Figure 4.5. We find for trans-bent ArSiSiAr that the gross population of the three orbitals on each fragment in the overall complex is $(\sigma)^{1.64}(\pi^y)^{0.94}(\pi^x)^{0.46}$ compared to $(\sigma)^2(\pi^y)^1(\pi^x)^0$ for a free fragment. Similar gross populations were obtained for E = Ge, Sn.

Also shown in Figure 4.5 are the molecular orbitals of the trans-bent Pb compound with θ = 94.3^o. We see that σ^*_{EE} and σ_{EE} are of lowest energy. They are almost solely made up of $\tilde{\sigma}^*$ and $\tilde{\sigma}$, respectively, with the first appearing as π–bonding and the second as π–anti-bonding, in accordance with the discussion above. As the HOMO, we now find the in plane π–orbital π^x_{EE} made up of $\tilde{\pi}^{x*}$ whereas the LUMO has become π^y_{EE}. It would appear that a longer E–E distance and smaller C-E-E angle makes the σ–type overlap between the two π^x fragments in π^x_{EE} more stabilizing than the π–type overlap in π^y_{EE} with the result that π^{x*}_{EE} now is of lower energy than π^y_{EE} and occupied whereas π^y_{EE} has become the LUMO. Frenking and coworkers found a similar switchover for the HEEH model compounds [193]. However, as far as we are aware this

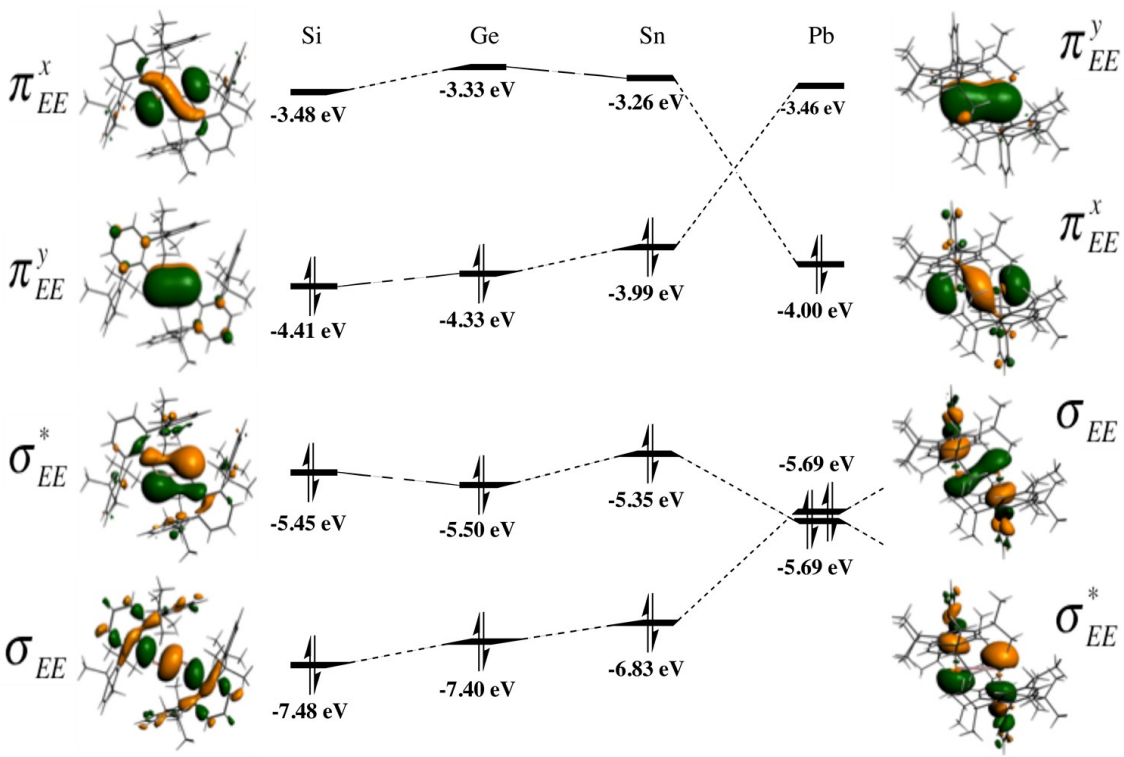

Figure 4.5: Molecular Orbitals of trans-bent ArEEAr for E = Si and Pb as well as the corresponding orbital energies for E = Si, Ge, Sn, and Pb.

is the first rationale given of the cross-over in terms of the decreasing bonding overlap in $\tilde{\pi}^y$ compared to $\tilde{\pi}^{x*}$ as the E–E bond distance increases. Frenking [193] and others [191] have interpreted the crossover as caused by an increasing stability of the doublet compared to the quartet in ER towards heavier congeners of E. Certainly, this might be a contributing factor as well. The gross population of each Ar*Pb fragment in trans-bent Ar*PbPbAr* is $(\sigma)^{1.92}(\pi^x)^{1.04}(\pi^y)^{0.06}$ compared to $(\sigma)^2(\pi^x)^1(\pi^y)^0$ for the free fragment.

Figure 4.6 depicts the molecular orbitals obtained for the linear Si and Pb compounds with their corresponding energies as well as the energy levels of the Ge and Sn compounds. The MOs of the Si compound are comprised of two π–bonding and one σ–bonding combination. Lowest in energy is $\sigma_{EE}(\tilde{\sigma})$ followed by $\sigma^x_{EE}(\tilde{\pi}^x)$ and $\sigma^y_{EE}(\tilde{\pi}^y)$. The lowest lying empty orbital is $\sigma^*_{EE}(\tilde{\sigma}^*)$. As shown in Figure 4.6, the same occupation and ordering is found for the Ge and Sn compounds although the gap between π^y_{EE} and σ^*_{EE} decreases. For the linear Pb compound we find that σ^*_{EE} now becomes occupied whereas π^y_{EE} takes on the role as the LUMO. Thus, for E = Si, Ge, Sn the σ^*_{EE}

orbital is empty because of the strongly anti-bonding σ–overlap in the linear ArEEAr molecule. This is in spite of the fact that the constituting σ fragment orbitals are more stable than the corresponding π^x, π^y components. Instead the HOMO is made up of π^y_{EE} where the lower stability of π^y compared to σ is compensated for by a bonding π–overlap. Through the series E = Si, Ge, Sn and Pb, the stabilizing π–overlap is reduced and the anti-bonding σ–overlap diminished. As a result σ^*_{EE} first approach π^x_{EE}, π^y_{EE} and then dips below the two π–orbitals at E = Pb. The gross populations in linear ArEEAr are $(\sigma)^{1.24}(\pi^x)^{0.98}(\pi^y)^{0.94}$ for E = Si with similar values for E = Ge, Sn and $(\sigma)^{1.86}(\pi^x)^{0.94}(\pi^y)^0$ for E = Pb.

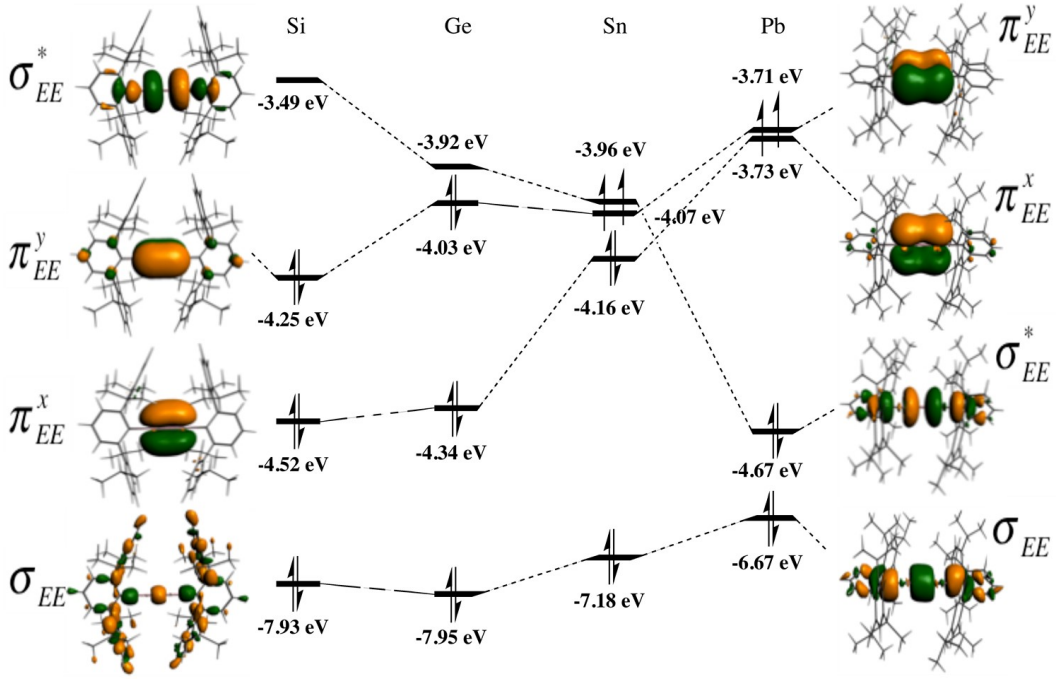

Figure 4.6: Molecular Orbitals of linear ArEEAr for E = Si and Pb and the corresponding orbital energies for E = Si, ge, Sn, and Pb.

4.3.3 NOCV-ETS analysis of trans-bent compounds based on ArE fragments with a doublet state

Starting with the E–E bond formed from two doublet ArE fragments of opposite spin polarization (ArE$\uparrow\downarrow\uparrow$ and $\downarrow\uparrow\downarrow$ EAr) we provide the ΔE_{EE} bond energy decomposition according to eq (4.2) in Table 1 for E = Si using 4 different functionals LDA, BP86, B3LYP and BHLYP. As expected, the Pauli term ΔE_{Pauli} is large and positive.

Table 4.1: ETS[a] Analysis for Trans-bent Ar′SiSiAr′ Carried Out with Different Functionals (Energies in kcal/mol)

Functional	ΔE_{Pauli}	ΔE_{elstat}	ΔE_{steric} [b]	ΔE_{orb}	ΔE_{disp}	ΔE_{int} [c]
LDA	117.2	-70.1	47.1	-129.6	-17.8	-100.2
BP86	141.4	-69.6	71.8	-123.3	-27.5	-79.0
B3LYP	149.6	-72.3	77.3	-119.8	-24.7	-67.2
BHLYP	153.8	-77.0	76.8	-121.1	-17.8	-62.0

[a]Based on doublet fragments. [b]Steric interaction energy, $\Delta E_{\text{steric}} = \Delta E_{\text{Pauli}} + \Delta E_{\text{elstat}}$. [c]Fragment interaction energy, $\Delta E_{\text{int}} = \Delta E_{\text{steric}} + \Delta E_{\text{orb}} + \Delta E_{\text{disp}}$.

It is significantly less repulsive for LDA with 117.2 kcal/mol than for the other three functionals with 141.4 kcal/mol (BP86), 149.6 kcal/mol (B3LYP) and 153.8 kcal/mol (BHLYP), respectively. The Pauli contribution is in part cancelled by the numerically large and attractive (negative) electrostatic contribution that is quite similar for the different functionals. It is customary [217, 218, 223] to combine the numerically large ΔE_{elstat} and ΔE_{Pauli} contributions into the smaller steric interaction energy

$$\Delta E_{\text{steric}} = \Delta E_{\text{Pauli}} + \Delta E_{\text{elstat}}. \tag{4.9}$$

The steric term represents the total destabilizing interaction of the occupied orbitals on the two fragments. It is usually positive when we, as in the case here, are dealing with neutral fragments and ranges from 47.1 kcal/mol (LDA) to 77.3 kcal/mol (B3LYP), Table 4.1. The fact that LDA in general underestimates Pauli repulsion is the primary reason why this functional most often overestimates bond energies.

The van der Waals dispersion ΔE_{disp} is stabilizing and far from negligible with contributions between -17.8 kcal/mol (LDA) and -27.8 kcal/mol (BP86) depending on the functional, Table 4.1. A large part of ΔE_{disp} comes from the van der Waals interaction between Pr^i groups on different fragments. Stable ArEEAr compounds often contains Pr^i groups and it is thus clear from our analysis that one of the roles played by Pr^i is to stabilize the ArE dimer through ΔE_{disp}. This contribution has previously been neglected in theoretical studies of ArEEAr [213, 214, 215]. The orbital interaction, ΔE_{orb}, is numerically large and stabilizing, Table 4.1. It is further quite similar for the

Table 4.2: ETS[a] Analysis for Trans-bent Compounds Carried Out with the BP86 Functional for the Real Systems (Energies in kcal/mol)

ArEEAr	ΔE_{Pauli}	ΔE_{elstat}	ΔE_{steric} [b]	ΔE_{orb}	ΔE_{disp}	ΔE_{int} [c]	ΔE_{prep}	ΔE_{EE} [f]
Si[d]	141.4	-69.6	71.8	-123.3	-27.5	-79.0	41.2	-37.8
Ge[d]	168.7	-91.8	76.9	-121.6	-29.1	-73.7	43.9	-29.8
Sn[d]	122.2	-71.3	50.9	-81.4	-26.2	-56.7	28.0	-28.7
Pb[e]	121.5	-84.6	37.0	-71.7	-44.0	-78.7	13.7	-65.0

[a]Based on doublet fragments. [b]Steric interaction energy, $\Delta E_{\text{steric}} = \Delta E_{\text{Pauli}} + \Delta E_{\text{elstat}}$. [c]Fragment interaction energy, $\Delta E_{\text{int}} = \Delta E_{\text{steric}} + \Delta E_{\text{orb}} + \Delta E_{\text{disp}}$. [d]Ar′ = C_6H_3-2,6-(C_6H_3-2,6-iPr_2)$_2$. [e]Ar* = C_6H_3-2,6-(C_6H_2-2,4,6-iPr_3)$_2$. [f] $\Delta E_{\text{EE}} = \Delta E_{\text{int}} + \Delta E_{\text{prep}}$.

four functionals and makes up the leading term in the expression for the interaction energy, ΔE_{int}, between the two distorted doublet fragments given by

$$\Delta E_{\text{int}} = \Delta E_{\text{steric}} + \Delta E_{\text{disp}} + \Delta E_{\text{orb}}. \tag{4.10}$$

It is important to note that LDA has the most stabilizing interaction energy with ΔE_{int} = -100.2 kcal/mol as a result of the weaker steric repulsion. On the other hand, for the other functionals ΔE_{int} decreases gradually in absolute terms as -79.0 kcal/mol (BP86), -67.2 kcal/mol (B3LYP) and -62.0 kcal/mol (BHLYP).

Table 4.2 provides an ETS analysis of the E–E bond in the real trans-bent ArEEAr systems for E = Si, Ge, Sn and Pb based on the BP86 functional. It is clear from the table that the steric interaction energy ΔE_{steric} follows the trend Si $\sim$ Ge $>$ Sn $>$ Pb, as the E–E distance increases in going from Ge to Pb. A similar trend is observed for $-\Delta E_{\text{orb}}$. One would thus expect from eq (4.10) that $-\Delta E_{\text{int}}$ would decrease as Si $\sim$ Ge $>$ Sn $>$ Pb through the series towards the heavier congener. We see instead the trend Si $\sim$ Ge $>$ Sn $<$ Pb as $-\Delta E_{\text{int}}$ is larger for Pb than for Sn. This reversal is due to ΔE_{disp} which is more stabilizing for E = Pb than for any of the other elements as a result of the larger number of Pr^i groups on each Ar*Pb fragment (Ar* = C_6H_3-2,6-(C_6H_2-2,4,6-Pr^i_3)$_2$) compared to Ar′E (E = Si, Ge, Sn; Ar′ = C_6H_3-2,6-(C_6H_3-2,6-Pr^i_2)$_2$). It might appear counter intuitive that the steric interaction decreases with the core size of E. However this is compensated for by a longer E–E distance. Also the longer E–E bond

Table 4.3: ETS[a] Analysis for Trans-bent ArEEAr Model Systems Carried Out with the BP86 Functional (Energies in kcal/mol)

ArEEAr	ΔE_{Pauli}	ΔE_{elstat}	ΔE_{steric} [b]	ΔE_{orb}	ΔE_{disp}	ΔE_{int} [c]
Si[d]	131.8	-65.2	66.6	-116.0	-14.6	-64.0
Ge[d]	158.7	-86.8	71.9	-113.6	-15.7	-57.4
Sn[d]	114.4	-66.5	47.9	-74.9	-15.0	-42.0
Pb[d]	84.8	-65.2	19.6	-51.0	-9.8	-41.2

[a]Based on doublet fragments. [b]Steric interaction energy, $\Delta E_{\text{steric}} = \Delta E_{\text{Pauli}} + \Delta E_{\text{elstat}}$. [c]Total interaction energy, $\Delta E_{\text{int}} = \Delta E_{\text{steric}} + \Delta E_{\text{orb}} + \Delta E_{\text{disp}}$. [d]Ar′ = C_6H_3-2,6-$(C_6H_5)_2$.

diminish the steric interaction between the two Ar groups for the real systems. We can probe the influence of the isopropyl groups further by replacing all of them in the real systems with hydrogens and reoptimize the C–H distances while keeping the rest of the framework frozen. It follows from Table 4.3 that the Pr^i removal reduces the steric repulsion, ΔE_{steric}, as one might expect. On the other hand, there is a substantial reduction in the dispersive stabilization, ΔE_{disp}, and a somewhat smaller numerical decrease in the orbital interaction energy, ΔE_{orb}. We shall discuss the decrease in $-\Delta E_{\text{orb}}$ shortly. Here we note that the net effect of the Pr^i removal is to reduce $-\Delta E_{\text{int}}$ in absolute terms through the loss of dispersion and thus reduce the strength of the E–E bond.

In order to calculate the total bond energy, ΔE_{EE}, between the two ArE monomers according to

$$\Delta E_{\text{EE}} = \Delta E_{\text{int}} + \Delta E_{\text{prep}} \tag{4.11}$$

we need as well the preparation term, ΔE_{prep}. In the current case where we are using the fragments in their electronic ground-state, this term represents the energy required to change the two fragments from the doublet ground-state to the distorted doublet state in the overall molecule. The term ΔE_{prep} decreases from E = Ge to E = Pb, Table 4.2. We observed a lower preparation term for E = Si compared to E = Ge. The total bond energy, ΔE_{EE}, decreased in absolute terms from E = Si to E = Sn and increases again towards E = Pb with the numerically largest value. This is indicative of the strong dispersive stabilization for E = Pb. Without ΔE_{disp} the bond energy, $-\Delta E_{\text{EE}}$ would

Table 4.4: NOCV[a] Contributions[b] to ΔE_{orb} [c] for the Trans-bent Compounds Carried Out with the BP86 Functional for the Real Systems (Energies in kcal/mol)

ArEEAr	$\Delta E_{\text{orb}}^{\pi^y}$	$\Delta E_{\text{orb}}^{\sigma-\pi^*}$	$\Delta E_{\text{orb}}^{\sigma^*-\pi}$	$\Delta E_{\text{orb}}^{\pi^{x*}}$	$\Delta E_{\text{orb}}^{\text{rest}}$
Si[d]	-32.4	-36.6	-38.2		-13.4
Ge[d]	-33.1	-35.7	-35.6		-14.2
Sn[d]	-23.1	-19.2	-25.1		-11.8
Pb[e]				-45.4	-24.7

[a]Based on doublet fragments. [b]See Figures 4.7 and 4.9. [c] ΔE_{orb} = $\Delta E_{\text{orb}}^{\pi^y}$ + $\Delta E_{\text{orb}}^{\sigma-\pi^*}$ + $\Delta E_{\text{orb}}^{\sigma^*-\pi}$ + $\Delta E_{\text{orb}}^{\pi^{x*}}$ + $\Delta E_{\text{orb}}^{\text{rest}}$. [d]Ar′ = C_6H_3-2,6-(C_6H_3-2,6-iPr_2)$_2$. [e]Ar* = C_6H_3-2,6-(C_6H_2-2,4,6-iPr_3)$_2$.

decrease from Si to Pb as found by Takagi and Nagase [214] in their pioneering study where ΔE_{disp} was neglected. In Table 4.4 we provide the NOCV decomposition of ΔE_{orb} based on the BP86 functional for E = Si, Ge, Sn and Pb according to

$$\Delta E_{\text{orb}} = \Delta E_{\text{orb}}^{\pi^y} + \Delta E_{\text{orb}}^{\sigma-\pi^*} + \Delta E_{\text{orb}}^{\sigma^*-\pi} + \Delta E_{\text{orb}}^{\text{rest}}. \tag{4.12}$$

The change in density $\Delta\rho_k$ corresponding to the three major contributions, $\Delta E_{\text{orb}}^{\pi^y}$, $\Delta E_{\text{orb}}^{\sigma-\pi^*}$, and $\Delta E_{\text{orb}}^{\sigma^*-\pi}$ are depicted in Figure 4.7 for E = Si.

The analysis is based on two doublet fragments each with the electronic configuration $(\sigma)^2(\pi^y)^1(\pi^x)^0$. We provide in addition for each $\Delta\rho_k$ in Figure 4.8 the corresponding pair of NOCV orbitals (ψ_{-k}, ψ_k) contributing to $\Delta\rho_k$ according to eq (4.7).

Figure 4.7a illustrates the π^y–bond formed by out-flow of α–electron density ($\Delta\rho_{\text{orb}}^{\pi^y,\alpha}$) from the occupied fragment π^y–orbital on the left side (orange) and an in-flow to the empty π^y–orbital on the right (green) side. The corresponding NOCVs are shown in Figure 4.8a. Here Ψ_{-1}^{α} represents the orthogonalized occupied fragment π^y–orbital on the left side and Ψ_{-1}^{α} the empty π^y–orbital on the right side. The corresponding charge flow of β–electron density in the opposite direction $\Delta\rho_{\text{orb}}^{\pi^y,\beta}$ is omitted from Figure 4.7. However, Figure 4.7a contains the sum $\Delta E_{\text{orb}}^{\pi^y}$. It follows from Figure 4.7a and Table 4.4 that the contribution to ΔE_{orb} from $\Delta\rho_{\text{orb}}^{\pi^y}$ amounts to $\Delta E_{\text{orb}}^{\pi^y}$ = -32.4 kcal/mol. The term $\Delta E_{\text{orb}}^{\pi^y}$ is obviously related to the formation of the π_{EE}^{y} orbital, which is the HOMO in Figure 4.5.

Figure 4.7b displays relocation of charge $\Delta\rho_{\text{orb}}^{\sigma^*-\pi,\alpha}$ from the $\tilde{\sigma}^*$ combination de-

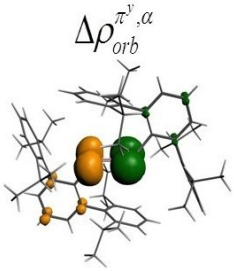

(a) $\Delta E_{\text{orb}}^{\pi^y,\alpha} = -16.2$ kcal/mol

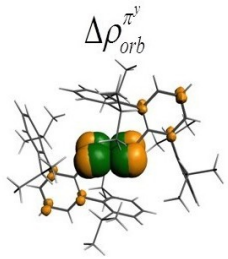

(b) $\Delta E_{\text{orb}}^{\pi^y} = -32.4$ kcal/mol

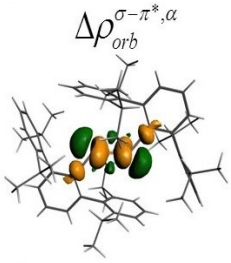

(c) $\Delta E_{\text{orb}}^{\sigma-\pi^*,\alpha} = -18.3$ kcal/mol

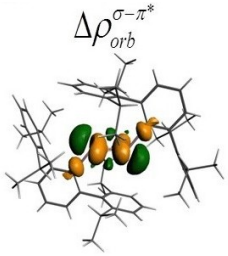

(d) $\Delta E_{\text{orb}}^{\sigma-\pi^*} = -36.6$ kcal/mol

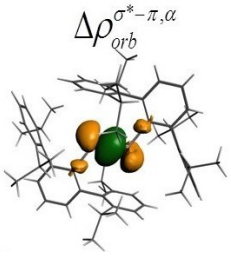

(e) $\Delta E_{\text{orb}}^{\sigma^*-\pi,\alpha} = -19.1$ kcal/mol

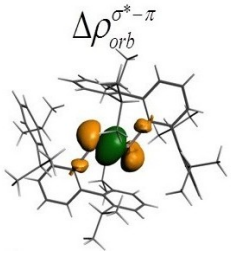

(f) $\Delta E_{\text{orb}}^{\sigma^*-\pi} = -38.2$ kcal/mol

Figure 4.7: NOCV deformation densities for the trans-bent Si compounds based on doublet fragments. The NOCV deformation densities on the left are the individual α contributions and those on right are the sum of α and β contributions. The individual β contributions are omitted. (a) and (b) Contours of the π^y–NOCV deformation density with the corresponding energy contributions. The contour values are 0.003 au. (c) and (d) Contours of the σ^*/π–NOCV deformation density with the corresponding energy contributions. The contour values are 0.003 au. (e) and (f) Contours of the σ/π^*–NOCV deformation density with the corresponding energy contributions. The contour values are 0.003 au. Green represents positive contours and orange negative contours.

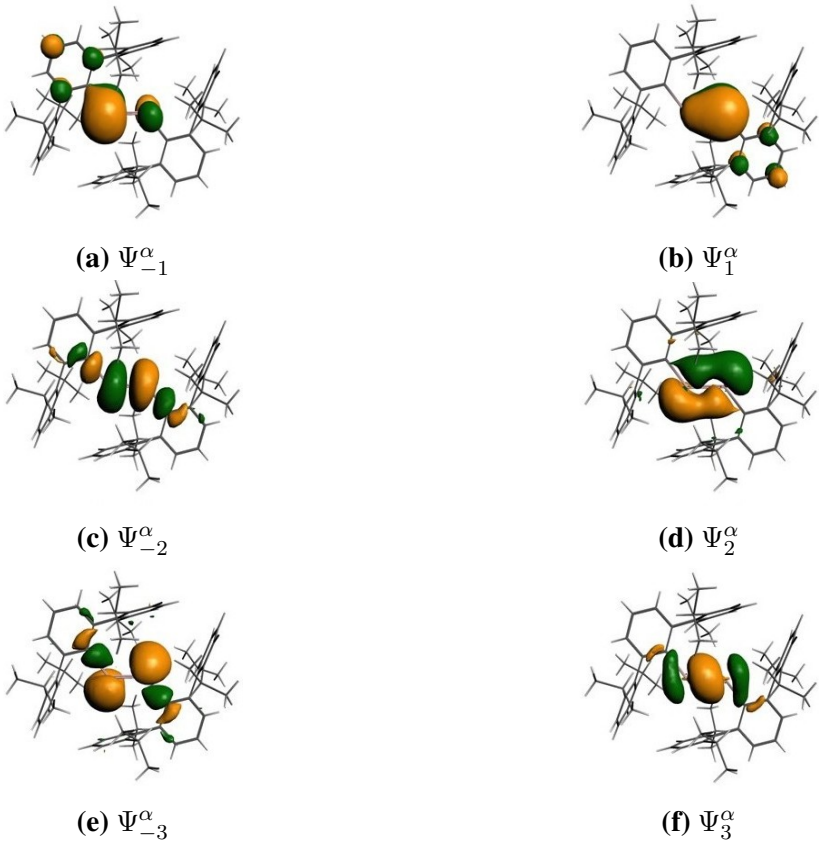

(a) Ψ^{α}_{-1} **(b)** Ψ^{α}_{1}

(c) Ψ^{α}_{-2} **(d)** Ψ^{α}_{2}

(e) Ψ^{α}_{-3} **(f)** Ψ^{α}_{3}

Figure 4.8: NOCVs for the three major contributions to $\Delta\rho_{\text{orb}}$ for trans-bent ArSiSiAr based on doublet fragments.

picted in Figure 4.8b as Ψ^{α}_{-2} to $\tilde{\pi}^{x}$ depicted in Figure 4.8b as Ψ^{α}_{2}. The figure illustrates both the α–density relocation $\Delta\rho^{\sigma^*-\pi,\alpha}_{\text{orb}}$ and the total change $\Delta\rho^{\sigma^*-\pi}_{\text{orb}} = \Delta\rho^{\sigma^*-\pi,\alpha}_{\text{orb}} + \Delta\rho^{\sigma^*-\pi,\beta}_{\text{orb}}$. The orbital stabilization due to $\Delta\rho^{\sigma^*-\pi}_{\text{orb}}$ amounts to $\Delta E^{\sigma^*-\pi}_{\text{orb}}$ = -36.6 kcal/mol, Figure 4.7b. It is obvious that $\Delta\rho^{\sigma^*-\pi}_{\text{orb}}$ is associated with the formation of the σ^*_{EE} orbital in Figure 4.5. Figure 4.7c depicts transfer of α–electron density ($\Delta\rho^{\sigma-\pi^*,\alpha}_{\text{orb}}$) from $\tilde{\sigma}$ shown in Figure 4.8c as Ψ^{α}_{-3} to $\tilde{\pi}^{x*}$ given in Figure 4.8c as Ψ^{α}_{3}. Also presented is $\Delta\rho^{\sigma-\pi^*}_{\text{orb}} = \Delta\rho^{\sigma-\pi^*,\alpha}_{\text{orb}} + \Delta\rho^{\sigma-\pi^*,\beta}_{\text{orb}}$. It is clear that $\Delta\rho^{\sigma-\pi^*}_{\text{orb}}$ corresponds to the formation of σ_{EE} in Figure 4.5. The stabilization corresponding to $\Delta\rho^{\sigma-\pi^*}_{\text{orb}}$ is $\Delta E^{\sigma-\pi^*}_{\text{orb}}$ = -38.2 kcal/mol. Finally shown in Table 4.4 is $\Delta E^{\text{rest}}_{\text{orb}}$ = -13.4 kcal/mol. It represents primarily charge polarization on the aryl rings and is not shown in Figure 4.7. Going next from E = Si to E = Ge and Sn leads to deformation densities $\Delta\rho^{\pi^y}_{\text{orb}}$, $\Delta\rho^{\sigma^*-\pi}_{\text{orb}}$ and $\Delta\rho^{\sigma-\pi^*}_{\text{orb}}$ that are qualitatively similar from one element to the next. Further, the corresponding energy contributions $\Delta E^{\pi^y}_{\text{orb}}$, $\Delta E^{\sigma^*-\pi}_{\text{orb}}$ and $\Delta E^{\sigma-\pi^*}_{\text{orb}}$ are seen to be comparable for E = Si and Ge before they decline in absolute terms for E = Sn as the E–E distance increases. In summary, our NOCV analysis indicates that trans-bent ArEEAr for E = Si, Ge and Sn has a triple bond consisting of an out-of plane π–bond and two in-plane bonds. One in-plane bond is made up of $\tilde{\sigma}^*$ (65 %) and $\tilde{\pi}^{x}$ (35 %) from Figure 4.4 and the other of $\tilde{\sigma}$ (70 %) and $\tilde{\pi}^{x*}$ (30 %). For a given E all three bond components have about the same strength, Table 4.4. For Ar*PbPbAr* we find only one important bond component corresponding to $\Delta\rho^{\pi^x}_{\text{orb}}$, Figure 4.9. It represents transfer of α–density from an occupied in-plane π^x orbital on one fragment to an empty π^x orbital on the other fragment, $\Delta\rho^{\pi^x,\alpha}_{\text{orb}}$, as well as transfer of β–density in the opposite direction, $\Delta\rho^{\pi^x,\beta}_{\text{orb}}$, Figure 4.9.

The total contribution to ΔE_{orb} from $\Delta\rho^{\pi^x}_{\text{orb}}$ is $\Delta E^{\pi^x}_{\text{orb}}$ = -45.4 kcal/mol. Thus in Ar*PbP-bAr* we have only a single bond. This is consistent with the MO diagram in Figure 4.5 where both σ_{EE} and σ^*_{EE} are occupied and made up solely of $\tilde{\sigma}$ and $\tilde{\sigma}^*$, respectively. Thus, combined they do not contribute to the bond order. The only contribution comes from π^{x*}_{EE} made up of $\tilde{\pi}^{x*}$ which at the trans-bent angle of 94.3^o forms a σ–type bond as illustrated in Figures 4.4 and 4.5. With a bond order of 1, one might have expected the E–E link to be weaker for E = Pb than for the three other

(a) $\Delta E^{\sigma,\alpha}_{\text{orb}} = -22.7$ kcal/mol **(b)** $\Delta E^{\sigma}_{\text{orb}} = -22.7$ kcal/mol

Figure 4.9: NOCV deformation densities for the trans-bent Pb compound based on doublet fragments. Contours of the σ–NOCV deformation density with the corresponding energy contributions. The NOCV deformation density, $\Delta\rho^{\sigma,\alpha}_{\text{orb}}$, is the α contribution and $\Delta\rho^{\sigma}_{\text{orb}}$ is the sum of α and β contributions. The β contribution, $\Delta\rho^{\sigma,\beta}_{\text{orb}}$, is omitted. The contour values are 0.002 au. Green represents positive contours and orange negative contours.

Table 4.5: NOCV[a] Contributions to ΔE_{orb} [b] for the Trans-bent ArEEAr[c] Model Compounds Carried Out with the BP86 Functional (Energies in kcal/mol)

ArEEAr	$\Delta E^{\pi^y}_{\text{orb}}$	$\Delta E^{\sigma-\pi^*}_{\text{orb}}$	$\Delta E^{\sigma^*-\pi}_{\text{orb}}$	$\Delta E^{\pi^{x*}}_{\text{orb}}$	$\Delta E^{\text{rest}}_{\text{orb}}$
Si[c]	-32.3	-36.7	-38.1		-8.9
Ge[c]	-33.1	-35.7	-35.6		-9.2
Sn[c]	-22.8	-19.5	-25.0		-7.6
Pb[c]				-44.7	-6.3

[a]Based on doublet fragments. [b] $\Delta E_{\text{orb}} = \Delta E^{\pi^y}_{\text{orb}} + \Delta E^{\sigma-\pi^*}_{\text{orb}} + \Delta E^{\sigma^*-\pi}_{\text{orb}} + \Delta E^{\pi^{x*}}_{\text{orb}} + \Delta E^{\text{rest}}_{\text{orb}}$. [c]Ar = C_6H_3-2,6-$(C_6H_5)_2$.

elements with formal triple bonds. Indeed ΔE_{orb} is smallest for E = Pb in absolute terms. However, this is compensated for by a modest steric interaction and a very favourable van der Waals attraction ΔE_{disp}, Table 4.4. As a result -ΔE_{int} for Pb is comparable to that of silicon and larger than that of E = Ge and Sn, Table 4.4. We have also calculated the NOCV contributions to ΔE_{orb} for the model systems ArEEAr with Ar = C_6H_3-2,6-$(C_6H_5)_2$ where all isopropyl groups are replaced with hydrogens, see Table 4.5.

It is remarkable to note that each of the bonding components changes by less than 1 kcal/mol. Thus the direct electronic influence of the isopropyl groups on the E–E bond is minimal. There is some reduction in the stabilization $\Delta E^{\text{rest}}_{\text{orb}}$ as the isopropyl groups are replaced by hydrogen atoms. It represents the loss of hyperconjugation into the σ^* orbitals on Pr^i induced by steric interactions. It is clear from the above discussion that

Table 4.6: NOCV[a] Contributions[b] to ΔE_{orb} [c] for the Trans-bent Ar′SiSiAr′ [c] Carried Out with different Functionals (Energies in kcal/mol)

ArEEAr	$\Delta E_{\text{orb}}^{\pi^y}$	$\Delta E_{\text{orb}}^{\sigma-\pi^*}$	$\Delta E_{\text{orb}}^{\sigma^*-\pi}$	$\Delta E_{\text{orb}}^{\text{rest}}$
LDA	-35.6	-38.4	-39.8	-13.1
BP86	-32.4	-36.6	-38.2	-13.4
B3LYP	-33.1	-34.5	-35.9	-13.8
BHLYP	-49.5	-29.7	-21.4	-17.8

[a]Based on doublet fragments. [b]See Figure 4.7. [c] $\Delta E_{\text{orb}} = \Delta E_{\text{orb}}^{\pi^y} + \Delta E_{\text{orb}}^{\sigma-\pi^*} + \Delta E_{\text{orb}}^{\sigma^*-\pi} + \Delta E_{\text{orb}}^{\text{rest}}$.

the NOCV-ETS scheme can provide a detailed analysis of quite complex systems without having to make use of simplified models such as REER (R = H, Me). In fact such models are unable to reveal the most important factors for the stability of the ArEEAr complexes, namely the favourable dispersive interactions of the isopropyl groups on different E atoms. Further, the insight provided here suggests ways in which one might stabilize the lighter ArEEAr congeners by adding more isopropyl groups. However, such a strategy might somewhat be hampered by the steric constraints introduced by the shorter E–E distance. This provides to some extent an explanation to why the Si (Ar′SiSiAr′ type) compound is yet to be synthesized.

Also shown in Table 4.6 is the NOCV analysis of trans-bent Ar′SiSiAr′ for LDA, BP86, B3LYP and BHLYP. We note that ΔE_{orb} as well as the three major contributions $\Delta E_{\text{orb}}^{\pi^y}$, $\Delta E_{\text{orb}}^{\sigma^*-\pi}$ and $\Delta E_{\text{orb}}^{\sigma-\pi^*}$ changes little in going from LDA to BP86 and B3LYP. For BHLYP there is somewhat larger variations in the three contributing terms to ΔE_{orb}. However, ΔE_{orb} is the same for all four functionals within 4 kcal/mol. Thus, the large over binding found for LDA is not associated with ΔE_{orb} but rather with ΔE_{Pauli}, as previously mentioned.

A NOCV-ETS analysis of the factors influencing the trans-bent angle in ArEEAr. Tables 4.7 and 4.8 report the ETS analysis of the Si and Pb compounds, respectively, as a function of ∠C-E-E angle. It is clear from Table 4.8 that ΔE_{int} has a minimum close to the optimized angle at $\theta = 120^o$. This angle is a compromise between ΔE_{orb} + ΔE_{disp} which prefers a smaller angle and ΔE_{steric} for which angles larger than 120° is

Table 4.7: ETS[a] Analysis for Ar′SiSiAr′, where the angle (θ) Ar′–Si–Si is varied (Energies in kcal/mol)

θ^b	ΔE_{Pauli}	ΔE_{elstat}	ΔE_{steric} [c]	ΔE_{orb}	ΔE_{disp}	ΔE_{int} [d]
80	1296.4	-544.6	751.8	-474.8	-51.6	225.4
90	601.3	-254.3	347.0	-270.6	-48.0	28.4
100	304.9	-127.1	177.8	-184.5	-42.0	-48.6
110	197.7	-84.1	113.6	-153.1	-35.0	-74.5
120	171.7	-78.1	93.6	-144.8	-28.5	-79.7
130	141.9	-70.0	71.9	-123.3	-26.7	-78.0
140	199.1	-96.9	102.2	-151.0	-18.7	-67.5
150	222.6	-107.0	115.6	-156.7	-15.6	-56.7

[a]Based on doublet fragments. [b] θ in degrees. [c]Steric interaction energy, $\Delta E_{\text{steric}} = \Delta E_{\text{Pauli}} + \Delta E_{\text{elstat}}$. [c]Fragment interaction energy, $\Delta E_{\text{int}} = \Delta E_{\text{steric}} + \Delta E_{\text{orb}} + \Delta E_{\text{disp}}$.

Table 4.8: ETS[a] Analysis for Ar*PbPbAr*, where the angle (θ) Ar′–Pb–Pb is varied (Energies in kcal/mol)

θ^b	ΔE_{Pauli}	ΔE_{elstat}	ΔE_{steric} [c]	ΔE_{orb}	ΔE_{disp}	ΔE_{int} [d]
80	265.5	-155.2	110.3	-99.0	-65.2	-53.9
90	140.2	-95.2	45.0	-76.4	-51.0	-82.3
100	108.6	-76.2	32.4	-66.9	-35.6	-70.2
110	98.6	-68.0	30.6	-59.7	-24.8	-53.8
120	93.1	-62.0	31.1	-57.0	-18.0	-43.9
130	87.6	-56.1	31.5	-52.0	-13.7	-34.2
140	81.2	-50.0	31.1	-45.6	-11.0	-25.5
150	74.3	-44.4	29.9	-38.7	-9.5	-18.3

[a]Based on doublet fragments. [b] θ in degrees. [c]Steric interaction energy, $\Delta E_{\text{steric}} = \Delta E_{\text{Pauli}} + \Delta E_{\text{elstat}}$. [c]Fragment interaction energy, $\Delta E_{\text{int}} = \Delta E_{\text{steric}} + \Delta E_{\text{orb}} + \Delta E_{\text{disp}}$.

preferred. For E = Pb, we see the same trends. However, now the steric interaction is reduced due to the longer E–E distance. As a result the equilibrium is close to $\theta = 90^o$.

The NOCV-ETS analysis provided in Tables 4.7 and 4.8 affords the first study of the factors determining the trans-bent in the real systems. Previously such studies have been limited to REER models with R = H, Me. While REER compounds might be of interest in their own right they are unable to simulate the actual steric and dispersive interactions found in ArEEAr. It is thus not surprising that REER realize conformations not observed by ArEEAr. Even in the trans-bent conformation the E–E distances and θ

Table 4.9: Singlet–Triplet Energy Gap (ΔE_{ST}) for the four ArEEAr (E = Si, Ge, Sn, Pb) Compounds in their Ground-State Trans-Bent Geometry (Energies in eV)

ΔE_{ST} [a]						
Compounds	LDA	BLYP	BP86	PBE	B3LYP	BHLYP
$Si_2Ar'_2$	-1.33	-1.22	-1.14	-1.18	-8.9	-1.01
$Ge_2Ar'_2$	-1.16	-1.10	-0.98	-1.03	-9.2	-0.90
$Sn_2Ar'_2$	-0.94	-0.90	-0.77	-0.83	-7.6	-0.74
$Pb_2Ar^*_2$	-0.45	-0.50	-0.37	-0.40	-6.3	-0.29

[a]The negative sign indicates that the singlet state is of lower energy than the triplet state. All of the trans-bent compounds showed a singlet ground-state.

angles in REER can differ considerably from those observed in ArEEAr, especially for E = Sn, Pb [190, 191].

4.3.4 Singlet-triplet Gap

We have so far assumed that all of our ArEEAr systems have a ground-state that can be described as a closed shell singlet. It follows from our analysis in Figure 4.5 that ArEEAr (E = Si, Ge, Sn) for such a singlet has the conformation $(\sigma_{EE})^2$ $(\sigma^*_{EE})^2$ $(\pi^y_{EE})^2$ $(\pi^x_{EE})^0$ $(\pi^{x*}_{EE})^0$ whereas ArPbPbAr has the configuration $(\sigma_{EE})^2$ $(\sigma^*_{EE})^2$ $(\pi^x_{EE})^2$ $(\pi^y_{EE})^0$ $(\pi^{y*}_{EE})^0$. The corresponding singlet closed shell determinantal wave functions are in conventional DFT given by the Kohn-Sham determinantal $\Psi^{\mathrm{S}}_1 = |\sigma_{EE}\bar{\sigma}_{EE}\sigma^*_{EE}\bar{\sigma}^*_{EE}\pi^y_{EE}\bar{\pi}^y_{EE}|$ for E= Si, Ge, Sn and the corresponding KS determinant $\Psi^{\mathrm{S}}_2 = |\sigma_{EE}\bar{\sigma}_{EE}\sigma^*_{EE}\bar{\sigma}^*_{EE}\pi^x_{EE}$ $\bar{\pi}^x_{EE}|$ for E = Pb. Here the "bar" indicates an orbital of β–spin. However, the possibility exists that one or more of the electron pairs are weakly coupled so that a high-spin triplet state with the valence configuration $(\sigma_{EE})^2$ $(\sigma^*_{EE})^2$ $(\pi^y_{EE})^1$ $(\pi^x_{EE})^1$ $(\pi^{y*}_{EE})^0$ is preferred. We have carried out calculations on the adiabatic triplet-singlet energy gap in order to investigate this possibility. The calculations were based on the SF-CV(2)-DFT scheme with the triplet as a reference.

Table 4.9 displays the calculated adiabatic gap for the four compounds with a trans-bent geometry using the LDA-VWN, BP86, BLYP, PBE, B3LYP and BHLYP functionals. The estimated vertical gaps are slightly functional dependent [152, 39, 220]

as found in previous studies. The largest vertical singlet-triplet gaps in absolute terms were obtained for LDA and the smallest were calculated for the hybrid functionals (B3LYP and BHLYP). All the compounds revealed a negative gap for the trans-bent systems, which mean that the singlet is of lower energy than the triplet. This is in agreement with previous theoretical studies on REER systems, including a spin-flip time-dependent-DFT calculation (SF-TD-DFT) [191] which is nearly identical to our SF-CV(2)-DFT procedure. Thus the calculated gaps with B3LYP are -25.2 kcal/mol (Si), -22.4 kcal/mol (Ge), -18,2 kcal/mol (Sn), -6.0 kcal/mol (Pb) for the real system compared to -32.4 kcal/mol (Si), -27.6 kcal/mol (Ge), -2.0 kcal/mol (Sn), -6.4 kcal/mol (Pb) for MeEEMe using the same functional. We attribute the substantial difference for E = Sn to the use [191] of a model system that differs in key geometrical parameters from those used in ArEEAr. Thus the Sn–Sn distance in MeSnSnMe was 0.4 Å longer than in ArSnSnAr.

4.3.5 Diradical character

The fact that the spin-flip calculations revealed a singlet ground-state does not necessary mean that all electrons are perfectly paired as in Ψ_1^{S} or Ψ_2^{S}. The singlet could in full or in part be open-shell with two electrons of opposite spins in different orbitals. In fact SF-CV(2) (and SF-TD-DFT) [191] is in contrast to regular KS-DFT able to describe a system as a mixture of open and closed shell singlets with a wave function for ArEEAr that is given by

$$\Psi_{\mathrm{SF}}^{\mathrm{S}} = C_1\Psi_1^{\mathrm{S}} + C_2\Psi_2^{\mathrm{S}} + C_3\Psi_3^{\mathrm{S}} + \sum_{n_{\mathrm{SF}}}^{N_{\mathrm{SF}}} C_{n_{\mathrm{SF}}}\Psi_{n_{\mathrm{SF}}}^{\mathrm{S}} \tag{4.13}$$

according to eq (3.3). In eq (4.13), $\Psi_1^{\mathrm{S}} = |\sigma_{EE}\bar{\sigma}_{EE}\sigma^*_{EE}\bar{\sigma}^*_{EE}\pi^y_{EE}\bar{\pi}^y_{EE}|$ is generated from $\Psi_1^{\mathrm{T}} = |\sigma_{EE}\bar{\sigma}_{EE}\sigma^*_{EE}\bar{\sigma}^*_{EE}\pi^y_{EE}\pi^x_{EE}|$ by the spin-flip substitution $\pi^x_{EE} \rightarrow \pi^{\bar{y}}_{EE}$ whereas $\Psi_2^{\mathrm{S}} = |\sigma_{EE}\bar{\sigma}_{EE}\sigma^*_{EE}\bar{\sigma}^*_{EE}\pi^x_{EE}\bar{\pi}^x_{EE}|$ is obtained from Ψ_1^{T} by the spin-flip replacement $\pi^y_{EE} \rightarrow \pi^{\bar{x}}_{EE}$. Further, $\Psi_3^{\mathrm{S}} = 1/\sqrt{2}\{|\sigma_{EE}\bar{\sigma}_{EE}\sigma^*_{EE}\bar{\sigma}^*_{EE}\pi^x_{EE}\bar{\pi}^y_{EE}| + |\sigma_{EE}\bar{\sigma}_{EE}\sigma^*_{EE}\bar{\sigma}^*_{EE}\pi^y_{EE}\bar{\pi}^x_{EE}|\}$ is reached from by the spin-flip transpositions $\pi^x_{EE} \rightarrow \pi^{\bar{x}}_{EE}$ and $\pi^y_{EE} \rightarrow \pi^{\bar{y}}_{EE}$. Finally, $\Psi_{n_{\mathrm{SF}}}^{\mathrm{S}}$ corresponds to one of the N_{SF} possible remaining spin-flip re-

placements generated by substituting one of the occupied orbitals of Ψ_1^{T} and $\Psi_{-1}^{\mathrm{T}} = |\sigma_{EE}\bar{\sigma}_{EE}\sigma^*_{EE}\bar{\sigma^*}_{EE}\bar{\pi}^y_{EE}\bar{\pi}^x_{EE}|$ with one of the corresponding vacant orbitals of opposite spin. In eq (4.13), Ψ_1^{S} and Ψ_2^{S} represent the closed shell singlet character of $\Psi_{\mathrm{SF}}^{\mathrm{S}}$ whereas Ψ_3^{S} and the sum over all $\Psi_{n_{\mathrm{SF}}}^{\mathrm{S}}$ represent the open shell or diradical side of $\Psi_{\mathrm{SF}}^{\mathrm{S}}$. We find for E = Si, Ge, Sn, that the dominating contribution comes from C_1. For a given functional the C_1 values differ little between elements and for a given element C_1 ranges from C_1 = 0.99 (LDA) to C_1 = 0.93 (BHLYP). The remaining part comes from many small $\Psi_{n_{\mathrm{SF}}}^{\mathrm{S}}$ contributions that represent the diradical nature. Thus, our analysis indicate a diradical character of around 5 % (or less) that is constant for all three elements E = Si, Ge, Sn. For E = Pb the dominating contribution is the closed shell Ψ_2^{S} with $C_2 \approx$ 0.95. Thus for Pb the maximum diradicaloid character is also 5 %.

Jung *et al.* [191] pointed to eq (4.13) as a way in which to assess the degree of diradicaloid nature in the E–E bonds. Unfortunately, they did not report the different weights and used only SF-TD-DFT to calculate the singlet-triplet splitting. The authors assessed instead the degree of diradical character from a natural orbital analysis based on *ab initio* complete active space SCF (CASSCF) [224] calculations. Such an analysis describes the electron configuration of REER (E = Si, Ge, Sn) with fractional occupations as $(\sigma_{EE})^2(\sigma^*_{EE})^{2-\delta_1}(\pi^y_{EE})^{2-\delta_2}(\pi^x_{EE})^{\delta_1}(\pi^{y*}_{EE})^{\delta_2}$ rather than $(\sigma_{EE})^2(\sigma^*_{EE})^2(\pi^y_{EE})^1(\pi^x_{EE})^1(\pi^{y*}_{EE})^0$ for KS-DFT and Hartree-Fock. The fractional occupations numbers δ_1 and δ_2 are from qualitative considerations taken to mean that the degree of diradical character is $(\delta_1 + \delta_2)\times 10^2$ %. In this way the authors concluded that the diradical contribution was between 30 % – 25 % for E = Si, Ge, Sn and 8 % for E = Pb. For E = Si, Ge, and Sn, this would mean that the combined sum of the squares of all weights $C^2_{n_{\mathrm{SF}}}$ corresponding to $\Psi_{n_{\mathrm{SF}}}^{\mathrm{S}}$ for the spin-flip replacements $\sigma^*_{EE} \rightarrow \bar{\pi}^y_{EE}$, $\bar{\sigma}^*_{EE} \rightarrow \pi^y_{EE}$, $\pi^x_{EE} \rightarrow \bar{\pi}^{y*}_{EE}$ and $\bar{\pi}^x_{EE} \rightarrow \pi^{y*}_{EE}$ with respect to the triplet reference should be between 0.30 and 0.25. In our SF-CV(2)-DFT calculations we find this contributions to be two orders of magnitude smaller and more in line with what one would expect in view of the large calculated singlet-triplet splitting. The diradical singlet components such as from the spin-flip replacements $\sigma^*_{EE} \rightarrow \bar{\pi}^y_{EE}$, $\bar{\sigma}^*_{EE} \rightarrow \pi^y_{EE}$, $\pi^x_{EE} \rightarrow \bar{\pi}^{y*}_{EE}$ and $\bar{\pi}^x_{EE} \rightarrow \pi^{y*}_{EE}$ appear as pure

excited singlet states well above the first triplet.

4.4 Concluding Remarks

The present study is the first that has given a detailed analysis of the role played by isopropyl groups in stabilizing the E–E bond in ArEEAr (where E = Si, Ge, Sn, Pb and Ar = terphenyl ligand). This analysis was carried out by employing the NOCV method together with the ETS scheme. In the NOCV-ETS analysis we consider ArEEAr as formed from two ArE fragments with a doublet ground-state configuration $\sigma^2\pi^1$. For E = Si, Ge and Sn, it revealed one π–bond perpendicular to the CEEC plane and two σ/π type bonds in the plane while similar bonding pictures have been obtained in previous model studies [190, 191, 193] with Ar = H, CH_3, the NOCV-ETS scheme was able to obtain quantitative estimates for the strength of the various σ/π components without artificial truncations of the system. Especially it was shown that all three bonding component have the same strength. Thus ArEEAr with E = Si, Ge and Sn should be considered to have a triple bond. The Ar*PbPbAr* system was found to have a single σ–bond with a $\angle$C-Pb-Pb trans-bent angle close to 90°. Such a crossover in bonding has been observed before [191, 193] and rationalized as caused by an increasing stability of the doublet compared to the quartet in EAr. We point out that a contributing factor is a reduction of the out of plane bonding overlap in $\bar{\pi}^y$ compared to the $\bar{\pi}^{x*}$ as the E–E bond distance increases, Figure 4.4.

As a completely new aspect, the NOCV-ETS analysis was able to show that the electronic influence of the isopropyl substituents on the σ/π components differ little from that of hydrogen atoms. Rather the stabilizing influence of the isopropyl substituents stems from dispersive van der Waals attractions between Pr^i groups on aryl rings attached to different E atoms as well as hyperconjugation involving donation into σ^* orbitals on Pr^i. The dispersive interaction amounts to -27.5 kcal/mol (Si), -29.1 kcal/mol (Ge), -26.2 kcal/mol (Sn) and -44.0 kcal/mol (Pb). The larger dispersive stabilization for lead reflects the fact that the longer Pb–Pb and Pb–C bonds sterically allow

for more isopropyl groups with Ar = C_6H_3-2,6-(C_6H_2-2,4,6-Pr^i_3)$_2$. Compared to the other elements where Ar = C_6H_3-2,6-(C_6H_3-2,6-Pr^i_2)$_2$. Thus, in spite of the lower bond order, the Pb–Pb bond strength is stronger than for the other elements as the weaker bonding interaction ΔE_{orb} is more than compensated for by a weaker steric repulsion and a more favourable dispersive attraction. The NOCV-ETS analysis revealed that the observed trans-bent angles are a compromise between steric factors that favours larger angles and electronic factors (ΔE_{orb} + ΔE_{disp}) favouring smaller angles. The trans-bent angle θ has so far been studies by REER model systems (R = H, Me) where ΔE_{disp} is absent and ΔE_{steric} different. It is thus not surprising that the E–E distances and θ angles in REER can differ considerably from those observed in ArEEAr, especially for E = Sn, Pb [191]. It is finally concluded from our quantitative SF-CV(2)-DFT calculations that the real ArEEAr systems reveal little if any diradical character of the E–E bond in contrast to a previous qualitative analysis of model systems.

Chapter 5

Application of Time-Dependent and Time-Independent Density Functional Theory to Rydberg Transitions

5.1 Introduction

The description of excited states by DFT has largely been based on TD-DFT [52, 53, 57, 58, 59, 60, 225] in which the density induced change in the exchange correlation potential $\hat{V}_{XC}^{\mathrm{KS}}(\vec{r})$ due to a time-dependent perturbation enables one to estimate transition energies and other excited-state properties. It is thus evident that the success of TD-DFT depends strongly on how well the approximate density functional at hand describes $\hat{V}_{XC}^{\mathrm{KS}}(\vec{r})$.

It is known that functionals based on the local density approximation (LDA) or its generalized gradient approximation (GGA) give rise to an $\tilde{V}_{XC}^{\mathrm{KS}}(\vec{r})$ that is less stabilizing than the potential $\hat{V}_{XC}^{\mathrm{KS}}(\vec{r})$ from an exact functional derived from high level wave function theory [1, 61, 62, 63]. The result is that energies for both occupied ($\tilde{\epsilon}_i$) and virtual ($\tilde{\epsilon}_a$) orbitals derived from $\tilde{V}_{XC}^{\mathrm{KS}}(\vec{r})$ are much higher than those (($\hat{\epsilon}_i$),($\hat{\epsilon}_a$)) obtained from $\hat{V}_{XC}^{\mathrm{KS}}(\vec{r})$. The weak character of $\tilde{V}_{XC}^{\mathrm{KS}}(\vec{r})$ also manifests itself at medium and large distances r from the molecular centre of mass where $\tilde{V}_{XC}^{\mathrm{KS}}(\vec{r})$ is decaying exponentially with r whereas $\hat{V}_{XC}^{\mathrm{KS}}(\vec{r})$ decays as $\sim -1/r$.

The insufficient stabilization of $\tilde{V}_{XC}^{\mathrm{KS}}(\vec{r})$ for both medium values of r in the valence region and large values of r in the density tail is not necessarily detrimental for TD-DFT excitation energies based on $\tilde{V}_{XC}^{\mathrm{KS}}(\vec{r})$. The reason for this is that TD-DFT excitation energies largely depend on the difference $\tilde{\epsilon}_a - \tilde{\epsilon}_i$. Thus, considerable errors in $\tilde{\epsilon}_i$, $\tilde{\epsilon}_a$ might cancel in $\tilde{\epsilon}_a - \tilde{\epsilon}_i$ if the average potential experienced by ψ_i and ψ_a have similar deviations from $\hat{V}_{XC}^{\mathrm{KS}}(\vec{r})$. This appears to be the case for valence tran-

sitions $\psi_i \rightarrow \psi_a$ where the overlap S_{ia} between the two densities $\psi_i\psi_i$ and $\psi_a\psi_a$ is large [83, 91]. However, the error in $\tilde{V}_{XC}^{KS}(\vec{r})$ clearly manifests itself in cases where S_{ia} is small such as charge transfer excitations [64, 71, 72, 84, 80, 85, 226] and Rydberg transitions [1, 61, 62, 63]. Nevertheless, it has been possible to obtain acceptable results even in cases where S_{ia} is small by constructing specialized potentials [1, 61, 62, 63, 64, 71, 72, 83, 84, 80, 85, 86, 87, 88, 89, 90] in which the proper $-1/r$ decay is enforced. Unfortunately, the specialized potentials might in some cases lead to poorer results for "regular" transitions in which $S_{ia} >> 0$.

In wave function theory excited states are described not only by response theory but equally well by variational approaches in which excited states are localized as stationary points on energy surfaces above the ground-state [227, 228]. In this case an excitation energy is determined straightforwardly as a total energy difference. As already mentioned, in DFT, response theory has been prevalent in excited-state studies in the form of the ATD-DFT scheme. Nevertheless, variational DFT approaches have also been used with some success. They include ensemble DFT [40, 41, 42, 229], variation of bifunctionals [96], change in self-consistent field (ΔSCF) [13, 14, 15, 43, 44, 45, 46] and others [97, 230]. Perhaps the best known is the ΔSCF scheme by Slater [13, 43] which historically was introduced before TD-DFT.

There has been some doubt as to the general validity [231] of using excited-state variation theory based on DFT given the status of DFT as a ground-state theory. However, we have recently shown that adiabatic TD-DFT can be derived from a variational approach in connection with our development of the CV-DFT method [47, 232] for the description of excited states. It has been shown previously [47, 232] that the variational CV-DFT approach to second-order in U_{ai} is equivalent to adiabatic TD-DFT based on response theory both [47] within the TDA [175] and in the general case [232]. Further, to all orders in U_{ai}, CV-DFT is equivalent to ΔSCF in those cases where the transition can be described by a single orbital replacement $\psi_i \rightarrow \psi_a$ [48].

We have in previous studies been able to treat charge transfer transitions [50, 93] and other "difficult" cases such as $\pi \rightarrow \pi^*$ excitations in cyclic acenes [233] and cyanines

[234] successfully even with local functionals provided that terms to all orders in U_{ai} were taken into account in our CV-DFT approach. However, this requires that U_{ai} is fully optimized [51] and that the basis of occupied $\{\phi_i(1);\, i = 1,occ\}$ and virtual $\{\phi_a(1);\, a = 1,vir\}$ ground-state orbitals are allowed to relax (RSCF-CV(∞)-DFT) [49]. It is our objective in the present investigation to illustrate that Rydberg transitions for which $S_{ia} \sim 0$ equally well can be described by RSCF-CV(∞)-DFT even for LDA and related GGA functionals.

Since Rydberg transitions are characterized by a single orbital replacement $\psi_v \rightarrow \psi_r$, RSCF-CV($\infty$)-DFT will give results very similar to ΔSCF. We shall in the following base our numerical calculations on ΔSCF whereas the discussion will make use of CV-DFT that connects ΔSCF and adiabatic TD-DFT.

5.2 Theoretical Details

5.2.1 Computational Methods

In CV(2)-DFT or ATD-DFT/TDA the triplet excitation energy for a transition involving a single orbital replacement ($r \rightarrow v$) takes on the form [52]

$$\Delta E_{\mathrm{T}}^{\mathrm{CV(2)}} = \Delta E_{\mathrm{T}}^{\mathrm{ATD\text{-}DFT/TDA}} = [\epsilon_r(\rho^0) - \epsilon_v(\rho^0)] + K_{rvrv} - K_{rv\bar{r}\bar{v}} \tag{5.1}$$

whereas the singlet excitation energy is given by [52]

$$\Delta E_{\mathrm{S}}^{\mathrm{CV(2)}} = \Delta E_{\mathrm{S}}^{\mathrm{ATD\text{-}DFT/TDA}} = [\epsilon_r(\rho^0) - \epsilon_v(\rho^0)] + K_{rvrv} + K_{rv\bar{r}\bar{v}}. \tag{5.2}$$

In RSCF-CV(∞)-DFT [46, 49] the triplet transition energy for an excitation that can be represented by a single orbital replacement ($v \rightarrow r$) [232] and the corresponding singlet energy are given in eqs (2.38) and (2.39), respectively.

5.2.2 Computational Details

We have carried out all DFT calculations by employing a developers version of the ADF 2012 program [181]. Our calculations employed a standard triple-ζ Slater type

orbital (STO) basis with two sets of polarization functions for all atoms (TZ2P) [235] as well as an extended quadruple-ζ STO basis with three sets of polarization functions and two diffuse functions (ET-QZ3P-2DIFFUSE) [1, 181] on each atom. We shall refer to the latter as the Extended basis for short. Use was made of the LDA in the VWN parametrization [36] and the BP86 generalized gradient approximation (GGA) with the correlation part by Perdew [38] and the exchange part by Becke [37]. We employed further the B3LYP and hybrid functional by Becke [39] with the correlation functional taken from Lee $et\ al.$ [152]. Here B3LYP has 20 % HF exchange. Use has also been made of length corrected functionals (LC). In the LC functional, the regions of electron–electron interaction are divided into "long" and "short" range parts by dividing the Coulomb operator into two pieces:

$$\frac{1}{r_{12}} = \underbrace{\frac{w(\omega, r_{12})}{r_{12}}}_{\text{SR}} + \underbrace{\frac{1 - w(\omega, r_{12})}{r_{12}}}_{\text{LR}} \tag{5.3}$$

where r_{12} is the inter-electronic distance $r_{12} = |\vec{r}_1 - \vec{r}_2|$ whereas w is some kind of continuous switching function that goes to 1 as r_{12} goes to zero and to zero as r_{12} becomes large. The parameter ω determines how rapidly the switching occurs. This type of division has been introduced by a number of groups to combine DFT and wave function theory [86, 87, 88, 89]. The most widely used form for $w(\omega,r_{12})$ is the error function [86, 87, 88, 89] as it gives rise to integrals that are readily evaluated in connection with Gaussian basis sets. An alternative choice is the exponential function

$$w(\omega, r_{12}) = \exp(-\omega r_{12}) \tag{5.4}$$

which in combination with the r_{12}^{-1} operator gives the Yukawa potential [236, 237]. The exponential choice for $w(\omega, r_{12})$ in eq (5.4) has been used for both Gaussian [236, 237] and Slater type basis sets [238]. We employ here $w(\omega, r_{12})$ in eq (5.4) with ω = 0.40 and ω = 0.75. The local functional used in conjunction with LC was BP86. Here LC combined with BP86 for ω = 0.40 is termed LCBP86* whereas the combination with ω = 0.75 is called LCBP86. All electrons were treated variationally without the use of the frozen core approximation [181]. The parameter for the precision of the numerical

integration was set to a (standard) value of 5.0. A special auxiliary STO basis was employed to fit the electron density in each cycle for an accurate representation of the exchange and Coulomb potentials [181].

5.2.3 Molecular Models

All structures were taken from Ref. [63].

5.3 Results and Discussion

5.3.1 TD-DFT Calculations on Rydberg Excitations

It is well established that functionals based on the local density approximation and GGA in conjunction with TD-DFT afford poor estimates of Rydberg excitation energies and the same is true for many hybrid functionals such as B3LYP. As already mentioned, the failure of the above functionals stems from the fact that their $\tilde{V}_{XC}^{\mathrm{KS}}(\vec{r})$ is less stabilizing than the potential $\hat{V}_{XC}^{\mathrm{KS}}(\vec{r})$ from an exact functional for both medium values of r in the valence region and large values of r in the density tail where $\tilde{V}_{XC}^{\mathrm{KS}}(\vec{r})$ is decaying exponentially with r whereas $\hat{V}_{XC}^{\mathrm{KS}}(\vec{r})$ decays as $\sim -1/r$ [1, 61, 62, 63]. Here r is the distance to the molecular centre of mass. The deficiencies can been overcome [1, 61, 62, 63, 86, 87, 239] in the case of Rydberg transitions by modifying $\tilde{V}_{XC}^{\mathrm{KS}}(\vec{r})$ in such a way that it becomes more stabilizing and decays properly as $\sim -1/r$. Thus, several functionals are available that with TD-DFT can calculate Rydberg transitions to within $\pm$ 0.3 eV of experiment.

We display in Table 5.1 calculations of the excitation energies for four singlet Rydberg states of N_2 based on ATD-DFT/TDA and five different functionals employing an extended basis with diffuse STOs [1].

The calculated Rydberg excitation energies for LDA, BP86 and B3LYP are too low compared to experiment with deviations of more that 1 eV. As such the results displayed in Table 5.1 are representative of several published [1, 61, 62, 63] studies on Rydberg transitions based on TD-DFT and LDA, GGA or hybrid functionals. The origin of the

Table 5.1: Rydberg Singlet Excitation Energies[a] for N_2 Calculated with ATD-DFT/TDA Using an extended basis set[b] and five different functionals.

	State	Transition	LDA	BP86	B3LYP	LCBP86*[c]	LCBP86[d]	Expt.[e]
N_2	$^1\Sigma_g^+$	$\sigma_g \rightarrow 3s\sigma_g$	10.21	9.87	11.03	11.51	12.36	12.20
	$^1\Pi_u$	$\sigma_g \rightarrow 3p\sigma_u$	10.60	10.16	11.43	11.92	12.73	12.90
	$^1\Sigma_u^+$	$\sigma_g \rightarrow 3p\sigma_u$	10.52	10.38	11.51	12.01	13.32	12.98
	$^1\Pi_u$	$\pi_u \rightarrow 3s\sigma_g$	11.67	11.20	11.87	12.49	13.02	13.24
		MAE	1.66	1.94	1.10	0.68	0.18	
		RMSD	2.11	2.44	1.38	0.86	0.23	

[a]Energies in eV. [b]Ref. [1]. [c]Refers to LC functional combined with BP86 and ω = 0.40. [d]Represents LC functional combined with BP86 and ω = 0.75. [e]Ref. [240].

deviation is obviously the failure of $\tilde{V}_{XC}^{\text{KS}}(\vec{r})$ to be sufficiently stabilizing compared to $\hat{V}_{XC}^{\text{KS}}(\vec{r})$ in both the valence region where ϕ_v is dominant and the density tail where the Rydberg orbital ϕ_r has its density maximum.

We can asses the relative error of $\tilde{V}_{XC}^{\text{KS}}(\vec{r})$ from the two regions by observing in the first place that the Rydberg transition can be considered as an ionization out of ϕ_v in A = N_2 with the ionization potential IP(A, ϕ_v) followed by the electron capture of ϕ_r by A^+ = N_2 with only a single electron in ϕ_v. With the electron affinity of A^+ = N_2^+ given by EA(A^+, ϕ_v, ϕ_r, S), we can write the singlet Rydberg excitation energy for the $\phi_v \rightarrow \phi_r$ transition as [234]

$$\Delta E_{\text{S}}(\phi_v \rightarrow \phi_r) = \text{IP}(\text{A}, \phi_v) + \text{EA}(\text{A}^+, \phi_v, \phi_r, \text{S}) \tag{5.5}$$

whereas the corresponding triplet energy is given by

$$\Delta E_{\text{S}}(\phi_v \rightarrow \phi_r) = \text{IP}(\text{A}, \phi_v) + \text{EA}(\text{A}^+, \phi_v, \phi_r, \text{T}). \tag{5.6}$$

In ATD-DFT/TDA one has that IP(A, ϕ_v) = $-\epsilon_v(\rho^0)$ [234] whereas EA(A^+, ϕ_v, ϕ_r, S) = $\epsilon_v(\rho^0)$ + K_{rvrv} + $K_{rv\bar{r}\bar{v}}$ and EA(A^+, ϕ_v, ϕ_r, T) = $\epsilon_v(\rho^0)$ + K_{rvrv} - $K_{rv\bar{r}\bar{v}}$ [52, 234]. In fact, a substitution of the expressions for IP(A, ϕ_v), EA(A^+, ϕ_v, ϕ_r, S) and EA(A^+, ϕ_v, ϕ_r, T) in terms of orbital energies and *K* integrals affords for $\Delta E_{\text{T}}(\phi_v \rightarrow \phi_r)$ the energy expression for $\Delta E_{\text{T}}^{\text{ATD-DFT/TDA}} = \Delta E_{\text{T}}^{\text{CV(2)}}$ of eq (5.1) whereas $\Delta E_{\text{S}}(\phi_v \rightarrow \phi_r)$ results in $\Delta E_{\text{S}}^{\text{ATD-DFT/TDA}} = \Delta E_{\text{S}}^{\text{CV(2)}}$ eq (5.2).

Table 5.2: IP[a] of N_2 and EA[a,b] of N_2^+ Calculated for ATD-DFT/TDA Using an extended basis set[c] and five different functionals.

Energy Term	LDA	BP86	B3LYP	LCBP86*[d]	LCBP86[e]	Expt.
IP(N_2, σ_g)	10.38	10.36	11.86	14.20	15.86	15.58[f,g]
IP(N_2, π_u)	11.91	11.74	12.84	15.39	16.74	17.07[g]
EA(N_2^+, σ_g, $3s\sigma_g$, S)	-0.17	-0.49	-0.83	-2.69	-3.50	-3.38[b]
EA(N_2^+, σ_g, $3p\pi_u$, S)	0.22	-0.20	-0.43	-2.28	-3.13	-2.68[b]
EA(N_2^+, σ_g, $3p\sigma_u$, S)	0.14	0.02	-0.35	-2.19	-2.54	-2.60[b]
EA(N_2^+, π_u, $3s\sigma_g$, S)	-0.24	-0.54	-0.97	-2.90	-3.72	-3.83[b]

[a]Energies in eV. [b]Evaluated as EA(A^+, ϕ_v, ϕ_r, S) = $\Delta E_S(\phi_v \rightarrow \phi_r)$ − IP(A, ϕ_v). [c]Ref. [1]. [d]Refers to LC functional combined with BP86 and ω = 0.40. [e]Represents LC functional combined with BP86 and ω = 0.75. [f]Ref. [241]. [g]Ref. [240].

In N_2, the ionizations are out of $\epsilon_v = \sigma_g$, π_u and experimental values are available for IP(A, σ_g) [241] and IP(A, π_u) [242], see Table 5.2. The experimental estimates for EA(A^+, ϕ_v, ϕ_r, T) and EA(A^+, ϕ_v, ϕ_r, S) can be obtained from the observed triplet $\Delta E_T(\phi_v \rightarrow \phi_r)$ and singlet $\Delta E_S(\phi_v \rightarrow \phi_r)$ Rydberg excitation energies by the help of eqs (5.1) and (5.2). They are given in Table 5.2, where they are compared to the affinities EA(A^+, ϕ_v, ϕ_r, S) obtained from ATD-DFT/TDA calculations for 5 different functionals. We note that LDA, BP86 and B3LYP as expected underestimate both IP(A, σ_g) and $-$EA(A^+, ϕ_v, ϕ_r, S) due to the weak $\tilde{V}_{XC}^{KS}(\vec{r})$ potential. However in absolute terms IP(A, ϕ_v) for the valence orbital ϕ_v carries a larger error of up to 5 eV compared to $-$EA(A^+, ϕ_v, ϕ_r, S) for the Rydberg orbital ϕ_r where the error is up to 3 eV. As a consequence $\Delta E_S(\phi_v \rightarrow \phi_r)$ = IP(A, ϕ_v) − ($-$EA(A^+, ϕ_v, ϕ_r, S)) is underestimated. The imbalanced description of IP(A, ϕ_v) and $-$EA(A^+, ϕ_v, ϕ_r, S) for LDA, BP86 and B3LYP due to $\tilde{V}_{XC}^{KS}(\vec{r})$ is generally observed in TD-DFT studies on Rydberg Transitions and extends also to many other GGA and hybrid functionals.

The difference in the accuracy of $\tilde{V}_{XC}^{KS}(\vec{r})$ for the Rydberg and valence regions has previously been discussed extensively for N_2 by Gruening $et\ al.$ [243].

We include in Table 5.1 as well results from LCBP86 and LCBP86* calculations on the same N_2 Rydberg transitions discussed above. In LCBP86 and LCBP86* we combine BP86 at short inter electronic distances (r_{12}) with HF at large values of r_{12}. Thus,

these functionals have a $\tilde{V}_{XC}^{\mathrm{KS}}(\vec{r}$ potential with the right $\sim -1/r$ decay. We see that the LC functionals indeed afford better estimates of the Rydberg transition energies with deviations that are similar to the accuracy obtained by the improved functionals mentioned above [1, 61, 62, 63, 86, 87, 239]. It is further clear from Table 2 that LCBP86 within ATD-DFT/TDA affords accurate estimates of both IP(A, σ_g) and $-$EA(A$^+$, ϕ_v, ϕ_r, S). Thus, the good agreement with experiment in the calculated Rydberg excitation energies for LCBP86 is not due to a cancellation of errors. Also included in Table 5.1 is results from LCBP86* with ω = 0.40. In this case we note a larger deviation in $\Delta E_{\mathrm{S}}(\phi_v \rightarrow \phi_r)$, IP(A, σ_g) and $-$EA(A$^+$, ϕ_v, ϕ_r, S) based on ATD-DFT/TDA. Nevertheless, the performance of LCBP86* is still better than for LDA, BP86 and B3LYP in the case of ATD-DFT/TDA. We have seen that Rydberg transitions are underestimated by TD-DFT due to an imbalance in the error of $\tilde{V}_{XC}^{\mathrm{KS}}(\vec{r})$. Thus $\tilde{V}_{XC}^{\mathrm{KS}}(\vec{r})$ lacks more stabilization in the valence realm than in the Rydberg region. Such an imbalance is in general a possibility for transitions $\psi_i \rightarrow \psi_a$ where the overlap S_{ia} between the two densities $\psi_i\psi_i$ and $\psi_a\psi_a$ is small. On the other hand, for $\psi_i \rightarrow \psi_a$ transitions where the overlap S_{ia} is large one can expect the error in $\tilde{V}_{XC}^{\mathrm{KS}}(\vec{r})$ experienced by ψ_i and ψ_a to be comparable resulting in a cancellation of errors. Thus in this case TD-DFT might lead to acceptable excitation energies even for LDA, GGAs and hybrids. It has been pointed out by Verma and Bartlett [77, 243, 244] that good functionals not only should afford reliable excitation energies with TD-DFT but also accurate ionization potentials and affinities. We shall return to this point shortly.

5.3.2 ΔSCF Calculations on Rydberg Excitations

For Rydberg transitions that can be represented by a single orbital replacement ($\psi_i \rightarrow \psi_a$) both ΔSCF and RSCF-CV($\infty$)-DFT affords for the triplet energy ($\Delta E_{\mathrm{T}}^{\mathrm{CV}(\infty)}$) the expression of eq (2.38) whereas the singlet excitation energy ($\Delta E_{\mathrm{S}}^{\mathrm{CV}(\infty)}$) is given by eq (2.39) [234]. In the case of HF, $\Delta E_{\mathrm{S}}^{\mathrm{CV}(\infty)} = \Delta E_{\mathrm{S}}^{\mathrm{CV}(2)}$ and $\Delta E_{\mathrm{T}}^{\mathrm{CV}(\infty)} = \Delta E_{\mathrm{T}}^{\mathrm{CV}(2)}$ with $\Delta E_{\mathrm{Rel}}^{\mathrm{S}}(R) = \Delta E_{\mathrm{Rel}}^{\mathrm{T}}(R) = 0$. This follows from the fact that $K_{rrrr} = K_{vvvv} = 0$ and $K_{rvrv} + K_{rv\bar{r}\bar{v}} = -2K_{rrvv} + K_{rr\bar{v}\bar{v}}$ whereas $-K_{rr\bar{v}\bar{v}} = K_{rvrv} + K_{rv\bar{r}\bar{v}}$. Where all these relations

can be derived from the general HF condition [234]

$$K_{pqrs} = -K_{prqs}. \tag{5.7}$$

However, for any other known functional, $\{\Delta E_{\mathrm{S}}^{\mathrm{CV}(\infty)} - \Delta E_{\mathrm{Rel}}^{\mathrm{S}}(R)\} \neq \Delta E_{\mathrm{S}}^{\mathrm{CV}(2)}$ and $\{\Delta E_{\mathrm{T}}^{\mathrm{CV}(\infty)} - \Delta E_{\mathrm{Rel}}^{\mathrm{T}}(R)\} \neq \Delta E_{\mathrm{T}}^{\mathrm{CV}(2)}$ eq (5.7) is no longer satisfied.

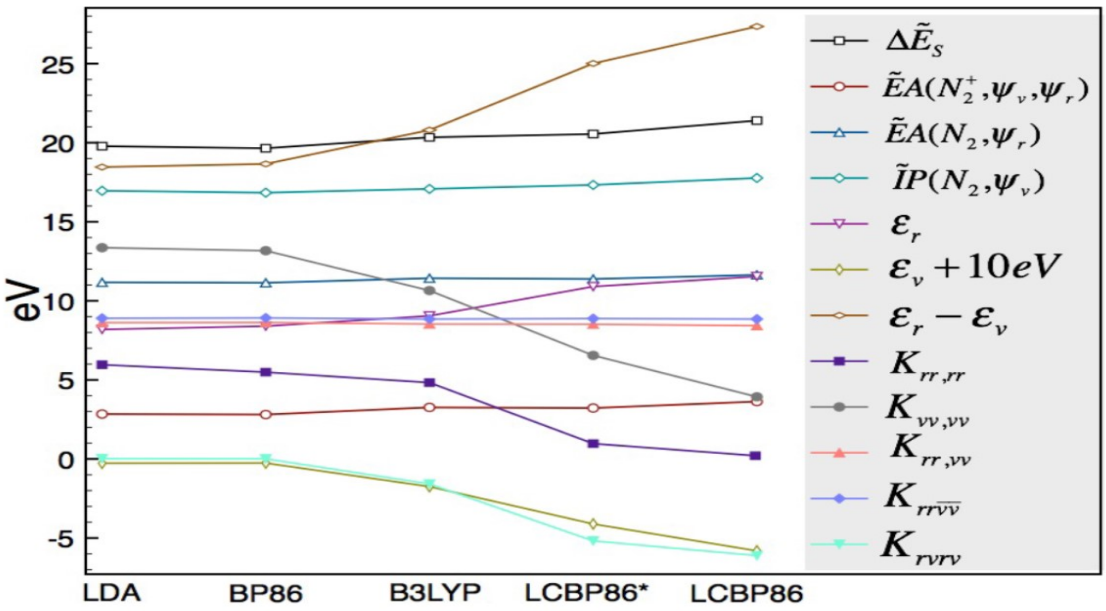

Figure 5.1: Energy terms contributing to the unrelaxed singlet excitation energy $\Delta\tilde{E}_{\mathrm{S}}$ for the Rydberg transition $\psi_v \rightarrow \psi_r$, see eq (5.12), for 5 different functional and the TZ2P basis set. $\tilde{\mathrm{I}}\mathrm{P}(\mathrm{N}_2, \psi_v)$ is the unrelaxed ionization potential, eq (5.8). $\tilde{\mathrm{E}}\mathrm{A}(\mathrm{N}_2, \psi_r)$ is the unrelaxed electron affinity of N_2 with-respect-to electron capture by the Rydberg orbital ψ_r, eq (5.11). $\tilde{\mathrm{E}}\mathrm{A}(\mathrm{N}_2^+, \psi_v, \psi_r, \mathrm{S})$ is the unrelaxed electron affinity with-respect-to electron capture by the Rydberg orbital ψ_r of N_2^+ with a single electron in ψ_v when the product is a singlet, eq (5.9). (Throughout, $\psi_v = \sigma_g$ and $\psi_r = 3s\sigma_g$)

We plot in Figure 5.1 for TZ2P the numerical values of K_{rrrr}, K_{vvvv}, K_{rrvv}, $-K_{rr\bar{v}\bar{v}}$ and K_{rvrv} as well as ϵ_r and ϵ_v in the case of N_2 for 5 different functionals (LDA, BP86, LCBP86, LCBP86*, B3LYP) with $\psi_v = \sigma_g$ and $\psi_r = 3\mathrm{s}\sigma_g$.

In Figure 5.1, LDA and BP86 both have large "self-interaction errors" ($K_{rrrr} \neq K_{vvvv} \neq 0$) of 5 eV ($K_{rrrr}$) and 10 eV ($K_{vvvv}$), respectively. The error is reduced as we introduce an increasing portion of HF exchange and reaches eventually 1 eV or less for LCBP86. The relation $K_{rrvv} + K_{rvrv} = 0$ is disobeyed by as much as 7 eV for LDA and BP86. The deviation is reduced to 1 eV for LCBP86. Without orbital relaxation, we have for ΔSCF and RSCF-CV(∞)-DFT that the ionization energy from $\psi_v = \sigma_g$ is

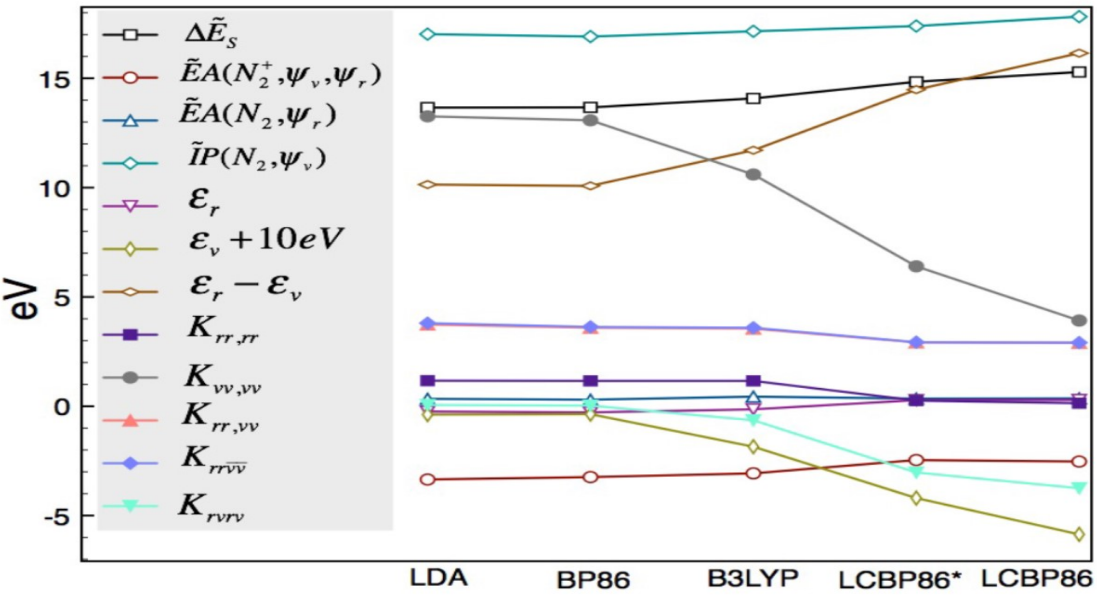

Figure 5.2: Energy terms contributing to the unrelaxed singlet excitation energy $\Delta\tilde{E}_S$ for the Rydberg transition $\psi_v \rightarrow \psi_r$, see eq (5.12), for 5 different functional and the extended basis set [1]. $\tilde{I}P(N_2, \psi_v)$ is the unrelaxed ionization potential, eq (5.8). $\tilde{E}A(N_2, \psi_r)$ is the unrelaxed electron affinity of N_2 with-respect-to electron capture by the Rydberg orbital ψ_r, eq (5.11). $\tilde{E}A(N_2^+, \psi_v, \psi_r, S)$ is the unrelaxed electron affinity with-respect-to electron capture by the Rydberg orbital ψ_r of N_2^+ with a single electron in ψ_v when the product is a singlet, eq (5.9). (Throughout, $\psi_v = \sigma_g$ and $\psi_r = 3s\sigma_g$)

given by [234]

$$\tilde{I}P = \tilde{I}P(N_2, \psi_v) = -\epsilon_v + \frac{1}{2}K_{vvvv} \tag{5.8}$$

where the superscript "$\sim$" is used to distinguish the expression in eq (5.8) from the ATD-DFT/TDA expression $IP(N_2, \psi_v) = -\epsilon_v$ [234]. It follows from the plot of $\tilde{I}P(N_2, \psi_v) = \tilde{I}P(N_2, \sigma_g)$ in Figure 5.1 that it is much less sensitive to the choice of functionals than the individual components $-\epsilon_v$ and $1/2K_{vvvv}$, especially for LDA, BP86, B3LYP and LCBP86*. Thus in eq (5.8) an increase in $-\epsilon_v$ is balanced by a decrease in $1/2K_{vvvv}$ when going towards functionals with increasing HF content. In ATD-DFT/TDA where $IP(N_2, \psi_v) = -\epsilon_v$, such a compensation from the "self-interaction" term $1/2K_{vvvv}$ is absent. In absolute terms $\tilde{I}P(N_2, \psi_v)$ calculated according to eq (5.8) with $\psi_v = \sigma_g$ is below the experimental ionization potentials [240, 241] of Table 5.2 due to the lack of orbital relaxation. We shall introduce relaxation shortly. Without relaxation we have for ΔSCF and RSCF-CV(∞)-DFT (ΔDFT and SCF-CV(∞)-DFT) that the electron

affinity corresponding to the electron capture by ψ_r N_2^+ with the singly occupied ψ_v orbital is given as

$$\tilde{EA}(N_2^+) = \tilde{EA}(N_2^+, \psi_v, \psi_r, S) = \epsilon_r + \frac{1}{2}K_{rrrr} - 2K_{rrvv} + K_{rr\bar{v}\bar{v}} \tag{5.9}$$

if the resulting N_2 state is a singlet. The corresponding triplet expression is

$$\tilde{EA}(N_2^+) = \tilde{EA}(N_2^+, \psi_v, \psi_r, T) = \epsilon_r + \frac{1}{2}K_{rrrr} - K_{rr\bar{v}\bar{v}}. \tag{5.10}$$

We note again from Figure 5.1 that $\tilde{EA}(N_2^+, \psi_v, \psi_r, S)$ for a given set (ψ_v, ψ_r) only are moderately functional dependent although ϵ_r and the ***K*** integrals varies considerably with the amount of HF exchange. This is especially the case for LDA, BP86, B3LYP and LCBP86*. The same is the case for $\tilde{EA}(N_2^+, \psi_v, \psi_r, T)$, although it is not plotted in Figure 5.1. The actual affinities calculated with the TZ2P basis are positive and 2 eV above the negative experimental values in Table 5.2. The underlying reason for that is not only a lack of relaxation but also an inability of the TZ2P basis to describe properly ψ_r. Also shown in Figure 5.1 is the electron affinity of the neutral N_2 molecule without relaxation

$$\tilde{EA}(N_2) = \tilde{EA}(N_2, \psi_r) = \epsilon_r + \frac{1}{2}K_{rrrr} \tag{5.11}$$

corresponding to the capture of an single electron by ψ_r = 3sσ_g with orbital relaxation neglected. Again $\tilde{EA}(N_2)$ is much less sensitive to the choice of functional than the defining contributions K_{rrrr} and ϵ_r. In absolute terms $\tilde{EA}(N_2)$ is likely of the wrong sign and numerically much too large. The reason is again the poor description of ψ_r. We present finally in Figure 5.1 the Rydberg singlet transition energy

$$\Delta\tilde{E}_S = \tilde{EA}(N_2^+, \psi_v, \psi_r, S) + \tilde{IP}(N_2, \psi_v). \tag{5.12}$$

Due to the errors in $\tilde{IP}(N_2, \psi_v)$ and $\tilde{EA}(N_2^+, \psi_v, \psi_r, S)$ discussed above, Rydberg transitions based on TZ2P are severely overestimated compared to experiment. Turning next to the results in Figure 5.2 based on the extended basis [1], we note that the largest change compared to the TZ2P results is the stabilization of ϵ_r and the reduction in

Table 5.3: Rydberg Singlet Excitation Energies[a] for N_2 Calculated with ΔSCF Using an extended basis set[b] and five different functionals.

	State	Transition	LDA	BP86	B3LYP	LCBP86*[c]	LCBP86[d]	Expt.[e]
N_2	$^1\Sigma_g^+$	$\sigma_g \rightarrow 3s\sigma_g$	12.00	11.88	12.25	12.42	12.93	12.20
	$^1\Pi_u$	$\sigma_g \rightarrow 3p\sigma_u$	12.71	12.48	12.87	13.15	13.61	12.90
	$^1\Sigma_u^+$	$\sigma_g \rightarrow 3p\sigma_u$	12.79	12.55	12.95	13.25	13.72	12.98
	$^1\Pi_u$	$\pi_u \rightarrow 3s\sigma_g$	13.69	13.30	13.16	13.49	13.51	13.24
	$^3\Sigma_g^+$	$\sigma_g \rightarrow 3s\sigma_g$	11.80	11.68	12.01	12.18	12.66	12.00
		MAE	0.25	0.25	0.04	0.23	0.62	
		RMSD	0.27	0.34	0.05	0.24	0.65	

[a]Energies in eV. [b]Ref. [1]. [c]Refers to LC functional combined with BP86 and ω = 0.40. [d]Represents LC functional combined with BP86 and ω = 0.75. [e]Ref. [240].

K_{rrrr}. We have in addition to a lesser extent a drop in K_{rrvv} and $K_{rr\bar{v}\bar{v}}$. These changes are brought about by the ability of the extended basis to describe the diffuse nature of ψ_r = 3sσ_g. As a result the calculated affinities $\tilde{\text{EA}}(N_2^+, \sigma_g, 3s\sigma_g, S)$ are now negative, although still above the experimental values due to the lack of orbital relaxation. Also, the affinities $\tilde{\text{EA}}(N_2^+, \sigma_g, 3s\sigma_g, S)$ are only moderately functional dependent. Further, ϵ_v and K_{vvvv} are only marginally influenced by the basis set change since the valence orbital $\psi_v = \sigma_g$ already is well described by TZ2P. For this reason the calculated $\tilde{\text{IP}}(N_2, \sigma_g)$ values in the two figures are quite similar.

Finally the calculated Rydberg excitation energies in Figure 5.2 are in much better agreement with experiment compared to Figure 5.1 due to the proper description of ψ_r = 3sσ_g. However, they are still too high as a result of the lack of relaxation.

In Table 5.3 are given the calculated Rydberg transition energies with the extended basis and the relaxation included based on ΔSCF. The improvement over ATD-DFT/TDA for LDA, BP86, B3LYP and LCBP86* with ω = 0.4 is remarkable. Thus, the RMSD is reduced from 2.11 eV (LDA), 2.44 eV (BP86),1.38 eV (B3LYP) and 0.86 eV (LCBP86*) for ATD-DFT/TDA in Table 5.1 to 0.27 eV (LDA), 0.34 eV (BP86), 0.05 eV (B3LYP) and 0.24 (LCBP86*) for ΔSCF in Table 5.3. The only exception is LCBP86 with ω = 0.75 where ATD-DFT/TDA affords 0.23 eV compared to 0.69 eV for ΔSCF. The

Table 5.4: IP[a] of N_2 and EA[a] of N_2^+ Calculated with ΔSCF Using an extended basis set[b] and five different functionals.

Energy Term	LDA	BP86	B3LYP	LCBP86*[c]	LCBP86[d]	Expt.
IP(N_2, σ_g)	15.63	15.50	15.74	15.96	16.38	15.58[e,f]
IP(N_2, π_u)	17.46	17.07	16.87	17.22	17.18	17.07[f]
EA(N_2^+, σ_g, $3s\sigma_g$, S)	-3.64	-3.61	-3.49	-3.55	-3.44	-3.38[g]
EA(N_2^+, σ_g, $3p\pi_u$, S)	-2.92	-3.01	-2.87	-2.81	-2.77	-2.68[g]
EA(N_2^+, σ_g, $3p\sigma_u$, S)	-2.84	-2.95	-2.79	-2.71	-2.66	-2.60[g]
EA(N_2^+, π_u, $3s\sigma_g$, S)	-3.77	-3.77	-3.71	-3.73	-3.67	-3.83[g]
EA(N_2^+, σ_g, $3s\sigma_g$, T)	-3.82	-3.81	-3.73	-3.79	-3.72	-3.58[h]

[a]Energies in eV. [b]Ref. [1]. [c]Refers to LC functional combined with BP86 and ω = 0.40. [d]Represents LC functional combined with BP86 and ω = 0.75. [e]Ref. [241]. [f]Ref. [240]. [g]Evaluated as EA(A^+, ϕ_v, ϕ_r, S) = $\Delta E_S(\phi_v \rightarrow \phi_r)$ − IP(A, ϕ_v). [h]Evaluated as EA(A^+, ϕ_v, ϕ_r, T) = $\Delta E_T(\phi_v \rightarrow \phi_r)$ − IP(A, ϕ_v).

LCBP86 with ω = 0.75 for ATD-DFT/TDA affords a better description of the N_2 Rydberg transitions than ΔSCF must be considered fortuitous since ATD-DFT/TDA for a transition that can be represented by a single orbital replacement ($\psi_v \rightarrow \psi_r$) is an approximation to ΔSCF. We compare in Table 5.4 the ionization potentials (N_2) and electron affinities (N_2^+) calculated by ΔSCF to experiment. The agreement is in general excellent with RMSDs between 0.1 eV and 0.3 eV.

The only exception is LCBP86 with ω = 0.75 for which $\tilde{\mathrm{IP}}(N_2, \sigma_g)$ is overestimated by 0.8 eV. This deviation reflects itself in Rydberg excitations from σ_g that are too high by a similar amount. By contrast, we note that ionization potentials and electron affinities calculated by ATD-DFT/TDA in Table 5.2 carry errors of up to 5 eV. Fortunately these errors are somewhat smaller (1–2 eV) for the calculated Rydberg transition energies than for the ionization potentials and affinities from which they are calculated due to a cancelation of errors, see Table 5.2.

Verma and Bartlett [77, 243, 244] have stressed the importance of having functionals that within ATD-DFT afford not only accurate excitation energies but also ionization potentials and affinities.

The ΔSCF calculations on Rydberg transition energies for CO (Table 5.5), CH_2O (Table 5.6), C_2H_2 (Table 5.7), H_2O (Table 5.8), C_2H_4 (Table 5.9), Be (Table 5.10), Mg

Table 5.5: Rydberg Excitation Energies[a] for CO Calculated with ΔSCF Using an extended basis set[b] and five different functionals.

	State	Transition	LDA	BP86	B3LYP	LCBP86*[c]	LCBP86[d]	Expt.[e]
CO	$^1\Sigma^+$	$\sigma \rightarrow 3s\sigma$	10.64	10.52	10.76	10.88	11.17	10.78
	$^1\Sigma^+$	$\sigma \rightarrow 3p\sigma$	11.24	10.94	11.37	11.36	11.38	11.40
	$^1\Pi$	$\sigma \rightarrow 3p\pi$	11.29	11.03	11.33	11.53	11.79	11.53
	$^1\Sigma^+$	$\sigma \rightarrow 3d\sigma$	12.28	12.01	12.34	12.68	12.90	12.40
	$^3\Sigma^+$	$\sigma \rightarrow 3s\sigma$	10.28	10.15	10.39	10.44	10.68	10.40
	$^3\Sigma^+$	$\sigma \rightarrow 3p\sigma$	11.06	10.86	11.34	11.32	10.67	11.30
	$^3\Pi$	$\sigma \rightarrow 3p\pi$	11.18	10.97	11.28	11.42	11.67	11.55
		MAE	0.20	0.41	0.09	0.09	0.31	
		RMSD	0.22	0.43	0.13	0.12	0.37	

[a]Energies in eV. [b]Ref. [1]. [c]Refers to LC functional combined with BP86 and ω = 0.40. [d]Represents LC functional combined with BP86 and ω = 0.75. [e]Ref. [245].

Table 5.6: Rydberg Excitation Energies[a] for CH_2O Calculated with ΔSCF Using an extended basis set[b] and five different functionals.

	State	Transition	LDA	BP86	B3LYP	LCBP86*[c]	LCBP86[d]	Expt.[e]
CH_2O	$^1B_2$	$n \rightarrow 3sa_1$	7.01	6.91	6.96	7.13	7.29	7.09
	$^1A_2$	$n \rightarrow 3pb_2$	7.86	7.70	7.81	8.10	8.26	7.97
	$^1B_2$	$n \rightarrow 3pa_1$	7.74	8.47	8.19	8.24	8.43	8.12
	$^1A_2$	$n \rightarrow 3pb_1$	8.20	8.00	8.12	8.35	8.50	8.38
	$^1A_2$	$n \rightarrow 3pb_1$	9.17	8.93	9.21	9.65	9.81	9.22
	$^3B_2$	$n \rightarrow 3sa_1$	6.83	6.73	6.84	6.97	7.18	6.83
	$^3A_1$	$n \rightarrow 3pb_2$	7.73	7.58	7.72	7.98	8.18	7.79
	$^3B_2$	$n \rightarrow 3pa_1$	7.57	8.32	7.99	8.20	8.23	7.96
		MAE	0.16	0.27	0.09	0.17	0.32	
		RMSD	0.21	0.28	0.12	0.20	0.34	

[a]Energies in eV. [b]Ref. [1]. [c]Refers to LC functional combined with BP86 and ω = 0.40. [d]Represents LC functional combined with BP86 and ω = 0.75. [e]Ref. [246].

Table 5.7: Rydberg Excitation Energies[a] for C_2H_2 Calculated with ΔSCF Using an extended basis set[b] and five different functionals.

	State	Transition	LDA	BP86	B3LYP	LCBP86*[c]	LCBP86[d]	Expt.[e]
C_2H_2	$^1\Pi_u$	$\pi_u \rightarrow 3s\sigma_g$	8.38	8.10	7.98	8.24	8.21	8.16
	$^1\Pi_g$	$\pi_u \rightarrow 3s\sigma_u$	8.49	8.15	8.16	8.90	8.75	9.00
	$^1\Sigma_g^+$	$\pi_u \rightarrow 3p\pi_u$	9.18	8.80	8.79	9.14	9.15	9.21
	$^1\Pi_u$	$\pi_u \rightarrow 3d\sigma_g$	9.25	9.12	9.70	9.68	9.64	9.24[f]
	$^3\Pi_u$	$\pi_u \rightarrow 3s\sigma_g$	8.27	8.00	7.92	8.14	8.13	8.07
	$^3\Pi_g$	$\pi_u \rightarrow 3s\sigma_u$	8.28	7.89	7.97	8.79	9.04	8.90
	$^3\Sigma_g^+$	$\pi_u \rightarrow 3p\pi_u$	9.03	8.67	8.65	8.95	8.93	8.98
	$^3\Pi_u$	$\pi_u \rightarrow 3d\sigma_g$	9.05	9.23	9.14	9.70	9.62	9.17
		MAE	0.22	0.36	0.42	0.18	0.18	
		RMSD	0.31	0.50	0.52	0.25	0.24	

[a]Energies in eV. [b]Ref. [1]. [c]Refers to LC functional combined with BP86 and ω = 0.40. [d]Represents LC functional combined with BP86 and ω = 0.75. [e]Ref. [247]. [f]Ref. [248].

Table 5.8: Rydberg Excitation Energies[a] for H_2O Calculated with ΔSCF Using an extended basis set[b] and five different functionals.

	State	Transition	LDA	BP86	B3LYP	LCBP86*[c]	LCBP86[d]	Expt.[e]
H_2O	$^1B_1$	$b_1 \rightarrow 3sa_1$	7.78	7.44	7.38	7.58	7.65	7.40
	$^1A_2$	$b_1 \rightarrow 3pb_2$	9.36	8.88	8.93	9.30	9.42	9.10
	$^1A_1$	$a_1 \rightarrow 3pa_1$	9.92	9.74	9.71	9.88	10.02	9.70
	$^1B_1$	$b_1 \rightarrow 3pa_1$	10.28	9.84	9.83	10.39	10.13	10.01
	$^1A_1$	$b_1 \rightarrow 3pb_1$	10.27	9.86	9.91	10.21	10.29	10.16
	$^3B_1$	$b_1 \rightarrow 3sa_1$	7.42	7.09	7.06	7.23	7.31	7.00
	$^3A_2$	$b_1 \rightarrow 3pb_2$	9.13	8.73	8.79	9.12	9.25	8.90
	$^3A_1$	$a_1 \rightarrow 3pa_1$	9.54	9.28	9.27	9.39	9.45	9.30
	$^3A_1$	$b_1 \rightarrow 3pb_1$	10.04	9.62	9.63	9.92	9.95	9.81
	$^3B_1$	$b_1 \rightarrow 3pa_1$	10.21	9.80	9.79	10.25	9.95	9.98
		MAE	0.26	0.14	0.12	0.24	0.22	
		RMSD	0.27	0.17	0.14	0.21	0.24	

[a]Energies in eV. [b]Ref. [1]. [c]Refers to LC functional combined with BP86 and ω = 0.40. [d]Represents LC functional combined with BP86 and ω = 0.75. [e]Ref. [249].

Table 5.9: Rydberg Excitation Energies[a] for C_2H_4 Calculated with ΔSCF Using an extended basis set[b] and five different functionals.

	State	Transition	LDA	BP86	B3LYP	LCBP86*[c]	LCBP86[d]	Expt.[e]
C_2H_4	$^1B_{3u}$	$\pi \rightarrow 3s(a_g)$	7.39	7.11	6.99	7.30	7.27	7.11
	$^1B_{1g}$	$\pi \rightarrow 3s\sigma(b_{2u})$	7.91	7.55	7.51	8.26	8.24	7.80
	$^1B_{2g}$	$\pi \rightarrow 3p\sigma(b_{1u})$	8.01	7.68	7.63	8.29	8.26	7.90
	^1A_g	$\pi \rightarrow 3p\pi(b_{3u})$	8.43	8.05	8.01	8.38	8.35	8.28
	$^1B_{3u}$	$\pi \rightarrow 3d\sigma(a_g)$	8.76	8.36	8.33	8.29	8.49	8.62
	$^1B_{3u}$	$\pi \rightarrow 3d\delta(a_g)$	8.96	8.97	–	8.83	9.08	8.90
	$^1B_{2u}$	$\pi \rightarrow 3d\delta(b_{1g})$	9.13	8.80	8.70	9.22	9.18	9.05
	$^1B_{1u}$	$\pi \rightarrow 3d\pi(b_{2g})$	9.23	9.21	8.91	9.26	9.79	9.33
	$^3B_{3u}$	$\pi \rightarrow 3s(a_g)$	7.25	6.99	6.92	7.18	7.18	6.98
	$^3B_{1g}$	$\pi \rightarrow 3s\sigma(b_{2u})$	7.82	7.51	7.48	8.22	8.21	7.79
	$^3B_{2g}$	$\pi \rightarrow 3p\sigma(b_{1u})$	7.90	7.56	7.53	8.24	8.23	7.79
	^3A_g	$\pi \rightarrow 3p\pi(b_{3u})$	8.29	7.93	7.89	8.19	8.13	8.15
	$^3B_{3u}$	$\pi \rightarrow 3d\sigma(a_g)$	8.70	8.34	8.31	8.71	8.44	8.57
		MAE	0.13	0.18	0.26	0.23	0.23	
		RMSD	0.15	0.20	0.28	0.28	0.29	

[a]Energies in eV. [b]Ref. [1]. [c]Refers to LC functional combined with BP86 and ω = 0.40. [d]Represents LC functional combined with BP86 and ω = 0.75. [e]Ref. [250].

Table 5.10: Rydberg Excitation Energies[a] for Be Calculated with ΔSCF Using an extended basis set[b] and five different functionals.

	State	Transition	LDA	BP86	B3LYP	LCBP86*[c]	LCBP86[d]	Expt.[e]
Be	^1S	$2s \rightarrow 3s$	6.39	6.11	6.26	6.40	6.79	6.78
	^1P	$2s \rightarrow 3p$	6.89	6.66	6.79	7.06	7.10	7.46
	^1D	$2s \rightarrow 3d$	7.73	7.40	7.50	7.90	7.96	7.99
	^3S	$2s \rightarrow 3s$	6.07	6.09	6.19	6.16	6.34	6.46
	^3P	$2s \rightarrow 3p$	6.63	6.60	6.74	6.88	6.97	7.30
	^3D	$2s \rightarrow 3d$	7.45	7.40	7.61	7.81	7.95	7.69
		MAE	0.42	0.57	0.43	0.29	0.19	
		RMSD	0.45	0.60	0.47	0.31	0.23	

[a]Energies in eV. [b]Ref. [1]. [c]Refers to LC functional combined with BP86 and ω = 0.40. [d]Represents LC functional combined with BP86 and ω = 0.75. [e]Kramida, A.; Ralchenko, Y.; NIST ASD Team **2013**. *NIST Atomic Spectra Database* (ver. 5.1) [Online]. Available: http://physics.nist.gov/asd [2014, June 19]. National Institute of Standards and Technology, Gaithersburg, MD.

(Table F.1) and Zn (Table C.2). Each table contains results from calculations on both singlet and triplet states using the extended [1] basis set and 5 different functionals.

Also given in the tables for each species is the performance of the 5 functionals in terms of mean absolute error (MAE) and root mean square deviation (RMSD). Table 5.11 summarizes the ΔSCF performance statistics for the various functionals in terms of RMSDs. The summary is based on 71 triplet or singlet Rydberg transitions involving 9 different species.

The best performance comes from the length corrected functional LCBP86* (ω = 0.4) with an average RMSD of 0.23 eV. It has an overall good consistency with the largest deviation coming from the two atoms Be (0.31) and Zn (0.34). Of similar accuracy are LDA and B3LYP both with a RMSD of 0.24 eV. We note that LDA would have fared as well as LCBP86* without the outlier Be (RMSD = 0.45 eV). The largest RMSD of 0.32 eV comes from BP86 and B3LYP. For LCBP86 the problem is with N_2 whereas BP86 has several outliers. It follows from Table 5 that ΔSCF performs notably better than ATD-DFT/TDA for standard functional where the latter method typically has

Table 5.11: Summary of RMSDs of Rydberg Excitation Energies[a] Calculated with ΔSCF Using an extended basis set[b] and five different functionals.

Species	No. of States	LDA	BP86	B3LYP	LCBP86*[c]	LCBP86[d]
N_2	5	0.27	0.34	0.05	0.23	0.62
CO	7	0.22	0.43	0.13	0.12	0.37
CH_2O	8	0.21	0.28	0.12	0.20	0.34
C_2H_2	8	0.31	0.50	0.52	0.25	0.24
H_2O	10	0.27	0.17	0.14	0.21	0.24
C_2H_4	13	0.15	0.20	0.28[e]	0.28	0.29
Be	6	0.45	0.60	0.47	0.31	0.23
Mg	6	0.18	0.35	0.19	0.13	0.12
Zn	8	0.18	0.25	0.27	0.34	0.46
RMSD		0.24	0.32	0.24	0.23	0.32

[a]Energies in eV. [b]Ref. [1]. [c]Refers to LC functional combined with BP86 and $\omega = 0.40$. [d]Represents LC functional combined with BP86 and $\omega = 0.75$. [e]Comprising 12 states.

errors exceeding 1 eV. On the other hand, specialized functionals are available that in conjunction with ATD-DFT affords Rydberg transitions with a RMSD that is less than 0.2 eV [1, 61, 62, 63].

5.4 Concluding Remarks

We have demonstrated that time independent density functional theory (ΔSCF and RSCF-CV-DFT) is able to describe Rydberg transitions surprisingly well for functionals such as LDA as well as the regular GGA scheme BP86 and the standard hybrid B3LYP. Our benchmarking included 71 triplet or singlet Rydberg transitions distributed over the 9 different species: N_2, CO (7), CH_2O (8), C_2H_2 (8), H_2O (10), C_2H_4 (13), Be (6), Mg (6) and Zn (8). LDA and B3LYP both had a RMSD of 0.24 eV whereas the RMSD for BP86 was 0.32 eV. This is far better than the RMSD for the same functionals using ATD-DFT where the errors can reach as much as 2 eV. The good performance of ΔSCF must be attributed to its well documented ability [50, 234] to afford reliable estimates of ionization potentials (IP) and electron affinities (EA) for standard GGA and hybrid functionals when orbital relaxation is taken into account. This is fully demonstrated for

N_2 in Table 5.4. Thus in the determination of singlet excitation energies as $\Delta E_S(\psi_v, \psi_r)$ = IP(N_2, ψ_v) $-$ ($-$EA(N_2^+, ψ_v, ψ_r, S)) we find the same accuracy for $\Delta E_S(\psi_v, \psi_r)$, IP($N_2$, ψ_v) and $-$EA(N_2^+, ψ_v, ψ_r, S). This is in contrast to ATD-DFT where IP(N_2, ψ_v) and $-$EA(N_2^+, ψ_v, ψ_r, S) carries errors of 5 eV and 3 eV, respectively, due to a different performance of $\tilde{V}_{XC}^{KS}(\vec{r})$ in the valence and Rydberg region. As a result $\Delta E_S(\psi_v, \psi_r)$ is determined with an accuracy of 2 eV due to error cancelations. For the length separated functionals LCBP86* (ω = 0.4) and LCBP86 (ω = 0.75) we find RMSDs of 0.24 eV and 0.32 eV respectively. This is not far from the accuracy obtained by ATD-DFT with fully optimized LC-functionals [86]. The computational effort involved for each ΔSCF (RSCF-CV-DFT) calculation on one excitation is similar to that of a ground-state SCF calculation.

Chapter 6

Application of Time-Dependent and Time-Independent Density Functional Theory to Electronic Transitions in Tetrahedral d^0 Metal Oxides

6.1 Introduction

Some of the first applications of DFT to chemical problems involved the studies of the electronic spectrum of permanganate and related tetraoxo complexes. It was demonstrated that the X_α method [13] and kindred schemes [14, 15, 251] based on the local density approximation (LDA) could reproduce the electronic spectrum of MnO_4^- and other tetraoxo complexes with a remarkable accuracy in contrast to $ab\ initio$ HF, and single and double configuration interaction (SDCI) calculations [12, 16, 252, 253]. The early DFT type calculations all employed a variational approach termed [13] ΔSCF in which an excitation was represented by the promotion from the $(i)^2$ ground-state configuration to the excited-state configuration ai and the associated excitation energy calculated as the difference between self-consistent Kohn-Sham energies of $(i)^2$ and ai. The ΔSCF scheme has been applied extensively to various systems [44, 45, 46] including the tetraoxo series [14, 15] with considerable success. It can be justified [254] for the first excited-state with a space and spin symmetry different from that of the ground-state. However, employing it to all excited states using the ground-state functional has been considered $ad\ hoc$ and unfounded in fundamental DFT theory [255]. In addition, not all transitions can be described by one Slater determinant representing a single orbital displacement $i \rightarrow a$ as it is assumed in ΔSCF. When the multi-determinantal nature of an excited-state is determined by symmetry, use can be made of schemes based on

the Slater sum rules [14, 15] or average of configuration considerations [18]. However, the multi-determinantal nature of a state resulting from near (accidental) degeneracies of two or more electronic configurations is not well represented by ΔSCF.

In Kohn-Sham DFT, the natural path to excited states would seem to be the ground-state response approach given the status of KS-DFT as a ground-state theory. Runge and Gross [53] have given the full time-dependent extension of the ground-state Kohn-Sham theory. Later, the time dependent density functional ground-state response theory (TD-DFT) [52] has been formulated that in principle should be able to describe excited-state properties without approximations. The exact TD-DFT requires the knowledge of the "true" ground-state functional as well as the frequency dependence of the energy response kernel related to this functional. In practice one has to resort to approximate ground-state functionals and neglect the frequency dependence of the kernel in what has now become known as the adiabatic TD-DFT approach [52, 57, 58, 59, 60, 225]. Over the past 20 years the ATD-DFT approach has become the workhorse in DFT based studies of excited states and its strengths and weaknesses are well documented [1, 66, 76, 83, 86, 87, 88, 89, 91, 256, 257, 258, 259, 260, 261, 262]. On the other hand progress beyond the adiabatic approximation has been slow although work in this direction is ongoing [65, 74, 75]. ATD-DFT has the distinct advantage over ΔSCF that it can deal with states that are multi determinantal. However, for the tetraoxo complexes of 3d metals the simulated spectra are not in as good agreement [263, 264] with experiment as ΔSCF [14, 15, 18] and the same can be said for many other transition metal complexes [265].

We have in previous studies been able to treat both Rydberg [79] and charge transfer transitions [50, 93] as well as other "difficult" cases such as $\pi \rightarrow \pi^*$ excitations in cyclic acenes [233] and cyanines [234] successfully even with local functionals provided that terms to all orders in U_{ai} were taken into account in our CV-DFT approach. However, this requires that U_{ai} is fully optimized [51] and that the basis of occupied $\{\psi_i;\ i$ = 1,$occ\}$ and virtual $\{\psi_a;\ a$ = 1,$vir\}$ ground-state orbital are allowed to relax (RSCF-CV(∞)-DFT) [49, 50]. It is our objective here to investigate how well RSCF-CV(∞)-

DFT is able to deal with the excitation energies for the series of tetraoxo complexes discussed here. We shall in our assessment compare to excitation energies from high level $ab\ initio$ wave function methods [17, 266, 267, 268, 269, 270, 271] as well as experiment.

6.2 Theoretical Details

6.2.1 Computational Method

In CV(2)-DFT or ATD-DFT/TDA the triplet excitation energy for a transition involving a single orbital replacement ($i \rightarrow a$) [234] can be seen from eq (5.1) whereas the singlet excitation energy is found in eq (5.2). The triplet-singlet separation energy in ATD-DFT/TDA can be expressed as [234]

$$\begin{aligned}\Delta E_{\mathrm{ST}}^{\mathrm{CV(2)}} = \Delta E_{\mathrm{S}}^{\mathrm{CV(2)}} - \Delta E_{\mathrm{T}}^{\mathrm{CV(2)}} =& 2K_{ai\bar{a}\bar{i}} \\ =& 2K_{aiai}^{\mathrm{C}} + 2K_{ai\bar{a}\bar{i}}^{XC} \\ \approx& 2K_{aiai}^{\mathrm{C}}. \end{aligned} \tag{6.1}$$

Here, $\approx$ indicates that $2K_{ai\bar{a}\bar{i}}^{XC}$ either is zero for HF or small for KS. Thus, $\Delta E_{\mathrm{ST}}^{\mathrm{CV(2)}}$ of eq (6.1) is determined by the Coulomb (but exchange type) integral $2K_{aiai}^{\mathrm{C}}$ that has the same form for HF and KS, and thus only depends indirectly on the functional through the shape of the orbitals as pointed out by Casida [52] and others [234, 262].

In RSCF-CV(∞)-DFT [49, 50] the triplet transition energy is defined in eq (2.38) and the corresponding singlet energy is given in eq (2.39). The singlet-triplet gap is given by [234]

$$\begin{aligned}\Delta E_{\mathrm{ST}}^{\mathrm{CV}(\infty)} =& \Delta E_{\mathrm{S}}^{\mathrm{CV}(\infty)} - \Delta E_{\mathrm{T}}^{\mathrm{CV}(\infty)} \\ =& -2K_{aaii} + 2K_{aa\bar{i}\bar{i}} + \Delta E_{\mathrm{Rel}}^{\mathrm{S}}(R) - \Delta E_{\mathrm{Rel}}^{\mathrm{T}}(R) \\ \approx& -2K_{aaii}^{XC} \end{aligned} \tag{6.2}$$

where $\approx$ represents the neglect of the terms $\Delta E_{\mathrm{Rel}}^{\mathrm{S}}(R) - \Delta E_{\mathrm{Rel}}^{\mathrm{T}}(R)$ and $2K_{aa\bar{i}\bar{i}}^{XC}$. For

functionals with a fraction, α $(0.0 \leq \alpha \leq 1.0)$, of HF-exchange we get

$$\begin{aligned}\Delta\tilde{E}_{\mathrm{ST}}^{\mathrm{CV}(\infty)} &= -2K_{aaii}^{XC(\mathrm{Hybrid})} \\ &= -2(1-\alpha)K_{aaii}^{XC} - 2\alpha K_{aaii}^{XC(\mathrm{HF})} \\ &= -2(1-\alpha)K_{aaii}^{XC} + 2\alpha K_{aiai}^{\mathrm{C}}. \end{aligned} \tag{6.3}$$

Thus, since from observations

$$0.0 < -K_{aaii}^{XC(\mathrm{KS})} < K_{aiai}^{\mathrm{C}}. \tag{6.4}$$

We find in general $\Delta\tilde{E}_{\mathrm{ST}}^{\mathrm{CV}(\infty)} < \Delta\tilde{E}_{\mathrm{ST}}^{\mathrm{CV}(2)}$ for pure DFT. However, as the fraction α of HF-exchange increases the difference decreases until pure HF with α = 1 where $\Delta\tilde{E}_{\mathrm{ST}}^{\mathrm{CV}(\infty)} = \Delta\tilde{E}_{\mathrm{ST}}^{\mathrm{CV}(2)}$. Thus, the expression for $\Delta\tilde{E}_{\mathrm{ST}}^{\mathrm{CV}(\infty)}$ is strongly functional dependent in contrast to $\Delta\tilde{E}_{\mathrm{ST}}^{\mathrm{CV}(2)}$ [234, 262].

6.2.2 Computational Details

We have carried out all DFT calculations by employing a developers version of the ADF 2012 program [181]. Our calculations employed a standard triple-ζ Slater type orbital (STO) basis with one (TZP) [235] or two (TZ2P) [235] sets of polarization functions for all atoms. Use was made of the LDA in the VWN parametrization [36] and the BP86 [37, 38]. We employed further the B3LYP and BHLYP, [152, 39] PBE [272] and PBE0 [273, 274] functionals. We have finally applied the length corrected functionals (LC). Here, LC combined with BP86 for ω = 0.40 is termed LCBP86* whereas the combination with ω = 0.75 is called LCBP86. All electrons were treated variationally without resorting to the frozen core approximation [181]. The parameter for the precision of the numerical integration was set to a (standard) value of 5.0. A special auxiliary STO basis was employed to fit the electron density in each cycle for an accurate representation of the exchange and Coulomb potentials [181] and relativistic effects were incorporated at the scalar ZORA level [221, 222].

6.2.3 Molecular Models

Experimental structures idealized to tetrahedral T_d symmetry were used throughout [18].

6.3 Results and Discussion

The study presented in this work include results for the 3d complexes MnO_4^-, CrO_4^{2-} and VO_4^{3-}, as well as their 4d congeners RuO_4, TcO_4^- and MoO_4^{2-}, and 5d homologues OsO_4, ReO_4^- and WO_4^{2-}. Considerations have been given to LDA, the GGAs; BP86 and PBE as well as the hybrids B3LYP, BHLYP, PBE0 and the length corrected functionals LCBP86* and LCBP86.

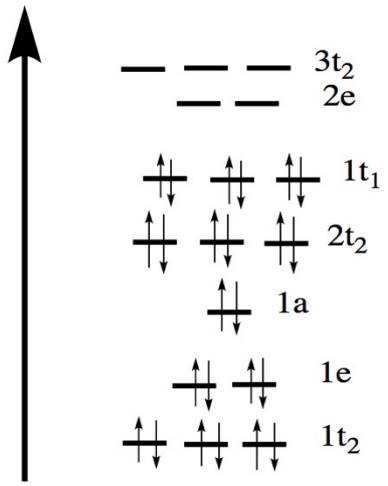

Figure 6.1: Orbital level diagram for d^0 tetraoxo complexes.

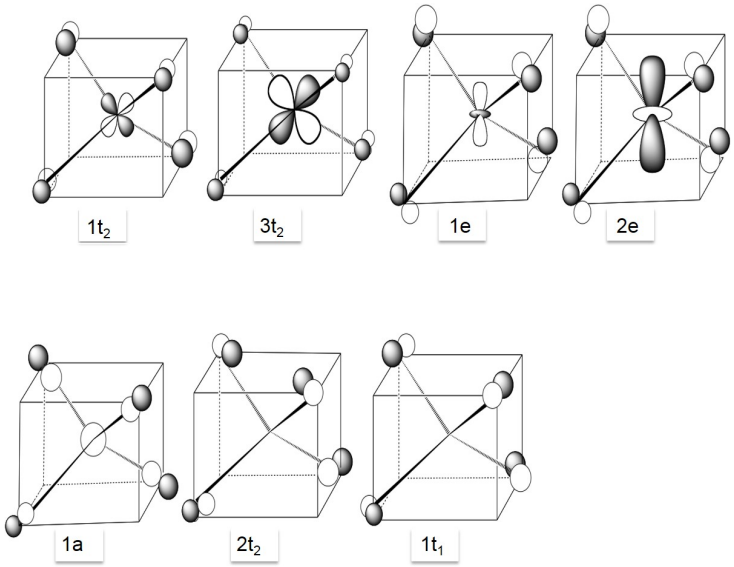

Figure 6.2: Frontier molecular orbitals of d^0 tetraoxo complexes.

Table 6.1: Calculated Excitation Energies[a,b] for MnO_4^- Based on $ab\ initio$ Wave Function Methods.

	HF[17]	SDCI[16]	SAC-CI[266]	EOM[269]	RAS-PT2[269]	CC2[270]	CC3[270]	Expt.[2]
	1.04	2.60	2.57	2.50	2.33	0.18	-0.34	2.40
	2.54	4.10	3.58	3.83	3.53	1.86	1.39	3.60
	2.94	4.50	3.72	4.03	4.20	–	–	4.10
MAE	1.20	0.39	0.24	0.15	0.08	2.00	2.49	
RMSD	1.19	0.37	0.19	0.13	0.08	1.99	2.48	

[a]Energies in eV. [b]First three dipole allowed transitions to singlet T_2 state

The valence excitations in tetraoxo complexes involve the removal of an electron from the $1t_1$, $2t_2$, $1a$, $1e$ and $1t_2$ levels represented by pure ligand orbitals ($1t_1$) or ligand dominated orbitals ($2t_2$, $1a$, $1e$ and $1t_2$) with a in-phase metal d-based orbitals component. The electron goes to a d-orbital with out-of-phase ligand contributions ($2e$, $3t_2$), Figures 6.1 and 6.2. The electronic spectrum of the prototypical tetraoxo system permanganate (MnO_4^-) has been studied extensively by both experimental and computational techniques.

The first $ab\ initio$ studies were on the HF level [12, 17, 252] followed by configuration interaction with both singles and doubles (CISD) [16, 253], symmetry adapted cluster-configuration interaction (SAC-CI) [266], equation of motion coupled cluster (EOM-CCSD) schemes [267, 268, 269, 270], self-consistent restricted active space (RASSCF or simply RAS) methods with a second-order perturbation theory (PT2) correction [269] as well as second- (CC2) and third-order (CC3) coupled cluster response theory [270]. We compare in Table 6.1 the calculated excitation energies for the three first dipole allowed transitions to singlet T_2 states with experiment. For the variational methods (HF, CISD, SAC-CI, RAS-PT2) we note a clear convergence towards the experimental values in going from the simplest (HF) to the most extensive $ab\ initio$ scheme (RAS-PT2). On the other hand, the two response methods CC2 and CC3 are seen to fail whereas CR-EOM-CCSD(T) [269] affords results quite similar to RAS-PT2 [269]. The excellent performance of RAS-PT2 testifies to the fact that static correlation is important for the description of MnO_4^- [251, 271]. The excited states of permanganate have also been studied by DFT schemes based on either variation or response theory. All the variational studies have so far adopted the ΔSCF approach [13]. In the earlier ΔSCF applications use was made of only the exchange part of the LDA functional (X_α) [14, 15] often in connection with the scattered wave approximation (SW-X_α) [275].

Table 6.2: Calculated Excitation Energies[a,b] for MnO_4^- Based on DFT Methods.

SW-Xα [275]	Xα[14, 15]	ΔSCF-LDA [18]	ATD-SAOP [276][,c]	ATD-B3LYP [269]	DFT/MRI [277]	Expt.[2]
2.30	2.48	2.71	3.08	2.81	2.74	2.40
3.30	3.96	4.02	4.12	3.88	4.21	3.60
4.70	4.15	4.22	5.01	4.41	4.80	4.10

[a]Energies in eV. [b]First three dipole allowed transitions to singlet T_2 state. [c]Long length corrected functional.

Later on, both exchange and correlation from the LDA functional have been included in the ΔSCF calculations [18].

The agreement with experiment [2, 278] is good as shown in Table 6.2. A more recent approach is the density functional theory based multi-reference configuration interaction (DFT/MRCI) scheme by Grimme and Waletzke [279]. It is similar to regular MRCI except that the diagonal terms are based on DFT. The off-diagonal terms are evaluated as in MRCI but scaled by a function that contains five global parameters obtained from a fit so as to reproduce a small set of experimental data. The calculated excitation energies [277] are quite good given that MnO_4^- was not in the training set, Table 6.2. Published response based DFT studies of permanganate are limited to the ATD-DFT calculations [263, 269, 276, 280, 281, 282]. They include [263, 281, 282] two investigations in which the full vibronic fine structure is simulated. The excitation energies afforded by ATD-DFT for MnO_4^-, in general, are too high when experimental structures are used, Table 6.2. We shall return to this point later. For both ΔSCF and ATD-DFT methods, there are several computational parameters that influence the calculated excitation energies aside from the use of a specific functional. One is the size of the basis set used. For the three lowest valence excitations involving transitions from $1t_1$, $2t_2$ to $2e$, $3t_2$ we find a TZ2P basis to be adequate, in line with previous observations [280]. The excitation energies from the corresponding smaller basis TZP differ typically by 0.05 eV from the TZ2P results and tend to be lower. Another factor is geometry. Usually optimized structures have somewhat longer M–O distances than experimental geometries [18, 269, 280]. We shall here make use of experimental structures in order to keep the number of computational variables at a minimum. Our choice typically leads to higher excitation energies (0.1 eV – 0.3 eV) than those obtained from optimized geometries. Many of the tetraoxo systems are anions with spectra observed in solution or in a host crystal. We find solvation in the form of COSMO [283, 284] to have a marginal influence on the calculated excitation energies (0.01 eV – 0.02 eV) for the transitions considered here as already noted by others [269, 282]. This is also confirmed by a recent ingenious experiment [278] where the permanganate spectrum was recorded

in vacuum and found to be blue-shifted by only 0.15 eV compared to solution. This is in contrast to the higher transitions from the ligands to diffuse metal s, p orbitals where solvation must be included in a proper description [280]. Since these higher transitions are not considered in this work, the comparisons are made with experimental results in solution only. For both ATD-DFT and RSCF-CV(∞)-DFT schemes, we have finally the choice of conducting calculations with or without the TDA [175]. Our calculations reveal that the use of the TDA has a minor influence on the calculated excitation energies with estimates that are typically slightly higher (0.05 eV – 0.10 eV) than those from a full calculation.

Table 6.3 displays root mean square deviations (RMSD) between the first three experimental dipole allowed transitions and the corresponding values calculated by ATD-DFT with a TZ2P basis. In total, of nine complexes were considered.

Table 6.3: RMSDs for Tetraoxo Excitation Energies based on ATD-DFT and a TZ2P basis set.[a,b,c,d,e]

Complex	LDA	BP86	PBE	B3LYP	BHLYP	PBE0	LCBP86*	LCBP86
MnO_4^-	0.50	0.51	0.52	0.44	0.39	0.48	0.42	0.34
CrO_4^{2-}	0.23	0.24	0.31	0.39	0.75	0.54	0.50	0.64
VO_4^{3-}	0.10	0.12	0.13	0.44	1.04	0.59	0.47	0.87
RuO_4	0.38	0.39	0.39	0.32	0.22	0.34	0.33	0.26
TcO_4^-	0.13	0.12	0.26	0.22	0.43	0.29	0.27	0.55
MoO_4^{2-}	0.21	0.20	0.20	0.12	0.64	0.23	0.22	0.63
OsO_4	0.34	0.37	0.38	0.34	0.32	0.38	0.37	0.39
ReO_4^-	0.33	0.31	0.30	0.16	0.26	0.14	0.12	0.28
WO_4^{2-}	0.56	0.52	0.51	0.19	0.36	0.09	0.08	0.40
Average 3d[f]	0.28	0.29	0.32	0.42	0.73	0.54	0.46	0.62
Average 4d+5d[g]	0.32	0.31	0.34	0.24	0.36	0.26	0.25	0.41
Total average 3d[h]	0.30	0.31	0.33	0.31	0.49	0.37	0.33	0.49

[a]Root mean square deviation. [b]The reference is the observed vertical excitation energies for the three first dipole allowed transitions. [c]For MoO_4^{2-} and WO_4^{2-} only, the first two experimental transitions are available. [d]Deviation are in eV. [e]No TDA was applied. [f]Average of the three 3d complexes. [g]Average of the six 4d and 5d complexes. [h]Average over all complexes.

Table 6.4: RMSDs for Tetraoxo Excitation Energies based on RSCF-CV(∞)-DFT and a TZ2P basis set.[a,b,c,d,e]

Complex	LDA	BP86	PBE	B3LYP	BHLYP	PBE0	LCBP86*	LCBP86
MnO_4^-	0.41	0.32	0.33	0.15	0.62	0.19	0.24	0.37
CrO_4^{2-}	0.40	0.31	0.34	0.09	0.55	0.04	0.22	0.32
VO_4^{3-}	0.25	0.14	0.16	0.07	0.18	0.14	0.27	0.37
RuO_4	0.32	0.28	0.28	0.21	0.44	0.22	0.19	0.31
TcO_4^-	0.10	0.13	0.13	0.25	0.13	0.29	0.27	0.17
MoO_4^{2-}	0.14	0.23	0.23	0.06	0.22	0.18	0.13	0.34
OsO_4	0.53	0.51	0.50	0.27	0.39	0.31	0.21	0.26
ReO_4^-	0.36	0.43	0.43	0.14	0.25	0.16	0.14	0.16
WO_4^{2-}	0.43	0.51	0.51	0.14	0.11	0.07	0.11	0.16
Average 3d[f]	0.35	0.26	0.28	0.10	0.45	0.12	0.24	0.35
Average 4d+5d[g]	0.31	0.34	0.34	0.19	0.27	0.22	0.19	0.24
Total average 3d[h]	0.33	0.31	0.32	0.16	0.34	0.18	0.21	0.28

[a]Root mean square deviation. [b]The reference is the observed vertical excitation energies for the three first dipole allowed transitions. [c]For MoO_4^{2-} and WO_4^{2-} only, the first two experimental transitions are available. [d]Deviation are in eV. [e]No TDA was applied. [f]Average of the three 3d complexes. [g]Average of the six 4d and 5d complexes. [h]Average over all complexes.

In Table 6.4 are given the same data for the RSCF-CV(∞)-DFT method. Table 6.5 provides actual calculated excitation energies based on ATD-DFT and RSCF-CV(∞)-DFT in comparison with experiment for MnO_4^- and TcO_4^-. Here the former is a representative for the 3d complexes whereas the latter typifies the heavier congeners. For MnO_4^- the ATD-DFT energies are uniformly too high compared to experiment. This is a general trend for the 3d complexes where the RMSDs calculated from the ATD-DFT results on average range from 0.3 eV for local functionals to 0.7 eV for BHLYP with the largest fraction of HF exchange. In the case of RSCF-CV(∞)-DFT, the MnO_4^- energies are somewhat too high (0.2 eV) for the local functionals and too low for BHLYP (0.3 eV) whereas B3LYP affords the best agreement with experiment. These RSCF-CV(∞)-DFT trends are typical for all the 3d complexes where the average RMSDs are 0.25 eV – 0.3 eV for GGAs, 0.1 eV for B3LYP and 0.45 eV for BHLYP.

ATD-DFT is seen to fare better among the heavier tetraoxo systems than the 3d homologous as exemplified by TcO_4^-. On average the three functionals B3LYP, PBE0 with an intermediate fraction of HF exchange and LCBP86* have the lowest RMSD of 0.2 eV whereas the local functionals (LDA, BP86, BPE) and BHLYP with the highest HF fraction and LCBP86 have a somewhat larger RMSD of 0.3 eV. Interestingly enough, the heavier tetraoxo systems reveal the same trend among the different functionals for RSCF-CV(∞)-DFT with a RMSD of 0.2 eV for B3LYP, PBE0 and LCBP86* and 0.3 eV for the remaining functionals. Thus, for the heavier tetraoxo complexes RSCF-CV(∞)-DFT does not constitute a clear improvement over ATD-DFT, which already is quite good. However, for the 3d complexes where the calculated ATD-DFT energies are too high, the RSCF-CV(∞)-DFT scheme seems to fare better at least for B3LYP.

Table 6.5: Calculated Excitation Energies based on RSCF-CV(∞)-DFT and ATD-DFT, for MnO_4^- and TcO_4^-.[a,b]

Method	LDA	BP86	PBE	B3LYP	BHLYP	PBE0	LCBP86*	LCBP86	Expt.
MnO_4^-									
ATD-DFT	2.86	2.87	2.87	2.88	2.98	2.92	2.81	2.82	2.40[2]
	3.93	3.93	3.94	3.96	3.93	4.02	3.99	3.96	3.60
	4.76	4.77	4.78	4.57	4.23	4.58	4.55	4.29	4.10
RSCF-CV(∞)-DFT	2.67	2.65	2.65	2.45	2.12	2.52	2.68	2.62	2.40
	3.96	3.86	3.86	3.63	2.64	3.71	3.85	3.99	3.60
	4.66	4.52	4.54	3.85	3.72	3.83	3.93	4.16	4.10
TcO_4^-									
ATD-DFT	4.48	4.48	4.47	4.57	4.74	4.62	4.61	4.82	4.35[285]
	5.19	5.20	5.20	5.40	5.71	5.49	5.48	5.87	5.10
	6.45	6.47	6.17	6.65	6.76	6.74	6.68	6.89	6.60
RSCF-CV(∞)-DFT	4.51	4.50	4.49	4.60	4.33	4.63	4.57	4.46	4.50
	5.01	4.93	4.93	5.37	5.15	5.49	5.43	5.27	5.10
	6.61	6.59	6.53	6.38	6.38	6.46	6.36	6.38	6.60

[a]Energies in eV. [b]TZ2P basis without use of the TDA.

Table 6.6: Comparisons between Multiplet Splittings Calculated by Different Methods for MnO_4^- and TcO_4^-.[a,b]

	MnO_4^-					MnO_4^-				
Method	ATD-DFT	RAS-PT2[270]	SAC-CI[270]	RSCF[c]	Expt.[2]	ATD-DFT	RAS-PT2[270]	SAC-CI[270]	RSCF[c]	Expt.[285]
Singlet										
$1T_1$	2.35	1.93	2.18	1.65		4.17	3.84	3.83	3.98	
$1T_2$	2.88	2.33	2.57	2.45	2.40	4.57	4.19	4.28	4.60	4.35
$2T_1$	3.74	3.39	3.33	3.18		4.80	4.66	4.61	4.65	
$2T_2$	3.94	3.53	3.58	3.63	3.60	5.40	5.08	5.29	5.37	5.10
$1E$	4.10	3.90	3.41	3.73		5.41	5.29	4.98	5.15	
$3T_1$	4.22	3.93	4.12	3.81		6.22	5.53	6.42	6.45	
$3T_2$	4.57	4.20	3.72	3.85	4.10	6.65	6.07	6.20	6.38	6.60
$1A_2$	4.16	3.89	4.46	4.21		6.43	6.04	6.54	6.78	
RMSD	0.44	0.05	0.24	0.15		0.32	0.26	0.25	0.25	

[a]Energies in eV. [b]TZ2P basis without use of the TDA. [c]RSCF-CV(∞)-DFT calculation.

The RSCF-CV(∞)-DFT scheme is in principle able to resolve not only the T_2 excited-state energy terms but all multiplets. We compare in Table 6.6 multiplet energies based on RSCF-CV(∞)-DFT and ATD-DFT with those obtained from the high-level wave function methods [269] RAS-PT2 and SAC-CI for MnO_4^- and TcO_4^-. Here the DFT calculations made use of B3LYP. The first excitation in MnO_4^- and TcO_4^- is dominated by the $1t_1 \rightarrow 2e$ orbital transition which gives rise to the $1T_1$ and $1T_2$ multiplets. All methods find the order $1T_1 < 1T_2$ which is in agreement with experiment [286]. A rough experimental estimate [285] of 0.5 eV is also in reasonable agreement with the calculated splittings. Here, RSCF-CV(∞)-DFT affords the largest estimate of 0.8 eV. The sizes of the DFT splittings are strongly functional dependent and tend to increase with the fraction of HF-exchange. The second excitation has a large contribution from the $2t_2 \rightarrow 2e$ orbital transition. It gives rise to the $2T_1$ and $2T_2$ terms that again unanimously are calculated to have the order $2T_1 < 2T_2$. There is no experimental information available. The third excitation is in part due to the $1t_1 \rightarrow 3t_2$ orbital transition with the multiplets $1E$, $3T_1$, $3T_2$, and $1A_2$. Here $1E$ is in all cases of lowest energy whereas $1A_2$ is at (or near) the top. For $3T_1$ and $3T_2$ the order $3T_1 < 3T_2$ is observed for all methods in the MnO_4^- case as well as ATD-DFT and RAS-PT2 in TcO_4^-, whereas it is reversed for SAC-CI and RSCF-CV(∞)-DFT for the same molecule and this is also the order obtained for CR-EOM-CCSD(T) [269]. Again, experimental data are not available. It is obvious that more work on better-characterized systems has to be carried out to assess the ability of RSCF-CV(∞)-DFT to resolve multiplets.

To date the triplet T_2 spin multiplets have eluded observation in spite of many attempts to characterize these presumably very short lived states [287]. For ATD-DFT and RSCF-CV(∞)-DFT, the triplet-singlet splittings are in most cases calculated to be somewhat larger for the more compact 3d complexes such as permanganate than the larger congeners such as TcO_4^-, Table 6.7. It follows from eq (5.1), (5.2) and (6.1) that the ATD-DFT/TDA splitting for a $i \rightarrow a$ transition is given by $\Delta E_{\mathrm{ST}}^{\mathrm{CV(2)}} = 2K_{aiai}^{\mathrm{C}}$ where K_{aiai}^{C} is a coulomb integral defined in eq (2.27). This expression is only indirectly functional dependent through the shape of the orbitals a, i. However, we clearly

Table 6.7: Calculated Triplet-Singlet Energies for the first three T_2 states in MnO_4^- and TcO_4^- based on RSCF-CV(∞)-DFT and ATD-DFT.[a,b]

Method	State	LDA	BP86	PBE	B3LYP	BHLYP	PBE0
MnO_4^-							
ATD-DFT	$1T_2$	0.94	0.94	0.94	1.40	2.08	1.56
	$2T_2$	0.55	0.56	0.56	0.85	1.24	0.93
	$3T_2$	0.82	0.80	0.80	0.91	1.20	0.90
RSCF-CV(∞)-DFT	$1T_2$	0.61	0.75	0.73	1.21	1.81	1.36
	$2T_2$	0.46	0.53	0.51	0.82	0.96	0.92
	$3T_2$	0.60	0.51	0.51	0.60	0.55	0.62
TcO_4^-							
ATD-DFT	$1T_2$	0.89	0.88	0.87	1.16	1.72	1.24
	$2T_2$	0.82	0.85	0.84	1.09	1.47	1.17
	$3T_2$	0.71	0.69	0.67	0.62	0.54	0.60
RSCF-CV(∞)-DFT	$1T_2$	0.61	0.74	0.72	1.17	1.34	1.10
	$2T_2$	0.48	0.55	0.53	0.84	1.28	0.92
	$3T_2$	0.46	0.44	0.43	0.58	0.66	0.53

[a]Energies in eV. [b]TZ2P basis without use of the TDA.

see this dependence in Table 6.7 where $\Delta E_{\text{ST}}^{\text{CV(2)}} = 2K_{aiai}^{\text{C}}$ increases with the fraction (α) of HF-exchange. The dependence reflects the decline in covalency with a growing α which leads to both M–O bonding (i = $2t_2$, $1a$, $1e$ and $1t_2$) and anti-bonding (a = $2e$, $3t_2$) orbitals being increasingly polarized towards M or O [251]. Similar trends are seen for calculations without the TDA. The triplet-singlet separation in RSCF-CV(∞)-DFT/TDA is according to eq (6.3) given by $\Delta\tilde{E}_{\text{ST}}^{\text{CV}(\infty)} = -\,2(1-\alpha)K_{aaii}^{XC} + 2\alpha K_{aiai}^{\text{C}}$ for a $i \rightarrow a$ transition. Here α is again the HF fraction, K_{aiai}^{C} is the Coulomb integral discussed above and $K_{aaii}^{XC(\text{KS})} = K_{aiai}^{XC(\text{KS})}$ is the local exchange correlation term defined in eq (2.29). Since from experience $0.0 < -K_{aaii}^{XC(\text{KS})} < K_{aiai}^{\text{C}}$, we find that $\Delta\tilde{E}_{\text{ST}}^{\text{CV}(\infty)} < \Delta\tilde{E}_{\text{ST}}^{\text{CV(2)}}$ for the local functionals with α = 0, Table 6.7. The fact that $\Delta\tilde{E}_{\text{ST}}^{\text{CV}(\infty)} < \Delta\tilde{E}_{\text{ST}}^{\text{CV(2)}}$ is in part responsible for the observation that ATD-DFT affords excitation energies that are higher than RSCF-CV(∞)-DFT. As we add HF exchange and increase α, $\Delta\tilde{E}_{\text{ST}}^{\text{CV}(\infty)}$ should approach $\Delta\tilde{E}_{\text{ST}}^{\text{CV(2)}}$. However, it follows from Table 6.7 that the two have not yet converged for BHLYP with α = 0.50.

6.4 Concluding Remarks

We have for the first time probed the ability of our newly developed RSCF-CV(∞)-DFT scheme to describe excited states of TM complexes. Use was made of the tetrahedral d^0 metal oxides as the first benchmark series since the tetra oxides have a long history as a challenging testing ground for new methods due to their complex electronic structure. We have investigated nine systems with three members from each transition series using eight different functionals and compared the results to findings based on ATD-DFT and experiment. We find for the 3d systems MnO_4^-, CrO_4^{2-}, and VO_4^{3-} that RSCF-CV(∞)-DFT affords excitation energies in better agreement with experiment than ATD-DFT for each of the functionals discussed here. The best agreement (RMSD = 0.1 eV) was obtained with the B3LYP and PBE0 hybrid functionals holding relatively modest HF exchange contributions of 20 % and 25 %, respectively. Local functionals fared slightly worse whereas a substantial increase in HF exchange as in BHLYP leads to sizable deviations (RMSD = 0.45 eV). By comparison, the ATD-DFT method tend to provide excitation energies for the 3d complexes that are uniformly too high, Table 6.3. For the heavier 4d and 5d congeners we find that RSCF-CV(∞)-DFT and ATD-DFT performs equally well with the smallest RMSDs of 0.2 eV encountered for B3LYP and PBE0. Work is now under way to benchmark RSCF-CV(∞)-DFT for other transition metal systems where accurate observations and high-level calculations are available. The benchmarking will also involve other properties such as the first-order change in density with respect to U that represents the transition density as well as the higher-order change that express the "active" charge rearrangement. Here direct comparison can be made to ATD-DFT that also provides both types of density change. However, in contrast to ATD-DFT, but in common with ΔSCF, our RSCF-CV(∞)-DFT scheme also affords orbital relaxation in response to the "active" density change. Thus in a transition represented by the orbital replacement $t_1 \rightarrow 2e$ the "active" change in density would be given by $\Delta\rho_{\text{active}} = 2e2e - 1t_1 1t_1$ which represents a charge transfer from the ligands to the d-orbitals making the metal center more electron rich. How-

ever, as shown previously in connection with ΔSCF, relaxation of the other orbitals tends to reduce or completely reduce the charge build-up on the metal. Thus, we hope that RSCF-CV(∞)-DFT will provide more realistic information about the total charge rearrangement involved in an excitation than ATD-DFT.

Chapter 7

Assessing the CV-DFT Method for Octahedral Transition Metal Complexes

7.1 Introduction

Electronic excitation within transition metal (TM) complexes poses theoretical problems even for the simpliest system. This is due to the complicated electronic structure of TM complexes [277]. This make TM complexes suitable as test sets for testing the performance of newly developed methods. Here, the emphasis is placed on charge transfer (CT) excitations in transition metal complexes. There are some experimental [288, 289] data for CT excitation energy in octahedral TM complexes as well as some high-level $ab\,initio$ calculation [290, 291, 292, 293, 294, 295, 296]. Work carried out by some high-level $ab\ initio$ methods towards the analysis of CT excitations in some octahedral transition metal complexes [269, 290, 291, 292, 293, 296, 297] affords highly accurate results, although at a high computational cost. Therefore, they are not suitable for routine calculations for large systems (20 or more atoms). A less computationally expensive alternative would be more practical.

With the success of Density Functional Theory (DFT) as a ground-state theory due to its reasonable compromise between low computational cost and accuracy, attempts have been made at adapting the theory for excited-state studies. A number of different methods have been developed within the framework of DFT, the most widely used amongst these methods is the Time-Dependent DFT (TD-DFT) [52, 53, 57, 58, 59, 60, 225]. Extensive benchmarking of TD-DFT revealed its insufficiency at describing Rydberg [1, 61, 62, 63] and Charge Transfer (CT) [64, 65, 66, 67, 68, 69, 70, 71, 72, 73] excitations. Attempts have been made at developing XC functionals with the correct

short range as well as medium and long range behaviour [1, 67, 68, 69, 70, 73, 84, 86, 89, 91, 237, 298, 299, 300, 301, 302, 303, 304, 305, 306, 307, 308, 309, 156, 310, 311] and finding a new theoretical approach within the DFT formalism for describing excited states [49, 279, 312, 313, 314, 315, 316].

Some of the difficulties encountered in the application of TD-DFT for Rydberg and CT excitations are to an extent resolved by these "tuned" functionals [1, 61, 62, 63, 64, 71, 72, 83, 84, 80, 85, 86, 87, 88, 89, 90], however, the most "tuned" of these functionals have high computational cost. A way to overcome this problems lies beyond the linear response approach, a variational approach proposed by Ziegler *et al.* that involves mixing virtual orbitals into each occupied orbital [47, 48, 49, 50, 51, 85, 232]. The resulting approach (RSCF-CV-DFT) incorporates the adiabatic TD-DFT (ATD-DFT) and ΔSCF [13, 14, 43, 44, 45, 46] as special cases.

The performance of RSCF-CV-DFT method in Rydberg (see Chapter 5) [317] and CT [50, 93] excitations have previously been assessed, however, the CT excitations were initially carried out on organic molecules. Additionally, we have previous analyzed the performance of the RSCF-CV-DFT [47, 49, 232] method for excitation in transition metal tetraoxo complexes [99], see Chapter 6. The method has so far shown very good performance for excitations that are poorly treated by TD-DFT and performs comparably well for those that are well treated by TD-DFT even at the RSCF-CV-DFT/LDA [36] level of theory. CT transitions within the octahedral transition metal complexes form part of the next test set for our newly developed orbital relaxed constricted variational DFT (RSCF-CV-DFT) method.

7.2 Theoretical Details

7.2.1 Computational Details

All calculations were carried out by a developers' version of the ADF 2012 program [181]. We employed a standard triple-ζ basis set with two polarization functions for all atoms (TZ2P) [235]. The functionals used in this work include the local density

approximation in the VWN parametrization [36], the BP86 generalized gradient approximation (GGA) with the Perdew correlation [38] part and the Becke exchange [37] part, PBE [272], and the hybrid functionals B3LYP (20 % Hartree-Fock exchange), BH-LYP (50 % Hartree-Fock exchange) by Becke [39] with the correlation part by Lee $et\ al.$ [152] and PBE0 (25 % Hartree-Fock exchange) [273, 274]. We have, additionally, in this work employed length corrected (LC) functionals [86, 87, 236, 237, 238].

We made use of $w(\omega, r_{12})$ values with ω = 0.40 and ω = 0.75, details are provided in Chapter 5 and elsewhere [79, 99]. The BP86 functional was used in conjunction with the LC; the LC combined with BP86 for ω = 0.40 is called LCBP86* whilst the combination with ω = 0.75 is termed LCBP86.

Use was not made of frozen core approximation [181]; all electrons were treated variationally. A special auxiliary STO basis was used to fit the electron density for an accurate representation of the exchange and coulomb potentials in each cycle [181]. The precision of the numerical integration was set to the standard value of 5.0.

7.2.2 Molecular Models

We have studied three octahedral transition metal complexes with our newly implemented RSCF-CV(∞)-DFT method. Experimental or geometry optimized structures were used in this work. Experimental geometries were obtained for $Cr(CO)_6$ [291], $[Fe(CN)_6]^{4-}$ [292], and geometry optimized structures where obtained for ($[Fe(CN)_5(py)]^{3-}$, py = pyridine) [293], Figure 7.1.

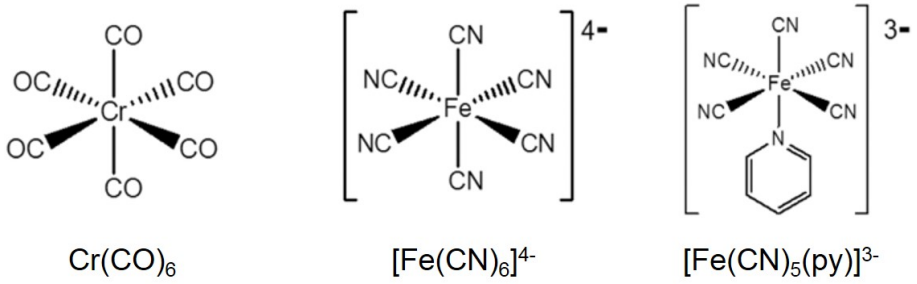

Figure 7.1: Structures of the complexes studied.

7.3 Results and Discussion

We present here, the electronic excitation energies of the octahedral TM complexes afforded by our CV-DFT method with a wide variety of functionals. The analyses will be primarily focused on $Cr(CO)_6$ and $[Fe(CN)_6]^{4-}$ where experimental excitation energies are available; otherwise, the comparison is made with a high-level $ab\ initio$ wavefunction method. The density change associated with the electronic transition affords a way to determine the type of transition under study. We shall, however, return to this point shortly.

We start first with $Cr(CO)_6$, the RSCF-CV(∞)-DFT results are displayed in Table 7.1. In its ground-state, the HOMO is made up of the triply degenerate $2t_{2g}$ orbital set and the LUMO and LUMO+1 comprise the $9t_{1u}$ and the $2t_{2u}$ sets, respectively. The experimental spectrum has previously been assigned [291, 318] and we are here interested in accurately predicting the excitation energies. Recent TD-DFT calculations carried out by Gray $et\ al.$ [319] showed that the energy difference between the gas phase calculations and the calculation carried out in solution (acetonitrile in this case) is $\sim$0.05 eV, and an energy difference of $\sim$0.06 eV between the experimental bands in vapor and in solution. Additionally, the absorption spectra remains largely unchanged irrespective of the medium used [288].

The two intensely absorbing states (metal to ligand charge transfer (MLCT) states) are of interest here. The first MLCT state (1^1T_{1u}, $2t_{2g} \rightarrow 9t_{1u}$) is well described by TD-DFT, however, the second state (2^1T_{1u}, $2t_{2g} \rightarrow 2t_{2u}$) is overestimated and the calculated excited states are functional dependent [319, 320, 321]. Finally, Daniel $et\ al.$ [322] showed that calculations carried out on geometry optimized structures in general afford lower excitation energies than those carried out with the experimental structure, although there are a hand full of exceptions. The difference is between $\sim$0.01 to $\sim$0.5 eV.

To reduce the variables to consider, the calculations on $Cr(CO)_6$ were carried out with the experimental structures. We show in Table 7.1 the results of the excitation

energies carried with the RSCF-CV(∞)-DFT method. Comparison is made to the experimental energies where available, otherwise, use is made of the RASPT2 [291] and CASPT2 [288] results. Also shown in the table is the root-mean-square deviations (RMSDs) calculated with-respect-to the two available experimental excitation energies. We see, in general, a good performance by the RSCF-CV(∞)-DFT method.

The results afforded by RSCF-CV(∞)-DFT/LDA (0.02) gives the best performance followed by PBE (0.03) and BP86 (0.04), whilst BHLYP and LCBP86 trail at 0.54 eV. The calculated excitation energies are not severely functional dependent, except in the 1^1T_{1g}, 2^1T_{1u} and 1^3T_{1g} states. Our method shows performance identical to the TD-DFT/B3LYP [277] performance even for the LDA and GGAs, see Table E.1 in appendix E.

The errors in the calculated excitation energies increase from B3LYP to BHLYP for the hybrid functions, Table 7.2. There is a correlation between the percentage of exact exchange and the error in the calculated energies, BHLYP which has the highest exact exchange (50 %) gave the highest RMSD of 0.54 eV. As for the LC functionals, LCBP86 which is closer to the BP86 functional gave an RMSD of 0.54 eV and the LCBP86* functional which is closer to HF an RMSD of 0.27 eV.

Table 7.1: Calculated Excitation Energies[a] for $Cr(CO)_6$ based on the RSCF-CV(∞)-DFT method.

STATE	RASPT2[b]	LDA	BP86	PBE	B3LYP	PBE0	BHLYP	LCBP86*[c]	LCBP86[d]	Expt.[e]
Singlet										
1^1T_{1g}(MC)	4.98	5.33	5.14	5.17	4.85	5.25	4.52	4.78	4.97	
1^1T_{1u}(MLCT)	4.50	4.45	4.39	4.40	4.48	4.62	4.68	4.61	4.37	4.44
2^1T_{1u}(MLCT)	5.42	5.46	5.47	5.47	5.73	5.93	6.20	6.23	5.85	5.48
Triplet										
1^3T_{1g}(MC)	4.28[f]	4.72	4.88	4.91	4.54	4.62	4.15	4.18	4.49	
1^3T_{2g}(MC)	4.64[f]	4.63	4.59	4.60	4.39	4.45	4.17	4.45	4.59	
RMSD	0.06	0.02	0.04	0.03	0.18	0.34	0.54	0.54	0.27	

[a]Energies in eV. [b] Ref. [290]. [c]Represents LC functional combined with BP86 with ω = 0.75. [d]Refers to LC functional combined with BP86 using ω = 0.4. [e]Ref. [288]. [f]Ref. [291]

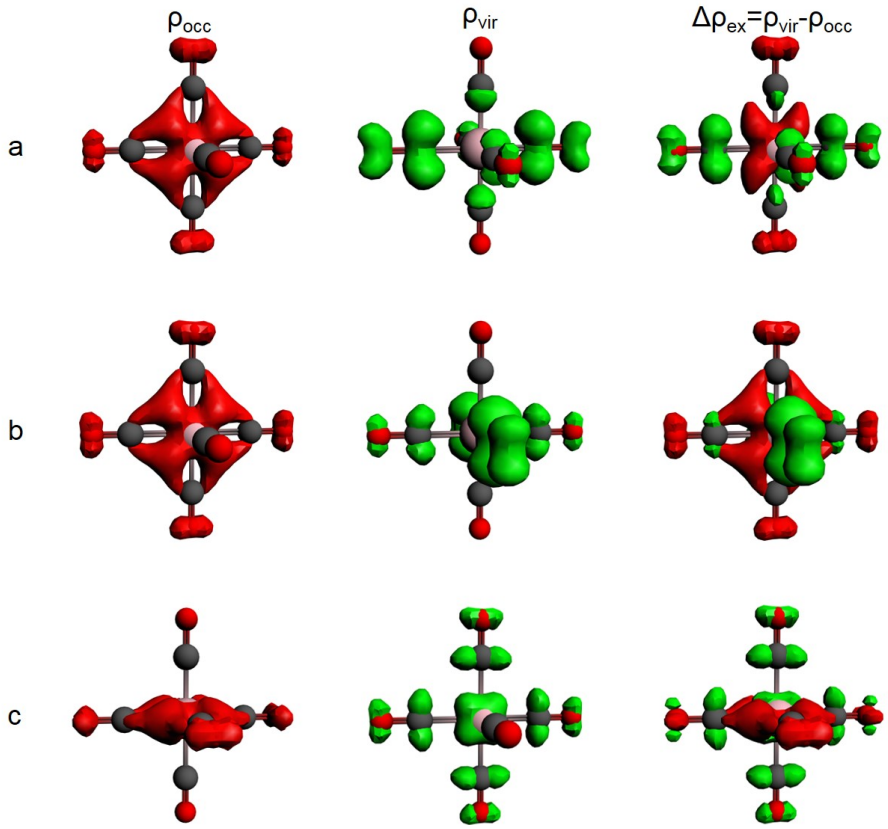

Figure 7.2: $\Delta\rho$ associated with the $CrCO_6$, red signifies depletion and green shows accumulation of density. (a) The density change associated with the 1^1T_{1u} state. (b) exemplify the density redistribution associated with the 2^1T_{1u} state. (c) Densities accompanying the calculated 1^1T_{1g} state. (a) and (b) are MLCT-type transitions and (c) is an example of MC-type transition.

Table 7.2: Calculated IP and EA[a] for the two MLCT excitations in $Cr(CO)_6$ based on the RSCF-CV(∞)-DFT method.

STATE	LDA	BP86	PBE	B3LYP	PBE0	BHLYP	LCBP86*[b]	LCBP86[c]	Expt.[d]
IP($2t_{2g}$)	9.29	8.99	8.90	8.62	8.65	8.14	8.57	8.85	8.20
EA($Cr(CO)_6^+$, $2t_{2g}$, $9t_{1u}$, S)	-4.84	-4.60	-4.50	-4.14	-4.03	-3.46	-3.96	-4.48	-3.76
EA($Cr(CO)_6^+$, $2t_{2g}$, $2t_{2u}$, S)	-3.83	-3.52	-3.43	-2.89	-2.72	-1.91	-2.34	-3.00	-2.72

[a]Energies in eV. [b]Represents LC functional combined with BP86 with ω = 0.75. [c]Refers to LC functional combined with BP86 using ω = 0.4.
[d]Ref. [323].

To determine the source of the error, the excitation energy is decomposed into the ionization potential (IP) of the complex and electron affinity (EA) of the cation resulting from the ionization. The expression for IP obtained by removing an electron from $2t_{2g}$ is given by

$$\begin{aligned} \text{IP}(\text{Cr(CO)}_6) =& \text{IP}(\text{Cr(CO)}_6, 2t_{2g}) \\ =& -\epsilon_{2t_{2g}} + \frac{1}{2}K_{2t_{2g}2t_{2g},2t_{2g}2t_{2g}} + \tilde{\Delta}E_{\text{Rel}}^{\text{IP}} \end{aligned} \tag{7.1}$$

the accompanying electron capture by the $9t_{1u}$ or $2t_{2u}$ orbital is given as

$$\begin{aligned} \text{EA}(\text{Cr(CO)}_6^+, \text{S}) =& \text{EA}(\text{Cr(CO)}_6^+, 2t_{2g}, 9t_{1u}, \text{S}) \\ =& \epsilon_{9t_{1u}} + \frac{1}{2}K_{9t_{1u}9t_{1u},9t_{1u}9t_{1u}} - 2K_{9t_{1u}9t_{1u},2t_{2g}2t_{2g}} \\ &+ K_{2\bar{t}_{2g}2\bar{t}_{2g},9t_{1u}9t_{1u}} + \tilde{\Delta}E_{\text{Rel}}^{\text{EA,S}} \end{aligned} \tag{7.2}$$

and the corresponding triplet expression is given by

$$\begin{aligned} \text{EA}(\text{Cr(CO)}_6^+, \text{T}) =& \text{EA}(\text{Cr(CO)}_6^+, 2t_{2g}, 9t_{1u}, \text{T}) \\ =& \epsilon_{9t_{1u}} + \frac{1}{2}K_{9t_{1u}9t_{1u},9t_{1u}9t_{1u}} \\ &- K_{9\bar{t}_{1u}9\bar{t}_{1u},2t_{2g}2t_{2g}} + \tilde{\Delta}E_{\text{Rel}}^{\text{EA,T}}. \end{aligned} \tag{7.3}$$

From eqs (7.1), (7.2) and (7.3), we are able to analyze in depth the errors present in the excitation energy for Cr(CO)_6) where the experimental IP(Cr(CO)_6)) and EA(Cr(CO)_6^+) are available.

Table 7.3: Calculated Excitation Energies[a] for $[Fe(CN)_6]^{4-}$ based on the RSCF-CV(∞)-DFT method.

STATE	CASPT2[b]	LDA	BP86	PBE	B3LYP	PBE0	BHLYP	LCBP86*[c]	LCBP86[d]	Expt.[e]
Singlet										
1^1T_{1g}(MC)	3.60	4.17	3.72	3.75	3.42	3.35	3.04	3.35	3.64	3.80–3.94
3^1T_{1u}(MLCT)	–	5.57	5.57	5.64	6.10	6.44	–	–	6.34	5.69–5.89
4^1T_{1u}(MLCT)	–	5.83	5.80	5.72	6.25	6.63	–	–	6.93	6.20
1^1T_{2g}(MC)	4.33	4.05	3.74	4.12	4.47	4.46	4.47	4.14	4.37	4.43–4.77
Triplet										
1^3T_{1g}(MC)	2.67	3.60	3.39	3.41	2.98	2.90	2.49	2.56	2.93	2.94
RMSD	0.20[f]	0.42	0.41	0.33	0.25	0.44	0.40[f]	0.29[f]	0.44	

[a]Energies in eV. [b] Ref. [292]. [c]Represents LC functional combined with BP86 with ω = 0.75. [d]Refers to LC functional combined with BP86 using ω = 0.4. [e]Ref. [289]. [f]Calculated with 3 excitation energies.

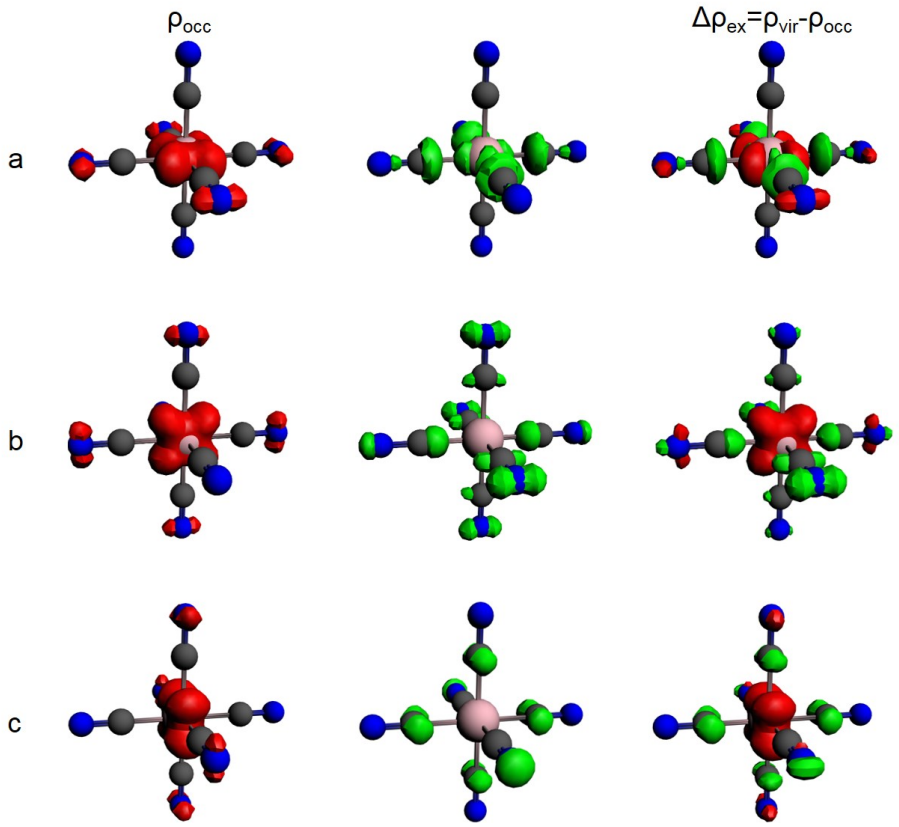

Figure 7.3: $\Delta\rho$ associated with the $Fe(CN)_6^{4-}$. (a) The density change associated with the 1^1T_{1g} state. (b) exemplify the density redistribution associated with the 3^1T_{1u} state. (c) Densities accompanying the calculated 3^1T_{1u} state. (a) is an example of MC-type transition, (b) and (c) are MLCT-type transitions. Red signifies loss and green shows gain in density.

The numerical values of the integrals $K_{2t_{2g}2t_{2g},2t_{2g}2t_{2g}}$ and $K_{9t_{1u}9t_{1u},9t_{1u}9t_{1u}}$ decrease on going from the local to the hybrid functionals, and they are zero for HF. The IPs decreases from LDA and approaches the experimental IP for the functionals with some percentage of HF exchange and the LC functionals, Table 7.2. The IP($Cr(CO)_6$) and EA($Cr(CO)_6^+$) are overestimated numerically for LDA and the GGA functionals, however, we can see from Table 7.1 that these functionals afford accurate excitation energies. This is due to error cancellation when we combine the IP($Cr(CO)_6$) and

EA(Cr(CO)$_6^+$) to give the excitation energies given by

$$\begin{aligned}
\Delta E_{\mathrm{S}}^{\mathrm{CV}(\infty)} =& \mathrm{IP}(\mathrm{Cr(CO)}_6, 2t_{2g}) + \mathrm{EA}(\mathrm{Cr(CO)}_6^+, 2t_{2g}, 9t_{1u}, \mathrm{S}) \\
=& \Big(- \epsilon_{2t_{2g}} + \frac{1}{2} K_{2t_{2g}2t_{2g},2t_{2g}2t_{2g}} + \tilde{\Delta} E_{\mathrm{Rel}} \Big) + \\
& \Big(\epsilon_{9t_{1u}} + \frac{1}{2} K_{9t_{1u}9t_{1u},9t_{1u}9t_{1u}} - 2K_{9t_{1u}9t_{1u},2t_{2g}2t_{2g}} \\
& + K_{9\bar{t}_{1u}9\bar{t}_{1u},2t_{2g}2t_{2g}} + \tilde{\Delta} E_{\mathrm{Rel}} \Big) \\
=& \left[\epsilon_{9t_{1u}} \left(\rho^0 \right) - \epsilon_{2t_{2g}} \left(\rho^0 \right) \right] + \frac{1}{2} K_{9t_{1u}9t_{1u}9t_{1u}9t_{1u}} + \frac{1}{2} K_{2t_{2g}2t_{2g}2t_{2g}2t_{2g}} \\
& - 2K_{9t_{1u}9t_{1u}2t_{2g}2t_{2g}} + K_{9t_{1u}9t_{1u}2\bar{t}_{2g}2\bar{t}_{2g}} + \Delta E_{\mathrm{Rel}}^{\mathrm{S}}(R)
\end{aligned} \tag{7.4}$$

here $\Delta E_{\mathrm{Rel}}^{\mathrm{S}}(R) = \tilde{\Delta} E_{\mathrm{Rel}}^{\mathrm{IP}} + \tilde{\Delta} E_{\mathrm{Rel}}^{\mathrm{EA,S}}$ for a singlet excitation.

We consider next the $[\mathrm{Fe(CN)}_6]^{4-}$ complex, Table 7.3. The RMSDs here were calculated with the lower numbers of the experimental [289] excitation energies ranges where applicable. There are some theoretical calculation carried with with TD-DFT [277] and other DFT based approaches [277] as well as some high-level $ab\ initio$ methods [292].

Again, our method shows good performance by the LDA and GGA functionals, the difference is that the inclusion of the exact exchange as in the case of the hybrid functionals, does not worsen the overall performance. As we pointed out earlier, the errors in the excitation energies can be understood much more clearly by decomposing the energies into IP and EA. With this approach, we can see that the good performance by the method compared to with the experimental excitation energies is as a result of, to some extent, error cancellation. Additionally, we find that as the fraction of the HF exchange increases, the IP becomes

$$\mathrm{IP} \approx -\epsilon_i. \tag{7.5}$$

We found in these complexes that, our method affords excitation energies in good comparison with the experimental values even in cases where the IP and the EA were overestimated numerically. Although, our previous analyses of the Rydberg excitations with SCF-CV(∞)-DFT method showed that obtaining accurate IP and EA is key to getting accurate excitation energies [79].

In general, the RSCF-CV(∞)-DFT method overestimated the excitation energies in the $[Fe(CN)_5(py)]^{3-}$ complexes by $\sim$0.45 eV. Here, the comparison is made to the CASPT2 calculations [293]. Displayed in Table 7.4 are the excitation energies, the first six are MLCT and the last two are MC (significant $d \rightarrow d$ character) excitations. The first two low-lying MLCT states are overestimated by the local and hybrid functionals but are underestimated by the LC functionals. The RSCF-CV(∞)-DFT method shows better performance for the higher energy MLCT as well as the MC states, although the overall performance is poor. However, our results are comparable to the results obtained by Thiel [277] with the DFT/MRCI approach, see Table E.2 in Appendix E.

To summarise, our RSCF-CV(∞)-DFT method shows the best performance for the neutral $Cr(CO)_6$ complex even for the local functionals. It is closely followed by the $[Fe(CN)_6]^{4-}$, where the best performance comes from the B3LYP functional. The excitation energies for $[Fe(CN)_5(py)]^{3-}$ afforded by the RSCF-CV(∞)-DFT method were overestimated for most of the states studied.

Table 7.4: Calculated Excitation Energies[a] for $[Fe(CN)_5(py)]^{3-}$ based on the RSCF-CV(∞)-DFT method.

STATE	CASPT2[b]	LDA	BP86	PBE	B3LYP	PBE0	BHLYP	LCBP86*[c]	LCBP86[d]
1^1A_1(MLCT)	0.96	1.18	1.54	1.53	1.66	2.40	2.13	0.49	0.42
1^1A_2(MLCT)	0.72	1.71	1.61	1.57	1.22	1.80	0.97	0.97	1.47
1^1B_1(MLCT)	0.77	1.73	1.64	1.14	–	1.91	1.00	1.73	1.87
2^1B_1(MLCT)	1.34	1.76	1.97	1.32	–	2.31	2.38	2.78	2.32
2^1A_2(MLCT)	1.36	2.45	2.28	2.89	1.84	2.71	2.20	2.06	1.91
1^1B_2(MLCT)	1.49	2.03	1.84	1.74	1.42	2.46	2.47	2.69	2.32
2^1B_2(MC)	2.89	2.28	2.09	2.12	2.08	2.49	2.80	2.80	2.63
3^1B_1(MC)	3.03	2.38	2.16	1.34	–	2.91	2.87	3.50	2.49
RMSD		0.74	0.76	0.94	0.45[e]	1.03	0.73	0.82	0.74

[a]Energies in eV. [b] Ref. [293]. [c]Represents LC functional combined with BP86 with ω = 0.75. [d]Refers to LC functional combined with BP86 using ω = 0.4. [e]Calculated with 5 excitation energies.

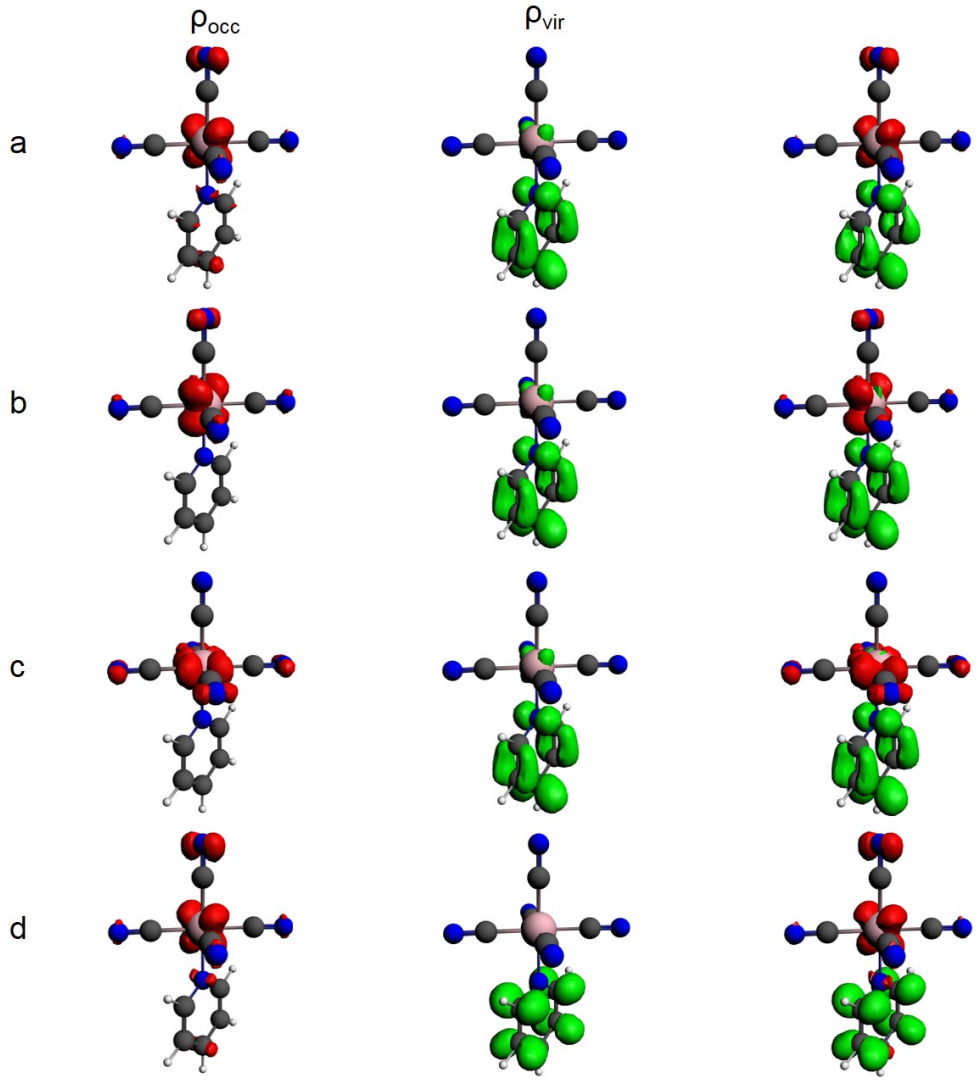

Figure 7.4: $\Delta\rho$ associated with the $[Fe(CN)_5(py)]^{3-}$. (a), (b), (c) and (d) represent the 1^1A_1, 1^1A_2, 1^1B_1 and 1^1B_2 states, respectively. All plotted density shown here depict MLCT-type transitions. Red signifies depletion and green shows accumulation of density.

We turn next to the electronic density change that accompanies the electronic excitation. Figure 7.2(a and b) shows the plot of the density changes associated with the electronic transitions in $Cr(CO)_6$. We show in the figure, the charge redistribution; where the density depletion occurs ($\rho_{2t_{2g}}$), the accumulation ($\rho_{9t_{1u}}$ or $\rho_{2t_{2u}}$) as well as the density change ($\Delta\rho_{\text{ex}} = \rho_{9t_{1u}} - \rho_{2t_{2g}}$) resulting from the total change in density associated with the electronic transition.

For the MLCT transition, the $\rho_{2t_{2g}}$ (Figure 7.2a) is situated on the Cr metal centre and the area is space spun by the density is reminiscent of the d_{yz}, and the $\rho_{9t_{1u}}$ as well

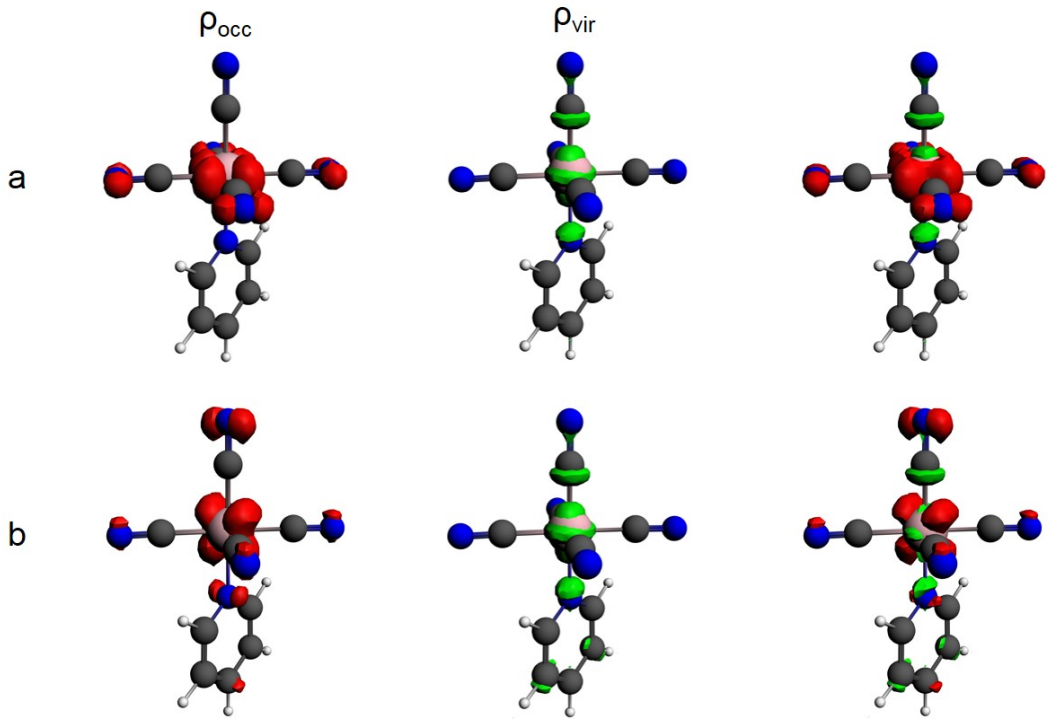

Figure 7.5: $\Delta\rho$ associated with the $[Fe(CN)_5(py)]^{3-}$. (a) The density change associated with the 2^1B_2 state. (b) exemplify the density redistribution associated with the 3^1B_1 state. All densities depict MC-type transitions. Red signifies loss and green shows gain in density.

as $\rho_{2t_{2u}}$ is mostly situated on the equatorial CO ligands. The occupied density is in the yz-plane and the virtual density signifying the accumulation is situated on the CO ligand and there is little interaction between them as can be seen from the difference. The movement of density is from the metal centre to the ligands corresponding to an intra-molecular charge transfer transition. It is clear from the Figure 7.2c that, this transition has a significant $d \rightarrow d$ character. In the density plots that follow, we see a depletion in the density situated on the metal with some contribution from the CO in the xy-plane and accumulation of density largely on the central Cr metal along the yz-plane with some accumulation on the CO ligands in the same plane. The overlap integral $S_{2t_{2g}9t_{1u}}$ is nonzero but very small in this case, see the density difference.

Displayed in Figure 7.3 are the density plots for $[Fe(CN)_6]^{4-}$. We make here a similar observation as made for $Cr(CO)_6$. The differences in the density plots representing the MC transition are; there is much more significant accumulation on the CN^- ligands, and the density accumulation is in the same plane (xy-plane) as the depletion density

($d_{x^2-y^2}$ to d_{xy}). As for the MLCT, the associated density movement is identical to that of $Cr(CO)_6$, see Figure 7.3(b and c).

Figure 7.4 shows the change corresponding to the excitations in the $[Fe(CN)_5(py)]^{3-}$ complex. For the MLCT transitions, the reduction in density is in general around the central Fe atom in different planes and the density gain is around the py ligand with smaller density accumulation on the central atom.

However, we see a larger separation between the donor and acceptor regions (r) of this complex. The MC transitions distinctly show $d \rightarrow d$ transitions with varying contributions from the py ligand, Figure 7.5. This is an example of CT transitions where the donor and acceptor regions are distinctly separated.

7.4 Concluding Remarks

For intra-molecular CT transitions, the performance of the RSCF-CV(∞)-DFT method depends on the separation (r) between the donor and acceptor regions of the complex. For complexes where the donor and acceptor regions are close, the RSCF-CV(∞)-DFT method shows a superior performance compared to the ATD-DFT method even with the local functionals. However, as r gets larger, the excitation energies become more functional dependent and less accurate. More work is necessary to provide an in depth explanation of the performance of our method as a function of r.

Further, the accuracy of our method for smaller r is not attributable to the ability of our method to afford accurate values of the IP of the complex and the EA of the cation formed (in case of a neutral complex) but due to some error cancellation that occurs when we combine the IP and EA to obtain the excitation energy.

The density change associated with the electronic transitions afforded by our method clearly shows the regions of density depletion and accumulation. From these density plots, a transition can be unambiguously labeled as MLCT or MC excitation. This is important because an excitation in our method and in general is characterized by the loss of an electron in the space spanned by the occupied orbitals and an electron gain in

the region spanned by the virtual orbitals.

Chapter 8

The formulation of a constricted variational density functional theory for double excitations

8.1 Introduction

In quantum mechanics excited states are described by methods that are based on either response theory or variational schemes [227, 228]. Both approaches have led to methods that are highly accurate for organic molecules [324]. The accurate wave function schemes scale as n^6 with the number of electrons. They are thus rather expensive for larger systems although attempts to introduce a more favourable scaling are under way [325, 326, 327].

Density functional theory constitutes a popular alternative to $ab\ initio$ wave function methods with a good compromise between computational speed and accuracy due to its favourable scaling as n^2 or better. Excited states have for the most part been dealt with by approaches based on response theory such as the TD-DFT method [52, 53]. This is in line with the fact that DFT is well established as a ground-state theory. Nevertheless variational DFT approaches have also been used with some success starting with the ΔSCF scheme by Slater [43].

Although both DFT and TD-DFT in principle are exact theories, their practical implementations are based on approximations. For TD-DFT, the source of error does not only involve the employment of approximate functionals but also the almost universal use of the adiabatic approximation [65]. Whilst many of the problems originally encountered in the application of TD-DFT to charge transfer and Rydberg transitions [1, 86, 87, 88, 89] have been address by the introduction of more appropriate functionals the description of pure double electron excitations as well as single electron transition

with some double excitation character is still a problem [65] that only can be solved by going beyond the adiabatic approximation (ATD-DFT). It is as a consequence not possible to treat double excitations with the standard adiabatic approaches and schemes that go beyond ATD-DFT are still under development [54, 55, 66, 74, 75, 76]. The CV-DFT method is able to treat charge transfer transitions even with local functionals when terms to all orders in U_{ai} are taken into account. However, this requires that U_{ai} is fully optimized and that the basis of occupied $\{\phi_i(1)$; i = 1,$occ\}$ and virtual $\{\phi_a(1)$; a = 1,$vir\}$ ground-state orbital are allowed to relax (RSCF-CV(∞)-DFT) [176].

The objective of the current study is to demonstrate that it is possible to extend RSCF-CV(∞)-DFT to double excitations. It will further be shown that it with certain limitations is possible to derive a second-order CV(2)-DFT theory that can be considered as an extension of ATD-DFT to double excitations.

8.2 The constricted variational density functional theory applied to a single transition

The RSFC-CV(∞)-DFT scheme [49] has already been descried in great details for single electron transitions in Chapter 2 and subsequent chapters. Nevertheless we shall here sketch the part of the theory that will be important for its extension to double transitions.

8.2.1 Generation of excited-state orbitals for a single electron transition

In CV(n)-DFT [48, 49, 51, 93], we construct excited-state KS-orbitals by performing a unitary transformation among occupied $\{\phi_i(1)$; i = 1,$occ\}$ and virtual $\{\phi_a(1)$; a = 1,$vir\}$ ground-state orbitals

$$Y^I \begin{pmatrix} \phi_{occ} \\ \phi_{vir} \end{pmatrix} = e^{U^I} \begin{pmatrix} \phi_{occ} \\ \phi_{vir} \end{pmatrix} = \left(\sum_{m=0}^{\infty} \frac{(U^I)^m}{m!} \right) \begin{pmatrix} \phi_{occ} \\ \phi_{vir} \end{pmatrix} = \begin{pmatrix} \psi^I_{occ} \\ \psi^I_{vir} \end{pmatrix} \tag{8.1}$$

to order m in Ref. [48]. Here ϕ_{occ} and ϕ_{vir} are concatenated column vectors containing the sets of occupied $\{\phi_i(1)$; i = 1,$occ\}$ and virtual $\{\phi_a(1)$; a = 1,$vir\}$ ground-state

KS-orbitals whereas ϕ^I_{occ} and ϕ^I_{vir} are concatenated column vectors containing the resulting sets $\{\phi^I_i(1);\ i = 1,occ\}$ and $\{\phi^I_a(1);\ a = 1,vir\}$ of occupied and virtual orbitals corresponding to the single electron transition I. The unitary transformation matrix Y^I is in eq (8.1) expressed in terms of a skew symmetric matrix U^I as

$$Y = e^U = I + U + \frac{U^2}{2} + ... = \sum_{m=0}^{\infty} \frac{U^m}{m!} = \sum_{m=0}^{\infty} \frac{(U^2)^m}{(2m)!} + U \sum_{m=0}^{\infty} \frac{(U^2)^m}{(2m+1)!}. \quad (8.2)$$

Here, $U^I_{ij} = U^I_{ab} = 0$ where "i, j" refer to the occupied set $\{\phi_i(1);\ i = 1,occ\}$ whereas "a, b" refer to $\{\phi^I_a(1);\ a = 1,vir\}$. The elements of U^I are the variational mixing matrix elements that combine virtual and occupied ground-state orbitals in the excited-state with $U^I_{ai} = -U^I_{ia}$. Thus, the entire matrix U^I is made up of $occ \times vir$ independent elements U^I_{ai} that also can be organized in the column vector $\vec{U}^I$. For a given $\vec{U}^I$ we can by the help of eq (8.2) generate a set of "occupied" excited-state orbitals

$$\phi^I_i = \sum_{p}^{occ+vir} Y^I_{pi}\phi_p = \sum_{j}^{occ} Y^I_{ji}\phi_j + \sum_{a}^{vir} Y^I_{ai}\phi_a \quad (8.3)$$

that are orthonormal to order m in U^I_{ai}. Summing up all orders in U the occupied excited-state orbitals from the unitary transformation can be written in compact form [48, 49, 51] as

$$\phi^I_i = \cos[\eta\gamma^I_i]\phi^I_{i_o} + \sin[\eta\gamma^I_i]\phi^I_{i_v};(i = 1, occ). \quad (8.4)$$

Here [48, 49, 51] γ^I_i(i = 1,occ) is a set of eigenvalues to

$$(V^I)^+ U^I W^I = 1\gamma^I \quad (8.5)$$

where γ^I is a diagonal matrix of dimension occ. Further

$$\phi^I_{i_o} = \sum_{j}^{occ} (W^I)_{ji}\phi_j \quad (8.6)$$

and

$$\phi^I_{i_v} = \sum_{b}^{vir} (V^I)_{bi}\phi_b \quad (8.7)$$

where "i, j" run over the occupied ground-state orbitals and b over the virtual ground-state orbitals. The orbitals defined in eq (8.6) and (8.7) were first introduced by Amos

and Hall [98] as the corresponding occupied and virtual orbital pair that is mixed in the unitary transformation defined by U^I. They have been explored in connection with electron excitations as Natural Transition Orbitals (NTO) by Martin [328] since they give a more compact description of the excitations than the canonical orbitals. Thus, a transition that involves several $i \rightarrow a$ replacements among canonical orbitals can often be described by a single replacement $\phi^I_{i_o} \rightarrow \phi^I_{i_v}$ in terms of NTOs. In that case $\gamma^I_j = \pi/2$ for $a = i$ whereas $\gamma^I_j = 0$ for $a \neq i$ [48, 49, 51]. The first occ virtual excited-state orbitals are given by

$$\phi^I_a = \sin[\eta\gamma^I_i]\phi^I_{i_o} - \cos[\eta\gamma^I_i]\phi^I_{i_v}; (a = i = 1, occ) \tag{8.8}$$

and the remaining a = occ+1,vir virtual orbitals as

$$\phi^I_a = \phi^I_{i_v}; (a = i = occ + 1, vir). \tag{8.9}$$

To second-order in U^I_{ai} the excited-state occupied orbitals reads

$$\phi^I_i = \phi_i(1) + \sum_a^{vir} U^I_{ai}\phi_a(1) - \frac{1}{2}\sum_a^{vir}\sum_j^{occ} U^I_{ai}U^I_{aj}\phi^*_j + \mathcal{O}^{(3)}[U^I] \tag{8.10}$$

and the virtual orbitals

$$\phi^I_a = \phi_a(1) - \sum_i^{occ} U^I_{ai}\phi_i(1) - \frac{1}{2}\sum_b^{vir}\sum_i^{occ} U^I_{ai}U^I_{bi}\phi^*_b(1) + \mathcal{O}^{(3)}[U^I]. \tag{8.11}$$

For spin conserving transitions only U elements combining virtual and occupied orbitals of α–spin ($\alpha \rightarrow \alpha$ transitions) or β–spin ($\beta \rightarrow \beta$ transitions) are non-zero. For spin-flip ($\alpha \rightarrow \beta$) or ($\beta \rightarrow \alpha$) transitions only U elements combining virtual and occupied orbitals of different spins can be non-zero. In the procedure above we started with the ground-state KS-determinant

$$\Psi_0 = |\phi_1\phi_2\phi_3 \ldots \phi_i\phi_j \ldots \phi_n| \tag{8.12}$$

and generate the KS-determinant for the one-electron transition I

$$\Psi_I = |\phi^I_1\phi^I_2\phi^I_3 \ldots \phi^I_i\phi^I_j \ldots \phi^I_n|. \tag{8.13}$$

We observe from eq (8.4) that ϕ_i^I consists of a linear combination of occupied and virtual ground-state orbitals. It should be noted that the occupied $\{\phi_i(1);\, i = 1,occ\}$ and virtual $\{\phi_a(1);\, a = 1,vir\}$ orbitals making up the set $\{\phi_p(1);\, p = 1,occ + vir\}$ can be of different symmetry. Thus $\{\phi_i(1);\, i = 1,occ\}$ are not symmetry orbitals. The only requirement is that any product $\phi_i\phi_a$ must belong to the same symmetry as the excited-state under consideration. Note also that for spin conserving transitions ϕ_i and ϕ_a are of the same spin whereas ϕ_i and ϕ_a are of different spin for spin-flip transitions. Finally $\Psi_I = |\phi_1^I\phi_2^I\phi_3^I \ldots \phi_i^I\phi_j^I \ldots \phi_n^I|$ is not necessarily an eigenfunction of S^2. Thus use must be made of sum rules [14] in order to calculate energies of spin-states.

8.2.2 Expressing excited-state densities for single electron excitation

The excited-state density in terms of NTOs reads [48, 49, 51]

$$\rho^I = \rho^0 + \Delta\rho^I \tag{8.14}$$

where

$$\begin{aligned}
\Delta\rho^I =& \Delta\tilde{\rho}^I + \Delta\hat{\rho}^I \\
=& \sum_i^{occ} \sin^2[\eta\gamma_i^I]\big(\phi_{i_v}^I(1)\phi_{i_v}^I(1') - \phi_{i_o}^I(1)\phi_{i_o}^I(1')\big) \\
&+ \sum_i^{occ} \sin[\eta\gamma_i^I]\cos[\eta\gamma_i^I]\big(\phi_{i_o}^I(1)\phi_{i_v}^I(1') + \phi_{i_o}^I(1')\phi_{i_v}^I(1)\big)
\end{aligned} \tag{8.15}$$

and to second-order

$$\begin{aligned}
\Delta\rho^{I,(2)} =& \Delta\tilde{\rho}^{I,(2)} + \Delta\hat{\rho}^{I,(2)} \\
=& \sum_i^{occ}\sum_a^{vir} U_{ai}^I\big(\phi_a(1')\phi_i(1) + \phi_a(1)\phi_i(1')\big) \\
&+ \sum_i^{occ}\sum_a^{vir}\sum_b^{vir} U_{ai}^I U_{bi}^I \phi_a(1')\phi_b(1) \\
&- \sum_i^{occ}\sum_j^{occ}\sum_a^{vir} U_{ai}^I U_{aj}^I \phi_i(1')\phi_j(1).
\end{aligned} \tag{8.16}$$

8.2.3 Evaluating excitation energies for single electron transitions

We obtain after some manipulations [48, 49, 51] the following excited-state energy expression

$$E^I - E^0 = \Delta E^I = \sum_i^{occ} \sin^2[\eta\gamma_i^I] \left(\epsilon_{i_v}^I(\rho^0 + \frac{1}{2}\Delta\hat{\rho}^I) - \epsilon_{i_o}^I(\rho^0 + \frac{1}{2}\Delta\hat{\rho}^I) \right) + \sum_i^{occ}\sum_j^{occ} \sin[\eta\gamma_i^I]\cos[\eta\gamma_i^I]\sin[\eta\gamma_j^I]\cos[\eta\gamma_j^I] K_{i_o^I i_v^I j_o^I j_v^I}. \quad (8.17)$$

The definitions of the K integrals are shown in eqs (2.26), (2.27), (2.28), and (2.29). In eq (8.17) $\epsilon_{i_o^I}(\rho^0 + 1/2\Delta\rho^I)$ and $\epsilon_{i_v^I}(\rho^0 + 1/2\Delta\rho^I)$ correspond to orbital energies of $\epsilon_{i_o^I}(\rho^0)$ and $\epsilon_{i_v^I}(\rho^0)$, respectively, evaluated for a density at the midpoint (or transition state) [43] between that of the ground-state and the excited-state. To second-order in U we have [48, 49, 51]

$$\Delta E^{I(2)} = \sum_i^{occ}\sum_a^{vir} U_{ai}^I U_{ai}^I [\epsilon_a(\rho^0) - \epsilon_i(\rho^0)] + \sum_i^{occ}\sum_j^{occ}\sum_a^{vir}\sum_b^{vir} U_{ai}^I U_{bj}^I K_{aibj}. \quad (8.18)$$

This is identical to the energy expression for the ATD-DFT theory [52, 53] within the TDA [175] as discussed in Chapter 2 and Refs. [74, 83, 85, 88, 89, 91, 226]. We see that both $\Delta E^{I(2)}$ of eq (8.18) and ΔE^I in eq (8.17) have a "diagonal" term containing a weighted sum of the relative energies for the various configurations $(i)(a)$ or $(\phi_{i_o}^I)(\phi_{i_v}^I)$ in terms of orbital energy differences as well as a "off-diagonal" term accounting for the interaction between the different configurations. In ATD-DFT/TDA or CV(2)-DFT/TDA the "diagonal" terms are only correct to second-order in U and involve just ground-state orbital energy differences whereas ΔE^I contains orbital energy differences based on the "transition state" [43]. For the "off-diagonal" terms, the form is quite similar in $\Delta E^{I(2)}$ and ΔE^I. For each excited-state I, we optimize U^I with respect to ΔE^I using standard techniques where $\Delta E^{I(2)}$ is taken as a starting point [48, 49, 51]. However in order to avoid a collapse to the ground-state ($U^I = 0$) we introduce the constraint shown in eq (2.62) as

$$\sum_i^{occ} \sin^2[\eta\gamma_i^I] = 1. \quad (8.19)$$

This ensures according to eq (8.15) that one electron is transferred from the occupied $\{\phi^I_{i_o}(1);\ i$ = 1,$occ\}$ to the virtual $\{\phi^I_{i_v}(1);\ i$ = 1,$occ\}$ ground-state orbitals. To second-order the constraint in eq (2.62) reduces to $U^{I+}U^I = 1$. We ensure in addition that $Tr(U^{I+}U^K) = 0$ for the excited states K = 1,$I-1$ that are below the excited-state I. This will prevent a variational collapse of higher states on those of lower energy [48, 49, 51].

8.3 Double Excitations

Having generated $\Psi_I = |\phi^I_1\phi^I_2\phi^I_3\ldots\phi^I_i\phi^I_j\ldots\phi^I_n|$ and the associated set of occupied $\{\phi^I_i(1);\ i$ = 1,$occ\}$ and virtual $\{\phi^I_a(1);\ a$ = 1,$vir\}$ reference orbitals we can now perform a second unitary transformation

$$\begin{aligned}\tilde{Y}^J\begin{pmatrix}\phi^I_{occ}\\ \phi^I_{vir}\end{pmatrix} =& e^{\tilde{U}^J}\begin{pmatrix}\phi^I_{occ}\\ \phi^I_{vir}\end{pmatrix} = \left(\sum_{m=0}^{\infty}\frac{(\tilde{U}^J)^m}{m!}\right)\begin{pmatrix}\phi^I_{occ}\\ \phi^I_{vir}\end{pmatrix}\\ =& e^{\tilde{U}^J}e^{U^I}\begin{pmatrix}\phi_{occ}\\ \phi_{vir}\end{pmatrix} = \begin{pmatrix}\psi^{I,J}_{occ}\\ \psi^{I,J}_{vir}\end{pmatrix}.\end{aligned} \tag{8.20}$$

In this way we generate $\Psi_{I,J} = |\phi^{I,J}_1\phi^{I,J}_2\phi^{I,J}_3\ldots\phi^{I,J}_i\phi^{I,J}_j\ldots\phi^{I,J}_n|$ with the occupied $\{\phi^{I,J}_i(1);\ i$ = 1,$occ\}$ and virtual orbitals $\{\phi^{I,J}_a(1);\ a$ = 1,$vir\}$. For the first unitary transformation U^I has $occ\times vir$ elements. It means that we can construct $occ\times vir$ different orthogonal matrices. Thus, we have $\{U^I;\ I$ = 1,$occ\times vir\}$ different transformations or one-electron transitions. We also have $\{\tilde{U}^J;\ J$ = 1,$occ\times vir\}$ distinct matrices for the second unitary transformations. Thus we have altogether $(occ\times vir)\times(occ\times vir)$ two electron transitions.

8.3.1 Generating excited-state orbitals for a double electron transition

Generating the second excitation in eq (8.20) will only lead to a change in those orbitals that are directly influenced by the unitary transformation. Thus, if the second excitation is concerned with an $\alpha\rightarrow\alpha$ transition all occupied β orbitals are unchanged (frozen) and the same as in the I'th reference state. The same will be the case for a number of α orbitals. This is not realistic since all occupied orbitals should be able to respond to

the change in the overall potential caused by the second excitation. To remedy this we shall allow for a relaxation of the set of occupied $\{\phi_i^I(1);\, i = 1,occ\}$ and virtual $\{\phi_a^I(1);\, a = 1,vir\}$ reference orbitals to second-order in the mixing matrix R by introducing the new set of relaxed occupied

$$\psi_i^I(1) = \phi_i^I(1) + \sum_a^{vir} R_{ai}\phi_a^I(1) - \frac{1}{2}\sum_a^{vir}\sum_j^{occ} R_{ai}R_{aj}\phi_j^I + \mathcal{O}^{(3)}[R] \tag{8.21}$$

and unoccupied reference orbitals

$$\psi_a^I(1) = \phi_a^I(1) - \sum_i^{occ} R_{ai}\phi_i^I(1) - \frac{1}{2}\sum_b^{vir}\sum_i^{occ} R_{ai}R_{bi}\phi_b^I(1) + \mathcal{O}^{(3)}[R]. \tag{8.22}$$

Here it is implicitly understood that we will have a different set of matrix elements R_{ai} for each (*I,J*) pair. We can now generate the orbitals for the double excitations (I,J) from the transformation

$$\tilde{Y}^J\begin{pmatrix}\psi_{occ}^I\\ \psi_{vir}^I\end{pmatrix} = e^{\tilde{U}^J}\begin{pmatrix}\psi_{occ}^I\\ \psi_{vir}^I\end{pmatrix} = \left(\sum_{m=0}^{\infty}\frac{(\tilde{U}^J)^m}{m!}\right)\begin{pmatrix}\psi_{occ}^I\\ \psi_{vir}^I\end{pmatrix} = \begin{pmatrix}\psi_{occ}^{I,J}\\ \psi_{vir}^{I,J}\end{pmatrix} \tag{8.23}$$

and subsequently express the KS-determinant for the doubly excited-state (I,J) as $\Psi_{I,J} = |\psi_1^{I,J}\psi_2^{I,J}\psi_3^{I,J}\ldots\psi_i^{I,J}\psi_j^{I,J}\ldots\psi_n^{I,J}|$ where now

$$\psi_i^{I,J} = \cos[\eta\gamma_i^{I,J}]\psi_{i_o}^I + \sin[\eta\gamma_i^{I,J}]\psi_{i_v}^I;(i = 1, occ) \tag{8.24}$$

with $(\psi_{i_o}^I,\psi_{i_v}^I)$ representing the corresponding (8.4) eigenvectors to U^I with the common eigenvalue γ_i^I. The occupied orbitals to second-order in $\tilde{U}^J$ are given by

$$\psi_i^{I,J} = \psi_i^I(1) + \sum_a^{vir}\tilde{U}_{ai}^J\psi_a^I(1) - \frac{1}{2}\sum_a^{vir}\sum_j^{occ}\tilde{U}_{ai}^J\tilde{U}_{aj}^J\phi_j^J + \mathcal{O}^{(3)}[\tilde{U}^J]. \tag{8.25}$$

8.3.2 Expressing excited-state densities for double excitations

We can write down the density of the doubly excited-state (I,J) as

$$\rho^{I,J} = \rho^I + \Delta\rho^I + \Delta\tilde{\rho}^{I,J} + \Delta\rho^{I,J_{(0,1+2)}} \tag{8.26}$$

where $\Delta\rho^I$ defined in eq (8.15) is the (unrelaxed) change in density due to the first excitation. Further

$$\begin{aligned}\Delta\rho^{I,J} = &\sum_i^{occ}\sin^2[\eta\gamma_i^{I,J}]\big(\psi_{i_v}^I(1)\psi_{i_v}^I(1') - \psi_{i_o}^I(1)\psi_{i_o}^I(1')\big)\\ &+ \sum_i^{occ}\sin[\eta\gamma_i^{I,J}]\cos[\eta\gamma_i^{I,J}]\big(\psi_{i_o}^I(1)\psi_{i_v}^I(1') + \psi_{i_o}^I(1')\psi_{i_v}^I(1)\big)\end{aligned} \tag{8.27}$$

represents primarily the change in density due to $\tilde{U}^J$ whereas

$$\begin{aligned}\Delta\rho^{I,J_{0,1+2}} \approx & \sum_{i}^{occ}\big(\psi_{i_v}^I(1)\psi_{i_v}^I(1') - \phi_{i_o}^I(1)\phi_{i_o}^I(1')\big) \\ = & \sum_{i}^{occ}\sum_{a}^{vir}\Big(\sum_{b}^{vir} R_{ai}^{I,J}R_{bi}^{I,J}\phi_a^I(1)\phi_b^I(1') - \sum_{j}^{occ} R_{ai}^{I,J}R_{aj}^{I,J}\phi_i^I(1)\phi_j^I(1')\Big) \\ & + \sum_{i}^{occ}\sum_{a}^{occ} R_{ai}^{I,J}\big(\phi_i^I(1)\phi_a^I(1') + \phi_i^I(1')\phi_a^I(1)\big) \end{aligned} \tag{8.28}$$

constitutes the part of the change in density ($\Delta\rho^{0,1+2}$) that is zero-order in $\tilde{U}^J$ and up to second-order in $R^{I,J}$. Finally, to second-order in $\tilde{U}^J$ and zero-order in $R^{I,J}$

$$\begin{aligned}\Delta\rho^{I,J_2} = & \sum_{i}^{occ}\sum_{a}^{vir}\Big(\sum_{b}^{vir} \tilde{U}_{ai}^J\tilde{U}_{bi}^J\phi_a^I(1)\phi_b^I(1') - \sum_{j}^{occ} \tilde{U}_{ai}^J\tilde{U}_{aj}^J\phi_i^I(1)\phi_j^I(1')\Big) \\ & + \sum_{i}^{occ}\sum_{a}^{occ} \tilde{U}_{ai}^J\big(\phi_i^I(1)\phi_a^I(1') + \phi_i^I(1')\phi_a^I(1)\big) \end{aligned} \tag{8.29}$$

where the density to all orders in $\tilde{U}^J$ is given as

$$\begin{aligned}\Delta\rho^{I,J} = & \sum_{i}^{occ}\sin^2[\eta\gamma_i^{I,J}]\big(\phi_{i_v}^I(1)\phi_{i_v}^I(1') - \phi_{i_o}^I(1)\phi_{i_o}^I(1')\big) \\ & + \sum_{i}^{occ}\sin[\eta\gamma_i^{I,J}]\cos[\eta\gamma_i^{I,J}]\big(\phi_{i_o}^I(1)\phi_{i_v}^I(1') + \phi_{i_o}^I(1')\phi_{i_v}^I(1)\big). \end{aligned} \tag{8.30}$$

8.3.3 Evaluating excitation energies for double electron transitions

The excitation energy for the transition from the ground-state to the doubly excited-state (I,J) can now with the help of eq (8.26) be written as

$$\begin{aligned}\Delta E^{I,J} = & \Delta E^I + \Delta\tilde{E}^{I,J_{(0,1+2)}} + \sum_{i}^{occ}\sin^2[\eta\gamma_i^{I,J}]\Big(\epsilon_{i_v^I}\Big(\rho^I + \frac{1}{2}\big[\Delta\tilde{\rho}^I + \Delta\rho^{I,J}\big]\Big) \\ & - \epsilon_{i_o^I}\Big(\rho^I + \frac{1}{2}\big[\Delta\tilde{\rho}^I + \Delta\rho^{I,J}\big]\Big)\Big) \\ & + \sum_{i}^{occ}\sum_{j}^{occ}\sin[\eta\gamma_i^{I,J}]\cos[\eta\gamma_i^{I,J}]\sin[\eta\gamma_j^{I,J}]\cos[\eta\gamma_j^{I,J}]K_{i_o^I i_v^I j_o^I j_v^I} \end{aligned} \tag{8.31}$$

where the subscripts i_o^I, i_v^I, j_o^I, j_v^I refer to the relaxed orbitals $\psi_{i_o}^I(1)$, $\psi_{i_v}^I(1)$, $\psi_{j_o}^I(1)$, $\psi_{j_v}^I(1)$ and the kernel in $K_{i_o^I i_v^I j_o^I j_v^I}$ is evaluated at $\rho = \rho^I$. The last two terms in eq (8.31)

accounts primarily for the contribution to $\Delta E^{I,J}$ from $\tilde{U}^J$. Further

$$\Delta E^{I,J_{(0,1+2)}} = \sum_{i}^{occ}\sum_{a}^{vir} R_{ai}^{I,J} R_{ai}^{I,J} \left[\epsilon_a(\rho^0 + \Delta\rho^I) - \epsilon_i(\rho^0 + \Delta\rho^I)\right] + \sum_{i}^{occ}\sum_{j}^{occ}\sum_{a}^{vir}\sum_{b}^{vir} R_{ai}^{I,J} R_{bj}^{I,J} K_{aibj}. \tag{8.32}$$

This term originates from the density relaxation $\Delta E^{I,J_{(0,1+2)}}$. Further the indices a, b, i, j refers to the reference orbitals ψ_a^I, ψ_b^I, ψ_i^I, ψ_j^I and the kernel in K_{aibj} is evaluated at $\rho = \rho^I$.

8.3.4 Optimization of $R^{I,J}$ and $\tilde{U}^J$

A quadratic expansion of $\Delta E^{I,J}[\tilde{U}^J, R^{I,J}]$ from $(\tilde{U}^{0,J}, R^{0,I,J})$ in powers of $\Delta\tilde{U}^J$, $\Delta R^{I,J}$ allows us to write

$$\begin{aligned}\Delta E^{I,J}[\tilde{U}^J, R^{I,J}] =& \Delta E^{I,J}[\tilde{U}^{0,J}, R^{0,I,J}] + \sum_{ai}\left(\frac{d\Delta E^{I,J}}{d\tilde{U}_{ai}^J}\right)_0 \Delta\tilde{U}_{ai}^J \\ &+ \sum_{ai}\left(\frac{d\Delta E^{I,J}}{dR_{ai}^{I,J}}\right)_0 \Delta R_{ai}^{I,J} + \frac{1}{2}\sum_{ai}\sum_{bj}\left(\frac{d^2\Delta E^{I,J}}{d\tilde{U}_{ai}^J d\tilde{U}_{bj}^J}\right)_0 \Delta\tilde{U}_{ai}^J \Delta\tilde{U}_{bj}^J \\ &+ \frac{1}{2}\sum_{ai}\sum_{bj}\left(\frac{d^2\Delta E^{I,J}}{dR_{ai}^{I,J} dR_{bj}^{I,J}}\right)_0 \Delta R_{ai}^{I,J}\Delta R_{ai}^{I,J} + \sum_{ai}\sum_{bj}\left(\frac{d^2\Delta E^{I,J}}{d\tilde{U}_{ai}^J dR_{bj}^{I,J}}\right)_0 \\ &\times \Delta\tilde{U}_{ai}^J \Delta R_{bj}^{I,J} + \mathcal{O}^{[3]}[R^{I,J}, \tilde{U}^J]\end{aligned} \tag{8.33}$$

or

$$\begin{aligned}\Delta E_M(\tilde{U}^J, R^{I,J}) =& E_M(\tilde{U}^{0,J}, R^{0,I,J}) + \left(\Delta\vec{\tilde{U}}^J\ \Delta\vec{R}^{I,J}\right)\begin{pmatrix}\vec{g}^{\tilde{U}} \\ \vec{g}^R\end{pmatrix} \\ &+ \frac{1}{2}\left(\Delta\vec{\tilde{U}}^J\ \Delta\vec{R}^{I,J}\right)\begin{bmatrix}\mathbf{H}^{\tilde{U},\tilde{U}} & \mathbf{H}^{\tilde{U},R} \\ \mathbf{H}^{R,\tilde{U}} & \mathbf{H}^{R,R}\end{bmatrix}\begin{pmatrix}\Delta\vec{\tilde{U}}^J \\ \Delta\vec{R}^{I,J}\end{pmatrix} + \mathcal{O}^{[3]}\end{aligned} \tag{8.34}$$

from which we can obtain expressions for the gradients $\vec{g}^{\tilde{U}}$, $\vec{g}^R$ and Hessians $\mathbf{H}^{\tilde{U},\tilde{U}}$, $\mathbf{H}^{R,\tilde{U}}$ etc. by a comparison between eq (8.33) and (8.34). The requirement that the gradient must be zero at the minimum point $(\tilde{U}^{0,J} + \Delta\tilde{U}^J, R^{0,I,J} + \Delta R^{I,J})$ provides after differentiation of eq (8.33) with respect to $\Delta\tilde{U}^J$ and $\Delta R^{I,J}$ the set of equations

$$\begin{pmatrix}\vec{g}^{\tilde{U}} \\ \vec{g}^R\end{pmatrix} + \begin{bmatrix}\mathbf{H}^{\tilde{U},\tilde{U}} & \mathbf{H}^{\tilde{U},R} \\ \mathbf{H}^{R,\tilde{U}} & \mathbf{H}^{R,R}\end{bmatrix}\begin{pmatrix}\Delta\vec{\tilde{U}}^J \\ \Delta\vec{R}^{I,J}\end{pmatrix} = 0 \tag{8.35}$$

from which we can obtain $\Delta\tilde{U}^J$ and $\Delta R^{I,J}$ iteratively [49, 51]. The optimization of $\tilde{U}^J$ is carried out with the constraint

$$\sum_{i}^{occ} \sin^2[\eta\gamma_i^{I,J}] = 1. \tag{8.36}$$

This guarantees that one electron is transferred from the occupied $\{\psi_{i_o}^J;\ i$ = 1,$occ\}$ to the virtual $\{\psi_{i_v}^J;\ i$ = 1,$occ\}$ reference state orbitals. We ensure in addition that $Tr(U^{I+}U^K) = 0$ for the excited states K = 1,$I-1$ that are below the state I [49, 51] in order to avoid a variational collapse of I unto states of lower energy.

8.3.5 Simplified second-order theory for double excitations

There are instances in which U used in the first unitary transformation of eq (8.1) and $\tilde{U}$ used in the second unitary transformation of eq (8.20) commutes. These are cases in which the two excitations involve different sets of orbitals. Examples would be two spin conserving transitions encompassing different spins or two different spin-flip transitions starting from orbitals of different spins. It could also involve orbitals of different symmetry. In those cases the indices (a,i) of both $U \equiv U^I$ and $\tilde{U} \equiv U^J$ refer to the same original set of virtual $\{\phi_a;\ a$ = 1,$vir\}$ and occupied $\{\phi_i;\ i$ = 1,$occ\}$ ground-state orbitals. We can thus write the orbitals to second-order in U^I for the first unitary transformation in eq (8.1) as

$$\phi_i^I = \phi_i(1) + \sum_{a}^{vir} U_{ai}^I \phi_a(1) - \frac{1}{2}\sum_{a}^{vir}\sum_{j}^{occ} U_{ai}^I U_{aj}^I \phi_j^* + \mathcal{O}^{(3)}[U^I] \tag{8.37}$$

and the orbitals from the second unitary transformation due to U^J as

$$\phi_i^J = \phi_i(1) + \sum_{a}^{vir} U_{ai}^J \phi_a(1) - \frac{1}{2}\sum_{a}^{vir}\sum_{j}^{occ} U_{ai}^J U_{aj}^J \phi_j^* + \mathcal{O}^{(3)}[U^I] \tag{8.38}$$

to second-order in U^J. In eq (8.37) the summation is over the I-set of occupied and virtual orbitals that participate in the unitary transformation defined by U^I whereas the summation in eq (8.38) is over the J-set of orbitals involved in the transformation due to U^J. The total change in density due to the (I, J) double excitation becomes to

second-order in (U^L_{ai}, U^L_{bj})

$$\sum_L^{I,J} \Delta\rho^K = \sum_L^{I,J} \Bigg(\sum_i^{occ} \sum_a^{vir} \sum_b^{vir} U^L_{ai} U^L_{bi} \phi_a(1)\phi_b(1') - \sum_i^{occ} \sum_j^{occ} \sum_a^{vir} U^L_{ai} U^L_{aj} \phi_i(1)\phi_j(1') + \sum_i^{occ/2} \sum_a^{vir/2} U^L_{ai} \big[\phi_i(1)\phi_a(1') + \phi_i(1')\phi_a(1)\big] \Bigg) + \mathcal{O}^{[3]}(U^I_{ai}, U^I_{bj}) \tag{8.39}$$

which is simply the sum of the density changes due to the two separate transitions I and J. We finally have for the transition energy of the double excitation

$$\Delta E^{I,J} = \sum_L^{I,J} \Bigg[\sum_i^{occ} \sum_a^{vir} U^L_{ai} U^L_{ai} \big(\epsilon_a(\rho^0) - \epsilon_i(\rho^0)\big) + \sum_i^{occ} \sum_j^{occ} \sum_a^{vir} \sum_b^{vir} U^L_{ai} U^L_{bj} \times \big(K_{aibj} + K_{aijb}\big) \Bigg] + 2 \sum_i^{occ/2} \sum_j^{occ/2} \sum_a^{vir/2} \sum_b^{vir/2} U^I_{ai} U^J_{bj} \big(K_{aibj} + K_{aijb}\big) \tag{8.40}$$

which is the sum of excitation energies of the two one-electron transitions plus a coupling term. We can rewrite eq (8.40) on matrix form as

$$\Delta E^{I,J} = \sum_L^{I,J} (U^L)^+ A^L U^L + 2 U^I K^{I,J} U^J \tag{8.41}$$

where the definitions of A^L and $K^{I,J}$ should be clear from a comparison between eq (8.40) and (8.41). We can next write $U^I = U^I_0 + \Delta U^I$ and $U^J = U^J_0 + \Delta U^J$. Here U^I_0 diagonalizes A^I with the eigenvalue ΔE^I_0 and U^J_0 diagonalizes A^J with the eigenvalue ΔE^J_0 . Thus ΔE^I_0 and ΔE^J_0 are the transition energies for the two uncoupled one electron excitations to I and J from an ATD-DFT or CV(2) calculations. We now have

$$\Delta E^{I,J} = \Delta E^{I,J}_0 + (\Delta U^I)^+ A^I \Delta U^I + (\Delta U^J)^+ A^J \Delta U^J + 2 U^I_0 K^{I,J} \Delta U^J + 2 \Delta U^I K^{I,J} U^J_0 + 2 \Delta U^I K^{I,J} \Delta U^J \tag{8.42}$$

where we have introduced

$$\Delta E^{I,J}_0 = (U^I_0)^+ A^I U^I_0 + (U^J_0)^+ A^J U^J_0 + 2 U^I_0 K^{I,J} U^J_0 \tag{8.43}$$

and used that

$$(\Delta U^I)^+ A^I U^I_0 = (\Delta U^J)^+ A^J U^J_0 = (U^I_0)^+ A^I \Delta U^I = (U^J_0)^+ A^J \Delta U^J = 0 \tag{8.44}$$

since U_0^I and U_0^J are eigenfunctions to A^I and A^J, respectively. A differentiation of $\Delta E^{I,J}$ with respect to (ΔU^I, ΔU^J) affords for the optimal set (ΔU^I, ΔU^J) the equation

$$\begin{bmatrix} A^I & K^{I,J} \\ K^{J,I} & A^J \end{bmatrix} \begin{pmatrix} \Delta U^I \\ \Delta U^J \end{pmatrix} = \begin{pmatrix} K^{I,J} U_0^I \\ K^{I,J} U_0^J \end{pmatrix} \tag{8.45}$$

from which we can determine (ΔU^I, ΔU^J) iteratively. To a first approximation the transition energy for the double excitation can be determined by $\Delta E_0^{I,J}$ of eq (8.43) where we see that $\Delta E_0^{I,J}$ is different than the two one electron transition energies $(U_0^I)^+ A^I U_0^I$ and $(U_0^J)^+ A^J U_0^J$ due to the coupling term $2U_0^I K^{I,J} U_0^J$. A more accurate estimate is $\Delta E^{I,J}$ of eq (8.42).

8.4 Concluding remarks

We have here shown that it is possible to extend the constricted variational DFT method from a single to a double electron transition. Key to this extension is the introduction of two consecutive unitary transformations generated by U and $\tilde{U}$. In its most general formulation the double electron transition energy is calculated to all orders in U and $\tilde{U}$. We have previously shown that the CV-DFT method for a single electron to second-order in U is equivalent to ATD-DFT. It is shown here that the second-order CV-DFT method under certain conditions can be extended to double excitations. When these conditions are satisfied, our second-order CV-DFT scheme can be considered as equivalent to a ATD-DFT theory for double excitations.

Chapter 9

Summary and Outlook

We have presented in this thesis, an analyses of the performance of the CV-DFT method for the determination of excited-state properties. The main objective was to apply our method in the studies of electronically complex systems, and provide an explanation for the cases where it affords accurate performances (when compared to experimental or some high level $ab\ initio$ results) as well as cases where it under-performs. Throughout this work, comparisons were made to other DFT based approaches especially the ΔSCF-DFT and the ATD-DFT methods, and some explanations of the strengths and weaknesses of these methods are provided.

In Chapter 3, we assessed the performance of the SF-CV(2)-DFT method for the calculation of exchange coupling constant (J) when applied to a series of triply-bridged Cu(II) dinuclear complexes. A comparison of the J values obtained with SF-CV(2)-DFT to those due to the BS-DFT method as well as experimental results is provided. Our methodology showed comparable performance to those obtained by the BS-DFT method with B3LYP and BHLYP functionals. Overall, the results from the theoretical calculations showed a strong functional dependence. The SF-CV(2)-DFT method in addition to providing almost identical results as the BS-DFT method for hybrid functionals, has the capacity to provide a description of the different spin-states in terms of a configuration interaction of the microstates. This makes our method suitable for the determination of ground- and excited-state properties of systems with multi-determinantal ground-state description.

We deviated slightly from the general theme of this work in Chapter 4. Here, we carried out a study of the bonding in the heavier group 14 analogues. The analysis was carried out with the NOCV-ETS method, it was based on two ArE fragments in their

doublet ground-state configuration. For E = Si, Ge and Sn, our analysis revealed three types of bonds whereas the ArPbPbAr system was found to have only a single bond with a C–Pb–Pb trans-bent angle close to 90°. With the help of the NOCV-ETS scheme, we were able to obtain qualitative as well as quantitative estimates for the strength of the various components of the real systems without the need for any modifications to the systems. We showed that the isopropyl substituents on the components play a stabilizing role due to the van der Waal attractions between Pr^i groups on aromatic rings attached to heavier group 14 atoms as well as hyperconjugation involving donation into orbitals on Pr^i. The larger number of Pr^i groups on the Pb system is responsible for the highly stable Pb compound. Consequently, large number of Pr^i groups on a ligand is necessary for the formation of stable systems that would otherwise be unstable.

Previous studies carried out on the model systems (where Ar = H, CH_3) by other researchers showed a significant diradical character. The SF-CV(2)-DFT method was applied and it provided proof that support the conclusion that the real systems studied here have a singlet ground-state and they have very little to no diradical character.

Next, we surveyed the performance of ΔSCF and RSCF-CV(∞)-DFT method for the studies of Rydberg transitions in 9 different species. In total, 71 triplet or singlet Rydberg transitions were examined. Our method showed good performance for both local and hybrid functionals. The performance was considerably better than that of the ATD-DFT method with the local and hybrid functionals but not as accurate as ATD-DFT with highly "specialized" functionals. The success of our method for the Rydberg transitions was due to its ability to afford good estimates of the IP and the EA even for the local functionals when orbital relaxation is included. The errors in the ATD-DFT method for Rydberg transition is due to its inability to provide accurate IPs and EAs with the regular functionals.

The next test set we considered was the tetraoxo d^0 TM complexes, Chapter 6. The ATD-DFT method as well as the RSCF-CV(∞)-DFT method were employed in this benchmark calculations. This test set contains the 3d complexes, the 4d congeners as well as the 5d homologues. The RSCF-CV(∞)-DFT method performed better than

the ATD-DFT method for the 3d complexes. The ATD-DFT method showed a better performance amongst the heavier tetraoxo systems. For the 4d and 5d complexes, we saw a comparable performance for both RSCF-CV(∞)-DFT and ATD-DFT methods with the different functionals. The performance of the RSCF-CV(∞)-DFT methood, exemplified the idea that our method performed well in cases where the ATD-DFT method under performs and showed nearly identical performance for the cases where the ATD-DFT method performs with remarkable accuracy.

The preliminary results on the CT excitations, shown in Chapter 7, were carried out on three octahedral complexes. Our RSCF-CV(∞)-DFT method showed good performance for the complexes with short distance between the donor and acceptor regions. This observation was true even for the local functionals. The plotted density change accompanying the excitation gave a clear indication of the kind of excitation under consideration, although, further work needs to be carried out to make these densities easily accessible in a graphical user interface (GUI). Future work would be carried out on other octahedral complexes (such as $[Fe(bpy)_3]^{2+}$ [329], bpy = bipyridine), *trans*(Cl)-Ru(bpy)$Cl_2(CO)_2$ [295] and ($[Ru(II)(NH_3)_5(MeQ^+)]^{3+}$, MeQ^+ = N-methyl-4,4'-bipyridinium) [294]) as well as systems in which there is a clear separation between the donor and acceptor (r) regions. Further, the performance of our method as a function of r in systems in which r is adjustable will be studied. This is a necessary requirement for making improvements on our method before it an be used for the studies of chemically interesting problem by computational and experimental chemist alike.

In Chapter 8, we provided a way of extending the RSCF-CV(∞)-DFT method to double excitations. Additionally, we demonstrated a procedure for double excitation within the CV(2)-DFT theory that can also be considered as an extension to the ATD-DFT method when the TDA is enforced. Future work here would involve the application of this method to the studies of electronic excitation in systems where double excitations are important.

To summarise, we have so far reviewed the performance of the CV-DFT method from its initial formulation (CV(2)-DFT) to the more recent RSCF-CV(∞)-DFT method.

The CV(2)-DFT method is identical to the ATD-DFT method, however, in the CV(2)-DFT method, we can easily include higher-order terms. Going beyond the second-order and adiabatic formulation of TD-DFT is the focus of ongoing research, however, within the CV-DFT scheme, we have shown clearly an approach for going beyond the second-order formulation. The higher-order terms are contained in K integrals that are explainable from the point of view interaction of singly-excited Slater determinant with a doubly-excited Slater determinant, $\left\langle \Psi_{i\to a}|H|\Psi_{\substack{i\to b\\ j\to c}} \right\rangle$, doubles interacting with other doubles, $\left\langle \Psi_{\substack{i\to a\\ j\to b}}|H|\Psi_{\substack{i\to c\\ j\to d}} \right\rangle$, etc. These interactions between singly and doubly-excited Slater determinants are important for excitations with significant doubles character. The RSCF-CV(∞)-DFT method is identical to ΔSCF-DFT method for single orbital replacement type excitations. So far, our method has shown performances nearly identical to ATD-DFT for excitations accurately described by ATD-DFT, and a superior performance for excitations poorly represented by the ATD-DFT method. Additionally, extensions have been made to the CV-DFT method for double excitations, this is an important modification for the analysis of excitations with significant doubles character, if the important doubles are to be added artificially. Lastly, we have demonstrated that the CV-DFT method is a viable alternative to the TD-DFT method, however, more "benchmarking" and improvements are needed before it can be used as a "blackbox" approach for chemically analysis.

Appendix A

First Appendix

Tables A.1–A.3 display the results for Complexes 6 – 8 based on SF-CV(2)-DFT with $a(^3\text{A})$ for no symmetry.

Table A.1: Lower Excited States for Complex 6 Based on SF-CV(2)-DFT Calculations Using LDA-VWN Functional

C_1 Symmetry			
State	E, cm^{-1}	Contributing microstates	%
^3A	0	b(^3A)	98
1^1A	288	a(^1A)	35
		c(^1A)	26
2^1A	5955	b(^1A)	52
		a(^1A)	47
3^1A	6674	a(^1A)	17

Table A.2: Lower Excited States for Complex 7 Based on SF-CV(2)-DFT Calculations Using LDA-VWN Functional

C_1 Symmetry			
State	E, cm^{-1}	Contributing microstates	%
^3A	0	b(^3A)	98
1^1A	283	a(^1A)	40
		c(^1A)	32
2^1A	6066	b(^1A)	67
		a(^1A)	32
3^1A	6595	a(^1A)	27
		c(^1A)	66

Table A.3: Lower Excited States for Complex 8 Based on SF-CV(2)-DFT Calculations Using LDA-VWN Functional

C_1 Symmetry			
State	E, cm^{-1}	Contributing microstates	%
^3A	0	b(^3A)	96
1^1A	315	b(^1A)	97
2^1A	5601	a(^1A)	96
		c(^1A)	2
3^1A	6978	a(^1A)	2
		c(^1A)	96

Appendix B

Second Appendix

Tables B.1–B.3 display the remaining results from SF-CV(2)-DFT calculations.

Table B.1: Lower Excited States for Complex 9 Based on SF-CV(2)-DFT Calculations Using LDA-VWN Functional

C_s Symmetry			
State	E, cm^{-1}	Contributing microstates	%
$^3A''$	0	b($^3A''$)	98
$1^1A'$	166	a($^1A'$)	65
		b($^1A'$)	33
$^1A''$	5730	($^1A''$)	100
$2^1A'$	6356	b($^1A'$)	66
		a($^1A'$)	34

Table B.2: Lower Excited States for Complex 10 Based on SF-CV(2)-DFT Calculations Using LDA-VWN Functional

C_s Symmetry			
State	E, cm^{-1}	Contributing microstates	%
$^3A''$	0	b($^3A''$)	98
$1^1A'$	304	a($^1A'$)	50
		b($^1A'$)	49
$^1A''$	6074	($^1A''$)	100
$2^1A'$	6482	a($^1A'$)	50
		b($^1A'$)	50

Table B.3: Lower Excited States for Complex 11 Based on SF-CV(2)-DFT Calculations Using LDA-VWN Functional

C_1 Symmetry			
State	E, cm^{-1}	Contributing microstates	%
^3A	0	b(^3A)	95
1^1A	325	b(^1A)	95
2^1A	5853	a(^1A)	89
		c(^1A)	7
3^1A	6677	a(^1A)	7
		c(^1A)	89

Appendix C

Third Appendix

Table C.1: Rydberg Excitation Energies[a] for Mg Calculated with ΔSCF Using an extended basis set[b] and five different functionals.

	State	Transition	LDA	BP86	B3LYP	LCBP86*[c]	LCBP86[d]	Expt.[e]
Mg	^1S	$2s \rightarrow 4s$	5.27	4.91	5.19	5.58	5.65	5.39
	^1D	$2s \rightarrow 3d$	5.92	5.53	5.68	5.95	5.90	5.75
	^1P	$2s \rightarrow 4pd$	5.90	5.66	5.78	6.00	5.98	6.12
	^3S	$2s \rightarrow 4s$	5.05	4.98	5.13	5.18	5.20	5.11
	^3D	$2s \rightarrow 3d$	5.66	5.51	5.70	5.88	5.90	5.95
	^3P	$2s \rightarrow 4p$	5.70	5.54	5.70	5.85	5.85	5.93
		MAE	0.18	0.35	0.19	0.12	0.13	
		RMSD	0.20	0.38	0.21	0.13	0.15	

Table C.2: Rydberg Excitation Energies[a] for Zn Calculated with ΔSCF Using an extended basis set[b] and five different functionals.

	State	Transition	LDA	BP86	B3LYP	LCBP86*[c]	LCBP86[d]	Expt.[e]
Zn	^1S	$4s \rightarrow 5s$	6.96	6.64	6.70	6.72	6.59	6.92
	^1P	$4s \rightarrow 5p$	7.71	7.38	7.35	7.61	7.49	7.80
	^1D	$4s \rightarrow 4d$	7.81	7.46	7.43	7.72	7.51	7.74
	^1S	$4s \rightarrow 6s$	7.93	8.18	7.97	8.39	8.32	8.19
	^1P	$4s \rightarrow 6pd$	8.26	8.32	8.62	9.30	9.56	8.51
	^3S	$4s \rightarrow 5s$	6.81	6.60	6.58	6.55	6.35	6.65
	^3P	$4s \rightarrow 5p$	7.58	7.29	7.29	7.46	7.48	7.60
	^3D	$4s \rightarrow 4d$	7.76	7.46	7.46	7.68	7.50	7.78
	^3S	$4s \rightarrow 6s$	7.82	8.14	7.92	8.34	8.15	8.11
	^3P	$4s \rightarrow 6p$	8.20	8.22	8.77	9.00	9.19	8.44
		MAE	0.15	0.21	0.25	0.25	0.35	
		RMSD	0.18	0.25	0.27	0.34	0.46	

[a]Energies in eV. [b]Ref. [1]. [c]Refers to LC functional combined with BP86 and ω = 0.40. [d]Represents LC functional combined with BP86 and ω = 0.75. [e]Kramida, A.; Ralchenko, Y.; NIST ASD Team **2013**. *NIST Atomic Spectra Database* (ver. 5.1) [Online]. Available: http://physics.nist.gov/asd [2014, June 19]. National Institute of Standards and Technology, Gaithersburg, MD.

Appendix D

Fourth Appendix

The procedure for the calculation of the R^β matrix in RSCF-CV(∞)-DFT is as follows; first, the gradient of eq (2.60) with respect to R^β is given by

$$\frac{d\Delta E_{\mathrm{M}}^{(\infty,2)}}{dR_{ai}^\beta} = \int F_{\mathrm{KS}}^\beta[\rho_0^\alpha + \Delta\hat{\rho}_\alpha^U, \rho_0^\beta + \Delta\rho_\beta^{R(1)}]\left[\frac{\partial\Delta\rho_\beta^{R(1)}}{\partial R_{ai}^\beta}\right]_0 d\nu + \int F_{\mathrm{KS}}^\beta[\rho_0^\alpha + \Delta\hat{\rho}_\alpha^U, \rho_0^\beta + \Delta\rho_\beta^{R(2)}]\left[\frac{\partial\Delta\rho_\beta^{R(2)}}{\partial R_{ai}^\beta}\right]_0 d\nu = V_{ai} \tag{D.1}$$

where

$$\frac{\partial\Delta\rho_\beta^{R(1)}}{\partial R_{ai}^\beta} = \psi_a^{\beta*}(1)\psi_i^\beta(1') + \psi_i^{\beta*}(1)\psi_a^\beta(1') \tag{D.2}$$

$$\frac{\partial\Delta\rho_\beta^{R(2)}}{\partial R_{ck}^\beta} = 2\sum_a^{vir/2} R_{ak}\psi_a^{\beta*}(1)\psi_c^\beta(1') - 2\sum_j^{occ/2} R_{ck}^\beta\psi_j^{\beta*}(1)\psi_k^\beta(1'). \tag{D.3}$$

Here, "i, j, k" refer to the occupied canonical orbitals and "a, b, c" to the virtual ones. Note that the derivatives in eq (D.1) are taken at R^β = R_0^β which means that the second term in eq (D.1) is zero at the very first iteration. Thus, the gradient is reduced in that case to

$$V_{ai}^0 = \int F_{\mathrm{KS}}^\beta[\rho_0^\alpha + \Delta\hat{\rho}_\alpha^U, \rho_0^\beta + \Delta\rho_\beta^{R(1)}][\psi_a^{\beta*}(1)\psi_i^\beta(1') + \psi_i^{\beta*}(1)\psi_a^\beta(1')]d\nu. \tag{D.4}$$

Now by making use of the Tailor series expansion for the Fock operator

$$\int F_{\mathrm{KS}}[\rho_0 + \Delta\rho_1]\Delta\rho_2 d\nu = \int F_{\mathrm{KS}}[\rho_0]\Delta\rho_2 d\nu + \iint \Delta\rho_1 f_{\mathrm{HX}C}\Delta\rho_2 d\nu_1 d\nu_2 \tag{D.5}$$

eq (D.4) can be rewritten as

$$V_{ai}^0 = \sum_{bc}\sum_{ai}\Delta\hat{\mathrm{P}}_{bc}^U K_{bc,\bar{a}\bar{i}} + \sum_{jk}\sum_{ai}\Delta\hat{\mathrm{P}}_{jk}^U K_{jk,\bar{a}\bar{i}}. \tag{D.6}$$

Here, $\Delta\hat{\mathrm{P}}^U$ is the density matrix corresponding to the transition defined by eq (2.48) [48], and the *K* integrals are defined by eqs (2.26), (2.27), (2.28), and (2.29). However,

the same type of integrals as in eq (D.6) is evaluated in wave function theory as the matrix elements between the following Slater determinants [330]

$$|\dots\psi_c^\alpha\psi_i^\beta\dots| \overset{K_{bc,\bar{a}\bar{i}}}{\rightarrow} |\dots\psi_b^\alpha\psi_a^\beta\dots| \tag{D.7}$$

$$|\dots\psi_k^\alpha\psi_i^\beta\dots| \overset{K_{jk,\bar{a}\bar{i}}}{\rightarrow} |\dots\psi_j^\alpha\psi_a^\beta\dots| \tag{D.8}$$

i.e. they describe the interaction between the single and double electron transitions. Further, the Hessian of eq (2.60) with respect to R^β is given by

$$\begin{aligned}\frac{d^2\Delta E_M^{(\infty,2)}}{dR_{ai}^\beta dR_{bj}^\beta} =& K_{\bar{a}\bar{i},\bar{b}\bar{j}} + K_{\bar{a}\bar{i},\bar{j}\bar{b}} + \int F_{\text{KS}}^\beta\left[\rho_0^\alpha + \Delta\hat{\rho}_\alpha^U, \rho_0^\beta + \Delta\rho_\beta^{R(2)}\right] \\ &\times \left[\frac{\partial^2\Delta\rho_\beta^{R(2)}}{\partial R_{ai}^\beta\partial R_{bj}^\beta}\right]_0 d\nu = H_{\bar{a}\bar{i},\bar{b}\bar{j}}\end{aligned} \tag{D.9}$$

$$\frac{\partial^2\Delta\rho_\beta^{R(2)}}{\partial R_{ai}^\beta\partial R_{bj}^\beta} = \psi_a^\beta(1)\psi_b^{\beta*}(1')\delta_{\bar{i}\bar{j}} - \psi_i^\beta(1)\psi_j^{\beta*}(1')\delta_{\bar{a}\bar{b}}. \tag{D.10}$$

It can be seen that the Hessian defined by eq (D.9) and (D.10) differs from the one of the second-order theory. Based on eqs (D.1) and (D.9), the R^β matrix is obtained from the following response equation

$$R^\beta = \mathbf{H}^{-1}V \tag{D.11}$$

which is solved iteratively in RSCF-CV(∞)-DFT. Alternatively, the inverse of $\mathbf{H}$ can be obtained from its spectral resolution

$$R^\beta = \sum_I \frac{1}{\omega_I}(U^{I\beta}\otimes U^{I\beta})V \tag{D.12}$$

where $\otimes$ is the Kronecker or outer product, and ω_I and $U^{I\beta}$ is the Ith eigenvalue of $\mathbf{H}$ and its eigenvector:

$$\mathbf{H}U^{I\beta} = \omega_I U^{I\beta}. \tag{D.13}$$

The summation in eq (D.12) is over all one-electron excitations of the singly excited-state Hessian $\mathbf{H}$. Equation (D.12) can also be rewritten for each matrix element as

$$R_{ai}^\beta = \sum_I U_{ai}^{I\beta}C^{I\beta} \tag{D.14}$$

where

$$C^{I\beta} = \frac{1}{\omega_I} \sum_{bj} U_{bj}^{I\beta} V_{bj}. \tag{D.15}$$

Thus, $C^{I\beta}$ play the role of CI coefficients for the doubly-excited states, when R^β from eq (D.14) is substituted into the RSCF-CV(∞)-DFT KS-determinant:

$$\begin{aligned}
\Psi_M^{U,R} =& |\psi_1'^{\alpha} \dots \psi_i'^{\alpha} \dots \psi_n'^{\alpha} \phi_1^{\beta} \dots \phi_i^{\beta} \dots \phi_n^{\beta}| \\
\rightarrow& |\psi_1'^{\alpha} \dots \psi_i'^{\alpha} \dots \psi_n'^{\alpha} \psi_1^{\beta} \dots \psi_i^{\beta} \dots \psi_n^{\beta}| \\
&+ \sum_I C^{I\beta} |\psi_1'^{\alpha} \dots \psi_i'^{\alpha} \dots \psi_n'^{\alpha} \phi_1^{I\beta} \dots \phi_i^{I\beta} \dots \phi_n^{I\beta}| + \mathcal{O}^{(2)}[R]
\end{aligned} \tag{D.16}$$

with

$$\phi_i^{I\beta} = \sum_a^{vir/2} U_{ai}^{I\beta} \psi_a^{\beta}. \tag{D.17}$$

It should be stressed here that although eq (D.16) formally includes the summation over all eigenvectors of $\mathbf{H}$, only a few of them are actually included due to the perturbation operator V and inverse eigenvalues.

Appendix E

Fifth Appendix

Table E.1: Calculated Excitation Energies[a] for $Cr(CO)_6$ based on the TD-DFT and DFT/MRI methods.

STATE	DFT/MRI[b]	TD-CAMB3LYP[b]	TD-PBE0[b]	TD-PBE[b]	Expt.[c]
Singlet					
1^1T_{1g}(MC)	4.90/4.76/475	4.99	5.08	5.37	
1^1T_{1u}(MLCT)	4.71/4.70/4.70	4.83	4.71	4.14	4.44
2^1T_{1u}(MLCT)	5.71	6.42	6.31	5.78	5.48
Triplet					
1^3T_{1g}(MC)	4.53/4.54/4.62	4.48	4.50	4.89	
1^3T_{2g}(MC)	4.54/4.71/4.72	4.76	4.79	5.01	

[a]Energies in eV. [b] Ref. [277]. [c]Ref. [288]. [f]Ref. [291]

Table E.2: Calculated Excitation Energies[a] for $[Fe(CN)_5(py)]^{3-}$ based on the DFT/MRI and TD-DFT methods.

STATE	DFT/MRI[b]	TD-CAMB3LYP[b]	TD-PBE0[b]	TD-PBE[b]
1^1A_1(MLCT)	1.16	2.19	1.99	1.98
1^1A_2(MLCT)	0.53	1.74	1.27	0.84
1^1B_1(MLCT)	0.52	1.61	2.22	0.79
2^1B_1(MLCT)	1.38	2.76	2.47	1.11
2^1A_2(MLCT)	1.33	2.62	2.09	1.07
1^1B_2(MLCT)	1.39	2.49	2.01	1.36
2^1B_2(MC)	2.82	2.92	3.07	3.33
3^1B_1(MC)	2.93	2.96	3.11	3.63

[a]Energies in eV. [b] Ref. [277].

Appendix F

Sixth Appendix

Table F.1: Conversion from Atomic unit to SI unit.

Quantity	Symbol	Atomic unit (au)	SI unit
Mass of an electron	m_e	1	9.10938×10^{-31} kg
Electronic charge	e	1	1.60218×10^{-19} C
Reduced Planck's constant	$\hbar$	1	1.05457×10^{-34} Js

Bibliography

[1] P. R. T. Schipper, O. V. Gritsenko, S. J. A. van Gisbergen, and E. J. Baerends, "Molecular calculations of excitation energies and (hyper)polarizabilities with a statistical average of orbital model exchange-correlation potentials," *Journal of Chemical Physics*, vol. 112, no. 3, pp. 1344–1352, 2000.

[2] S. L. Holt and C. J. Ballhausen, "Low temperature absorption spectra of $kmno_4$ in $kclo_4$," *Theoretica Chimica Acta*, vol. 7, no. 4, pp. 313–320, 1967.

[3] B. E. Bursten, M. L. Drummond, and J. Li, "Spiers memorial lecture the quantum chemistry of d- and f-element complexes: From an approximate existence to functional happiness," *Faraday Discussions*, vol. 124, pp. 1–24, 2003.

[4] M. Wolfsberg and L. Helmholz, "The spectra and electronic structure of the tetrahedral ions mno_4^-, cro_4^{2-}, and clo_4^-," *The Journal of Chemical Physics*, vol. 20, no. 5, pp. 837–843, 1952.

[5] R. Hoffmann, "An extended hückel theory. i. hydrocarbons," *The Journal of Chemical Physics*, vol. 39, no. 6, pp. 1397–1412, 1963.

[6] M. B. Hall and R. F. Fenske, "Electronic structure and bonding in methyl- and perfluoromethyl(pentacarbonyl)manganese," *Inorganic Chemistry*, vol. 11, no. 4, pp. 768–775, 1972.

[7] M. B. Hall, "Valence shell electron pair repulsions and the pauli exclusion principle," *Journal of the American Chemical Society*, vol. 100, no. 20, pp. 6333–6338, 1978.

[8] J. A. Pople, D. P. Santry, and G. A. Segal, "Approximate self-consistent molecular orbital theory. i. invariant procedures," *The Journal of Chemical Physics*, vol. 43, no. 10, pp. S129–S135, 1965.

[9] M. J. S. Dewar and W. Thiel, "Ground states of molecules. 38. the mndo method. approximations and parameters," *Journal of the American Chemical Society*, vol. 99, no. 15, pp. 4899–4907, 1977.

[10] J. J. P. Stewart, "Optimization of parameters for semiempirical methods ii. applications," *Journal of Computational Chemistry*, vol. 10, no. 2, pp. 221–264, 1989.

[11] D. R. Truax, J. A. Geer, and T. Ziegler, "Indo-mo calculation of the titanium halides," *The Journal of Chemical Physics*, vol. 59, no. 12, pp. 6662–6666, 1973.

[12] H. Hillier and V. R. Saunders, "Ab initio molecular orbital calculations of the ground and excited states of the permanganate and chromate ions," *Proceedings of the Royal Society of London A: Mathematical, Physical and Engineering Sciences*, vol. 320, no. 1541, pp. 161–173, 1970.

[13] J. C. Slater, "Statistical exchange-correlation in the self-consistent field," in *Advances in Quantum Chemistry* (P.-O. Löwdin, ed.), vol. 6 of *Advances in Quantum Chemistry*, pp. 1–92, Academic Press, 1972.

[14] T. Ziegler, A. Rauk, and E. J. Baerends, "On the calculation of multiplet energies by the hartree-fock-slater method," *Theoretica Chimica Acta*, vol. 43, no. 3, pp. 261–271, 1977.

[15] T. Ziegler, A. Rauk, and E. J. Baerends, "The electronic structure of tetrahedral oxo-complexes. the nature of the "charge transfer" transitions," *Chemical Physics*, vol. 16, no. 2, pp. 209–217, 1976.

[16] H. Johansen and S. Rettrup, "Limited configuration interaction calculation of the optical spectrum for the permanganate ion," *Chemical Physics*, vol. 74, no. 1, pp. 77–81, 1983.

[17] H. Hsu, C. Peterson, and R. M. Pitzer, "Calculations on the permanganate ion in the ground and excited states," *Journal of Chemical Physics*, vol. 64, no. 2,

pp. 791–795, 1976.

[18] A. C. Stückl, C. A. Daul, and H. Güdel, "Excited-state energies and distortions of d0 transition metal tetraoxo complexes: A density functional study," *Journal of Chemical Physics*, vol. 107, no. 12, pp. 4606–4617, 1997.

[19] D. Hegarty and M. A. Robb, "Application of unitary group methods to configuration interaction calculations," *Molecular Physics*, vol. 38, no. 6, pp. 1795–1812, 1979.

[20] K. Andersson, P.-Å. Malmqvist, and B. O. Roos, "Second-order perturbation theory with a complete active space self-consistent field reference function," *The Journal of Chemical Physics*, vol. 96, no. 2, pp. 1218–1226, 1992.

[21] B. Levy and G. Berthier, "Generalized brillouin theorem for multiconfigurational scf theories," *International Journal of Quantum Chemistry*, vol. 3, no. 2, pp. 247–247, 1969.

[22] M. Godefroid, J. Lievin, and J.-Y. Metz, "Symmetry adapted formulation of the generalized brillouin theorem," *International Journal of Quantum Chemistry*, vol. 40, no. 2, pp. 243–264, 1991.

[23] J. Olsen, B. O. Roos, P. Jørgensen, and H. J. A. Jensen, "Determinant based configuration interaction algorithms for complete and restricted configuration interaction spaces," *The Journal of Chemical Physics*, vol. 89, no. 4, pp. 2185–2192, 1988.

[24] P.-Å. Malmqvist, K. Pierloot, A. R. M. Shahi, C. J. Cramer, and L. Gagliardi, "The restricted active space followed by second-order perturbation theory method: Theory and application to the study of cuo_2 and cu_2o_2 systems," *The Journal of Chemical Physics*, vol. 128, no. 20, pp. 1–10, 2008.

[25] T. D. Crawford and H. F. Schaefer, *An Introduction to Coupled Cluster Theory for Computational Chemists*, pp. 33–136. John Wiley & Sons, Inc., 2007.

[26] R. J. Bartlett and J. F. Stanton, *Applications of Post-Hartree-Fock Methods: A Tutorial*, pp. 65–169. John Wiley & Sons, Inc., 2007.

[27] J. F. Stanton and R. J. Bartlett, "The equation of motion coupled-cluster method. a systematic biorthogonal approach to molecular excitation energies, transition probabilities, and excited state properties," *The Journal of Chemical Physics*, vol. 98, no. 9, pp. 7029–7039, 1993.

[28] C. Angeli, R. Cimiraglia, S. Evangelisti, T. Leininger, and J.-P. Malrieu, "Introduction of n-electron valence states for multireference perturbation theory," *The Journal of Chemical Physics*, vol. 114, no. 23, pp. 10252–10264, 2001.

[29] R. J. Buenker and S. D. Peyerimhoff, "Ci method for the study of general molecular potentials," *Theoretica chimica acta*, vol. 12, no. 3, pp. 183–199, 1968.

[30] F. Neese, "A spectroscopy oriented configuration interaction procedure," *The Journal of Chemical Physics*, vol. 119, no. 18, pp. 9428–9443, 2003.

[31] K. C. Kulander, K. R. S. Devi, and S. E. Koonin, "Time-dependent hartree-fock theory of charge exchange: Application to he^{2+} + he," *Physical Review A*, vol. 25, pp. 2968–2975, Jun 1982.

[32] K. R. S. Devi and J. D. Garcia, "Coriolis coupling effects in time-dependent hartree-fock calculations of ion-atom collisions," *Physical Review A*, vol. 30, pp. 600–603, Jul 1984.

[33] V. Maruhn-Rezwani, N. Grün, and W. Scheid, "Numerical solution of the time-dependent schrödinger equation and application to h^{+}-h," *Physical Review Letters*, vol. 43, pp. 512–515, Aug 1979.

[34] K. C. Kulander, "Time-dependent hartree-fock theory of multiphoton ionization: Helium," *Physical Review A*, vol. 36, pp. 2726–2738, Sep 1987.

[35] W. Kohn and L. J. Sham, "Self-consistent equations including exchange and correlation effects," *Physical Review*, vol. 140, pp. A1133–A1138, Nov 1965.

[36] S. H. Vosko, L. Wilk, and M. Nusair, "Accurate spin-dependent electron liquid correlation energies for local spin density calculation: a critical analysis," *Canadian Journal of Physics*, vol. 58, no. 8, pp. 1200–1211, 1980.

[37] A. D. Becke, "Density-functional exchange-energy approximation with correct asymptotic behavior," *Physical Review A*, vol. 38, pp. 3098–3100, Sep 1988.

[38] J. P. Perdew, "Density-functional approximation for the correlation energy of the inhomogeneous electron gas," *Physical Review B*, vol. 33, pp. 8822–8824, Jun 1986.

[39] A. D. Becke, "A new mixing of hartree-fock and local density-functional theories," *Journal of Chemical Physics*, vol. 98, no. 2, pp. 1372–1377, 1993.

[40] E. K. U. Gross, L. N. Oliveira, and W. Kohn, "Density-functional theory for ensembles of fractionally occupied states. ii. application to the he atom," *Physical Review A*, vol. 37, pp. 2821–2833, Apr 1988.

[41] N. I. Gidopoulos, P. G. Papaconstantinou, and E. K. U. Gross, "Spurious interactions, and their correction, in the ensemble-kohn-sham scheme for excited states," *Physical Review Letters*, vol. 88, pp. 033003–1–4, Jan 2002.

[42] T. A. K., "The energy density functional formalism for excited states," *Journal of Physics C: Solid State Physics*, vol. 12, no. 24, pp. 5419–5430, 1979.

[43] J. C. Slater and J. H. Wood, "Statistical exchange and the total energy of a crystal," *International Journal Quantum Chemistry*, vol. 5, no. S4, pp. 3–34, 1970.

[44] N. Besley, A. Gilbert, and P. Gill, "Self-consistent-field calculations of core excited states," *Journal of Chemical Physics*, vol. 130, no. 12, pp. 124308–1–7, 2009.

[45] J. Gavnholt, T. Olsen, M. Engelund, and J. Schiøtz, "Delta self-consistent field method to obtain potential energy surfaces of excited molecules on surfaces," *Physical Review B*, vol. 78, pp. 075441–1–10, aug 2008.

[46] T. Kowalczyk, S. R. Yost, and T. V. Voorhis, "Assessment of the deltascf density functional theory approach for electronic excitations in organic dyes," *Journal of Chemical Physics*, vol. 134, no. 5, pp. 054128–1–8, 2011.

[47] T. Ziegler, M. Seth, M. Krykunov, J. Autschbach, and F. Wang, "On the relation between time-dependent and variational density functional theory approaches for the determination of excitation energies and transition moments," *Journal of Chemical Physics*, vol. 130, pp. 154102–1–8, 2009.

[48] J. Cullen, M. Krykunov, and T. Ziegler, "The formulation of a self-consistent constricted variational density functional theory for the description of excited states," *Chemical Physics*, vol. 391, no. 1, pp. 11–18, 2011.

[49] M. Krykunov and T. Ziegler, "Self-consistent formulation of constricted variational density functional theory with orbital relaxation. implementation and applications," *Journal of Chemical Theory and Computation*, vol. 9, no. 6, pp. 2761–2773, 2013.

[50] M. Krykunov, M. Seth, and T. Ziegler, "Introducing constricted variational density functional theory in its relaxed self-consistent formulation (rscf-cv-dft) as an alternative to adiabatic time dependent density functional theory for studies of charge transfer transitions," *Journal of Chemical Physics*, vol. 140, no. 18, pp. 18A502–1–11, 2014.

[51] T. Ziegler, M. Krykunov, and J. Cullen, "The implementation of a self-consistent constricted variational density functional theory for the description of excited states," *Journal of Chemical Physics*, vol. 136, no. 12, pp. 124107–1–10, 2012.

[52] M. E. Casida, *Recent Advances in Density Functional Methods*, vol. 1, ch. Time-Dependent Density Functional response theory for molecules, pp. 155–193. World Scientific: Singapore, 1995.

[53] E. Runge and E. K. U. Gross, "Density-functional theory for time-dependent system," *Physics Review Letters*, vol. 52, pp. 997–1000, Mar 1984.

[54] M. E. Casida, "Propagator corrections to adiabatic time-dependent density-functional theory linear response theory," *The Journal of Chemical Physics*, vol. 122, no. 5, pp. 054111–1–9, 2005.

[55] M. E. Casida and M. Huix-Rotllant, "Many-body perturbation theory (mbpt) and time-dependent density-functional theory (td-dft): Mbpt insights about what is missing in, and corrections to, the td-dft adiabatic approximation," *Condensed Matter: Mesoscale and Nanoscale Physics*, vol. arXiv:1008.1478 [cond-mat.mes-hall], pp. 1–56.

[56] M. E. Casida, C. Jamorski, K. C. Casida, and D. R. Salahub, "Molecular excitation energies to high-lying bound states from time-dependent density-functional response theory: Characterization and correction of the time-dependent local density approximation ionization threshold," *The Journal of Chemical Physics*, vol. 108, no. 11, pp. 4439–4449, 1998.

[57] M. Petersilka, U. J. Grossmann, and E. K. U. Gross, "Excitation energies from time-dependent density-functional theory," *Physical Review Letters*, vol. 76, pp. 1212–1215, Feb 1996.

[58] R. Bauernschmitt and R. Ahlrichs, "Treatment of electronic excitations within the adiabatic approximation of time dependent density functional theory," *Chemical Physics Letters*, vol. 256, no. 4-5, pp. 454–464, 1996.

[59] S. J. A. van Gisbergen and J. G. Snijder, "A density functional theory study of frequency-dependent polarizabilities and van der waals dispersion coefficients for polyatomic molecules," *Journal of Chemical Physics*, vol. 103, no. 21, pp. 9347–9354, 1995.

[60] F. Furche and R. Alhrichs, "Adiabatic time-dependent density functional methods for excited state properties," *Journal of Chemical Physics*, vol. 117, no. 16, pp. 7433–7447, 2002.

[61] A. Wasserman and K. Burke, "Rydberg transition frequencies from the local density approximation," *Physical Review Letters*, vol. 95, pp. 163006–1–4, Oct 2005.

[62] D. J. Tozer and N. C. Handy, "Improving virtual kohn-sham orbitals and eigenvalues: Application to excitation energies and static polarizabilities," *Journal of Chemical Physics*, vol. 109, no. 23, pp. 10180–10189, 1998.

[63] A. P. Gaiduk, D. S. Firaha, and V. N. Staroverov, "Improved electronic excitation energies from shape-corrected semilocal kohn-sham potentials," *Physical Review Letters*, vol. 108, pp. 253005–1–5, Jun 2012.

[64] J. Autschbach, "Charge-transfer excitations and time-dependent density functional theory: Problems and some proposed solutions," *ChemPhysChem*, vol. 10, no. 11, pp. 1757–1760, 2009.

[65] P. Elliott, S. Goldson, C. Canahui, and N. T. Maitra, "Perspectives on double-excitations in tddft," *Chemical Physics*, vol. 391, no. 1, pp. 110–119, 2011.

[66] O. Gritsenko and E. J. Baerends, "Double excitation effect in non-adiabatic time-dependent density functional theory with an analytic construction of the exchange-correlation kernel in the common energy denominator approximation," *Physical Chemistry Chemical Physics*, vol. 11, pp. 4640–4646, 2009.

[67] Y. Tawada, T. Tsuneda, S. Yanagisawa, T. Yanai, and K. Hirao, "A long-range-corrected time-dependent density functional theory," *The Journal of Chemical Physics*, vol. 120, no. 18, pp. 8425–8433, 2004.

[68] E. Livshits and R. Baer, "A well-tempered density functional theory of electrons in molecules," *Physical Chemistry Chemical Physics*, vol. 9, pp. 2932–2941,

2007.

[69] J. Jaramillo, G. E. Scuseria, and M. Ernzerhof, "Local hybrid functionals," *The Journal of Chemical Physics*, vol. 118, no. 3, pp. 1068–1073, 2003.

[70] T. Stein, L. Kronik, and R. Baer, "Prediction of charge-transfer excitations in coumarin-based dyes using a range-separated functional tuned from first principles," *The Journal of Chemical Physics*, vol. 131, no. 24, 2009.

[71] J. Neugebauer, O. Gritsenko, and E. J. Baerends, "Assessment of a simple correction for the long-range charge-transfer problem in time- dependent density-functional theory," *Journal of Chemical Physics*, vol. 124, no. 21, pp. 214102–1–11, 2006.

[72] M. J. G. Peach, P. Bernfield, T. Helgaker, and D. J. Tozer, "Excitation energies in density functional theory: An evaluation and a diagnostic test," *Journal of Chemical Physics*, vol. 128, no. 4, pp. 044118–1–8, 2008.

[73] Y. Zhao and D. G. Truhlar, "Density functionals with broad applicability in chemistry," *Accounts of Chemical Research*, vol. 41, no. 2, pp. 157–167, 2008. PMID: 18186612.

[74] R. J. Cave, F. Zhang, N. T. Maitra, and K. Burke, "A dressed tddft treatment of the 2^1ag states of butadiene and hexatriene," *Chemical Physics Letters*, vol. 389, no. 1-3, pp. 39–42, 2004.

[75] G. Mazur and R. Wlodarczyk, "Application of the dressed time-dependent density functional theory for the excited states of linear polyenes," *Journal of Computational Chemistry*, vol. 30, no. 5, pp. 811–817, 2009.

[76] P. Romaniello, D. Sangalli, J. A. Berger, F. Sottile, L. G. Molinari, L. Reining, and G. Onida, "Double excitations in finite systems," *Journal of Chemical Physics*, vol. 130, no. 4, pp. 044108–1–11, 2009.

[77] P. Verma and R. J. Bartlett, "Increasing the applicability of density functional theory. iv. consequences of ionization-potential improved exchange-correlation potentials," *Journal of Chemical Physics*, vol. 140, no. 18, pp. 18A534–1–11, 2014.

[78] M. E. Casida, K. C. Casida, and D. R. Salahub, "Excited-state potential energy curves from time-dependent density-functional theory: A cross section of formaldehyde's 1a1 manifold," *International Journal of Quantum Chemistry*, vol. 70, no. 4-5, pp. 933–941, 1998.

[79] I. Seidu, M. Krykunov, and T. Ziegler, "Applications of time-dependent and time-independent density functional theory to rydberg transitions," *Journal of Physical Chemistry A*, vol. 119, no. 21, pp. 5107–5116, 2015. PMID: 25322281.

[80] A. Dreuw and M. Head-Gordon, "Failure of time-dependent density functional theory for long-range charge-transfer excited states: The zincbacteriochlorin-bacteriochlorin and bacteriochlorophyll-spher-oidene complexes," *Journal of American Chemical Society*, vol. 126, no. 12, pp. 4007–4016, 2004. PMID: 15038755.

[81] A. Dreuw, G. R. Fleming, and M. Head-Gordon, "Charge-transfer state as a possible signature of a zeaxanthin-chlorophyll dimer in the non-photochemical quenching process in green plants," *The Journal of Physical Chemistry B*, vol. 107, no. 27, pp. 6500–6503, 2003.

[82] A. Dreuw, G. R. Fleming, and M. Head-Gordon, "Chlorophyll fluorescence quenching by xanthophylls," *Physical Chemistry Chemical Physics*, vol. 5, pp. 3247–3256, 2003.

[83] D. Tozer, "Relationship between long-range charge-transfer excitation energy error and integer discontinuity in kohn-sham theory," *Journal of Chemical Physics*, vol. 119, no. 24, pp. 12697–12699, 2003.

[84] T. Stein, L. Kronik, and R. Baer, "Reliable prediction of charge transfer excitations in molecular complexes using time-dependent density functional theory," *Journal of American Chemical Society*, vol. 131, no. 8, pp. 2818–2820, 2009. PMID: 19239266.

[85] T. Ziegler, M. Seth, M. Krykunov, and J. Autschbach, "A revised electronic hessian for approximate time-dependent density functional theory," *Journal of Chemical Physics*, vol. 129, no. 18, pp. 184114–1–9, 2008.

[86] H. Iikura, T. Tsuneda, T. Tanai, and K. Hirao, "A long-range correction scheme for generalized-gradient-approximation exchange functionals," *Journal of Chemical Physics*, vol. 115, no. 8, pp. 3540–3544, 2001.

[87] J.-W. Song, M. A. Watson, and K. Hirao, "An improved long-range corrected hybrid functional with vanishing hartree-fock exchange at zero interelectronic distance (lc2gau-bop)," *Journal of Chemical Physics*, vol. 131, no. 14, pp. 144108–1–9, 2009.

[88] J. Heyd, G. E. Scuseria, and M. Ernzerhof, "Hybrid functionals based on a screened coulomb potential," *Journal of Chemical Physics*, vol. 118, no. 18, pp. 8207–8216, 2003.

[89] R. Baer and D. Neuhauser, "Density functional theory with correct long-range asymptotic behavior," *Physical Review Letters*, vol. 94, pp. 043002–1–4, Feb 2005.

[90] Y. Zhao and D. G. Truhlar, "Density functional for spectroscopy: No long-range self-interaction error, good performance for rydberg and charge-transfer states, and better performance on average than b3lyp for ground states," *Journal of Physical Chemistry A*, vol. 110, no. 49, pp. 13126–13130, 2006. PMID: 17149824.

[91] A. Dreuw, J. Weisman, and M. Head-Gordon, "Long-range charge-transfer excited states in time-dependent density functional theory require non-local exchange," *Journal of Chemical Physics*, vol. 119, no. 6, pp. 2943–2946, 2003.

[92] Y. Zhao and D. G. Truhlar, "Density functional for spectroscopy: No long-range self-interaction error, good performance for rydberg and charge-transfer states, and better performance on average than b3lyp for ground states," *The Journal of Physical Chemistry A*, vol. 110, no. 49, pp. 13126–13130, 2006. PMID: 17149824.

[93] T. Ziegler and M. Krykunov, "On the calculation of charge transfer transitions with standard density functionals using constrained variational density functional theory," *Journal of Chemical Physics*, vol. 133, no. 7, pp. 074104–1–11, 2010.

[94] P. Hohenberg and W. Kohn, "Inhomogeneous electron gas," *Physical Review*, vol. 136, pp. B864–B871, Nov 1964.

[95] R. van Leeuwen, "Mapping from densities to potentials in time-dependent density-functional theory," *Physical Review Letters*, vol. 82, pp. 3863–3866, May 1999.

[96] M. Levy and A. Nagy, "Variational density-functional theory for an individual excited state," *Physical Review Letters*, vol. 83, pp. 4361–4364, Nov 1999.

[97] M. Levy and J. P. Perdew, "Hellmann-feynman, virial, and scaling requisites for the exact universal density functionals. shape of the correlation potential and diamagnetic susceptibility for atoms," *Physical Review A*, vol. 32, pp. 2010–2021, oct 1985.

[98] A. T. Amos and G. G. Hall, "Single determinant wave functions," *Proceedings of the Royal Society of London A: Mathematical, Physical and Engineering Sciences*, vol. 263, no. 1315, pp. 483–493, 1961.

[99] I. Seidu, M. Krykunov, and T. Ziegler, "Applications of time-dependent and time-independent density functional theory to electronic transitions in tetrahedral d^0 metal oxides," *Journal of Chemical Theory and Computation*, vol. 11, no. 9, pp. 4041–4053, 2015.

[100] O. Kahn, ed., *Molecular Magnetishm*. New York: Wiley-VCH, 1 ed., 1993.

[101] D. Gatteschi, O. Kahn, and J. Miller, eds., *Magnetic Molecular Materials*. Nato Science Series E: Applied Sciences, Dordrecht: The Netherlands: Kluwer, 198 ed., 1991.

[102] E. Dagotto, "Correlated electrons in high-temperature superconductors," *Review of Modern Physics*, vol. 66, pp. 763–840, Jul 1994.

[103] E. I. Solomon, *Coupled Binuclear Copper Active Sites*, ch. 8, pp. 116–150.

[104] J. Yoon and E. I. Solomon, "Electronic structures of exchange coupled trigonal trimeric cu(ii) complexes: Spin frustration, antisymmetric exchange, pseudo-a terms, and their relation to o_2 activation in the multicopper oxidases," *Coordination Chemistry Reviews*, vol. 251, no. 3-4, pp. 379–400, 2007.

[105] W. Kaim and J. Rall, "Copper - a "modern" bioelement," *Angewandte Chemie International Edition in English*, vol. 35, no. 1, pp. 43–60, 1996.

[106] X. S. Tan, Y. Fujii, T. Sato, Y. Nakano, and M. Yashiro, "The crystal structures of glycylglycine and glycine complexes of cis,cis-1,3,5-triaminocyclohexane-copper(ii) as reaction intermediates of metal-promoted peptide hydrolysis," *Chemical Communications*, pp. 881–882, 1999.

[107] X. G. Zhao, W. H. Richardson, J.-L. Chen, J. Li, L. Noodleman, H.-L. Tsai, and D. N. Hendrickson, "Density functional calculations of electronic structure, charge distribution, and spin coupling in manganese-oxo dimer complexes," *Inorganic Chemistry*, vol. 36, no. 6, pp. 1198–1217, 1997. PMID: 11669688.

[108] F. Dole, A. Fournel, V. Magro, E. C. Hatchikian, P. Bertrand, and B. Guigliarelli, "Nature and electronic structure of the ni-x dinuclear center of desulfovibrio gigas hydrogenase. implications for the enzymatic mechanism," *Biochemistry*, vol. 36, no. 25, pp. 7847–7854, 1997. PMID: 9201928.

[109] W. Heisenberg, "Zur theorie des ferromagnetismus," *Zeitschrift für Physik*, vol. 49, no. 9-10, pp. 619–636, 1928.

[110] I. de P. R. Moreira, R. Costa, M. Filatov, and F. Illas, "Restricted ensemble-referenced kohn-sham versus broken symmetry approaches in density functional theory: Magnetic coupling in cu binuclear complexes," *Journal of Chemical Theory and Computation*, vol. 3, no. 3, pp. 764–774, 2007.

[111] F. Illas, I. de P. R. Moreira, C. de Graaf, and V. Barone, "Magnetic coupling in biradicals, binuclear complexes and wide-gap insulators: a survey of *ab initio* wave function and density functional theory approaches," *Theoretical Chemistry Accounts*, vol. 104, no. 3-4, pp. 265–272, 2000.

[112] T. Tokii, N. Hamamura, M. Nakashima, and Y. Muto, "Crystal structures and magnetic properties of novel μ-carboxylato-μ-hydroxo-bridged binuclear copper(ii) complexes with 1,10-phenanthroline," *Bulletin of the Chemical Society of Japan*, vol. 65, no. 5, pp. 1214–1219, 1992.

[113] C. López, R. Costa, F. Illas, E. Molins, and E. Espinosa, "Ferromagnetic copper(ii) complex containing ferrocenecarboxylato bridging ligands," *Inorganic Chemistry*, vol. 39, no. 20, pp. 4560–4565, 2000.

[114] C. López, R. Costa, F. Illas, C. de Graaf, M. M. Turnbull, C. P. Landee, E. Espinosa, I. Mata, and E. Molins, "Magneto-structural correlations in binuclear copper(ii) compounds bridged by a ferrocenecarboxylato(-1) and an hydroxo- or methoxo-ligands," *Dalton Transactions*, pp. 2322–2330, 2005.

[115] J. Sletten, "The structures of two oxalato-bridged cu dimers;

[cui$_2$(me$_4$en)$_2$(c$_2$o$_4$)(h$_2$o)$_2$](pf$_6$)$_2$.2h$_2$o and [cu$_2$(et$_5$dien)$_2$(c$_2$o$_4$)](pf$_6$)$_2$," *Acta Chemica Scandinavica A*, vol. 37, no. 7, pp. 569–578, 1983.

[116] M. Julve, M. Verdaguer, A. Gleizes, M. Philoche-Levisalles, and O. Kahn, "Design of μ-oxalato copper(ii) binuclear complexes exhibiting expected magnetic properties," *Inorganic Chemistry*, vol. 23, no. 23, pp. 3808–3818, 1984.

[117] P. de Meester, S. R. Fletcher, and A. C. Skapski, "Refined crystal structure of tetra-μ-acetato-bisaquodicopper(ii)," *Journal of Chemical Society, Dalton Transactions*, pp. 2575–2578, 1973.

[118] O. Castillo, I. Muga, A. Luque, J. M. Gutiérrez-Zorrilla, J. Sertucha, P. Vitoria, and P. Román, "Synthesis, chemical characterization, x-ray crystal structure and magnetic properties of oxalato-bridged copper(ii) binuclear complexes with 2,2′-bipyridine and diethylenetriamine as peripheral ligands," *Polyhedron*, vol. 18, no. 8-9, pp. 1235–1245, 1999.

[119] S. Youngme, J. Phatchimkun, N. Wannarit, N. Chaichit, S. Meejoo, G. A. van Albada, and J. Reedijk, "New ferromagnetic dinuclear triply-bridged copper(ii) compounds containing carboxylato bridges: Synthesis, x-ray structure and magnetic properties," *Polyhedron*, vol. 27, no. 1, pp. 304–318, 2008.

[120] C. Chailuecha, S. Youngme, C. Pakawatchai, N. Chaichit, G. A. van Albada, and J. Reedijk, "Dinuclear triply bridged copper(ii)-carboxylato compounds with different bischelating ligands: Synthesis, crystal structure, spectroscopic and magnetic properties," *Inorganica Chimica Acta*, vol. 359, no. 13, pp. 4168–4178, 2006.

[121] S. Youngme, C. Chailuecha, G. A. van Albada, C. Pakawatchai, N. Chaichit, and J. Reedijk, "Synthesis, crystal structure, spectroscopic and magnetic properties of doubly and triply bridged dinuclear copper(ii) compounds containing di-2-pyridylamine as a ligand," *Inorganica Chimica Acta*, vol. 357, no. 9, pp. 2532–2542, 2004.

[122] S. Youngme, C. Chailuecha, G. A. van Albada, C. Pakawatchai, N. Chaichit, and J. Reedijk, "Dinuclear triply-bridged copper(ii) compounds containing carboxylato bridges and di-2-pyridylamine as a ligand: synthesis, crystal structure, spectroscopic and magnetic properties," *Inorganica Chimica Acta*, vol. 358, no. 4, pp. 1068–1078, 2005.

[123] R. D. Willet, D. Gatteschi, and O. Kahn, eds., *Magneto-Structural Correlations in Exchange Coupled Systems*. Nato ASI Series C: Mathematical and Physcial Sciences, Dordrecht: The Netherlands: Reidel, 140 ed., 1985.

[124] A. Rodríguez-Fortea, E. Ruiz, P. Alemany, and S. Alvarez, "Magneto-structural correlations in trinuclear cu(ii) complexes: A density functional study," *Monatshefte für Chemie - Chemical Monthly*, vol. 134, no. 2, pp. 307–316, 2003.

[125] D. J. Hodgson, *The Structural and Magnetic Properties of First-Row Transition-Metal Dimers Containing Hydroxo, Substituted Hydroxo, and Halogen Bridges*, pp. 173–241. John Wiley & Sons, Inc., 2007.

[126] V. H. Crawford, H. W. Richardson, J. R. Wasson, D. J. Hodgson, and W. E. Hatfield, "Relation between the singlet-triplet splitting and the copper-oxygen-copper bridge angle in hydroxo-bridged copper dimers," *Inorganic Chemistry*, vol. 15, no. 9, pp. 2107–2110, 1976.

[127] E. Ruiz, P. Alemany, S. Alvarez, and J. Cano, "Toward the prediction of magnetic coupling in molecular systems: Hydroxo- and alkoxo-bridged cu(ii) binuclear complexes," *Journal of the American Chemical Society*, vol. 119, no. 6, pp. 1297–1303, 1997.

[128] E. Ruiz, P. Alemany, S. Alvarez, and J. Cano, "Structural modeling and magneto-structural correlations for hydroxo-bridged copper(ii) binuclear complexes," *Inorganic Chemistry*, vol. 36, no. 17, pp. 3683–3688, 1997. PMID: 11670060.

[129] S. Meenakumari, S. Tiwari, and A. R. Chakravarty, "Crystal structures, spectral and magnetic properties of (μ)(μ)dicopper(ii) complexes containing chelating amines," *Journal of Chemical Society, Dalton Transactions*, pp. 2175–2181, 1993.

[130] K.-S. Burger, P. Chaudhuri, and K. Wieghardt, "Moderately strong antiferromagnetic exchange coupling in a dinuclear complex containing a [μ]-hydroxo-[μ]-carboxylatodicopper(ii) core," *Journal of Chemical Society, Dalton Transactions*, pp. 247–248, 1996.

[131] Y. Nishida and S. Kida, "Crystal structures and magnetism of binuclear copper(ii) complexes with alkoxide bridges. importance of orbital complementarity in spin coupling through two different bridging groups," *Journal of Chemical Society, Dalton Transactions*, pp. 2633–2640, 1986.

[132] T. Kawata, M. Yamanaka, S. Ohba, Y. Nishida, M. Nagamatsu, T. Tokii, M. Kato, and O. W. Steward, "Crystal structures and magnetic properties of binuclear copper(ii) complexes with alkoxo and benzoato or silanecarboxylato bridges," *Bulletin of the Chemical Society of Japan*, vol. 65, no. 10, pp. 2739–2747, 1992.

[133] O. Castell, J. Miralles, and R. Caballol, "Structural dependence of the singlet-triplet gap in doubly bridged copper dimers: a variational {CI} calculation," *Chemical Physics*, vol. 179, no. 3, pp. 377–384, 1994.

[134] A. Bencini and D. Gatteschi, "Xα-sw calculations of the electronic structure and magnetic properties of weakly coupled transition-metal clusters. the $[cu_2cl_6]^{2-}$ dimers," *Journal of the American Chemical Society*, vol. 108, no. 19, pp. 5763–5771, 1986. PMID: 22175325.

[135] J. Miralles, J.-P. Daudey, and R. Caballol, "Variational calculation of small energy differences. the singlet-triplet gap in $[cu_2cl_6]^{2-}$," *Chemical Physics Letters*, vol. 198, no. 6, pp. 555–562, 1992.

[136] J. Cabrero, N. B. Amor, C. de Graaf, F. Illas, and R. Caballol, "Ab initio study of the exchange coupling in oxalato-bridged cu(ii) dinuclear complexes," *The Journal of Physical Chemistry A*, vol. 104, no. 44, pp. 9983–9989, 2000.

[137] C. Adamo, V. Barone, A. Bencini, F. Totti, and I. Ciofini, "On the calculation and modeling of magnetic exchange interactions in weakly bonded systems: the case of the ferromagnetic copper(ii) μ_2-azido bridged complexes," *Inorganic Chemistry*, vol. 38, no. 9, pp. 1996–2004, 1999. PMID: 11670977.

[138] F. F. de Biani, E. Ruiz, J. Cano, J. J. Novoa, and S. Alvarez, "Magnetic coupling in end-to-end azido-bridged copper and nickel binuclear complexes: A theoretical study," *Inorganic Chemistry*, vol. 39, no. 15, pp. 3221–3229, 2000. PMID: 11196857.

[139] L. Noodleman, "Valence bond description of antiferromagnetic coupling in transition metal dimers," *The Journal of Chemical Physics*, vol. 74, no. 10, pp. 5737–5743, 1981.

[140] L. Noodleman, D. A. Case, and A. Aizman, "Broken symmetry analysis of spin coupling in iron-sulfur clusters," *Journal of the American Chemical Society*, vol. 110, no. 4, pp. 1001–1005, 1988.

[141] L. Noodleman, C. Y. Peng, D. A. Case, and J.-M. Mouesca, "Orbital interactions, electron delocalization and spin coupling in iron-sulfur clusters," *Coordination Chemistry Reviews*, vol. 144, pp. 199–244, 1995.

[142] R. L. Martin and F. Illas, "Antiferromagnetic exchange interactions from hybrid density functional theory," *Physical Review Letters*, vol. 79, pp. 1539–1542, Aug 1997.

[143] R. Caballol, O. Castell, F. Illas, I. de P. R. Moreira, and J. P. Malrieu, "Remarks on the proper use of the broken symmetry approach to magnetic coupling," *The Journal of Physical Chemistry A*, vol. 101, no. 42, pp. 7860–7866, 1997.

[144] H. Chevreau, I. de P. R. Moreira, B. Silvi, and F. Illas, "Charge density analysis of triplet and broken symmetry states relevant to magnetic coupling in systems with localized spin moments," *The Journal of Physical Chemistry A*, vol. 105, no. 14, pp. 3570–3577, 2001.

[145] R. Valero, R. Costa, I. de P. R. Moreira, D. G. Truhlar, and F. Illas, "Performance of the m06 family of exchange-correlation functionals for predicting magnetic coupling in organic and inorganic molecules," *The Journal of Chemical Physics*, vol. 128, no. 11, 2008.

[146] P. Rivero, I. de P. R. Moreira, F. Illas, and G. E. Scuseria, "Reliability of range-separated hybrid functionals for describing magnetic coupling in molecular systems," *The Journal of Chemical Physics*, vol. 129, no. 18, 2008.

[147] P. Rivero, I. de P. R. Moreira, G. E. Scuseria, and F. Illas, "Description of magnetic interactions in strongly correlated solids via range-separated hybrid functionals," *Physical Review B*, vol. 79, p. 245129, Jun 2009.

[148] P. Rivero, C. Loschen, I. de P. R. Moreira, and F. Illas, "Performance of plane-wave-based lda+u and gga+u approaches to describe magnetic coupling in molecular systems," *Journal of Computational Chemistry*, vol. 30, no. 14, pp. 2316–2326, 2009.

[149] F. Illas, I. de P. R. Moreira, J. M. Bofill, and M. Filatov, "Spin symmetry requirements in density functional theory: The proper way to predict magnetic coupling constants in molecules and solids," *Theoretical Chemistry Accounts*, vol. 116, no. 4-5, pp. 587–597, 2006.

[150] F. Illas, I. de P. R. Moreira, J. M. Bofill, and M. Filatov, "Extent and limitations of density-functional theory in describing magnetic systems," *Physical Review B*, vol. 70, p. 132414, Oct 2004.

[151] R. Costa, I. de P. R. Moreira, S. Youngme, K. Siriwong, N. Wannarit, and F. Illas,

"Toward the design of ferromagnetic molecular complexes: Magnetostructural correlations in ferromagnetic triply bridged dinuclear cu(ii) compounds containing carboxylato and hydroxo bridges," *Inorganic Chemistry*, vol. 49, no. 1, pp. 285–294, 2010. PMID: 19957951.

[152] C. Lee, W. Yang, and R. G. Parr, "Development of the colle-salvetti correlation-energy formula into a functional of the electron density," *Physical Review B*, vol. 37, pp. 785–789, Jan 1988.

[153] Y. Zhao and D. G. Truhlar, "A new local density functional for main-group thermochemistry, transition metal bonding, thermochemical kinetics, and noncovalent interactions," *The Journal of Chemical Physics*, vol. 125, no. 19, 2006.

[154] Y. Zhao and D. G. Truhlar, "The m06 suite of density functionals for main group thermochemistry, thermochemical kinetics, noncovalent interactions, excited states, and transition elements: two new functionals and systematic testing of four m06-class functionals and 12 other functionals," *Theoretical Chemistry Accounts*, vol. 120, no. 1-3, pp. 215–241, 2008.

[155] O. A. Vydrov, J. Heyd, A. V. Krukau, and G. E. Scuseria, "Importance of short-range versus long-range hartree-fock exchange for the performance of hybrid density functionals," *The Journal of Chemical Physics*, vol. 125, no. 7, 2006.

[156] O. A. Vydrov and G. E. Scuseria, "Assessment of a long-range corrected hybrid functional," *The Journal of Chemical Physics*, vol. 125, no. 23, 2006.

[157] M. Filatov and S. Shaik, "Application of spin-restricted open-shell kohn-sham method to atomic and molecular multiplet states," *The Journal of Chemical Physics*, vol. 110, no. 1, pp. 116–125, 1999.

[158] M. Filatov and S. Shaik, "Diradicaloids: Description by the spin-restricted, ensemble-referenced kohn-sham density functional method," *The Journal of Physical Chemistry A*, vol. 104, no. 28, pp. 6628–6636, 2000.

[159] A. Kazaryan, J. Heuver, and M. Filatov, "Excitation energies from spin-restricted ensemble-referenced kohnsham method: A state-average approach," *The Journal of Physical Chemistry A*, vol. 112, no. 50, pp. 12980–12988, 2008. PMID: 18616234.

[160] D. Cremer, M. Filatov, V. Polo, E. Kraka, and S. Shaik, "Implicit and explicit coverage of multi-reference effects by density functional theory," *International Journal of Molecular Sciences*, vol. 3, no. 6, p. 604, 2002.

[161] I. de P. R. Moreira and F. Illas, "A unified view of the theoretical description of magnetic coupling in molecular chemistry and solid state physics," *Physical Chemistry Chemical Physics*, vol. 8, pp. 1645–1659, 2006.

[162] D. Muñoz, C. D. Graaf, and F. Illas, "Putting error bars on the ab initio theoretical estimates of the magnetic coupling constants: The parent compounds of superconducting cuprates as a case study," *Journal of Computational Chemistry*, vol. 25, no. 10, pp. 1234–1241, 2004.

[163] J. Casanovas, J. Rubio, and F. Illas, "Origin of magnetic coupling in la_2cuo_4," *Phys. Rev. B*, vol. 53, pp. 945–951, Jan 1996.

[164] C. de Graaf, C. Sousa, I. de P. R. Moreira, and F. Illas, "Multiconfigurational perturbation theory: An efficient tool to predict magnetic coupling parameters in biradicals, molecular complexes, and ionic insulators," *The Journal of Physical Chemistry A*, vol. 105, no. 50, pp. 11371–11378, 2001.

[165] A. J. Pérez-Jiménez, J. M. Pérez-Jordá, I. de P. R. Moreira, and F. Illas, "Merging multiconfigurational wavefunctions and correlation functionals to predict magnetic coupling constants," *Journal of Computational Chemistry*, vol. 28, no. 16, pp. 2559–2568, 2007.

[166] J. Miralles, O. Castell, R. Caballol, and J.-P. Malrieu, "Specific {CI} calculation of energy differences: Transition energies and bond energies," *Chemical Physics*,

vol. 172, no. 1, pp. 33–43, 1993.

[167] B. O. Roos, K. Andersson, M. P. Fülscher, P. A. Malmqvist, L. Serrano-Andrés, K. Pierloot, and M. Merchán, *Multiconfigurational Perturbation Theory: Applications in Electronic Spectroscopy*, vol. XCIII, ch. Advances in Chemical Physics: New Methods in Computational Quantum Mechanics, pp. 219–332. John Wiley & Sons: New York, 1996.

[168] B. O. Roos, P. Linse, P. E. M. Siegbahn, and M. R. A. Blomberg, "A simple method for the evaluation of the second-order-perturbation energy from external double-excitations with a {CASSCF} reference wavefunction," *Chemical Physics*, vol. 66, no. 1-2, pp. 197–207, 1982.

[169] K. Andersson, P.-Å. Malmqvist, B. O. Roos, A. J. Sadlej, and K. Wolinski, "Second-order perturbation theory with a casscf reference function," *The Journal of Physical Chemistry*, vol. 94, no. 14, pp. 5483–5488, 1990.

[170] H. Zhekova, M. Seth, and T. Ziegler, "Introduction of a new theory for the calculation of magnetic coupling based on spin-flip constricted variational density functional theory. application to trinuclear copper complexes which model the native intermediate in multicopper oxidases," *Journal of Chemical Theory and Computation*, vol. 7, no. 6, pp. 1858–1866, 2011.

[171] H. R. Zhekova, M. Seth, and T. Ziegler, "Calculation of the exchange coupling constants of copper binuclear systems based on spin-flip constricted variational density functional theory," *The Journal of Chemical Physics*, vol. 135, no. 18, 2011.

[172] A. I. Krylov, "Spin-flip equation-of-motion coupled-cluster electronic structure method for a description of excited states, bond breaking, diradicals, and triradicals," *Accounts of Chemical Research*, vol. 39, no. 2, pp. 83–91, 2006. PMID: 16489727.

[173] I. Shavitt, "The method of configuration interaction," in *Methods of Electronic Structure Theory* (H. F. S. III, ed.), vol. 3 of *Modern Theoretical Chemistry*, pp. 189–275, Springer US, 1977.

[174] W. Koch and M. C. Holthausen, eds., *A Chemist's Guide to Density Functional Theory*. New York: Wiley-VCH, 2 ed., 2001.

[175] S. Hirata and M. Head-Gordon, "Time-dependent density functional theory within the tamm-dancoff approximation," *Chemical Physics Letters*, vol. 314, no. 3-4, pp. 291–299, 1999.

[176] F. Wang and T. Ziegler, "Time-dependent density functional theory based on a noncollinear formulation of the exchange-correlation potential," *The Journal of Chemical Physics*, vol. 121, no. 24, pp. 12191–12196, 2004.

[177] F. Wang and T. Ziegler, "The performance of time-dependent density functional theory based on a noncollinear exchange-correlation potential in the calculations of excitation energies," *The Journal of Chemical Physics*, vol. 122, no. 7, 2005.

[178] F. Wang and T. Ziegler, "Use of noncollinear exchange-correlation potentials in multiplet resolutions by time-dependent density functional theory," *International Journal of Quantum Chemistry*, vol. 106, no. 12, pp. 2545–2550, 2006.

[179] F. Wang and W. Liu, "Comparison of different polarization schemes in open-shell relativistic density functional calculations," *Journal of the Chinese Chemical Society*, vol. 50, no. 3B, pp. 597–606, 2003.

[180] J. Gao, W. Liu, B. Song, and C. Liu, "Time-dependent four-component relativistic density functional theory for excitation energies," *The Journal of Chemical Physics*, vol. 121, no. 14, pp. 6658–6666, 2004.

[181] G. te Velde, F. M. Bickelhaupt, E. J. Baerends, C. F. Guerra, S. J. A. van Gisbergen, J. G. Snijders, and T. Ziegler, "Chemistry with adf," *Journal of Computational Chemistry*, vol. 22, no. 9, pp. 931–967, 2001.

[182] G. Christou, S. P. Perlepes, E. Libby, K. Folting, J. C. Huffman, R. J. Webb, and D. N. Hendrickson, "Preparation and properties of the triply bridged, ferromagnetically coupled dinuclear copper(ii) complexes $[cu_2(oac)_3(bpy)_2](clo_4)$ and $[cu_2(oh)(h_2o)(oac)(bpy)_2](clo_4)_2$," *Inorganic Chemistry*, vol. 29, no. 19, pp. 3657–3666, 1990.

[183] M. A. Buijse, "Program for symmetry calculations." clebschegordan.exe.

[184] L. Pu, B. Twamley, and P. P. Power, "Synthesis and characterization of 2,6-trip$_2$h$_3$c$_6$pbpbc$_6$h$_3$-2,6-trip$_2$ (trip = c$_6$h$_2$-2,4,6-i-pr$_3$): A stable heavier group 14 element analogue of an alkyne," *Journal of the American Chemical Society*, vol. 122, no. 14, pp. 3524–3525, 2000.

[185] M. Stender, A. D. Phillips, R. J. Wright, and P. P. Power, "Synthesis and characterization of a digermanium analogue of an alkyne," *Angewandte Chemie International Edition*, vol. 41, no. 10, pp. 1785–1787, 2002.

[186] C. Cui, M. Brynda, M. M. Olmstead, and P. P. Power, "Synthesis and characterization of the non-kekulé, singlet biradicaloid ar′ge(μ-nsime$_3$)$_2$gear′ (ar′ = 2,6-dipp$_2$c$_6$h$_3$, dipp = 2,6-i-pr$_2$c$_6$h$_3$)," *Journal of the American Chemical Society*, vol. 126, no. 21, pp. 6510–6511, 2004. PMID: 15161252.

[187] C. Cui, M. M. Olmstead, and P. P. Power, "Reactivity of ar′gegear′ (ar′ = c$_6$h$_3$-2,6-dipp$_2$, dipp = c$_6$h$_3$-2,6-ipr$_2$) toward alkynes: Isolation of a stable digermacyclobutadiene," *Journal of the American Chemical Society*, vol. 126, no. 16, pp. 5062–5063, 2004. PMID: 15099077.

[188] M. Stender, A. D. Phillips, and P. P. Power, "Formation of [ar*GeCH$_2$C(Me)C(Me)CH$_2$ch$_2$c(me)=]$_2$ (ar* = c$_6$h$_3$-2,6-trip$_2$; trip = c$_6$h$_2$-2,4,6-i-pr$_3$) via reaction of ar*gegear* with 2,3-dimethyl-1,3-butadiene: evidence for the existence of a germanium analogue of an alkyne," *Chemical Communications*, pp. 1312–1313, 2002.

[189] A. D. Phillips, R. J. Wright, M. M. Olmstead, and P. P. Power, "Synthesis and characterization of 2,6-dipp$_2$-h$_3$c$_6$snsnc$_6$h$_3$-2,6-dipp$_2$ (dipp = c$_6$h$_3$-2,6-pr$^i_2$): A tin analogue of an alkyne," *Journal of the American Chemical Society*, vol. 124, no. 21, pp. 5930–5931, 2002. PMID: 12022812.

[190] C. R. Landis and F. Weinhold, "Origin of trans-bent geometries in maximally bonded transition metal and main group molecules," *Journal of the American Chemical Society*, vol. 128, no. 22, pp. 7335–7345, 2006. PMID: 16734489.

[191] Y. Jung, M. Brynda, P. P. Power, and M. Head-Gordon, "Ab initio quantum chemistry calculations on the electronic structure of heavier alkyne congeners: Diradical character and reactivity," *Journal of the American Chemical Society*, vol. 128, no. 22, pp. 7185–7192, 2006. PMID: 16734470.

[192] P. P. Power, "Main-group elements as transition metals," *Nature*, vol. 463, pp. 171–177, Jan 2010.

[193] Y. Chen, M. Hartmann, M. Diedenhofen, and G. Frenking, "Theoretical studies of inorganic compounds. part 15. turning a transition state into a minimum - the nature of the bonding in diplumbylene compounds rpbpbr (r = h, ar)," *Angewandte Chemie, International Edition*, vol. 40, no. 11, pp. 2052–2055, 2001.

[194] M. Lein, A. Krapp, and G. Frenking, "Why do the heavy-atom analogues of acetylene e$_2$h$_2$ (e = si-pb) exhibit unusual structures?," *Journal of the American Chemical Society*, vol. 127, no. 17, pp. 6290–6299, 2005. PMID: 15853336.

[195] H. Lischka and H. J. Koehler, "Ab initio investigation on the lowest singlet and triplet state of disilyne (si$_2$h$_2$)," *Journal of the American Chemical Society*, vol. 105, no. 22, pp. 6646–6649, 1983.

[196] B. T. Colegrove and H. F. Schaefer, "trans-dimethyldisilyne (si$_2$(ch$_3$)$_2$): an achievable synthetic target," *Journal of the American Chemical Society*, vol. 113, no. 5, pp. 1557–1561, 1991.

[197] M. Bogey, H. Bolvin, C. Demuynck, and J. L. Destombes, "Nonclassical double-bridged structure in silicon-containing molecules: Experimental evidence in si_2h_2 from its submillimeter-wave spectrum," *Physical Review Letters*, vol. 66, pp. 413–416, Jan 1991.

[198] G. Trinquier and J. P. Malrieu, "Nonclassical distortions at multiple bonds," *Journal of the American Chemical Society*, vol. 109, no. 18, pp. 5303–5315, 1987.

[199] E. A. Carter and W. A. Goddard, "Relation between singlet-triplet gaps and bond energies," *The Journal of Physical Chemistry*, vol. 90, no. 6, pp. 998–1001, 1986.

[200] Y.-K. Han, C. Bae, Y. S. Lee, and S. Y. Lee, "Spin-orbit effects on structures of closed-shell polyatomic molecules containing heavy atoms calculated by two-component hartree-fock method," *Journal of Computational Chemistry*, vol. 19, no. 13, pp. 1526–1533, 1998.

[201] R. S. Grev, B. J. Deleeuw, and H. F. S. III, "Germanium-germanium multiple bonds: The singlet electronic ground state of ge_2h_2," *Chemical Physics Letters*, vol. 165, no. 2-3, pp. 257–264, 1990.

[202] Z. Palagyi, H. F. S. III, and E. Kapuy, "ge_2h_2: a germanium-containing molecule with a low-lying monobridged equilibrium geometry," *Journal of the American Chemical Society*, vol. 115, no. 15, pp. 6901–6903, 1993.

[203] N. O. J. Malcolm, R. J. Gillespie, and P. L. A. Popelier, "A topological study of homonuclear multiple bonds between the elements of group 14," *Journal of Chemical Society, Dalton Transactions*, pp. 3333–3341, 2002.

[204] L. T. Allen, W. H. Fink, and P. P. Power, "Theoretical studies of multiple bonds in gallium-gallium and germanium-germanium compounds," *Journal of Chemical Society, Dalton Transactions*, pp. 407–412, 2000.

[205] A. Sekiguchi, S. S. Zigler, R. West, and J. Michl, "A synthon for the silicon-silicon triple bond," *Journal of the American Chemical Society*, vol. 108, no. 14,

pp. 4241–4242, 1986.

[206] Y. Yamaguchi, B. H. DeLeeuw, C. A. Richards, H. F. Schaefer, and G. Frenking, "Application of the energy derivative analysis method to the cis monobridged equilibrium structures al_2h_2, si_2h_2, ga_2h_2, and ge_2h_2 and the comparable stationary points of b_2h_2 and c_2h_2," *Journal of the American Chemical Society*, vol. 116, no. 26, pp. 11922–11930, 1994.

[207] L. C. Snyder, Z. R. Wasserman, and J. W. Moskowitz, "Stability and bonding of disilyne and its isomers: A generalized valence bond-effective potential study," *International Journal of Quantum Chemistry*, vol. 21, no. 3, pp. 565–579, 1982.

[208] J. S. Binkley, "Theoretical study of the relative stabilities of c_2h_2 and si_2h_2 conformers," *Journal of the American Chemical Society*, vol. 106, no. 3, pp. 603–609, 1984.

[209] B. T. Luke, J. A. Pople, M. B. Krogh-Jespersen, Y. Apeloig, M. Karni, J. Chandrasekhar, and R. v. R. Schleyer, "A theoretical survey of unsaturated or multiply bonded and divalent silicon compounds. comparison with carbon analogs," *Journal of the American Chemical Society*, vol. 108, no. 2, pp. 270–284, 1986.

[210] N. Wiberg, W. Niedermayer, G. Fischer, H. Nöth, and M. Suter, "Synthesis, structure and dehalogenation of the disilene rclsi=siclr [r = $(tbu_3si)_2$mesi]," *European Journal of Inorganic Chemistry*, vol. 2002, no. 5, pp. 1066–1070, 2002.

[211] N. Wiberg, S. K. Vasisht, G. Fischer, and P. Mayer, "Disilynes. iii [1] a relatively stable disilyne rsi≡sir (r = sime$(sitbu_3)_2$)," *Zeitschrift für anorganische und allgemeine Chemie*, vol. 630, no. 12, pp. 1823–1828, 2004.

[212] A. Sekiguchi, R. Kinjo, and M. Ichinohe, "A stable compound containing a silicon-silicon triple bond," *Science*, vol. 305, no. 5691, pp. 1755–1757, 2004.

[213] S. Nagase, K. Kobayashi, and N. Takagi, "Triple bonds between heavier group 14 elements. a theoretical approach," *Journal of Organometallic Chemistry*,

vol. 611, no. 1-2, pp. 264–271, 2000.

[214] N. Takagi and S. Nagase, "Substituent effects on germanium-germanium and tin-tin triple bonds," *Organometallics*, vol. 20, no. 26, pp. 5498–5500, 2001.

[215] Z. Zhu, R. C. Fischer, B. D. Ellis, E. Rivard, W. A. Merrill, M. M. Olmstead, P. P. Power, J. D. Guo, S. Nagase, and L. Pu, "Synthesis, characterization and real molecule dft calculations for neutral organogallium(i) aryl dimers and monomers: Weakness of gallium–gallium bonds in digallenes and digallynes," *Chemistry - A European Journal*, vol. 15, no. 21, pp. 5263–5272, 2009.

[216] T. Ziegler and A. Rauk, "Carbon monoxide, carbon monosulfide, molecular nitrogen, phosphorus trifluoride, and methyl isocyanide as .sigma. donors and .pi. acceptors. a theoretical study by the hartree-fock-slater transition-state method," *Inorganic Chemistry*, vol. 18, no. 7, pp. 1755–1759, 1979.

[217] M. P. Mitoraj, A. Michalak, and T. Ziegler, "A combined charge and energy decomposition scheme for bond analysis," *Journal of Chemical Theory and Computation*, vol. 5, no. 4, pp. 962–975, 2009.

[218] R. Kurczab, M. P. Mitoraj, A. Michalak, and T. Ziegler, "Theoretical analysis of the resonance assisted hydrogen bond based on the combined extended transition state method and natural orbitals for chemical valence scheme," *The Journal of Physical Chemistry A*, vol. 114, no. 33, pp. 8581–8590, 2010. PMID: 20099799.

[219] S. Grimme, S. Ehrlich, and L. Goerigk, "Effect of the damping function in dispersion corrected density functional theory," *Journal of Computational Chemistry*, vol. 32, no. 7, pp. 1456–1465, 2011.

[220] J. P. Perdew., K. Burken, and M. Ernzerhof, "Generalized gradient approximation made simple," *Physical Review Letters*, vol. 77, pp. 3865–3868, Oct 1996.

[221] E. van Lenthe, E. J. Baerends, and J. G. Snijders., "Relativistic total energy using regular approximations," *The Journal of Chemical Physics*, vol. 101, no. 11,

pp. 9783–9792, 1994.

[222] E. van Lenthe, E. J. Baerends, and J. G. Snijders, "Relativistic regular two-component hamiltonians," *The Journal of Chemical Physics*, vol. 99, no. 6, pp. 4597–4610, 1993.

[223] W. H. E. Schwarz and H. Schmidbaur, "Observations and descriptions versus explanations-an example: Does nature, does theory know about steric hindrance?," *Chemistry - A European Journal*, vol. 18, no. 15, pp. 4470–4479, 2012.

[224] P. E. M. Siegbahn, J. Almlöf, A. Heiberg, and B. O. Roos, "The complete active space scf (casscf) method in a newton-raphson formulation with application to the hno molecule," *The Journal of Chemical Physics*, vol. 74, no. 4, pp. 2384–2396, 1981.

[225] F. Furche, "On the density matrix based approach to time-dependent density functional theory," *Journal of Chemical Physics*, vol. 114, no. 14, pp. 5882–5992, 2001.

[226] T. Ziegler, M. Seth, M. Krykunov, J. Autschbach, and F. Wang, "Is charge transfer transitions really too difficult for standard density functionals or are they just a problem for time-dependent density functional theory based on a linear response approach," *Journal of Molecular Structure:* $\{THEOCHEM\}$, vol. 914, no. 1-3, pp. 106–109, 2009.

[227] F. Jensen, ed., *Introduction to Computational Chemistry*. New York: Wiley, 2 ed., 2006.

[228] T. Helgaker, P. Jørgensen, and J. Olsen, eds., *Molecular Electronic Structure Theory*. New York: Wiley, 2000.

[229] F. M., "Assessment of density functional methods for obtaining geometries at conical intersections in organic molecules," *Journal of Chemical Theory and Computation*, vol. 9, no. 10, pp. 4526–4541, 2013. PMID: 24124402.

[230] A. Görling, "Density-functional theory beyond the hohenberg-kohn theorem," *Physical Review A*, vol. 59, pp. 3359–3374, May 1999.

[231] R. Gaudoin and K. Burke, "Lack of hohenberg-kohn theorem for excited states," *Physical Review Letters*, vol. 93, pp. 173001–1–4, Oct 2005.

[232] T. Ziegler, M. Krykunov, and J. Autschbach, "Derivation of the rpa (random phase approximation) equation of atddft (adiabatic time dependent density functional ground state response theory) from an excited state variational approach based on the ground state functional," *Journal of Chemical Theory and Computation*, vol. 10, no. 9, pp. 3980–3986, 2014.

[233] M. Krykunov, S. Grimme, and T. Ziegler, "Accurate theoretical description of the ^1l_a and ^1l_b excited states in acenes using the all order constricted variational density functional theory method and the local density approximation," *Journal of Chemical Theory and Computation*, vol. 8, no. 11, pp. 4434–4440, 2012.

[234] H. Zhekova, M. Krykunov, J. Autschbach, and T. Ziegler, "Application of time dependent and time independent density functional theory to the first π to π^* transition in cyanine dyes," *Journal of Chemical Theory and Computation*, vol. 10, no. 8, pp. 3299–3307, 2014.

[235] E. V. Lenthe and E. J. Baerends, "Optimized slater-type basis sets for the elements 1-118," *Journal of Computational Chemistry*, vol. 24, no. 9, pp. 1142–1156, 2003.

[236] Y. Akinaga and S. Ten-no, "Range-separation by the yukawa potential in long-range corrected density functional theory with gaussian-type basis functions," *Chemical Physics Letters*, vol. 462, no. 4-6, pp. 348–351, 2008.

[237] Y. Akinaga and S. Ten-No, "Intramolecular charge-transfer excitation energies from range-separated hybrid functionals using the yukawa potential," *International Journal of Quantum Chemistry*, vol. 109, no. 9, pp. 1905–1914, 2009.

[238] M. Seth and T. Ziegler, "Range-separated exchange functionals with slater-type functions," *Journal of Chemical Theory and Computation*, vol. 8, no. 3, pp. 901–907, 2012.

[239] C. Matteo, M. Odelius, D. Nordlund, A. Nilsson, and L. G. M. Pettersson, "Half or full core-hole in density functional theory x-ray absorption spectrum calculations of water?," *Physical Chemistry Chemical Physics*, vol. 15, pp. 2854–2858, 2005.

[240] S. B. Ben-Shlomo and U. Kaldor, "N_2 excitations below 15 ev by the multireference coupled-cluster method," *Journal of Chemical Physics*, vol. 92, no. 6, pp. 3680–3683, 1990.

[241] T. Trickl, E. F. Cronwell, Y. T. Lee, and A. H. Kung, "State-selective ionization of nitrogen in the $\chi\ ^2\gamma_g^+\ v_+ = 0$ and $v_+ = 1$ states by two-color $(1 + 1)$ photon excitation near threshold," *Journal of Chemistry Physics*, vol. 91, no. 10, pp. 6006–6012, 1989.

[242] W. Hwang, Y.-K. Kim, and M. E. Rudd, "New model for electron-impact ionization cross sections of molecules," *Journal of Chemical Physics*, vol. 104, no. 8, pp. 2956–2966, 1996.

[243] M. Gruening, O. V. Gritsenko, S. J. A. van Gisbergen, and E. J. Baerends, "On the required shape corrections to the local density and generalized gradient approximations to the kohn-sham potentials for molecular response calculations of (hyper)polarizabilities and excitation energies," *Chemical Physics*, vol. 116, no. 22, pp. 9591–9601, 2002.

[244] J. Autschbach and M. Srebro, "Delocalization error and functional tuning in kohn-sham calculations of molecular properties," *Accounts of Chemical Research*, vol. 47, no. 8, pp. 2592–2602, 2014. PMID: 24968277.

[245] E. S. Nielsen, P. Jørgensen, and J. Oddershede, "Transition moments and dynamic polarizabilities in a second order polarization propagator approach," *The Journal of Chemical Physics*, vol. 73, no. 12, pp. 6238–6246, 1980.

[246] D. J. Clouthier and D. A. Ramsay, "The spectroscopy of formaldehyde and thioformaldehyde," *Annual Review of Physical Chemistry*, vol. 34, no. 1, pp. 31–58, 1983.

[247] R. Dressler and M. Allan, "A dissociative electron attachment, electron transmission, and electron energy-loss study of the temporary negative ion of acetylene," *The Journal of Chemical Physics*, vol. 87, no. 8, pp. 4510–4518, 1987.

[248] A. S. Zyubin and A. M. Mebel, "Accurate prediction of excitation energies to high-lying rydberg electronic states: Rydberg states of acetylene as a case study," *The Journal of Chemical Physics*, vol. 119, no. 13, pp. 6581–6587, 2003.

[249] A. Chutjian, R. I. Hall, and S. Trajmar, "Electron-impact excitation of h_2o and d_2o at various scattering angles and impact energies in the energy-loss range 4.2-12 ev," *The Journal of Chemical Physics*, vol. 63, no. 2, pp. 892–898, 1975.

[250] L. Serrano-Andrés, M. Merchán, I. Nebot-Gil, R. Lindh, and B. O. Roos, "Towards an accurate molecular orbital theory for excited states: Ethene, butadiene, and hexatriene," *The Journal of Chemical Physics*, vol. 98, no. 4, pp. 3151–3162, 1993.

[251] M. Buijse and E. J. Baerends, "Analysis of nondynamical correlation in the metalligand bond. pauli repulsion and orbital localization in mno_4," *Journal of Chemical Physics*, vol. 93, no. 6, pp. 4129–4141, 1990.

[252] H. Hillier and V. R. Saunders, "Ab initio calculations of the excited states of the permanganate and chromate ions," *Chemical Physics Letters*, vol. 9, no. 3, pp. 219–221, 1971.

[253] H. Johansen, "Analysis of a configuration interaction calculation for a charge transfer transition in mno_4," *Molecular Physics*, vol. 49, no. 5, pp. 1209–1216, 1983.

[254] O. Gunnarsson and B. I. Lundqvist, "Exchange and correlation in atoms, molecules, and solids by the spin-density-functional formalism," *Physical Review B*, vol. 13, pp. 4274–4298, May 1976.

[255] U. von Barth, "Local-density theory of multiplet structure," *Physical Review A*, vol. 20, pp. 1693–1703, Oct 1979.

[256] D. Jacquemin, V. Wathelet, E. A. Perpète, and C. Adamo, "Extensive td-dft benchmark: Singlet-excited states of organic molecules," *Journal of Chemical Theory and Computation*, vol. 5, no. 9, pp. 2420–2435, 2009.

[257] D. Jacquemin, E. A. Perpète, I. Ciofini, and C. Adamo, "Accurate simulation of optical properties in dyes," *Accounts of Chemical Research*, vol. 42, no. 2, pp. 326–334, 2009. PMID: 19113946.

[258] D. Jacquemin, E. A. Perpète, G. E. Scuseria, I. Ciofini, and C. Adamo, "Td-dft performance for the visible absorption spectra of organic dyes: Conventional versus long-range hybrids," *Journal of Chemical Theory and Computation*, vol. 4, no. 1, pp. 123–135, 2008.

[259] S. Grimme and F. Neese, "Double-hybrid density functional theory for excited electronic states of molecules," *Journal of Chemical Physics*, vol. 127, no. 15, pp. 154116–1–8, 2007.

[260] R. Send, O. Valsson, and C. Filippi, "Electronic excitations of simple cyanine dyes: Reconciling density functional and wave function methods," *Journal of Chemical Theory and Computation*, vol. 7, no. 2, pp. 444–455, 2011.

[261] D. Jacquemin, Y. Zhao, R. Valero, C. Adamo, I. Ciofini, and D. G. Truhlar, "Verdict: Time-dependent density functional theory not guilty of large errors for

cyanines," *Journal of Chemical Theory and Computation*, vol. 8, no. 4, pp. 1255–1259, 2012.

[262] B. Moore and J. Autschbach, "Longest-wavelength electronic excitations of linear cyanines: The role of electron delocalization and of approximations in time-dependent density functional theory," *Journal of Chemical Theory and Computation*, vol. 9, no. 11, pp. 4991–5003, 2013.

[263] L. Jose, M. Seth, and T. Ziegler, "Molecular and vibrational structure of tetroxo d0 metal complexes in their excited states. a study based on time-dependent density functional calculations and franckcondon theory," *Journal of Physical Chemistry A*, vol. 116, no. 7, pp. 1864–1876, 2012. PMID: 22280538.

[264] J. Neugebauer, E. J. Baerends, and M. Nooijen, "Vibronic structure of the permanganate absorption spectrum from time-dependent density functional calculations," *Journal of Physical Chemistry A*, vol. 109, no. 6, pp. 1168–1179, 2005. PMID: 16833427.

[265] M. Rudolph, T. Ziegler, and J. Autschbach, "Time-dependent density functional theory applied to ligand-field excitations and their circular dichroism in some transition metal complexes," *Chemical Physics*, vol. 391, no. 1, pp. 92–100, 2011.

[266] H. Nakai, Y. Ohmori, and H. Nakatsuji, "Theoretical study on the ground and excited states of mno_4," *Journal of Chemical Physics*, vol. 95, no. 11, pp. 8287–8291, 1991.

[267] M. Nooijen, "Combining coupled cluster and perturbation theory," *Journal of Chemical Physics*, vol. 111, no. 24, pp. 10815–10826, 1999.

[268] M. Nooijen and V. Lotrich, "Extended similarity transformed equation-of-motion coupled cluster theory (extended-steom-cc): Applications to doubly excited

states and transition metal compounds," *Journal of Chemical Physics*, vol. 113, no. 2, pp. 494–507, 2000.

[269] J. Su, W.-H. Xu, C.-F. Xu, W. H. E. Schwarz, and J. Li, "Theoretical studies on the photoelectron and absorption spectra of mno_4^- and tco_4^-," *Inorganic Chemistry*, vol. 52, no. 17, pp. 9867–9874, 2013. PMID: 23957772.

[270] N. M. S. Almeida, R. G. McKinlay, and M. J. Paterson, "Excited electronic states of mno_4: Challenges for wavefunction and density functional response theories," *Chemical Physics*, vol. 446, p. 86, 2015.

[271] T. Ziegler, "A chronicle about the development of electronic structure theories for transition metal complexes," in *Molecular Electronic Structures of Transition Metal Complexes II* (D. M. P. Mingos, P. Day, and J. P. Dahl, eds.), vol. 143 of *Structure and Bonding*, pp. 1–38, Springer Berlin Heidelberg, 2012.

[272] J. P. Perdew, K. Burke, and M. Ernzerhof, "Perdew, burke, and ernzerhof reply," *Physical Review Letters*, vol. 80, pp. 891–891, Jan 1998.

[273] M. Ernzerhof and G. E. Scuseria, "Assessment of the perdew-burke-ernzerhof exchange-correlation functional," *Journal of Chemical Physics*, vol. 110, no. 11, pp. 5029–5036, 1999.

[274] C. Adamo and V. Barone, "Toward reliable density functional methods without adjustable parameters: The pbe0 model," *Journal of Chemical Physics*, vol. 110, no. 13, pp. 6158–6170, 1999.

[275] K. H. Johnson and F. C. Smith, "Scattered-wave model for the electronic structure and optical properties of the permanganate ion," *Chemical Physics Letters*, vol. 10, no. 2, pp. 219–223, 1971.

[276] S. J. A. van Gisbergen, J. G. Snijders, and E. J. Baerends, "Implementation of time-dependent density functional response equations," *Computer Physics Communications*, vol. 118, no. 23, pp. 119–138, 1999.

[277] D. Escudero and W. Thiel, "Assessing the density functional theory-based multireference configuration interaction (dft/mrci) method for transition metal complexes," *Journal of Chemical Physics*, vol. 140, no. 19, pp. 194105–1–8, 2014.

[278] J. Houmøller, S. H. Kaufman, K. Støchkel, L. C. Tribedi, S. B. Nielsen, and J. M. Weber, "On the photoabsorption by permanganate ions in vacuo and the role of a single water molecule. new experimental benchmarks for electronic structure theory," *ChemPhysChem*, vol. 14, no. 6, pp. 1133–1137, 2013.

[279] S. Grimme and M. Waletzke, "A combination of kohn-sham density functional theory and multi-reference configuration interaction methods," *Journal of Chemical Physics*, vol. 111, no. 13, pp. 5645–5655, 1999.

[280] P. Boulet, H. Chermette, C. Daul, F. Gilardoni, F. Rogemond, J. Weber, and G. Zuber, "Absorption spectra of several metal complexes revisited by the time-dependent density-functional theory-response theory formalism," *Journal of Physical Chemistry A*, vol. 105, no. 5, pp. 885–894, 2001.

[281] M. Dierksen and S. Grimme, "Density functional calculations of the vibronic structure of electronic absorption spectra," *Journal of Chemical Physics*, vol. 120, no. 8, pp. 3544–3554, 2004.

[282] M. Dierksen and S. Grimme, "The vibronic structure of electronic absorption spectra of large molecules: A time-dependent density functional study on the influence of exact hartreefock exchange," *Journal of Physical Chemistry A*, vol. 108, no. 46, pp. 10225–10237, 2004.

[283] A. Klamt and G. Schüürmann, "Cosmo: A new approach to dielectric screening in solvent with explicit expressions for the screening energy and its gradient," *Journal of Chemical Society, Perkin Transactions 2*, vol. 2, pp. 799–805, 1993.

[284] C. C. Pye and T. Ziegler, "An implementation of the conductor-like screening

model of solvation within the amsterdam density functional package," *Theoretical Chemistry Accounts*, vol. 101, no. 6, pp. 396–408, 1999.

[285] H. U. Güdel and C. J. Ballhausen, "Low temperature absorption spectra of tco_4 and reo_4 in $kclo_4$," *Theoretica Chimica Acta*, vol. 25, no. 4, pp. 331–337, 1972.

[286] C. J. Ballhausen and I. B. Trabjerg, "Confirmation of the red band system in mno_4 as $t_1 \leftarrow 1a_1$ from the effect of pressure on single crystal absorption spectra," *Molecular Physics*, vol. 24, no. 4, pp. 689–693, 1972.

[287] C. J. M. Coremans, J. H. van der Waals, J. Konijnenberg, A. H. Huizer, and C. A. G. O. Varma, "A search for the metastable triplet states of cro_4^{2-} and mno_4^{-} by transient absorption spectroscopy in crystals at low temperature," *Chemical Physics Letters*, vol. 125, no. 56, pp. 514–519, 1986.

[288] N. A. Beach and H. B. Gray, "Electronic structures of metal hexacarbonyls," *Journal of the American Chemical Society*, vol. 90, no. 21, pp. 5713–5721, 1968.

[289] J. B. Ayers and W. H. Waggoner, "Synthesis and properties of two series of heavy metal hexacyanoferrates," *Journal of Inorganic and Nuclear Chemistry*, vol. 33, no. 3, pp. 721–733, 1971.

[290] S. Vancoillie, H. Zhao, V. T. Tran, M. F. A. Hendrickx, and K. Pierloot, "Multiconfigurational second-order perturbation theory restricted active space (raspt2) studies on mononuclear first-row transition-metal systems," *Journal of Chemical Theory and Computation*, vol. 7, no. 12, pp. 3961–3977, 2011.

[291] K. Pierloot, E. Tsokos, and L. G. Vanquickenborne, "Optical spectra of ni(co)$_4$ and cr(co)$_6$ revisited," *The Journal of Physical Chemistry*, vol. 100, no. 41, pp. 16545–16550, 1996.

[292] K. Pierloot, E. V. Praet, L. G. Vanquickenborne, and B. O. Roos, "Systematic *ab initio* study of the ligand field spectra of hexacyanometalate complexes," *The Journal of Physical Chemistry*, vol. 97, no. 47, pp. 12220–12228, 1993.

[293] A. L. B. Formiga, S. Vancoillie, and K. Pierloot, "Electronic spectra of n-heterocyclic pentacyanoferrate(ii) complexes in different solvents, studied by multiconfigurational perturbation theory," *Inorganic Chemistry*, vol. 52, no. 18, pp. 10653–10663, 2013. PMID: 23992205.

[294] B. J. Coe, A. Avramopoulos, M. G. Papadopoulos, K. Pierloot, S. Vancoillie, and H. Reis, "Theoretical modelling of photoswitching of hyperpolarisabilities in ruthenium complexes," *Chemistry - A European Journal*, vol. 19, no. 47, pp. 15955–15963, 2013.

[295] D. Escudero and L. González, "Raspt2/rasscf vs range-separated/hybrid dft methods: Assessing the excited states of a ru(ii)bipyridyl complex," *Journal of Chemical Theory and Computation*, vol. 8, no. 1, pp. 203–213, 2012.

[296] C. de Graaf and C. Sousa, "Study of the light-induced spin crossover process of the [fe(ii)(bpy)$_3$]$^{2+}$ complex," *Chemistry - A European Journal*, vol. 16, no. 15, pp. 4550–4556, 2010.

[297] K. Pierloot, "Calculations of electronic spectra of transition metal complexes," in *Computational Photochemistry* (M. Olivucci, ed.), vol. 16 of *Theoretical and Computational Chemistry*, pp. 279–315, Elsevier, 2005.

[298] J. I. Fuks and N. T. Maitra, "Charge transfer in time-dependent density-functional theory: Insights from the asymmetric hubbard dimer," *Physical Review A*, vol. 89, p. 062502, Jun 2014.

[299] N. Kuritz, T. Stein, R. Baer, and L. Kronik, "Charge-transfer-like $\pi \rightarrow \pi^*$ excitations in time-dependent density functional theory: A conundrum and its solution," *Journal of Chemical Theory and Computation*, vol. 7, no. 8, pp. 2408–2415, 2011.

[300] B. M. Wong and J. G. Cordaro, "Coumarin dyes for dye-sensitized solar cells: A long-range-corrected density functional study," *The Journal of Chemical*

Physics, vol. 129, no. 21, 2008.

[301] A. W. Lange, M. A. Rohrdanz, and J. M. Herbert, "Charge-transfer excited states in a π-stacked adenine dimer, as predicted using long-range-corrected time-dependent density functional theory," *The Journal of Physical Chemistry B*, vol. 112, no. 20, pp. 6304–6308, 2008. PMID: 18438995.

[302] E. Epifanovsky, I. Polyakov, B. Grigorenko, A. Nemukhin, and A. I. Krylov, "Quantum chemical benchmark studies of the electronic properties of the green fluorescent protein chromophore. 1. electronically excited and ionized states of the anionic chromophore in the gas phase," *Journal of Chemical Theory and Computation*, vol. 5, no. 7, pp. 1895–1906, 2009.

[303] N. Govind, M. Valiev, L. Jensen, and K. Kowalski, "Excitation energies of zinc porphyrin in aqueous solution using long-range corrected time-dependent density functional theory," *The Journal of Physical Chemistry A*, vol. 113, no. 21, pp. 6041–6043, 2009. PMID: 19405520.

[304] J. Andzelm, B. C. Rinderspacher, A. Rawlett, J. Dougherty, R. Baer, and N. Govind, "Performance of dft methods in the calculation of optical spectra of tcf-chromophores," *Journal of Chemical Theory and Computation*, vol. 5, no. 10, pp. 2835–2846, 2009.

[305] A. Mohammed, H. Agren, and P. Norman, "Time-dependent density functional theory for resonant properties: resonance enhanced raman scattering from the complex electric-dipole polarizability," *Physical Chemistry Chemical Physics*, vol. 11, pp. 4539–4548, 2009.

[306] M. Pastore, E. Mosconi, F. D. Angelis, and M. Grätzel, "A computational investigation of organic dyes for dye-sensitized solar cells: Benchmark, strategies, and open issues," *The Journal of Physical Chemistry C*, vol. 114, no. 15, pp. 7205–7212, 2010.

[307] S. Kümmel and L. Kronik, "Orbital-dependent density functionals: Theory and applications," *Reviews of Modern Physics*, vol. 80, pp. 3–60, Jan 2008.

[308] T. Leininger, H. Stoll, H.-J. Werner, and A. Savin, "Combining long-range configuration interaction with short-range density functionals," *Chemical Physics Letters*, vol. 275, no. 3-4, pp. 151–160, 1997.

[309] T. M. Henderson, B. G. Janesko, and G. E. Scuseria, "Generalized gradient approximation model exchange holes for range-separated hybrids," *The Journal of Chemical Physics*, vol. 128, no. 19, 2008.

[310] B. M. Wong and T. H. Hsieh, "Optoelectronic and excitonic properties of oligoacenes: Substantial improvements from range-separated time-dependent density functional theory," *Journal of Chemical Theory and Computation*, vol. 6, no. 12, pp. 3704–3712, 2010. PMID: 21170284.

[311] R. M. Richard and J. M. Herbert, "Time-dependent density-functional description of the 1la state in polycyclic aromatic hydrocarbons: Charge-transfer character in disguise?," *Journal of Chemical Theory and Computation*, vol. 7, no. 5, pp. 1296–1306, 2011.

[312] E. D. Hedegård, F. Heiden, S. Knecht, E. Fromager, and H. J. A. Jensen, "Assessment of charge-transfer excitations with time-dependent, range-separated density functional theory based on long-range mp2 and multiconfigurational self-consistent field wave functions," *The Journal of Chemical Physics*, vol. 139, no. 18, 2013.

[313] P. Borowski, K. D. Jordan, J. Nichols, and P. Nachtigall, "Investigation of a hybrid tcscf-dft procedure," *Theoretical Chemistry Accounts*, vol. 99, no. 2, pp. 135–140, 1998.

[314] J. Gräfenstein, E. Kraka, and D. Cremer, "Density functional theory for open-shell singlet biradicals," *Chemical Physics Letters*, vol. 288, no. 5-6, pp. 593–

602, 1998.

[315] M. Filatov and S. Shaik, "A spin-restricted ensemble-referenced kohn-sham method and its application to diradicaloid situations," *Chemical Physics Letters*, vol. 304, no. 5-6, pp. 429–437, 1999.

[316] S. Grimme, "Density functional calculations with configuration interaction for the excited states of molecules," *Chemical Physics Letters*, vol. 259, no. 1-2, pp. 128–137, 1996.

[317] I. Seidu, H. R. Zhekova, M. Seth, and T. Ziegler, "Calculation of exchange coupling constants in triply-bridged dinuclear cu(ii) compounds based on spin-flip constricted variational density functional theory," *The Journal of Physical Chemistry A*, vol. 116, no. 9, pp. 2268–2277, 2012. PMID: 22320859.

[318] A. Rosa, E. J. Baerends, S. J. A. van Gisbergen, E. van Lenthe, J. A. Groeneveld, and J. G. Snijders, "Electronic spectra of $m(co)_6$ (m = cr, mo, w) revisited by a relativistic tddft approach," *Journal of the American Chemical Society*, vol. 121, no. 44, pp. 10356–10365, 1999.

[319] P. Hummel, J. Oxgaard, W. A. G. III, and H. B. Gray, "Ligand-field excited states of metal hexacarbonyls," *Inorganic Chemistry*, vol. 44, no. 7, pp. 2454–2458, 2005. PMID: 15792483.

[320] N. B. Amor, S. Villaume, D. Maynau, and C. Daniel, "The electronic spectroscopy of transition metal carbonyls: The tough case of $cr(co)_6$," *Chemical Physics Letters*, vol. 421, no. 4-6, pp. 378–382, 2006.

[321] C. Pollak, A. Rosa, and E. J. Baerends, "Crco photodissociation in $cr(co)_6$: reassessment of the role of ligand-field excited states in the photochemical dissociation of metalligand bonds," *Journal of the American Chemical Society*, vol. 119, no. 31, pp. 7324–7329, 1997.

[322] S. Villaume, A. Strich, C. Daniel, S. A. Perera, and R. J. Bartlett, "A coupled cluster study of the electronic spectroscopy and photochemistry of cr(co)$_6$," *Physical Chemistry Chemical Physics*, vol. 9, pp. 6115–6122, 2007.

[323] G. Cooper, J. C. Green, M. P. Payne, B. R. Dobson, and I. H. Hillier, "Photoelectron spectroscopy with variable photon energy. a study of the metal hexacarbonyls m(co)$_6$ where m = cr, mo, and w," *Journal of the American Chemical Society*, vol. 109, no. 13, pp. 3836–3843, 1987.

[324] M. Schreiber, M. R. Silva-Junior, S. P. A. Sauer, and W. Thiel, "Benchmarks for electronically excited states: Caspt2, cc2, ccsd, and cc3," *The Journal of Chemical Physics*, vol. 128, no. 13, pp. 134110–1–25, 2008.

[325] R. A. Mata and H.-J. Werner, "Calculation of smooth potential energy surfaces using local electron correlation methods," *The Journal of Chemical Physics*, vol. 125, no. 18, pp. 184110–1–9, 2006.

[326] I.-M. Høyvik, K. Kristensen, B. Jansik, and P. Jiørgensen, "The divide-expand-consolidate family of coupled cluster methods: Numerical illustrations using second order møller-plesset perturbation theory," *The Journal of Chemical Physics*, vol. 136, no. 1, pp. 014105–1–16, 2012.

[327] C. Riplinger and F. Neese, "An efficient and near linear scaling pair natural orbital based local coupled cluster method," *The Journal of Chemical Physics*, vol. 138, no. 3, pp. 034106–1–18, 2013.

[328] R. L. Martin, "Natural transition orbitals," *Journal of Chemical Physics*, vol. 118, no. 11, pp. 4775–4777, 2003.

[329] S. Dick, "Crystal structure of tris(2,2'-bipyridine)iron(ii) bis(hexafluorophosphate), $(c_{10}h_8n_2)_3fe(pf_6)_2$," *Zeitschrift für Kristallographie - New Crystal Structures*, vol. 213, no. 2, p. 356, 1998.

[330] A. Szabo and N. S. Ostlund, *Many-Electron Wave Functions and Operators*, ch. 2, pp. 70–72.

Copyright Permissions

Appendix G

Seventh Appendix

Copyright Clearance Center RightsLink®

Home | Create Account | Help | Live Chat

ACS Publications
Most Trusted. Most Cited. Most Read.

Title: Calculation of Exchange Coupling Constants in Triply-Bridged Dinuclear Cu(II) Compounds Based on Spin-Flip Constricted Variational Density Functional Theory

Author: Issaka Seidu, Hristina R. Zhekova, Michael Seth, et al

Publication: The Journal of Physical Chemistry A

Publisher: American Chemical Society

Date: Mar 1, 2012

Copyright © 2012, American Chemical Society

LOGIN

If you're a copyright.com user, you can login to RightsLink using your copyright.com credentials. Already **a RightsLink user** or want to learn more?

PERMISSION/LICENSE IS GRANTED FOR YOUR ORDER AT NO CHARGE

This type of permission/license, instead of the standard Terms & Conditions, is sent to you because no fee is being charged for your order. Please note the following:

- Permission is granted for your request in both print and electronic formats, and translations.
- If figures and/or tables were requested, they may be adapted or used in part.
- Please print this page for your records and send a copy of it to your publisher/graduate school.
- Appropriate credit for the requested material should be given as follows: "Reprinted (adapted) with permission from (COMPLETE REFERENCE CITATION). Copyright (YEAR) American Chemical Society." Insert appropriate information in place of the capitalized words.
- One-time permission is granted only for the use specified in your request. No additional uses are granted (such as derivative works or other editions). For any other uses, please submit a new request.

BACK | CLOSE WINDOW

Copyright © 2016 Copyright Clearance Center, Inc. All Rights Reserved. Privacy statement. Terms and Conditions.
Comments? We would like to hear from you. E-mail us at customercare@copyright.com

Appendix H

eighth Appendix

Copyright Clearance Center RightsLink®

Home | Create Account | Help | Live Chat

ACS Publications
Most Trusted. Most Cited. Most Read.

Title: Role Played by Isopropyl Substituents in Stabilizing the Putative Triple Bond in Ar'EEAr' [E = Si, Ge, Sn; Ar' = C6H3-2,6-(C6H3-2,6-Pri2)2] and Ar*PbPbAr* [Ar* = C6H3-2,6-(C6H2-2,4,6-Pri3)2]

Author: Issaka Seidu, Michael Seth, Tom Ziegler

Publication: Inorganic Chemistry

Publisher: American Chemical Society

Date: Aug 1, 2013

Copyright © 2013, American Chemical Society

LOGIN

If you're a copyright.com user, you can login to RightsLink using your copyright.com credentials. Already **a RightsLink user** or want to learn more?

PERMISSION/LICENSE IS GRANTED FOR YOUR ORDER AT NO CHARGE

This type of permission/license, instead of the standard Terms & Conditions, is sent to you because no fee is being charged for your order. Please note the following:

- Permission is granted for your request in both print and electronic formats, and translations.
- If figures and/or tables were requested, they may be adapted or used in part.
- Please print this page for your records and send a copy of it to your publisher/graduate school.
- Appropriate credit for the requested material should be given as follows: "Reprinted (adapted) with permission from (COMPLETE REFERENCE CITATION). Copyright (YEAR) American Chemical Society." Insert appropriate information in place of the capitalized words.
- One-time permission is granted only for the use specified in your request. No additional uses are granted (such as derivative works or other editions). For any other uses, please submit a new request.

BACK | CLOSE WINDOW

Copyright © 2016 Copyright Clearance Center, Inc. All Rights Reserved. Privacy statement. Terms and Conditions.
Comments? We would like to hear from you. E-mail us at customercare@copyright.com

Appendix I

Ninth Appendix

Copyright Clearance Center RightsLink®

Home | Create Account | Help | Live Chat

ACS Publications
Most Trusted. Most Cited. Most Read.

Title: Applications of Time-Dependent and Time-Independent Density Functional Theory to Rydberg Transitions

Author: Issaka Seidu, Mykhaylo Krykunov, Tom Ziegler

Publication: The Journal of Physical Chemistry A

Publisher: American Chemical Society

Date: May 1, 2015

Copyright © 2015, American Chemical Society

LOGIN

If you're a copyright.com user, you can login to RightsLink using your copyright.com credentials. Already **a RightsLink user** or want to learn more?

PERMISSION/LICENSE IS GRANTED FOR YOUR ORDER AT NO CHARGE

This type of permission/license, instead of the standard Terms & Conditions, is sent to you because no fee is being charged for your order. Please note the following:

- Permission is granted for your request in both print and electronic formats, and translations.
- If figures and/or tables were requested, they may be adapted or used in part.
- Please print this page for your records and send a copy of it to your publisher/graduate school.
- Appropriate credit for the requested material should be given as follows: "Reprinted (adapted) with permission from (COMPLETE REFERENCE CITATION). Copyright (YEAR) American Chemical Society." Insert appropriate information in place of the capitalized words.
- One-time permission is granted only for the use specified in your request. No additional uses are granted (such as derivative works or other editions). For any other uses, please submit a new request.

BACK | CLOSE WINDOW

Copyright © 2016 Copyright Clearance Center, Inc. All Rights Reserved. Privacy statement. Terms and Conditions.
Comments? We would like to hear from you. E-mail us at customercare@copyright.com

Appendix J

Tenth Appendix

Copyright Clearance Center RightsLink®

Home | Create Account | Help | Live Chat

ACS Publications
Most Trusted. Most Cited. Most Read.

Title: Applications of Time-Dependent and Time-Independent Density Functional Theory to Electronic Transitions in Tetrahedral d0 Metal Oxides

Author: Issaka Seidu, Mykhaylo Krykunov, Tom Ziegler

Publication: Journal of Chemical Theory and Computation

Publisher: American Chemical Society

Date: Sep 1, 2015

Copyright © 2015, American Chemical Society

LOGIN

If you're a copyright.com user, you can login to RightsLink using your copyright.com credentials. Already **a RightsLink user** or want to learn more?

PERMISSION/LICENSE IS GRANTED FOR YOUR ORDER AT NO CHARGE

This type of permission/license, instead of the standard Terms & Conditions, is sent to you because no fee is being charged for your order. Please note the following:

- Permission is granted for your request in both print and electronic formats, and translations.
- If figures and/or tables were requested, they may be adapted or used in part.
- Please print this page for your records and send a copy of it to your publisher/graduate school.
- Appropriate credit for the requested material should be given as follows: "Reprinted (adapted) with permission from (COMPLETE REFERENCE CITATION). Copyright (YEAR) American Chemical Society." Insert appropriate information in place of the capitalized words.
- One-time permission is granted only for the use specified in your request. No additional uses are granted (such as derivative works or other editions). For any other uses, please submit a new request.

BACK | CLOSE WINDOW

Copyright © 2016 Copyright Clearance Center, Inc. All Rights Reserved. Privacy statement. Terms and Conditions.
Comments? We would like to hear from you. E-mail us at customercare@copyright.com

Appendix K

Eleventh Appendix